WISSENSCHAFTLICHE MITTEILUNGEN

aus dem Institut für Meteorologie der Universität Leipzig

BAND 59

M. Wendisch (Hrsg.)

Meteorologische Arbeiten XXVI

Jahresbericht 2020

UNIVERSITÄT LEIPZIG

Wissenschaftliche Mitteilungen

aus dem
Institut für Meteorologie der Universität Leipzig

ISBN **978-3-9814401-9-5**

Meteorologische Arbeiten (XXVI) und Jahresbericht 2020 des Instituts für Meteorologie der Universität Leipzig

Hrsg.: Manfred Wendisch

Leipzig 2021

Band 59

Radar observations of geomagnetic disturbance effects on midlatitude mesosphere/lower thermosphere dynamics

Jacobi, Ch.[1], Lilienthal, F.[1], Korotyshkini, D.[2], Merzlyakov, E.[3], Stober G.[4]

[1] *Institute for Meteorology, Leipzig University, Stephanstr. 3, 04103 Leipzig, Germany, E-mail: jacobi@uni-leipzig.de*
[2] *Kazan (Volga Region) Federal University, Kazan, Russia*
[3] *Institute for Experimental Meteorology, Obninsk, Russia*
[4] *University of Bern, Institute of Applied Physics, Microwave Physics, Bern, Switzerland*

Summary: We analyse mesosphere/lower thermosphere (MLT) mean winds and tidal amplitudes observed by two meteor radars at Collm (51°N, 13°E) and Kazan (56°N, 49°E) with regard to their response to geomagnetic disturbances. To this end, we compare daily winds and tidal amplitudes for very quiet (Ap≤5) and unsettled/disturbed (Ap≥20) geomagnetic conditions. Zonal winds in the MLT tend to be more eastward/westward during disturbed conditions for all seasons. The summer equatorward meridional wind jet is weaker for disturbed geomagnetic conditions. Tendencies for geomagnetic effects on mean winds over Collm and Kazan qualitatively agree during most of the year. For the diurnal tide, amplitudes in summer are smaller in the mesosphere and greater in the lower thermosphere, but no clear tendency is seen for winter. Semidiurnal tidal amplitudes increase during geomagnetic active days in summer and winter. Terdiurnal amplitudes are slightly reduced in the mesosphere during disturbed days, but no clear effect is visible for the lower thermosphere. Overall, while there is a noticeable effect of geomagnetic variability on the mean wind, the effect on tidal amplitudes, except for the semidiurnal tide, is relatively small and partly different over Collm and Kazan.

Zusammenfassung: Wir untersuchen die Reaktion des mittleren Windes und der Gezeitenamplituden in der Mesosphäre / unteren Thermosphäre, gemessen mit zwei Meteorradaren in Collm (51°N, 13°E) und Kasan (56°N, 49°E) in Bezug auf den Effekt geomagnetischer Störungen. Dazu werden tägliche mittlere Winde und Gezeitenamplituden für sehr ruhige (Ap≤5) und unruhige / gestörte (Ap≥20) geomagnetische Bedingungen verglichen. Zonale Winde sind bei gestörten Bedingungen für alle Jahreszeiten mehr nach Osten / Westen gerichtet. Der sommerliche äquatorwärts gerichtete meridionale Jet ist bei gestörten geomagnetischen Bedingungen schwächer. Die Tendenzen für geomagnetische Effekte auf die mittleren Winde über Collm und Kasan stimmen während des größten Teils des Jahres qualitativ überein. Für die täglichen Gezeiten sind die Amplituden im Sommer in der Mesosphäre kleiner und in der unteren Thermosphäre größer, für den Winter ist jedoch keine eindeutige Tendenz zu erkennen. Die halbtägigen Gezeitenamplituden nehmen an geomagnetischen aktiven Tagen im Sommer und Winter zu. Dritteltägige Amplituden sind in der Mesosphäre an gestörten Tagen leicht reduziert, aber kein deutlicher Effekt ist für die untere Thermosphäre sichtbar. Während die geomagnetische Variabilität einen spürbaren Effekt auf den mittleren Wind hat, ist der Effekt auf die Gezeitenamplituden mit Ausnahme der halbtäglichen Gezeiten insgesamt relativ gering und teilweise für Collm und Kasan unterschiedlich.

1 Introduction

It has long been known that not only the ionized upper atmosphere, but also the neutral middle atmosphere, i.e. the stratosphere, mesosphere, and lower thermosphere, is influenced by external drivers. The possibly most well known one is solar variability (e.g., Keuer et al., 2007; Beig, 2011; Stober et al., 2014; Qian et al., 2019), which influences the middle atmosphere on the 11-year cycle time scale, but also on shorter time scales like the 27-day solar rotation (e.g., Rong et al., 2020). Another factor is particle precipitation, which may influence the atmosphere from the lower thermosphere down to the surface (Mironova et al., 2015) in a more irregular manner and which is also related to geomagnetic variability.

The exact effect of geomagnetic activity on the neutral atmosphere to date is not fully quantified. With the availability of radar observations in the mesosphere/lower thermosphere (MLT) region, the search for geomagnetic signatures has been performed based on these data, which are essentially horizontal winds at 80–100 km altitude. This has been done on the basis of case studies, epoch analyses (Singer et al., 1994), or in a more general statistical manner, i.e. in an attempt to quantify the influence of geomagnetic activity, often described by the Ap or Kp indices, on MLT winds (Fahrutdinova et al., 1999, 2001, 2013). The latter has also been done by including geomagnetic indices such as the Ap index in empirical relationships based on linear models of MLT wind variability (Pancheva et al., 2005). The response of the MLT to geomagnetic disturbances is not always clear. For example, Zhang et al. (2003) reported a different effect over Europe and Alaska, and related this to different effects during daytime and nighttime. This was also reported by Pancheva et al. (2007). Also Singer et al. (1994) revealed latitudinal differences of geomagnetic wind response.

Several analyses have beeen performed to investigate geomagnetic activity effects on the MLT over Kazan (Fahrutdinova et al., 1999, 2001, 2013). Parameters that had been taken into account were mean winds, diurnal (DT) and semidiurnal (SDT) tides, and also irregular structures. While there was a relatively clear effect on the mean wind, particularly a decrease of the mesospheric jets with increasing geomagnetic activity, effects on tides and especially irregular structures (connected with gravity waves) seemed to be less clear.

In this paper, we will analyse more recent MLT winds from radar observations at Kazan, in an attempt to substantiate the earlier measurements in the literature. Furthermore, we will make use of the Collm radar at a similar latitude, in order to analyze common features and possible non-zonal structures in the reaction of the MLT to geomagnetic activity. We will, in addition to the DT and SDT, also include the terdiurnal tide (TDT) signature into the analysis. The TDT has been shown to be a non-negligible factor in MLT dynamics and has been analysed by several MLT radars already (Beldon et al., 2006; Jacobi, 2012; Liu et al., 2019).

2 Instrument and dataset description

At Collm (51.3°N, 13.0°E), a VHF all-sky meteor radar, distributed under the brand name SKiYMET, was installed in summer 2004 (Jacobi et al., 2007). The radar operates on 36.2 MHz, and the main parameter observed are the MLT radial winds determined

from the Doppler shift of individual meteor trails. Details of the radar system and the radial wind determination principle can be found in Stober et al. (2012), and Lilienthal and Jacobi (2015). During 2015 the radar was upgraded by increasing the peak power to 15 kW, and replacing the Yagi antennas by crossed dipoles, while maintaining the transmit frequency (Stober et al., 2018). The heights of the individual meteor trail reflections vary between about 75 and 110 km, and the maximum meteor count rate is found at an altitude slightly below 90 km (e.g., Stober et al., 2008).

The Kazan (56°N, 49°E) SKiYMET radar has been operating since 2015 (Korotyshkin et al., 2019b). This radar is equipped with a 15 kW transmitter, allowing high meteor rates and thus providing sufficient statistics for whole day observation in the height region 80-100 km. Transmitting frequency is 29.75 MHz. The transmitting antenna consists of two 3-element Yagis. The receiving system consists of five 2-elements Yagis. Collm and Kazan mean winds and SDT parameters have been analyzed by Korotyshkin et al. (2019a). They found a non-significant mean wind difference connected with stationary planetary waves and a slight difference in latitude. They also found SDT differences that were attributed to nonmigrating, i.e. not sun-synchronous, tidal components.

The meteor radar hourly winds are computed applying a modified version of the so-called all-sky fit (Hocking et al., 2001; Stober et al., 2018). Daily mean winds have been calculated from these, and tidal amplitudes and phases have been calculated using the adaptive spectral filter described in Stober et al. (2017, 2020), and Baumgarten and Stober (2019). We use total tidal amplitudes calculated as the square-root of sum of the squared zonal and meridional amplitudes. We used data from August 2015, which is the beginning of the Kazan observations, to June 2020.

To characterize the geomagnetic activity, daily Ap indices (GFZ, 2020) have been used. We characterize quiet conditions by Ap≤5, which is actually a very strict requirement. Disturbed conditions are assumed to be connected with Ap≥20, also including unsettled geomagnetic conditions. This resulted in a total of days between about 170 (in autumn) and 250 (winter/spring) for the undisturbed conditions and between about 30 (winter to summer) and 70 (autumn) for disturbed/unsettled conditions. The change with season is due to the annual/semiannual variation in geomagnetic activity (e.g., Le Mouël et al., 2004). A histogram of daily Ap indices during the time interval of the investigation is shown in Fig. 1. We calculated 2015-2020 mean seasonal 3-monthly means of the daily mean winds and tidal amplitudes for both conditions.

3 Results

We present results for four seasons, namely winter (December - February, DJF), spring (March - May, MAM), summer (June - August, JJA) and autumn (September - November, SON). This includes seasonal means of mean winds for disturbed and undisturbed conditions and their differences for both stations in Figs. 2 and 3, and corresponding results for tidal amplitudes in Figs. 4 - 6.

3.1 Mean winds

Fig. 2 shows the 2015-2020 mean vertical profiles of the daily mean zonal wind for four seasons over Collm and Kazan for geomagnetically quiet conditions (respective left plots)

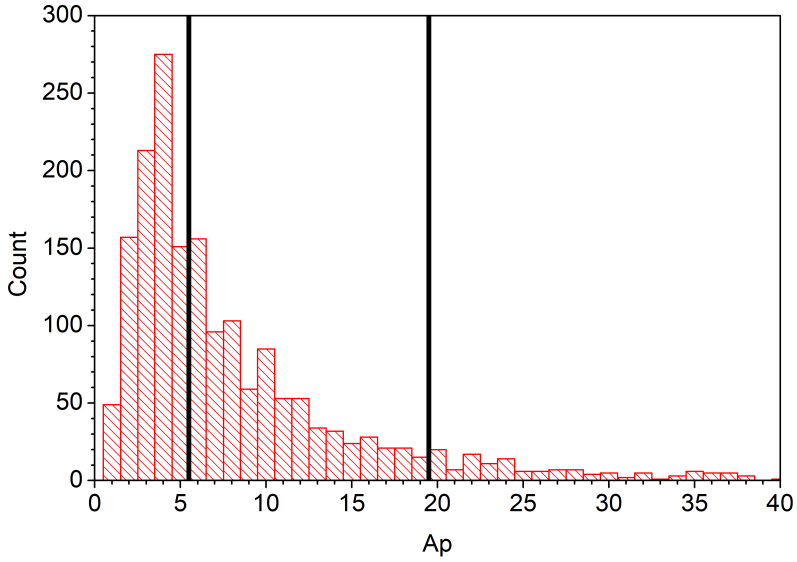

Figure 1: *Histogram of Ap indices during August 2015 and June 2020. The vertical lines show the chosen ranges for undisturbed and disturbed conditions.*

and the differences between winds during disturbed and quiet conditions (respective right plots). The error bars show the standard error of the mean winds. Since the number of individual daily means is on the order of 200 for undisturbed conditions, the standard error is very small, especially in summer when the day-to-day variability of winds is small. We also calculated winds for 5<Ap<20, and they mostly lie between those ones for disturbed and undisturbed conditions, if the differences between these are non-negligible. We do not show them here in order not to overload the figures.

The zonal wind vertical profiles show the known seasonal cycle of zonal mean winds (e.g., Schminder et al., 1997; Jacobi, 2012; Korotyshkin et al., 2019a), with easterly mesospheric winds in spring/summer and a wind reversal in the lower thermosphere, and mesospheric westerlies in autumn/winter with an indication of the lower thermospheric wind reversal which is, however, generally seen above the height range considered. The differences between disturbed and undisturbed conditions are on the order of 5 m/s, and they are positive (i.e. winds are more westerly during disturbed conditions) in the upper mesosphere and negative (more easterly winds during disturbed conditions) in the lower thermosphere throughout the year and qualitatively independent on season. Note that this leads to a weaker vertical wind gradient during disturbed conditions. This feature is mainly confirmed by Kazan radio meteor observations in the 1980s and 90s (Fahrutdinova et al., 1999, 2001). Note, however, that the differences are significant only at the upper altitudes during the equinoxes.

Arnold and Robinson (2001) modeled the response of the winter middle atmosphere on increased magnetic flux and found cooling in the polar stratosphere which leads to increased mesospheric zonal winds confirmed by our observations. Yi et al. (2018) observed decreasing density of the mid- to high-latitude mesosphere during geomagnetic storms, and proposed that this also influences mesospheric dynamics. Singer et al.

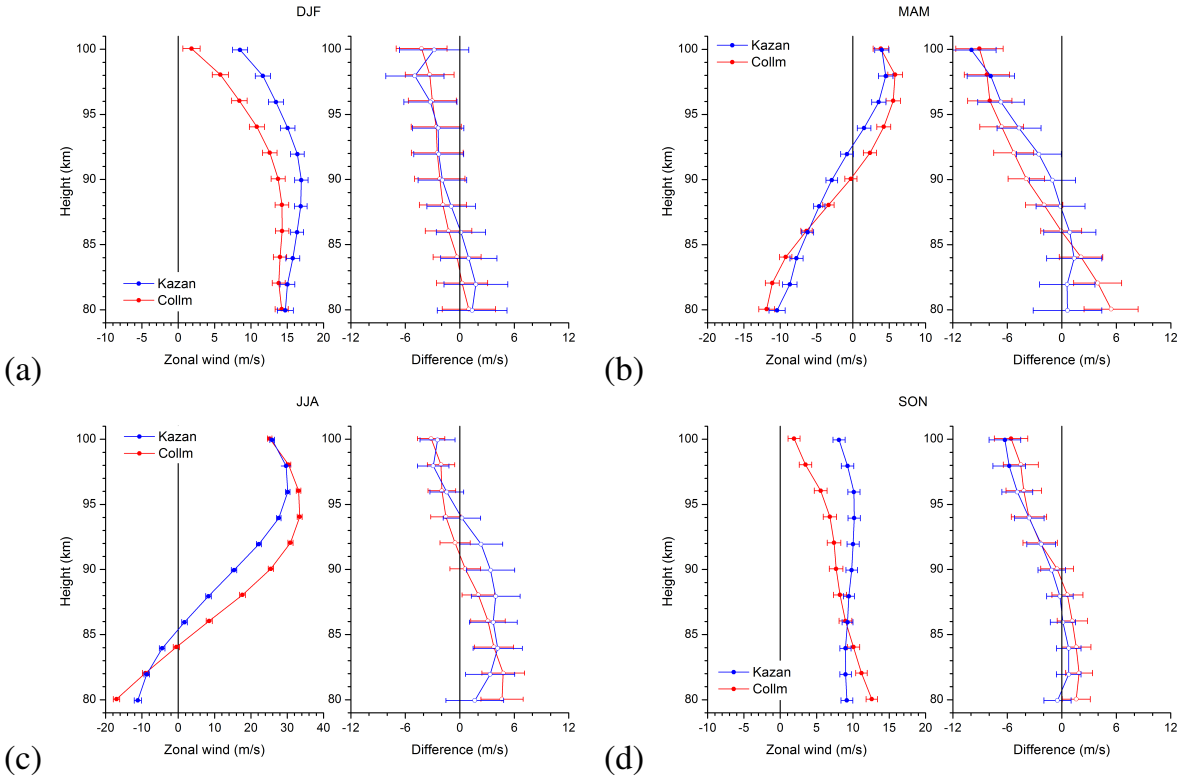

Figure 2: *Left plots: Long-term mean seasonal mean zonal mean winds during (a) DJF (b) MAM (c) JJA (d) SON over Kazan (blue) and Collm (red) for undisturbed conditions. Data are averages over* 2015 - 2020. *Error bars show standard error. The right plots in the respective panels show the differences for disturbed - undisturbed conditions. Solid symbols on the right plots indicate differences larger than 3 times the standard error.*

(1994), however, have shown negative wind effects at about 90 km based on a number of different radar systems over Europe but, on the other hand, also weak effect over Siberia and positive effect over Canada. This may be due to geomagnetic influences on the polar vortex, which may be shifted during geomagnetic storms (Hocke, 2017).

The meridonal winds in Fig. 3 are weaker, and southward in spring/summer and weak in winter as also known from earlier observations (Jacobi, 2012; Korotyshkin et al., 2019a). The differences are positive in spring and summer, i.e. the southward jet is weaker by about 4 m/s during disturbed conditions over both Collm and Kazan. Again, the differences are mostly small and in most cases not significant. This weaker meridional wind jet is connected with the weaker vertical zonal wind gradient (see Jacobi, 2012) and can be explained by weaker gravity wave filtering and resulting residual circulation in the case of a weaker mesospheric wind jet. During winter, the differences are again positive for Collm, but change sign with height over Kazan. During autumn the differences are weaker and differ over Collm and Kazan. The positive effect has already been shown by Fahrutdinova et al. (1999) for earlier Kazan observations, but has not been reported by Pancheva et al. (2005) from UK measurements at 90 km. On the other hand, Singer et al. (1994) reported weak geomagnetic effect on the mean wind.

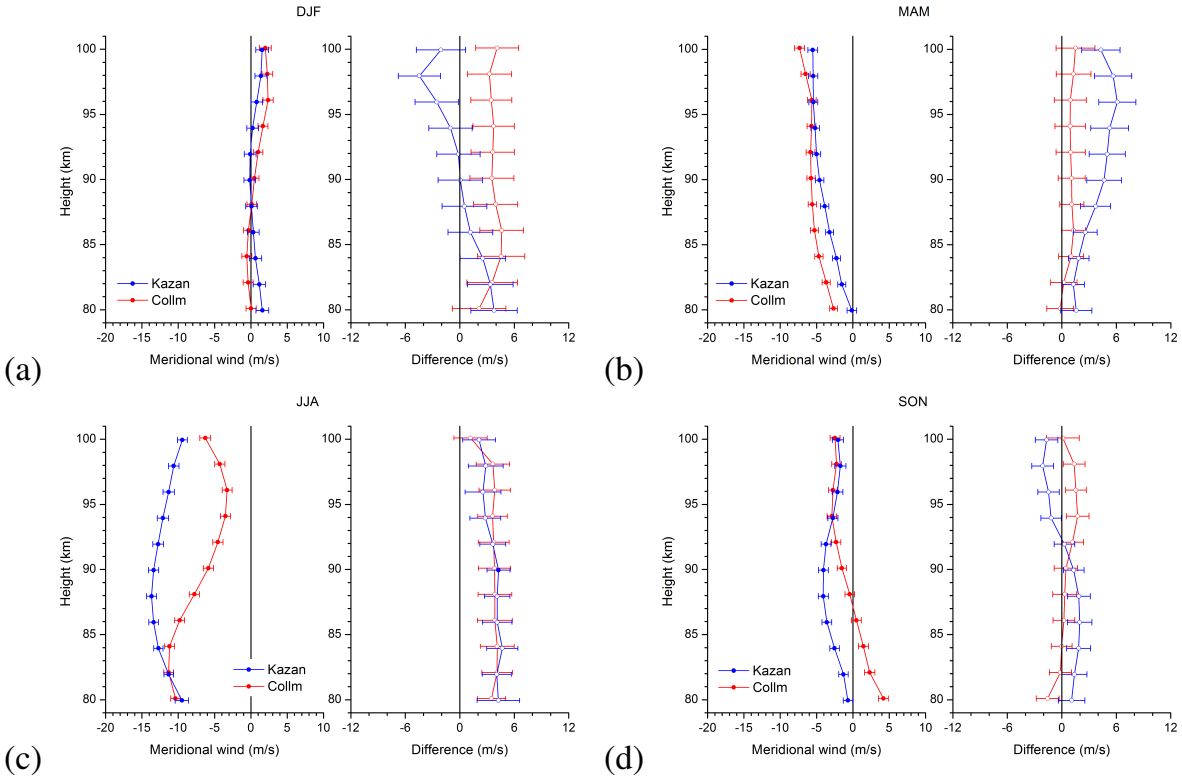

Figure 3: *As in Fig. 2, but for the meridional mean wind.*

3.2 Diurnal tide

Fig. 4 shows the 2015-2020 mean vertical profiles of the daily mean total DT amplitude for four seasons over Collm and Kazan, again for geomagnetically quiet conditions in the respective left plots, and the differences between winds during disturbed and quiet conditions are shown in the respective right plots. Maximum amplitudes are found in summer at the upper altitudes. Smallest amplitudes are seen at about 85–90 km altitude, with increasing amplitudes below and above. This qualitatively confirms climatological results as in Manson et al. (2002) or Jacobi (2012), that also show the upper mesosphere maximum and the increasing amplitudes in the thermosphere. Note, however, that earlier climatologies often relied on vector averaging of tidal amplitudes or regression analyses including data from more than one day, which effectively reduces the analyzed amplitudes, so that the rather strong amplitudes at 80 km are often not that strong in these climatologies. Comparing the vertical structure with the one shown by Fahrutdinova et al. (1999, 2001) gives very good qualitative correspondence. Only their amplitudes are somewhat smaller in general, which may be owing to long-term tidal variability, or a change of the Kazan radar systems.

During disturbed conditions in summer and partly in spring, DT amplitudes in the upper mesosphere are somewhat decreased, but they are enhanced in the lower thermosphere. This feature is consistently seen over both Collm and Kazan, although the differences are small. In autumn, DT amplitudes are reduced in the lower thermosphere, while there is no effect below approximately 90 km. In the lower thermosphere, differences are generally relatively strong during the equinoxes. In winter, the results for Collm and Kazan are contradicting. The results partly do not confirm the earlier ones

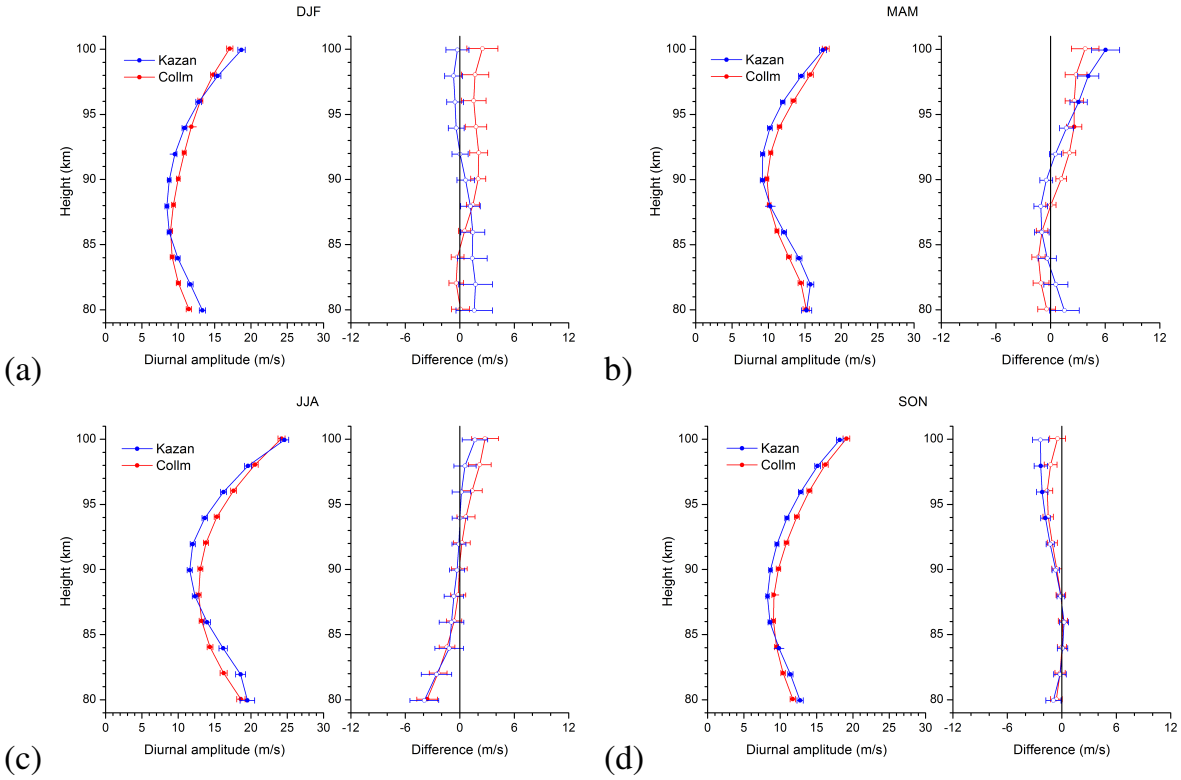

Figure 4: *As in Fig. 2, but for the total diurnal amplitude.*

by Fahrutdinova et al. (1999, 2001), who mainly found an increase of DT amplitudes for geomagnetically disturbed conditions.

3.3 Semidiurnal tide

Fig. 5 shows the 2015-2020 mean vertical profiles of the daily mean SDT amplitude. Maximum amplitudes are seen in winter, and generally amplitudes increase with altitude above 85 km, as is known from the literature (see Jacobi et al., 1999; Jacobi, 2012; Pokhotelov et al., 2018). As with the DT, the larger SDT amplitudes in the upper mesosphere are not well reproduced in early climatologies, owing to phase variability.

During winter, SDT amplitudes at altitudes above 85 km are clearly enhanced during geomagnetic disturbed days. This is, although weaker expressed, also the case for the Collm amplitudes in spring, but not for Kazan during this season. A tendency for increasing amplitudes, although not seen at greater altitudes over Collm, is also visible in summer. This was only weakly seen in earlier observations by Fahrutdinova et al. (1999). During spring and autumn, the SDT response to geomagnetic disturbances is unclear, and especially during spring it is different over the two stations. In the literature, also unclear or variable SDT response to geomagnetic variations has been reported (Singer et al., 1994).

3.4 Terdiurnal tide

Fig. 6 shows the 2015-2020 mean vertical profiles of the daily mean TDT amplitude. In winter, Collm and Kazan profiles are very similar at 90 km altitude and above. Below,

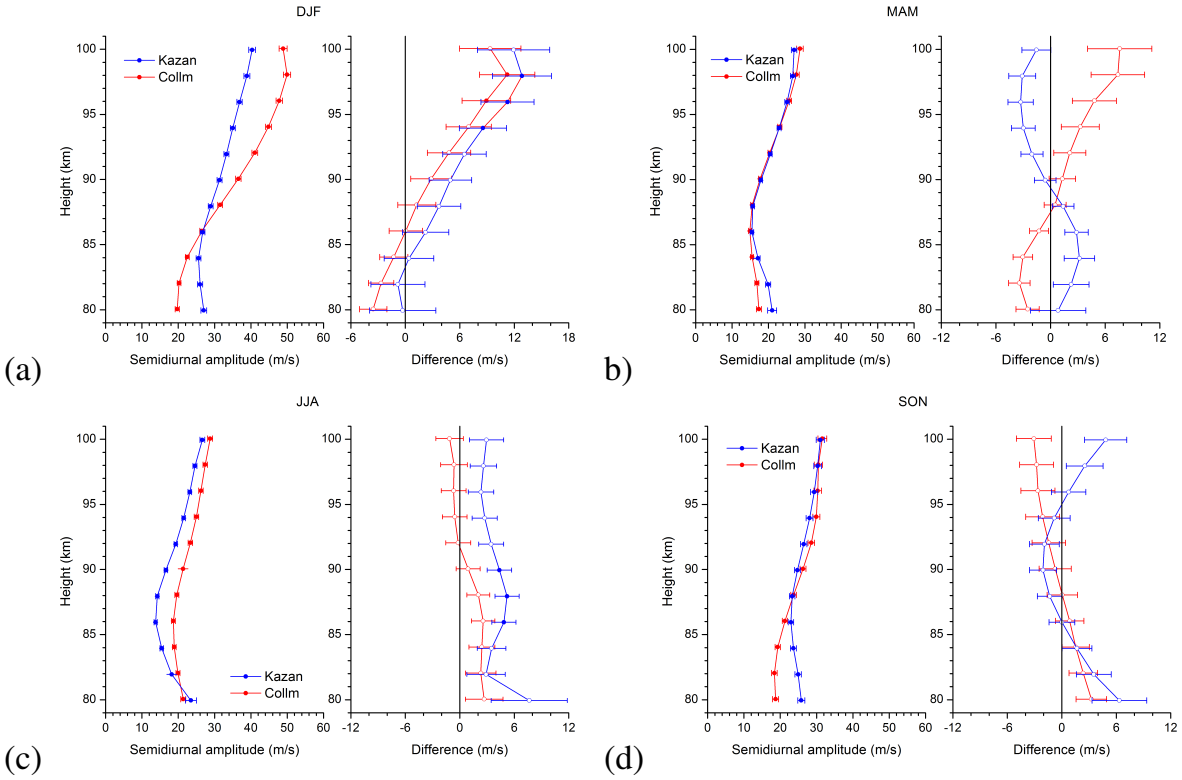

Figure 5: *As in Fig. 2, but for the total semidiurnal amplitude.*

Kazan amplitudes are larger, indicating nonmigrating components of the tide. In winter, mean tidal amplitudes are somewhat larger than in summer, in agreement with literature (e.g. Beldon et al., 2006; Jacobi, 2012).

Differences between disturbed and undisturbed days are small and, except for spring at lower altitudes, on the order of 1 m/s only. In autumn and spring, the amplitudes in the upper mesosphere are somewhat smaller for disturbed conditions. In the lower thermosphere, differences are small or, in autumn, the effects differ between Collm and Kazan. In spring and autumn the Collm upper mesosphere TDT amplitudes are generally smaller than the Kazan ones, and there is a tendency that they are more strongly reduced for disturbed days than the Kazan ones. To summarize, TDT amplitudes are generally slightly reduced in the mesosphere during disturbed days, but no clear effect is visible for the lower thermosphere.

4 Conclusions

Joint observations of MLT winds over Collm and Kazan during 2015 - 2020 by two all-sky meteor radars with very similar configuration have provided daily vertical profiles of mean winds and tidal amplitudes constructed from hourly horizontal winds. We analyze the response of mean winds and tidal amplitudes to geomagnetic disturbances and to this end compare winds and amplitudes for different geomagnetic conditions.

Zonal winds in both the mesosphere and lower thermosphere are weaker during disturbed conditions for both summer and winter. This results in more eastward winds in the mesosphere, and more westward winds in the lower thermosphere during the whole year, although the effect is not significant for most heights and seasons. Tendencies

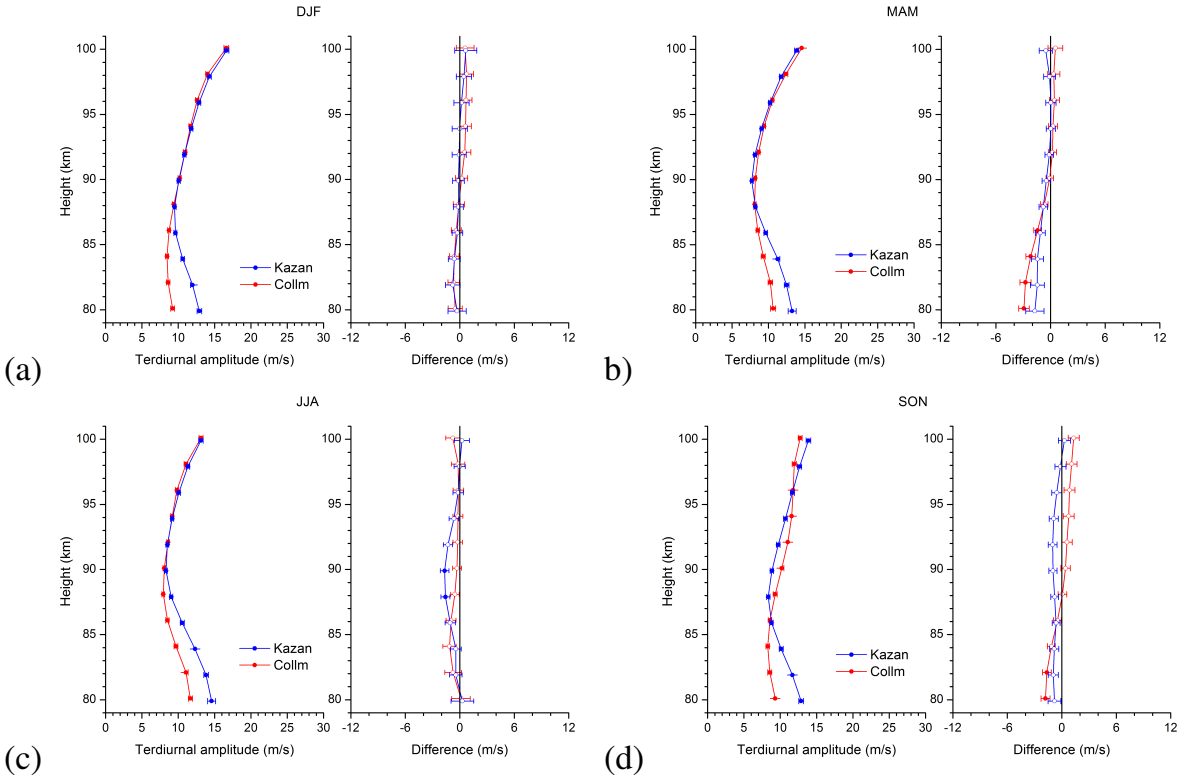

Figure 6: *As in Fig. 2, but for the total terdiurnal amplitude.*

over Collm and Kazan for mean wind geomagnetic effects qualitatively agreed during most of the year. These results confirm earlier observations and are also supported by model studies. The summer equatorward meridional wind jet is weaker for disturbed geomagnetic conditions, as has already been shown from earlier observations at Kazan. Although for single seasons and height gates the differences are mostly insignificant in our study, given the qualitatively similar differences during all seasons and the similarity with earlier observations we may conclude that the geomagnetic effect on the mean wind is, for the region of our observations, a robust feature throughout the last decades, and may be explained by cooling/heating effects in the middle atmosphere and thermosphere. However, meridional wind observations reported by Pancheva et al. (2005) did not confirm the meridional wind effect.

DT amplitudes in summer tend to be smaller in the mesosphere but greater in the lower thermosphere for disturbed conditions. No clear tendency is seen for winter. SDT amplitudes increase during geomagnetic active days in both summer and winter, but the effect is weak for other seasons than winter. TDT amplitudes are slightly reduced in the mesosphere during disturbed days, but no clear effect is visible for the lower thermosphere. Overall, while there is a tendency for a noticeable effect of geomagnetic variability on the mean wind, the geomagnetic effect on tidal amplitudes is small and partly different over Collm and Kazan. It is also not clear of which nature a possible influence on tides could be, except for an indirect one, i.e. a geomagnetic influence on stratospheric ozone, or the modification of propagation conditions through and influence on the background zonal winds. Given the weak or unsettled tidal response to geomagnetic disturbances this effect, however, seems to be small. In the future, model studies should be performed to also analyze the geomagnetic effect on tides.

Acknowledgements: CJ and FL acknowledge support by Deutsche Forschungsgemeinschaft through grants JA836/38-1 and JA836/43-1. DK and EM acknowledge support by RFBR through grant 18-505-12048. Ap indices have been provided by GFZ Potsdam on ftp://ftp.gfz-potsdam.de/pub/home/obs/kp-ap/wdc/yearly/.

References

Arnold, N. F. and Robinson, T. R.: Solar magnetic flux influences on the dynamics of the winter middle atmosphere, Geophys. Res. Lett., 28, 2381–2384, doi:10.1029/2000GL012825, 2001.

Baumgarten, K. and Stober, G.: On the evaluation of the phase relation between temperature and wind tides based on ground-based measurements and reanalysis data in the middle atmosphere, Ann. Geophys., 37, 581–602, doi:10.5194/angeo-37-581-2019, 2019.

Beig, G.: Long-term trends in the temperature of the mesosphere/lower thermosphere region: 2. Solar response, J. Geophys. Res.: Space Physics, 116, doi:10.1029/2011JA016766, 2011.

Beldon, C., Muller, H., and Mitchell, N.: The 8-hour tide in the mesosphere and lower thermosphere over the UK, 1988–2004, J. Atmos. Sol.-Terr. Phys., 68, 655–668, doi:10.1016/j.jastp.2005.10.004, 2006.

Fahrutdinova, A., Sherstyukov, O., and Maksyutin, S.: The effect of geomagnetic activity on the dynamics of the upper mesosphere-lower thermosphere and on parameters of the Es-layer, Adv. Space Res., 24, 1499 – 1502, doi:10.1016/S0273-1177(99)00714-0, 1999.

Fahrutdinova, A., Sherstyukov, O., and Maksyutin, S.: Geomagnetic activity influence on the dynamics of the upper mesosphere and lower thermosphere, Int. J. Geomag. Aeron., 2, 201–208, 2001.

Fahrutdinova, A., Maksyutin, S., and Elakhov, M.: Effects of sector structure of the interplanetary magnetic field on the upper mesosphere–lower thermosphere dynamics, Adv. Space Res., 52, 1959 – 1965, doi:10.1016/j.asr.2013.08.031, 2013.

GFZ: Indices of Global Geomagnetic Activity, `ftp://ftp.gfz-potsdam.de/pub/home/obs/kp-ap/wdc/yearly/`, accessed on 2020-08-27, 2020.

Hocke, K.: Response of the middle atmosphere to the geomagnetic storm of November 2004, J. Atmos. Sol.-Terr. Phys., 154, 86 – 91, doi:10.1016/j.jastp.2016.12.013, 2017.

Hocking, W., Fuller, B., and Vandepeer, B.: Real-time determination of meteor-related parameters utilizing modern digital technology, J. Atmos. Sol.-Terr. Phys., 63, 155 – 169, doi:10.1016/S1364-6826(00)00138-3, 2001.

Jacobi, C.: 6 year mean prevailing winds and tides measured by VHF meteor radar over Collm (51.3°N, 13.0°E), J. Atmos. Sol.-Terr. Phys., 78-79, 8–18, doi:10.1016/j.jastp.2011.04.010, 2012.

Jacobi, C., Portnyagin, Y., Solovjova, T., et al.: Climatology of the semidiurnal tide at 52–56°N from ground-based radar wind measurements 1985–1995, J. Atmos. Sol.-Terr. Phys., 61, 975 – 991, doi:10.1016/S1364-6826(99)00065-6, 1999.

Jacobi, C., Fröhlich, K., Viehweg, C., Stober, G., and Kürschner, D.: Midlatitude mesosphere/lower thermosphere meridional winds and temperatures measured with meteor radar, Adv. Space Res., 39, 1278 – 1283, doi:10.1016/j.asr.2007.01.003, 2007.

Keuer, D., Hoffmann, P., Singer, W., and Bremer, J.: Long-term variations of the mesospheric wind field at mid-latitudes, Ann. Geophys., 25, 1779–1790, doi:10.5194/angeo-25-1779-2007, 2007.

Korotyshkin, D., Merzlyakov, E., Jacobi, C., Lilienthal, F., and Wu, Q.: Longitudinal MLT wind structure at higher mid-latitudes as seen by meteor radars at central and Eastern Europe (13°E/49°E), Adv. Space Res., 63, 3154 – 3166, doi:10.1016/j.asr.2019.01.036, 2019a.

Korotyshkin, D., Merzlyakov, E., Sherstyukov, O., and Valiullin, F.: Mesosphere/lower thermosphere wind regime parameters using a newly installed SKiYMET meteor radar at Kazan (56°N, 49°E), Adv. Space Res., 63, 2132 – 2143, doi:10.1016/j.asr.2018.12.032, 2019b.

Le Mouël, J.-L., Blanter, E., Chulliat, A., and Shnirman, M.: On the semiannual and annual variations of geomagnetic activity and components, Ann. Geophys., 22, 3583–3588, doi:10.5194/angeo-22-3583-2004, 2004.

Lilienthal, F. and Jacobi, C.: Meteor radar quasi 2-day wave observations over 10 years at Collm (51.3° N, 13.0° E), Atmos. Chem. Phys., 15, 9917–9927, doi:10.5194/acp-15-9917-2015, 2015.

Liu, H., Tsutsumi, M., and Liu, H.: Vertical structure of terdiurnal tides in the Antarctic MLT region: 15-year observation over Syowa (69°S, 39°E), Geophys. Res. Lett., 46, 2364–2371, doi:10.1029/2019GL082155, 2019.

Manson, A. H., Meek, C., Hagan, M., et al.: Seasonal variations of the semi-diurnal and diurnal tides in the MLT: multi-year MF radar observations from 2–70° N, modelled tides (GSWM, CMAM), Ann. Geophys., 20, 661–677, doi:10.5194/angeo-20-661-2002, 2002.

Mironova, I. A., Aplin, K. L., Arnold, F., et al.: Energetic particle influence on the Earth's atmosphere, Space Sci. Rev., 194, 1–96, doi:10.1007/s11214-015-0185-4, 2015.

Pancheva, D., Mukhtarov, P., Mitchell, N., and Muller, H.: Empirical model of the dynamics in the mesosphere and lower thermosphere region over the UK, including solar and geomagnetic activity, J. Atmos. Sol.-Terr. Phys., 67, 197 – 209, doi:10.1016/j.jastp.2004.07.029, solar Activity Forcing of the Middle Atmosphere, 2005.

Pancheva, D., Singer, W., and Mukhtarov, P.: Regional response of the mesosphere–lower thermosphere dynamics over Scandinavia to solar proton events and geomagnetic storms in late October 2003, J. Atmos. Sol.-Terr. Phys., 69, 1075 – 1094, doi:10.1016/j.jastp.2007.04.005, 2007.

Pokhotelov, D., Becker, E., Stober, G., and Chau, J. L.: Seasonal variability of atmospheric tides in the mesosphere and lower thermosphere: meteor radar data and simulations, Ann. Geophys., 36, 825–830, doi:10.5194/angeo-36-825-2018, 2018.

Qian, L., Jacobi, C., and McInerney, J.: Trends and solar irradiance effects in the mesosphere, J. Geophys. Res.: Space Physics, 124, 1343–1360, doi:10.1029/2018JA026367, 2019.

Rong, P., von Savigny, C., Zhang, C., Hoffmann, C. G., and Schwartz, M. J.: Response of middle atmospheric temperature to the 27 d solar cycle: an analysis of 13 years of microwave limb sounder data, Atmos. Chem. Phys., 20, 1737–1755, doi:10.5194/acp-20-1737-2020, 2020.

Schminder, R., Kürschner, D., Singer, W., et al.: Representative height-time cross-sections of the upper atmosphere wind field over Central Europe 1990–1996, J. Atmos. Sol.-Terr. Phys., 59, 2177 – 2184, doi:10.1016/S1364-6826(97)00062-X, 1997.

Singer, W., Bremer, J., Hoffmann, P., et al.: Geomagnetic influences upon tides—winds from MLT radars, Journal of Atmospheric and Terrestrial Physics, 56, 1301 – 1311, doi:10.1016/0021-9169(94)90068-X, 1994.

Stober, G., Jacobi, C., Fröhlich, K., and Oberheide, J.: Meteor radar temperatures over Collm (51.3°N, 13°E), Adv. Space Res., 42, 1253 – 1258, doi:10.1016/j.asr.2007.10.018, 2008.

Stober, G., Jacobi, C., Matthias, V., Hoffmann, P., and Gerding, M.: Neutral air density variations during strong planetary wave activity in the mesopause region derived from meteor radar observations, J. Atmos. Sol.-Terr. Phys., 74, 55 – 63, doi:10.1016/j.jastp.2011.10.007, 2012.

Stober, G., Matthias, V., Brown, P., and Chau, J. L.: Neutral density variation from specular meteor echo observations spanning one solar cycle, Geophys. Res. Lett., 41, 6919–6925, doi:10.1002/2014GL061273, 2014.

Stober, G., Matthias, V., Jacobi, C., et al.: Exceptionally strong summer-like zonal wind reversal in the upper mesosphere during winter 2015/16, Ann. Geophys., 35, 711–720, doi:10.5194/angeo-35-711-2017, 2017.

Stober, G., Chau, J. L., Vierinen, J., Jacobi, C., and Wilhelm, S.: Retrieving horizontally resolved wind fields using multi-static meteor radar observations, Atmos. Meas. Tech., 11, 4891–4907, doi:10.5194/amt-11-4891-2018, 2018.

Stober, G., Baumgarten, K., McCormack, J. P., Brown, P., and Czarnecki, J.: Comparative study between ground-based observations and NAVGEM-HA analysis data in the mesosphere and lower thermosphere region, Atmos. Chem. Phys., 20, 11 979–12 010, doi:10.5194/acp-20-11979-2020, 2020.

Yi, W., Reid, I. M., Xue, X., et al.: High- and middle-latitude neutral mesospheric density response to geomagnetic storms, Geophys. Res. Lett., 45, 436–444, doi:10.1002/2017GL076282, 2018.

Zhang, S. P., Salah, J. E., Mitchell, N., et al.: Responses of the mesospheric wind at high latitudes to the April 2002 space storm, Geophys. Res. Lett., 30, doi:10.1029/2003GL018521, 2003.

Airborne observations of clouds in the Central Arctic during the Multidisciplinary drifting Observatory for the Study of Arctic Climate (MOSAiC) expedition

Klingebiel, M.[1], Ehrlich, A.[1], Schäfer, M.[1], Becker, S.[1], Jäkel, E.[1] Wendisch, M.[1]

[1] *Institute of Meteorology, Stephanstr. 3, 04103 Leipzig,*
E-mail: marcus.klingebiel@uni-leipzig.de

Summary: In August and September 2020, a group from the Leipzig Institute for Meteorology (LIM) participated in the research campaign MOSAiC-ACA. During this campaign the Polar 5 research aircraft was used to identify the cloud characteristics and their impact on the radiative energy budget, which are relevant for the role of clouds in Arctic amplification in the vicinity of Svalbard. In this report we will give an overview about the campaign and the instruments operated by LIM and point out the challenges which we faced while performing a research campaign in the middle of a global pandemic and in an Arctic environment with the second lowest sea ice coverage in the last 42 years.

Zusammenfassung: Im August und September 2020 hat eine Gruppe vom Leipziger Institut für Meteorologie (LIM) an der Forschungskampagne MOSAiC-ACA teilgenommen, um unter Verwendung des Forschungsflugzeuges Polar 5 die relevanten Wolkencharakteristiken und deren Einfluss auf das Strahlungsbudget zu identifizieren. Diese spielen eine Rolle bei der Arktischen Verstärkung in der Umgebung von Spitzbergen. In diesem Bericht geben wir eine Übersicht über die Kampagne und die Instrumente, die vom LIM verwendet wurden und erläutern die Herausforderungen, die uns während der Forschungskampagne in Mitten einer globalen Pandemie und in einer Arktischen Umgebung, in der die Eisbedeckung die zweitniedrigste innerhalb der letzten 42 Jahre war, begegneten.

1 Introduction

Throughout the last years, the Arctic experienced an enhanced warming, which is known as Arctic amplification. This process leads to e.g. a decrease in the amount of Arctic sea ice. To identify the role of clouds in Arctic amplification, we carried out the MOSAiC-Airborne observations in the Central Arctic (MOSAiC-ACA) campaign in August and September 2020 in the vicinity of Svalbard (Spitsbergen), which is related to the Multidisciplinary drifting Observatory for the Study of Arctic Climate (MOSAiC) expedition and the Transregional Collaborative Research Center ArctiC Amplification: Climate relevant Atmospheric and SurfaCe Processes, and Feedback Mechanisms ((AC)^3,Wendisch et al. (2021)). Figure 1 shows the tracks of all nine flights performed during the MOSAiC-ACA campaign including the Arctic sea ice coverage of September 2020 and the positions of the launched dropsondes.

The MOSAiC-ACA campaign extends the Arctic cloud measurements from the previous Arctic CLoud Observations Using airborne measurements during polar Day (ACLOUD, Wendisch et al. (2019)) and Airborne measurements of radiative and turbulent FLUXes (AFLUX) campaigns, which were conducted in May/June 2017 and March/April 2019, respectively.

When we planned the campaign, we did not expect such a low sea ice concentration for this time of year, which was quantified by the National Snow and Ice Data Center (NSIDC, 2020) to be the second lowest in the 42-year satellite record, behind only September 2012. This made the campaign very challenging, because the focus of our research is the marginal sea ice zone and therefore we need to be able to reach the ice with the research aircraft. On the other hand, this low sea ice concentration shows how urgent it is to collect atmospheric observations in this area to better understand the role of clouds and their radiative properties in a future ice-free environment.

What we also didn't expect in 2020 was the COVID-19 pandemic, which made it very challenging to perform a research campaign in a foreign country. Nevertheless, thanks to all our partners involved in the $(AC)^3$ project (see `http://www.ac3-tr.de` for more information), especially the administration of AWI, it was possible to realize the campaign, despite a lot of restrictions and requirements. To successfully carry out this campaign, only a small but highly motivated crew of 27 researchers, engineers and pilots managed flight operation, weather forecast, instrument operation and data handling. Even there was a second research aircraft involved in the campaign to measure sea ice concentrations, namely the Polar 6, we will only focus in this report on the atmospheric measurements from the Polar 5 aircraft, which was equipped with in-situ and remote sensing instruments to characterize Arctic boundary layer clouds. These measurements will primarily address seasonal differences by considering the previous campaigns in the scope of $(AC)^3$ and build the bridge between the ground-based observations of the Research Vessel (RV) Polarstern, the research station at Ny-Ålesund and satellite observations.

2 Aircraft and instruments

The Polar 5 aircraft is a Basler BT-67, which is specially modified to fly under extreme polar conditions. With advanced navigation systems, de-icing systems and landing gear, which combine skis and conventional tires, the aircraft can operate in severe weather conditions with temperatures down to -54°C (Wesche et al., 2016). During the MOSAiC-ACA campaign, the Polar 5 was equipped with several in-situ and remote sensing instruments to measure atmospheric parameters, the radiative energy budget and as well as cloud micro- and macrophysical properties. In addition, the Polar 5 is equipped with a dropsonde system, which allows for the launch of Vaisala RD-41 sondes to measure vertical profiles of temperature, humidity, pressure and winds. In this report, we will focus on the remote sensing instruments from LIM, which will be introduced in the following section.

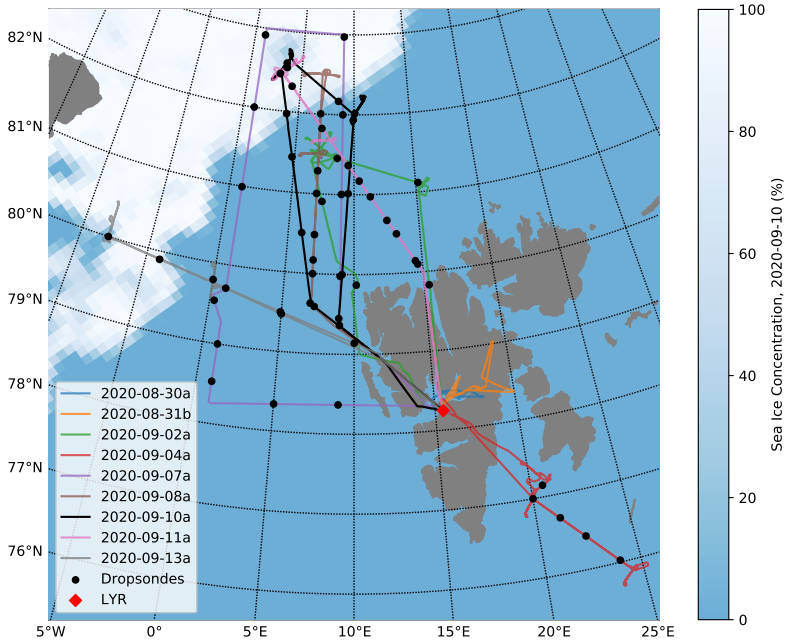

Figure 1: *Polar 5 flight tracks during the MOSAiC-ACA campaign. All in all, nine flights were conducted in the vicinity of Svalbard and 60 dropsondes were launched. All flights were performed from Longyearbyen Airport (LYR) located on the Svalbard archipelago. The sea ice concentration is based on AMSR-Satellite data and is the second lowest in the 42 years of satellite record.*

2.1 SMART Albedometer

During MOSAiC-ACA the Spectral Modular Airborne Radiation measurement sysTem (SMART) was configured to measure the spectral solar irradiance and radiance. For this purpose, four optical inlets are mounted at the aircraft fuselage and connected via optical fibers to grating spectrometers dispersing the incident radiation, which is detected by a single-line photodiode array. SMART covers a spectral range between 300 nm and 2200 nm wavelength and contains two optical shutters, which allow necessary simultaneous dark measurements for the spectrometers (Wendisch et al., 2019; Ehrlich et al., 2019).

2.2 AISA Hawk spectral imager

The Airborne Imaging Spectrometer for Applications (AISA) Hawk instrument (Pu, 2017; Ehrlich et al., 2019) consists of a downward-viewing push broom sensor aligned across the flight track to measure 2D fields of upward radiance. The push broom sensor contains 384 across-track pixels, where each pixel performs spectral measurements between the wavelength range of 930 nm and 2550 nm in 288 channels. With a 36° field of view (FOV) and a sampling frequency of 20 Hz, the instrument has a spatial resolution of 2 m, assuming a distance between aircraft and cloud of 1 km (Ruiz-Donoso et al., 2020).

2.3 AISA Eagle spectral imager

The AISA Eagle instrument is the second imaging spectrometer installed on Polar 5. It uses a measurement approach similar to AISA Hawk but focuses on shorter wavelengths with higher spectral and spatial resolution. With a single line push broom sensor consisting of 1024 across-track pixels measurements of 2D fields of upward radiance are performed in 488 channels covering a wavelength range between 400 nm and 970 nm. The FOV is 36.3° and delivers a spatial resolution below 1 m for a target at a distance of 1 km (Schäfer et al., 2015). During MOSAiC-ACA it was operated with a frame rate of 20 Hz to acquire an along-track spatial resolution comparable to that of AISA Hawk.

2.4 Nikon

A commercial digital camera (Nikon D5) measured the directional distribution of upward radiance in three spectral channels (RGB) of the lower hemisphere every 6 s. The camera was either equipped with a wide-angle lens (up to flight 8) or a fisheye-lens (flight 9 to flight 11). The two configurations allowed the cloud and surface observations of a large area within a FOV of 80° x 100° (wide-angle lens) and about 150° when using the fisheye-lens. The camera was fully calibrated with respect to its radiometric, geometric and spectral characteristics. The images were recorded in raw data format to gain the full dynamic range (14 bit) of the camera sensor chip with a spatial resolution of 5584 x 3728 pixels.

Nadir radiances measured by SMART, AISA Eagle, and Nikon from flight 9 (10 September 2020) were compared to verify the individual calibrations. During a period of three hours, observations of cloud tops, cloud profiles, and sea ice were performed which cover a broad range of different reflectivity. Combining the three instruments needs to account for the different spatial, temporal, and spectral resolutions. SMART and AISA Eagle spectra were convoluted with respect to the spectral response functions of the three spectral channels of the Nikon camera. AISA Eagle and Nikon data were spatially averaged to match the size of the SMART footprint of 2°. Figure 2 displays scatterplots of the radiance data using SMART as a reference. The correlation between SMART and AISA Eagle data (red dots) is consistent for all three channels with a correlation coefficient (R) of about 0.97 and an offset of 6%, which falls within the measurement uncertainty of the two instruments. The correlation coefficient between SMART and Nikon data is slightly lower with R = 0.94. The best agreement was found for the red and the green channels, while a significant offset of about 22% was derived for the blue channel. Finally, these findings were used to inter-calibrate the Nikon camera in order to provide a consistent data set.

2.5 Broadband solar and terrestrial radiation

Up- and downward broadband irradiances are obtained by using pairs of CMP 22 pyranometers and CGR4 pyrgeometers. The pyranometers cover a solar wavelength range between 0.2 and 3.6 µm, while the pyrgeometers cover a thermal infrared wavelength range between 4.5 and 42 µm. The sampling frequency is 20 Hz and the uncertainty of the sensors is less than 3% (Gröbner et al., 2014). To adjust the misalignment of the aircraft during flight for the downward direct solar irradiance, a method from Bannehr

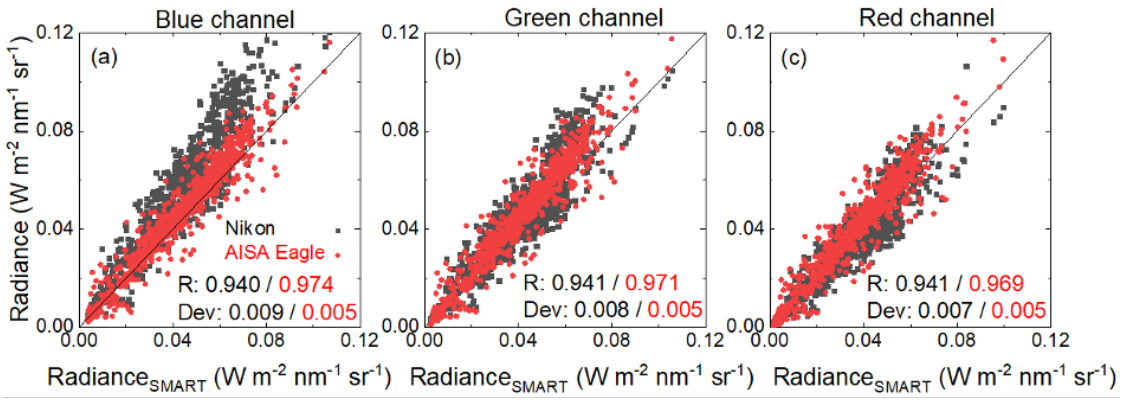

Figure 2: *Comparison of radiances in nadir direction measured by SMART, Nikon, and AISA Eagle on 10 September 2020. "Dev" represents the root mean squared error between the reference radiance of SMART and the radiances by Nikon (black) and AISA Eagle (red), respectively. R indicates the Pearson's correlation coefficient.*

Table 1: *Research flights in the vicinity of Svalbard with the number of dropsondes, the number of pictures recorded by the Nikon camera, the measurement time of each instrument and the total amount of the recorded data for each flight in Gigabytes (GB).*

					Measurement time				
Flight #	**Date**	**Flight duration**	**Dropsondes**	**Nikon pictures**	**Eagle**	**Hawk**	**Broadband**	**SMART**	**Data (GB)**
2	30.08.2020	0h 53m	-	342	0h 15m	0h 39m	0h 53m	0h 21m	22.7
4	31.08.2020	2h 15m	-	4273	0h 49m	1h 51m	2h 15m	2h 13m	216.5
5	02.09.2020	5h 31m	6	3120	2h 31m	2h 25m	5h 31m	5h 29m	277.3
6	04.09.2020	5h 31m	5	3107	1h 46m	1h 42m	5h 31m	0h 22m	214.2
7	07.09.2020	5h 41m	14	3476	4h 13m	3h 33m	5h 41m	5h 41m	410.4
8	08.09.2020	6h 05m	7	5517	2h 25m	2h 21m	6h 05m	6h 05m	318,5
9	10.09.2020	6h 16m	11	4738	4h 27m	4h 21m	6h 16m	6h 16m	475,6
10	11.09.2020	5h 40m	10	6063	1h 56m	1h 52m	5h 40m	4h 20m	292,1
11	13.09.2020	5h 46m	7	5640	1h 39m	1h 36m	5h 46m	5h 46m	261.4
	Total:	**44h 17m**	**60**	**36276**	**20h 01m**	**20h 20m**	**44h 17m**	**36h 33m**	**2489**

and Schwiesow (1993) and Boers et al. (1998) is applied. More specific details about these broadband solar and terrestrial radiation instruments operated on Polar 5 are given by Ehrlich et al. (2019).

3 Remote sensing measurements

During the campaign we performed 11 flights. The first flight was a test flight in Bremerhaven, Germany and the third flight was used for certification purposes, where the instruments were not switched on. The other flights in the vicinity of Svalbard are listed in Table 1, together with the flight duration, the number of launched dropsondes, the number of pictures recorded by the Nikon camera, the measurement time of each instrument and the amount of data recorded for each flight. In total, 2.5 TB were recorded by the remote sensing instruments from LIM.

In the following, we will focus on the remote sensing measurements from research flight 9 (the associated flight track is marked in black in Figure 1), which had the main purpose to investigate the differences of cloud properties over sea ice and open water. For this reason, the Polar 5 headed first to the north over the sea ice (82.5°N, 0.3°E) and

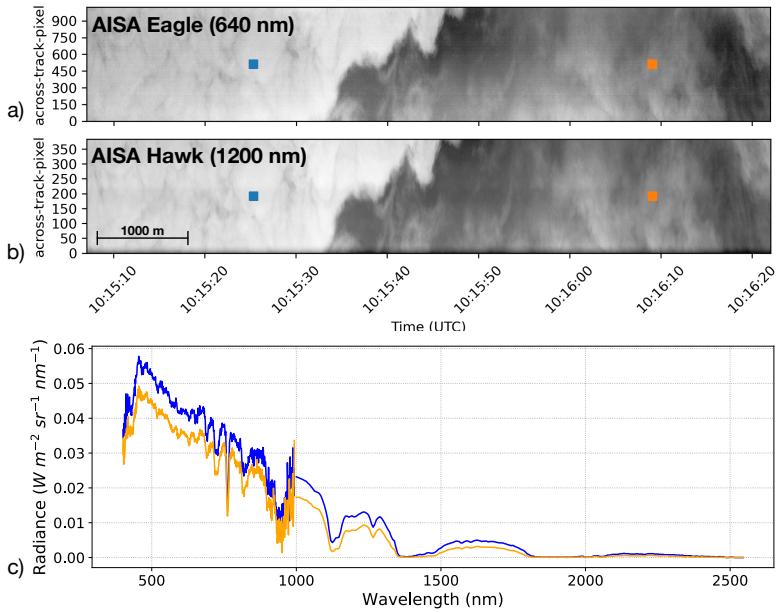

Figure 3: *2D fields of upward radiances, sampled by the AISA Eagle (a) and AISA Hawk (b) instrument. Spectral radiances at the locations marked with the square in (a) and (b) are given in panel (c) and show a combination of both instruments.*

sampled two cloud layers there, one ice cloud between 8600 and 8900 ft (2.6 and 2.7 km) and one liquid water cloud reaching from the ground to 5000 ft (1.5 km). Afterwards, the Polar 5 headed towards the open ocean (82°N, 10°E) and sampled a cloud reaching from the surface up to ~3000 ft (~900 m). Both cloud systems were probed in a staircase pattern.

A measurement example of AISA Eagle and AISA Hawk is given in Figure 3, which shows approximately one minute (~10 km) of measurements during flight 9 on 10 September 2020. During this flight section, the edge of a boundary layer cloud over open water was sampled with both instruments. This cloud edge is visible in Figure 3a and 3b between 10:15:30 UTC and 10:15:50 UTC. To demonstrate the capabilities of the spectral imagers, Figure 3c shows two combined AISA Eagle and AISA Hawk spectra for the center pixels marked by the blue and orange rectangles in Figure 3a and 3b. The spectra show higher radiance over the boundary layer cloud (blue rectangle) and lower radiance over a thinner cloud (orange rectangle). The spectra sampled by the AISA Hawk instrument (between 930 nm and 2550 nm) look smoother than from AISA Eagle due to the different spectral resolutions of both imagers.

Another example, given in Figure 4, shows the differences in broadband radiative cloud properties over Arctic sea ice (left panels) and open ocean (right panels). The albedo values exceeding 1 in Fig. 4c are due to horizontal photon transport. While the net terrestrial irradiance (orange line) is very similar over ice (Figure 4a) and over ocean (Figure 4b), the differences in the net solar irradiance are remarkable. Over ocean the net solar irradiance is 33 W m^{-2} higher than over Arctic ice. The cloud albedo, which is the ratio of the solar upward and downward irradiance, is higher over Arctic ice (Figure 4c) than over ocean (Figure 4d). This is plausible, because the ice surface reflects more solar radiation than the ocean. We will use these kind of measurements to analyze the typical

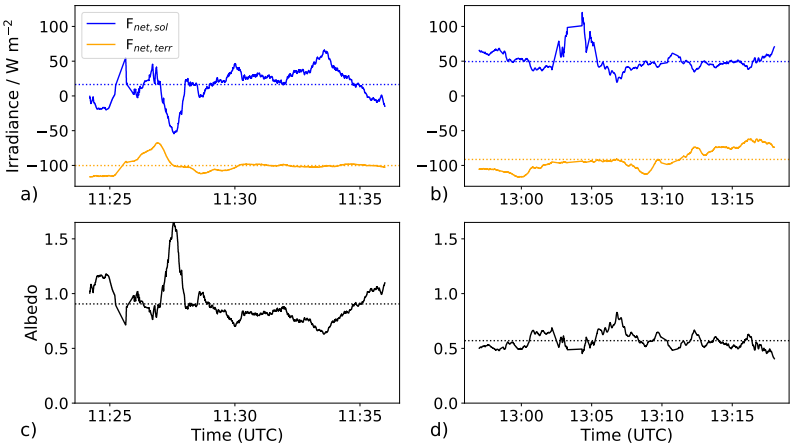

Figure 4: *Net solar and terrestrial irradiance over sea ice (a) and open ocean (b). The corresponding albedo over sea ice and open ocean is given in (c) and (d), respectively. The dotted lines indicate the mean value of each parameter.*

conditions over Arctic sea ice and open ocean in further studies. Combining the data from the MOSAiC-ACA campaign with those of the ACLOUD and AFLUX campaign will provide us with the opportunity to identify seasonal differences of the cloud radiative properties.

4 Conclusion and next steps

In August and September 2020, nine research flights with a total flight time of 44 hours were performed with the Polar 5 aircraft to study the cloud characteristics and their impact on the radiative energy budget, that are relevant for the role of clouds in Arctic amplification. First results from the spectral imagers and the broadband solar and terrestrial radiation measurements look very promising. The data indicate the spectral differences between different types of clouds and the differences over Arctic ice and ocean. Although we present only a very small part of the data, they show that the instruments were working properly, and we can use the data to reach more advanced scientific goals. In particular, we will use this dataset to analyze the different cloud properties over Arctic sea ice and ocean and will compare them with previous $(AC)^3$ campaigns as well as satellite observations and data from the RV Polarstern.

Acknowledgements

We gratefully acknowledge the funding by the Deutsche Forschungsgemeinschaft (DFG, German Research Foundation) – Project Number 268020496 5 – TRR 172, within the Transregional Collaborative Research Center “ArctiC Amplification: Climate Relevant Atmospheric and SurfaCe Processes, and Feedback Mechanisms $(AC)^3$.

References

Bannehr, L. and Schwiesow, R.: A Technique to Account for the Misalignment of Pyranometers Installed on Aircraft, Journal of Atmospheric and Oceanic Technology, 10, 774 – 777, doi:10.1175/1520-

0426(1993)010<0774:ATTAFT>2.0.CO;2, 1993.

Boers, R., Mitchell, R. M., and Krummel, P. B.: Correction of aircraft pyranometer measurements for diffuse radiance and alignment errors, Journal of Geophysical Research: Atmospheres, 103, 16 753–16 758, doi:10.1029/98JD01431, 1998.

Ehrlich, A., Wendisch, M., Lüpkes, C., et al.: A comprehensive in situ and remote sensing data set from the Arctic CLoud Observations Using airborne measurements during polar Day (ACLOUD) campaign, Earth System Science Data, 11, 1853–1881, doi:10.5194/essd-11-1853-2019, 2019.

Gröbner, J., Reda, I., Wacker, S., et al.: A new absolute reference for atmospheric longwave irradiance measurements with traceability to SI units, Journal of Geophysical Research: Atmospheres, 119, 7083–7090, doi:10.1002/2014JD021630, 2014.

NSIDC: Arctic sea ice decline stalls out at second lowest minimum, URL http://nsidc.org/arcticseaicenews/2020/09/, 2020.

Pu, R.: Hyperspectral Remote Sensing: Fundamentals and Practices (1st ed.), CRC Press., doi:10.1201/9781315120607, 2017.

Ruiz-Donoso, E., Ehrlich, A., Schäfer, M., et al.: Small-scale structure of thermodynamic phase in Arctic mixed-phase clouds observed by airborne remote sensing during a cold air outbreak and a warm air advection event, Atmospheric Chemistry and Physics, 20, 5487–5511, doi:10.5194/acp-20-5487-2020, 2020.

Schäfer, M., Bierwirth, E., Ehrlich, A., Jäkel, E., and Wendisch, M.: Airborne observations and simulations of three-dimensional radiative interactions between Arctic boundary layer clouds and ice floes, Atmospheric Chemistry and Physics, 15, 8147–8163, doi:10.5194/acp-15-8147-2015, 2015.

Wendisch, M., Macke, A., Ehrlich, A., et al.: The Arctic Cloud Puzzle: Using ACLOUD/PASCAL Multiplatform Observations to Unravel the Role of Clouds and Aerosol Particles in Arctic Amplification, Bulletin of the American Meteorological Society, 100, 841 – 871, doi:10.1175/BAMS-D-18-0072.1, 2019.

Wendisch, M., Handorf, D., Tegen, I., Neggers, R. A. J., and Spreen, G.: Glimpsing the ins and outs of the Arctic atmospheric cauldron, Eos, 102, doi:10.1029/2021EO155959, 2021.

Wesche, C., Steinhage, D., and Nixdorf, U.: Polar aircraft Polar5 and Polar6 operated by the Alfred Wegener Institute, Journal of large-scale research facilities Facilities, 2, doi:10.17815/jlsrf-2-153, 2016.

EUREC^{4}A: Overview of LIM contributions

Luebke, A.E.[1] and Röttenbacher, J.[1]
Ehrlich, A.[1], Schäfer, M.[1], Wolf, K.[1,*], Kalesse-Los, H.[1], Wendisch, M.[1], Stapf, J.[1], Thoböll, J.[1],

[1] *Leipzig Institute for Meteorology, Universität Leipzig, Leipzig, Germany*
[*] *Laboratory for Atmospheric and Space Physics, University of Colorado, Boulder, USA*

E-mail: anna.luebke@uni-leipzig.de, johannes.roettenbacher@uni-leipzig.de

Summary: From 17 January to 19 February 2020, the EUREC^{4}A campaign was carried out in the trade-wind region of the Atlantic Ocean, in the Caribbean Sea just off the East Coast of Barbados. With several research platforms, including research vessels and aircraft, each containing various types of instrumentation, the goal of the campaign was to acquire observations of cloud properties as well as information about the large-scale environment and interactions therein. Scientists from LIM contributed active and passive remote sensing instrumentation aboard the research vessel Meteor and the High Altitude and Long Range research aircraft (HALO). EUREC^{4}A uses the multi-platform approach, which provides synergy from the observations to research trade-wind clouds and dynamics. An overview of the contribution of LIM to EUREC^{4}A and first preliminary results are given here.

Zusammenfassung: Von 17. Januar bis 19. Februar 2020 fand die groß angelegte EUREC^{4}A Feldkampagne im Osten von Barbados im Karibischen Meer statt. In der vom Passatwind geprägten Region wurden mehrere Forschungsschiffe sowie -flugzeuge genutzt, um klimarelevante Prozesse in der Atmosphäre und im Ozean zu charakterisieren. Ziel war es mit Hilfe unterschiedliche Messstrategien und -instrumenten das Zusammenspiel der Wolken, der Meeresströmungen und der globalen Zirkulation umfassend zu dokumentieren. Ein Beitrag der Wissenschaftler:Innen des Leipziger Instituts für Meteorologie waren flugzeuggetragene Fernerkundungsmessungen, welche vom deutschen Forschungsflugzeug HALO aus in einer Höhe von bis zu 10 km gemacht wurden. Gleichzeitig wurden Fernerkundungsmessungen der Atmosphäre vom Forschungsschiff Meteor durchgeführt. Mit Hilfe eines Wolkenradars, eines Mikorwellenradiometers, und spektraler Messungen solarer Strahlung wurden von der FS Meteor aus die Passatwindwolken untersucht. Die Vielfalt an Messinstrumenten und -platformen ermöglicht dabei eine ganzheitliche Sicht auf die klimarelevanten Passatwindwolken und deren Dynamik in der Atmosphäre.

1 Introduction

The ElUcidating the RolE of Cloud-Circulation Coupling in ClimAte, or for short EUREC^{4}A, campaign in January and February of 2020 was one of the largest atmospheric and oceanic research campaigns ever to be conducted, comprising four research vessels, five aircraft, one remote sensing station on Barbados and many unmanned research crafts. As stated in Bony et al. (2017) and Stevens et al. (2021), the primary objectives of the campaign were:

- To quantify macrophysical and microphysical properties of trade-wind cumuli as a function of the large-scale environment, and
- To provide a reference data set that can be used as a benchmark for the modeling and satellite observation of shallow clouds and circulation

With the combination of the many platforms that employ a variety of measurement techniques and objectives, a broad view of trade-wind clouds is provided. The strategy for tackling this challenge was largely based on a synergistic approach. The research domain was centered just east of Barbados in the Caribbean Sea and focused on "Tradewind Alley", the central measurement area in a semi-circle defined by the Barbados-based Polarized C-Band Radar, POLDIRAD (Fig. 1, green area). Additional research vessels contributed to these measurements while also exploring the influence and evolution of ocean eddies that frequently ramble toward Barbados from the southeast, along the "Boulevard des Tourbillons" (Stevens et al., 2021). Among the many platforms were the German Research Vessel Meteor and the High Altitude LOng range research aircraft (HALO) operated by the DLR (Deutsches Zentrum für Luft- und Raumfahrt), which specifically included instruments operated by scientists from the Leipzig Institute for Meteorology (LIM). The following sections describe in more detail how observations from LIM-operated instrumentation contributed to capturing the broader cloud picture from various perspectives.

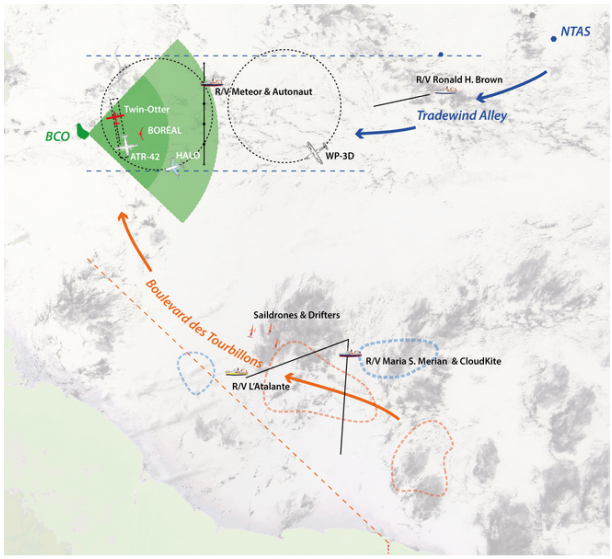

Figure 1: *Schematic illustration of the area of field operations during EUREC^{4}A. Green denotes the field of view of the C-Band Radar POLDIRAD (http://eurec4a.eu/overview/eurec4a).*

Table 1: *Overview of instrument specifications.*

Instrument	Time resolution	FOV	Wavelength range	Vertical resolution	Measured quantity	Derived/retrieved parameters	Platform
BACARDI	0.1 s	180°	0.2 – 3.6 µm (pyranometer); 4.5 – 42 µm (pyrgeometer)	integrated	Broadband solar (pyranometer) and terrestrial (pyrgeometer) irradiance	Albedo, net irradiance, heating rate profiles	HALO
VELOX	1 s	35° x 29°	7.7 – 12 µm	integrated	Emitted upward radiance, brightness temperature	Liquid water path, effective radius, cloud top and sea surface temperatures, surface type, 2D cloud mask	HALO
KT19	1 s	2.3°	9.6 – 11.5 µm	integrated	Emitted upward radiance, brightness temperature	Cloud top and sea surface temperatures, 1D cloud mask	HALO
SMART	1 s	180°	0.3 – 2.2 µm	integrated	Downward spectral irradiance	Cloud top reflectivity	HALO
LIMRAD	1.5 s	HPBW[a]: 0.56°	94 GHz (active); 89 GHz (passive)	22.4 m (0.3 – 3 km); 37.7 m (3 – 6.2 km); 42.1 m (6.2 – 13 km)	Radar reflectivtiy factor, Doppler velocity, polarimetric variables, brightness temperature at 89 GHz	Liquid water path, cloud top height, cloud mask, hydrometeor fraction	RV Meteor
LIMHAT	1 s	HPBW: 1.8° – 3.5° frequency dependent	22.2 – 31.4 GHz; 51.2 – 58.0 GHz	100 – 500 m parameter and height dependent	Brightness Temperature	Liquid water path, integrated water vapour	RV Meteor
CORAS	~6 s	2°	300 – 2200 nm	integrated	spectral solar downward radiance	Cloud optical thickness, effective radius	RV Meteor

[a]Half Power Beam Width

2 Platforms and LIM instrumentation

Clouds, dynamics and the interactions therein are a multi-dimensional challenge to observe and comprehensively capture. Overcoming this challenge therefore requires the use of multiple platforms and instruments. The participating LIM scientists contributed to this effort on two such platforms – HALO and the RV Meteor. Descriptions of the instrumentation and the observations during EUREC^{4}A are summarized in the following section and in Table 1.

2.1 HALO

The HALO aircraft flew with an instrument payload known as the cloud-observatory configuration (Stevens et al., 2019). With these instruments, the cloud population as well as their environment (i.e. dynamic and thermodynamic) can be simultaneously observed. Active and passive sensors were used to obtain a characterization of cloud field properties – microphyiscal, macrophysical and radiative – while dropsondes were used to collect in situ measurements of the vertical atmospheric profile. The flight track for HALO was carefully designed to observe the clouds as they develop and change while moving across the Atlantic trade-wind region but also with the intention of capturing the vertical thermodynamic motion. To this end, HALO flew in a pattern defined by large circles (approximately 220 km in diameter, one circle per hour) repeated in the same location over the course of each flight (see Fig. 1). Other flight patterns in this same measurement domain were also flown as well as flight maneuvers dedicated to the calibration of specific instruments. A total of 13 local research flights were performed throughout the course of the campaign, with an additional two ferry flights between Barbados and Germany. Most flights were approximately 9 hours in duration. Further information can be found in Bony et al. (2017), Stevens et al. (2021) and an article submitted to Earth System Science Data, "EUREC^{4}A's HALO", by Konow et al., which describe the results from the EUREC^{4}A campaign and the data product contributions from the HALO aircraft, respectively.

The LIM team operated three passive sensors on board HALO, two of which are new additions to this cloud-observatory configuration – a broadband radiometer package and a thermal infrared camera system. Each instrument is described in the following subsections and their respective positions on the aircraft can be seen in Fig. 2.

2.1.1 BACARDI

The new radiometer package on HALO, the Broadband AirCrAft RaDiometer Instrumentation (BACARDI), consists of two sets of Kipp and Zonen pyranometers (CMP 22) and pyrgeometers (CGR-4) mounted to the fuselage of the aircraft. With these four instruments, the upward and downward solar (0.2 – 3.6 µm) and terrestrial (4.5 – 42 µm) irradiances at flight level can be measured. Measurements from these broadband radiometers are necessary for quantifying the radiative forcing of the clouds in Tradewind Alley. It should be noted that this instrument is operated by colleagues at the DLR, and data processing is handled by the LIM team. A more detailed description of the instrument as well as a discussion concerning corrections applied in post-processing

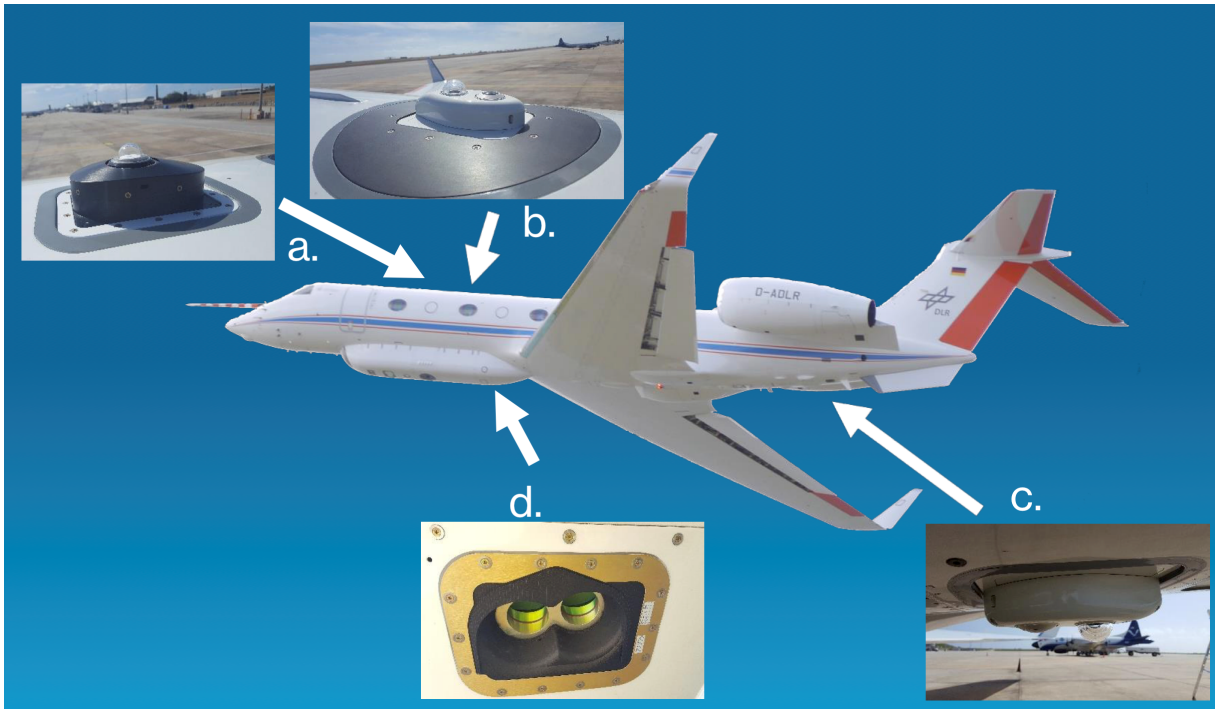

Figure 2: *Schematic depicting the position of LIM instruments on board HALO during the EUREC^{4}A campaign. Clockwise: a. SMART-Albedometer (downward spectral irradiance), b. BACARDI (downward broadband irradiance), c. BACARDI (upward broadband irradiance), d. VELOX.*

with respect to sensor response time, temperature dependence of the sensor and aircraft attitude can be found in an upcoming publication from Zöger et al., "A new efficient method to correct for the thermal offset of airborne broadband radiometer". BACARDI data has been published in the AERIS database (Ehrlich et al., 2021).

2.1.2 VELOX and KT19

The VELOX (Video airbornE Longwave Observations within siX channels) system consists of a thermal infrared (TIR) imager VELOX327k veL, manufactured by IR-CAM GmbH, Erlangen, Germany, and a KT19.85II infrared pyrometer, manufactured by HEITRONICS Infrarot Messtechnik, Wiesbaden, Germany, which serves as an additional reference. Both instruments are mounted together on the aircraft in a nadir-viewing position, where they observe the upward TIR radiance emitted by the clouds and surfaces below in two-dimensional images. At a typical cruising altitude of 10 km, VELOX has a field of view of 6.4 km x 5.1 km with a spatial resolution of 10 m. The observed radiance, or brightness temperature, can be used in retrievals of cloud properties such as liquid water path (LWP), effective radius (r_{eff}) and cloud top temperature (T_{ct}) as well as sea-surface temperature (T_{sea}) and surface type discrimination.

In order to carry out these retrievals, observations within various wavelength bands are needed. Basically, VELOX provides broadband measurements in the spectral wavelength range between 7.7 and 12 µm. However, this system contains a synchronously rotating filter wheel with six slots for bandpass and longpass filters; four of the slots are used for specific wavelength bands (8.648±0.55 µm, 10.74±0.39 µm, 11.66±0.81 µm and

11.50±0.20 µm; the two latter bands are cutoff at 12 µm based on the detector range), which correspond to different features of interest and are comparable to those used by MODIS (MODerate resolution Imaging Spectroradiometer) on the Terra and Aqua satellites, while the two remaining slots are for broadband (7.70 – 12.00 µm) observations. For further information about the VELOX system including calibrations and corrections to the data, please see the upcoming publication from Schäfer et al., "Introduction to the new airborne thermal infrared imager VELOX for remote sensing of cloud and surface properties".

Thus far, cloud masks were derived from the brightness temperature observations of both VELOX and KT19, respectively. Both are based on whether the measured brightness temperature meets a certain threshold relative to the brightness temperature of simulated cloud-free conditions. The measurement, or individual pixel in the case of VELOX, is then flagged as cloud-free, probably cloudy, or most-likely cloudy. The cloud mask data set is described and published in the AERIS database (Schäfer et al., 2021a,b) and is further explored alongside cloud mask products from other HALO instruments in the upcoming Konow et al. publication.

2.1.3 SMART

During EUREC^{4}A, the Spectral Modular Airborne Radiation measurement sysTem (SMART) measured downward irradiance in the spectral range between 0.3 µm and 2.2 µm. The spectral resolution (FWHM) of the instrument is 2 – 3 nm for wavelengths below 1.0 µm and 10 –15 nm for longer wavelengths. Notably, the instrument is mounted to a leveling platform to actively maintain a horizontal position. The irradiance measurements are used to calculate the cloud top reflectivity in combination with measurements by the spectral imager specMACS (Ewald et al., 2016). The data is also used in retrievals of cloud optical properties such as cloud optical thickness, effective diameter and thermodynamic phase. Wendisch et al. (2001) and Wendisch et al. (2016) provide further information. Data from the campaign is published in the AERIS database (Ehrlich, 2021).

2.2 RV Meteor

The RV Meteor's objective during the campaign was to measure along the same cross section of the HALO circle during the whole campaign to derive statistics of clouds inside this area (see Fig. 1). For this, the ship was steaming on a north-south transect between ~ 12° N and ~ 14°30′ N. It was equipped with a suite of in situ and remote sensing systems, of which only a few are mentioned here. For further details please refer to the cruise report (Mohr et al., 2020).

2.2.1 Remote sensing measurements

LIM contributed with remote sensing measurements to the atmospheric observations on Meteor. The LIM instruments on board the RV Meteor are shown in Fig. 3. They were placed on the starboard side of the 5th superstructure deck of the vessel to limit obstructions in the field of view of the instruments.

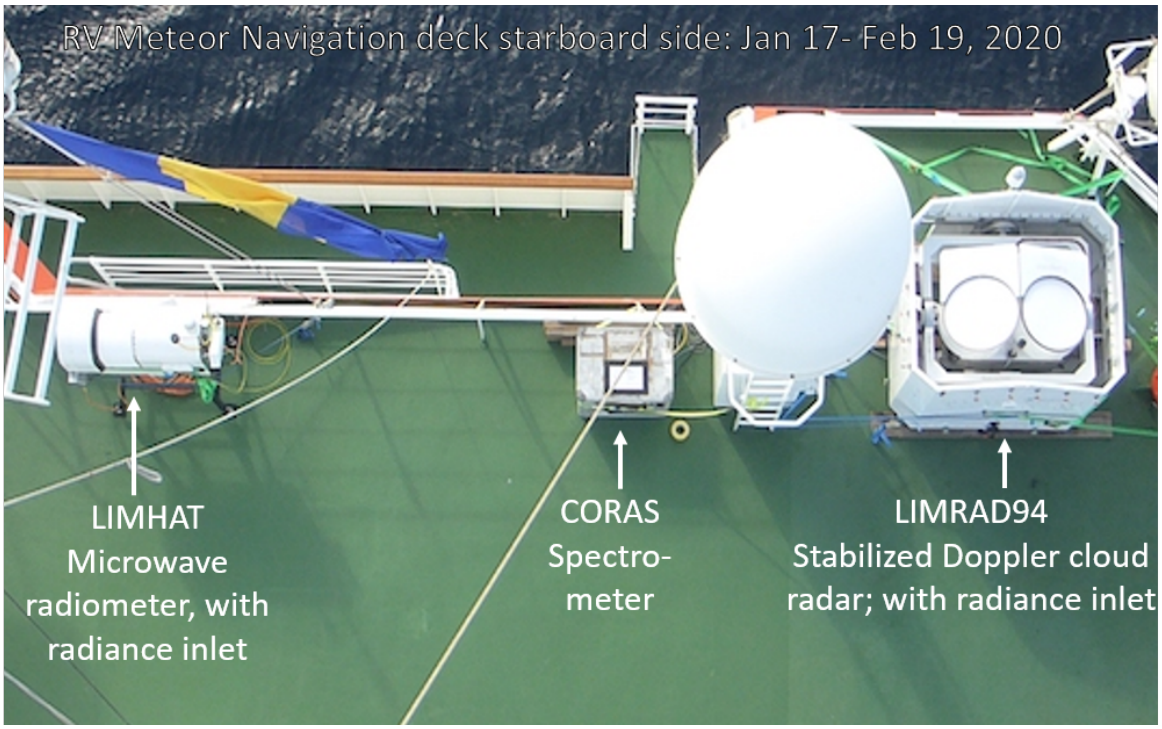

Figure 3: *Instrument setup on board the RV Meteor on the 5th superstructure deck from 17. Jan 2020 to 19. Feb 2020. From left to right: LIMHAT microwave radiometer with a radiance inlet, CORAS spectrometer, LIMRAD94 Doppler cloud radar inside a passive stabilization platform with a stabilized radiance inlet.*

Starting from the bow, the first instrument is the humidity and temperature profiler, HATPRO (LIMHAT) manufactured by Radiometer Physics GmbH (RPG), Meckenheim, Germany. LIMHAT uses a passive approach to retrieve profiles of relative humidity and temperature by measuring brightness temperatures in 14 channels around the water and oxygen absorption line in the atmosphere (Rose et al., 2005; Foth et al., 2015). From these measurements the liquid water path (LWP) as well as the integrated water vapour (IWV) in the atmospheric column above the instrument can be retrieved.

The second instrument is the spectral radiometer CORAS (COmpact RAdiation measurements System, Brückner et al. (2014)). During this cruise it was configured to measure zenith radiances transmitted through clouds to derive the cloud optical thickness as well as the effective cloud particle radius and cloud droplet number concentration by applying a retrieval method based on radiative transfer calculations.

The passive remote sensing was complemented by active remote sensing from a stabilized frequency modulated continuous wave (FMCW) W-band cloud radar (LIMRAD) manufactured by RPG (Küchler et al., 2017). It was placed inside a custom made cardanic mount, which reduces the impact of the roll and pitch motion of the ship on the vertical alignment of the radar. For off-zenith measurements, the horizontal wind would contaminate the retrieved vertical cloud particle velocity as this is derived from the measured Doppler velocity of the cloud particles. The radar samples the atmosphere by sending out three consecutive chirps. In each chirp, the frequency is slightly modulated to allow for a precise height measurement of the return signal. Thus, the vertical resolution of the radar changes with height (see Table 1). The sensitivity of the radar during

the campaign has been determined to be around −38 dBZ at 5 km. Sensitivity increases with decreasing height and thus, the cloud radar is able to detect very thin liquid clouds such as the trade-wind cumulus clouds, which were the main object of interest during the campaign. The LIMHAT and LIMRAD data sets have been published in the AERIS database (Kalesse-Los et al., 2020, 2021).

The remote sensing suite on board the RV Meteor was extended by a ceilometer on the 6th superstructure deck operated by the Max Planck Institute for Meteorology, Hamburg, which measured the backscatter at 1064 nm and is used to detect cloud base height. The ceilometer data set has also been published in the AERIS database (Jansen, 2020).

2.3 In situ and oceanic measurements

The ship was also equipped with in situ measurement instrumentation, such as the Mini Max Planck CloudKite operated by the Max Planck Institute for Dynamics and Self-Organization, Goettingen. It was used to fly a sonde into the clouds that provided measurements of the atmospheric state variables at sonde height and of cloud microphysical parameters such as the cloud droplet number concentration and cloud droplet size (Stevens et al., 2021). Another in situ measurement system on board was the Wide Range Aerosol Spectrometer EDM 665 (WRAS) which sampled the air at ship level to retrieve aerosol number concentrations in different size ranges.

In addition to atmospheric measurements, the ship routinely stopped to conduct oceanic measurements with the help of a Conductivity Temperature Depth (CTD) device. Thereby, profiles of conductivity, temperature and depth/pressure were retrieved as well as water samples from different depths. These water samples were then collected by the biologists from the Max Planck Institute for Marine Microbiology, Bremen, on board and prepared for further sampling on land.

3 Case study of collocated measurements

The following case study from 9 February 2020 illustrates the measurement capabilities for a cloud situation encountered during the campaign. For this case study we use a near HALO overpass with the RV Meteor at approximately 16:05 UTC, and thereby offer two perspectives - one view looking down onto the cloud with the VELOX instrument on board HALO and the other view looking up at the clouds with the cloud radar and ceilometer from RV Meteor. Due to the high ground speed of HALO compared to the RV Meteor, the temporal and spatial overlap between the two measurements is relatively small. While this is partly balanced by the larger field of view of VELOX, the radar samples only a narrow column above the ship, again reducing the potential overlap of the two measurements.

3.1 Ground-based remote sensing

An impression of the cloud condition as seen from Meteor is given in Fig. 4a. This gives a first impression of what an observer from the ground witnessed. Expanding the observation into the vertical cloud structure, Fig. 4c shows a time-height plot of radar reflectivity combined with the first ceilometer cloud base up to 3 km. The scene starts

with a few small broken clouds, followed by a more vertically extensive cloud with higher reflectivity. The ceilometer suggests a cloud base at around 800 m. Cloud top for the small scattered clouds is around 1600 m rising close to 3000 m for the larger cloud.

To characterize the cloud vertical structure with a statistical approach, the hydrometeor fraction is derived, which is the fraction of radar pixels with a measurement observed in each height bin for the specified time period, here 15:58 to 16:15 UTC on 9 February 2020. Figure 4b shows this hydrometeor fraction. The first thing to notice is that the maximum hydrometeor fraction during the observation period is below 30 %. This means that during the 17 minutes of observation, the radar only observed a cloud for about 5 minutes.

Furthermore, there are two cloud layers as can be seen by the drop of the hydrometeor fraction back to 6 % at 1950 m. Looking at Fig. 4c this corresponds to the vertically extensive cloud, whose top part is only loosely connected to the one below. Another prominent feature is shown in the lower part of the plot. It can be observed that hydrometeor fraction does not reach zero in the lowest radar range gates. Instead, it slowly rises, starting at 7.5 % and reaching about 11 % at 700 m. At this point a sharp increase towards the maximum value can be observed. The maximum value at 850 m corresponds with the cloud base also observed by the ceilometer. The signal seen below this height can be classified as virga, which is precipitation that does not reach the ground. The ceilometer is not able to detect these small rain particles, but the radar can. This synergy between the two instruments can therefore be used to detect virga events in an automated fashion, as has been done in Fig. 4c with the pink box. Finally, the hydrometeor fraction shows us that the maximum cloud top lies at 2700 m.

3.2 Airborne remote sensing

The same cloud scene is also observed by the airborne remote sensing instruments on HALO as it flies over the RV Meteor from east to west. As shown in Fig. 5, the VELOX imager captures the clouds observed by the radar on the RV Meteor as well as the surrounding cloud field. The cloud mask retrieval in this figure is based on three brightness temperature thresholds – 1 K, 1.5 K and 2 K – representing the difference of the brightness temperature of each pixel to cloud-free air. If only one threshold is reached, the pixel is flagged as *probably cloudy*, while if all are reached, the pixel is flagged as *most likely cloudy*. The scene shown in Fig. 5 reveals that the clouds in the vicinity of the RV Meteor fall mainly into the *most likely cloudy* category. Also, based on the image of the cloud field, the brokenness of the cloud deck agrees with the assessment from the radar that the observation of clouds during this period of time would be limited.

As mentioned, the overpass is relatively brief, with the RV Meteor remaining within VELOX's view for only about 30 seconds. Nevertheless, in the same way that the radar is able to provide a hydrometeor fraction over the vertical profile of the observed cloud, VELOX offers a cloud fraction for the two-dimensional scenes that it observes over the broader measurement domain, which is shown in Fig. 6. This particular time series takes place before, during and after the overpass, corresponding to the same duration of time shown in Figs. 4b and 4c. From this short example, the heterogeneity of the domain becomes clear. At the time of the overpass, the cloud field from the perspective of HALO rapidly shifts from a cloudy to a more clear field, with reported cloud fractions of the

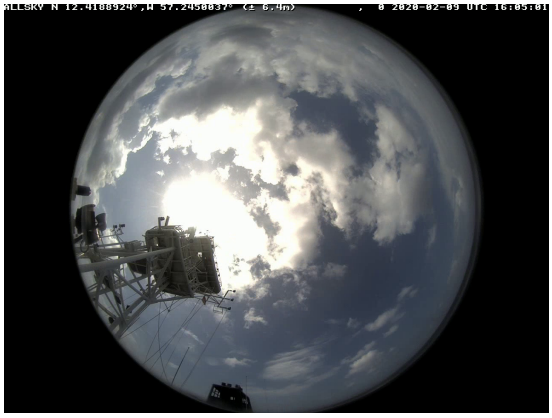

(a) *Picture from the all sky camera on board the RV Meteor of the cloud scene at 16:05 UTC.*

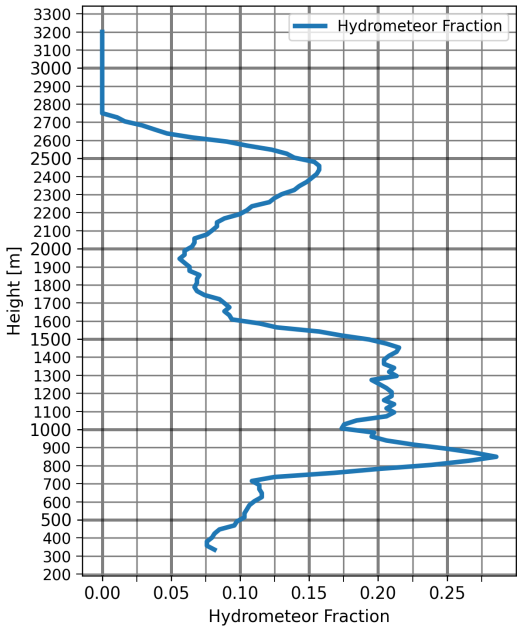

(b) *Hydrometeor Fraction in the lower Troposphere from 15:58 to 16:15 UTC.*

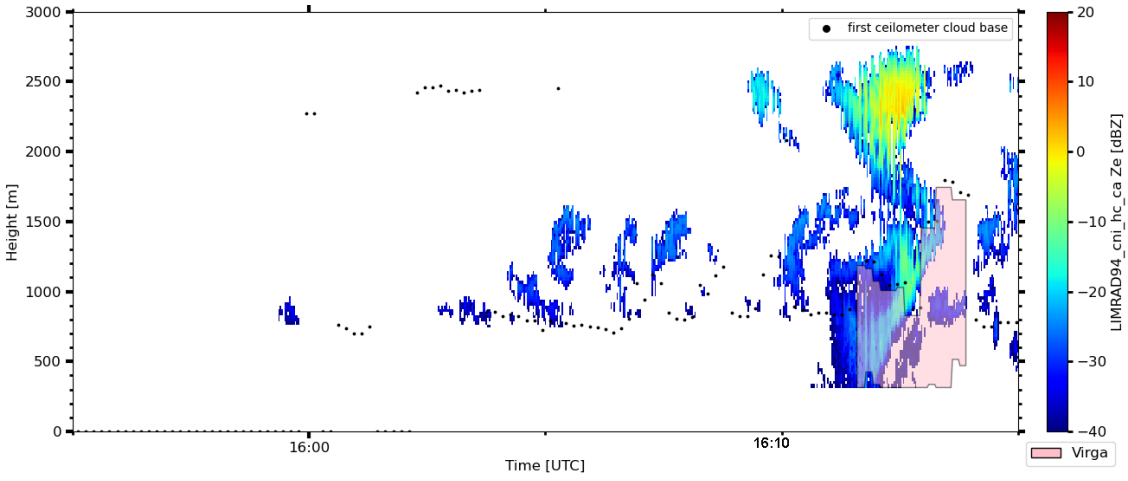

(c) *Time height plot of radar reflectivity and the lowest ceilometer cloud base (black dots). Radar signal below the ceilometer cloud base can be classified as virga (pink box).*

Figure 4: *RV Meteor viewpoint of the cloud scene on 9 February 2020.*

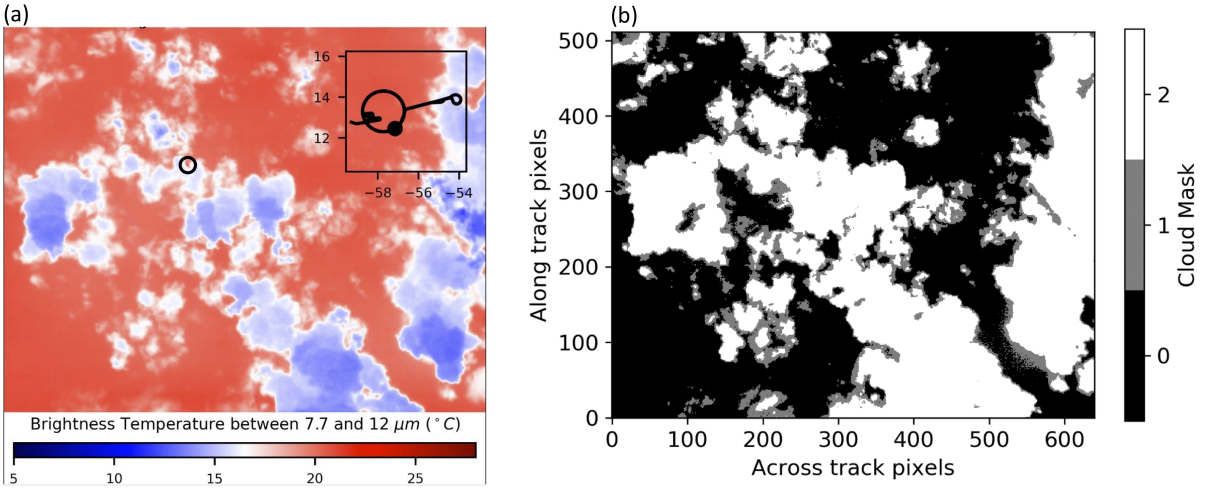

Figure 5: *Cloud images from VELOX at the time of the overpass (16:05:16 UTC shown here). a. Image with brightness temperature observations from the broadband channel. The flight track can be seen in the upper right corner, with the location of HALO marked as a filled, black circle. The smaller open circle in black in the center of the image indicates the position of the RV Meteor at this time. b. The cloud mask retrieved from the brightness temperature image at the same time. 0: no cloud, 1: probably cloudy, 2: most likely cloudy.*

scene between 21 % and 75 %.

Using this case study, we can discuss a common challenge in cloud research – how to define cloudiness. The sensitivities of the different instruments are a key point in that discussion. A cloud radar like the one on RV Meteor is most sensitive to large droplets, whereas an IR thermal imager like VELOX is sensitive to any amount of liquid water, including water vapor, independent of cloud particle size. Thus, in a case of clouds with low LWP, which also typically have small droplets, VELOX has the necessary sensitivity to detect them. On the other hand, the radar measurement technique is ideally suited to characterizing the vertical structure of the clouds and precipitation, whereas VELOX can define the cloudy versus cloud-free areas, based on emitted radiation, and the horizontal distribution of cloud properties across a broader field of view. Furthermore, the way in which the respective platforms travel relative to the movement of the cloud field also leads to differences in the spatial representation of the different measurements. While seemingly complex, having both perspectives, as well as the perspectives of the numerous other instruments involved in the campaign, ultimately serves the purpose of providing a more complete picture. Thus, the merits of a multi-platform campaign are clear.

4 Conclusions & Outlook

The EUREC^{4}A campaign in early 2020 mobilized a number of research aircraft and vessels, and took advantage of the Barbados Cloud Observatory nearby, to sample the clouds and large-scale dynamic structure of the Atlantic trade-wind region. Scientists from LIM were involved in this effort with instruments aboard the HALO aircraft and the RV Meteor. The utilization of instruments viewing from above and below as well

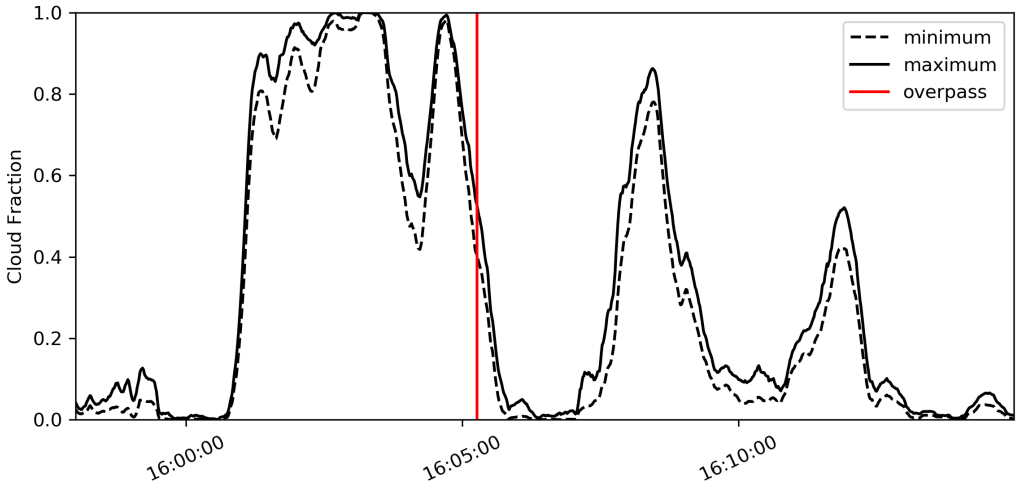

Figure 6: *Cloud fraction as derived from the VELOX camera, showing the minimum and maximum cloud fraction depending on brightness temperature differences to clear-sky. The minimum includes only "most likely cloudy" pixels, while the maximum also includes "probably cloudy" pixels.*

as employing complementary remote sensing techniques offers a unique and comprehensive view of these clouds. Specifically, the observations allow for studies of cloud imagery, profiles of the vertical hydrometeor structure, the radiative impact of the clouds, information and statistics on the macrophysical properties of the clouds as well as the potential for further retrievals revealing other microphysical properties.

This rich dataset is central to many current analyses as well as future work. The following provides a brief description of the activities at LIM specific to EUREC^{4}A data.

- In addition to the cloud mask data product from VELOX, which will continue to be fine-tuned, there is continuing work on retrievals of the cloud properties described in Sec. 2.1.2.

- An analysis to determine whether the cloud radiative forcing of trade wind cumuli is driven by the macrophysical or microphysical properties of the clouds, the mesoscale organization of the cloud field or some combination is in progress. By determining the sensitivity of the cloud radiative forcing to these quantities, the representation of these clouds in models can be assessed. The analysis includes cloud albedo, which has been calculated from the irradiance measurements of BACARDI in combination with radiative transfer simulations using libRadtran (Mayer and Kylling, 2005), and domain averaged cloud properties from GOES16 satellite observations during the campaign period. Future work on this topic will include use of the cloud mask and additional cloud properties derived from VELOX.

- A synergistic approach utilizing the obtained microphysical and macrophysical cloud properties from active and passive remote sensing on board the RV Meteor to derive cloud droplet number concentrations is also currently being worked on. The joint application, which includes solar zenith radiances, is currently being

tested for homogeneous stratocumulus in the absence of drizzle, assuming the adiabatic theory. The heterogeneous nature of the observed trade wind cumuli, as illustrated in Sec. 3, poses the inevitable problem of 3D radiative effects, which complicate or restrict microphysical radiance retrievals without the knowledge of the 2D/3D cloud fields. Further improvement for homogeneous cloud scenes, as suggested in the literature, can be achieved by combined forward modeling of radar reflectivity and solar zenith radiances.

- By combining the radar, ceilometer and HATPRO on board the RV Meteor, a couple of synergistic retrievals can be applied, which have been developed within the Cloudnet framework (Illingworth et al., 2007). The retrievals include a hydrometeor classification and a radar and lidar detection status, which can then be used to derive further statistics of the observed hydrometeors. The measurements can be compared to the measurements at the Barbados Cloud Observatory, which also operates as a Cloudnet site to study cloud evolution.

- The performance of the radar stabilization platform and the impact on the radar observation and derived products will be analyzed.

- Using the remote sensing observations on board the RV Meteor, the macrophysical characteristics of the trade wind cumulus clouds are being investigated.

References

Bony, S., Stevens, B., Ament, F., et al.: EUREC4A: A Field Campaign to Elucidate the Couplings Between Clouds, Convection and Circulation, Surv Geophys, 38, 1529–1568, doi:10.1007/s10712-017-9428-0, 2017.

Brückner, M., Pospichal, B., Macke, A., and Wendisch, M.: A new multispectral cloud retrieval method for ship-based solar transmissivity measurements, J. Geophys. Res. Atmos., 119, 11,338–11,354, doi:10.1002/2014JD021775, 2014.

Ehrlich, A.: Measurements of spectral, solar downward Irradiance with the Spectral Modular Airborne Radiation measurement sysTem (SMART) during the EUREC4A Field Campaign, doi:10.25326/157, AERIS, 2021.

Ehrlich, A., Wolf, K., Luebke, A., Zoeger, M., and Giez, A.: Broadband solar and terrestrial, upward and downward irradiance measured by BACARDI on HALO during the EUREC4A Field Campaign, doi:10.25326/160, AERIS, 2021.

Ewald, F., Kölling, T., Baumgartner, A., Zinner, T., and Mayer, B.: Design and characterization of specMACS, a multipurpose hyperspectral cloud and sky imager, Atmos. Meas. Tech., 9, 2015–2042, doi:10.5194/amt-9-2015-2016, 2016.

Foth, A., Baars, H., Girolamo, P. D., and Pospichal, B.: Water vapour profiles from Raman lidar automatically calibrated by microwave radiometer data during HOPE, Atmos Chem Phys, 15, 7753–7763, doi:10.5194/acp-15-7753-2015, 2015.

Illingworth, A. J., Hogan, R. J., O'Connor, E., et al.: Cloudnet: Continuous Evaluation of Cloud Profiles in Seven Operational Models Using Ground-Based Observations, Bull. Am. Meteorol. Soc., 88, 883–898, doi:10.1175/BAMS-88-6-883, 2007.

Jansen, F.: Ceilometer Measurements RV Meteor, EUREC4A, doi:10.25326/53, AERIS, 2020.

Kalesse-Los, H., Röttenbacher, J., Schäfer, M., and Emmanouilidis, A.: Microwave Radiometer Measurements RV Meteor, EUREC4A, doi:10.25326/77, AERIS, 2020.

Kalesse-Los, H., Röttenbacher, J., and Schäfer, M.: W-Band Radar Measurements RV Meteor, EUREC4A, doi:10.25326/164, AERIS, 2021.

Küchler, N., Kneifel, S., Löhnert, U., et al.: A W-Band Radar–Radiometer System for Accurate and Continuous Monitoring of Clouds and Precipitation, J Atmos Oceanic Technol, 34, 2375–2392, doi:10.1175/jtech-d-17-0019.1, 2017.

Mayer, B. and Kylling, A.: Technical note: The libRadtran software package for radiative transfer calculations – description and examples of use, Atmos Chem Phys, 5, 1855 – 1877, doi:10.5194/acp-5-1855-2005, 2005.

Mohr, W., Kinne, S., Rollo, C., et al.: EUREC4A Campaign, Cruise No. M161, 17 Jan 2020 - 03 Mar 2020, Bridgetown *Barbados* - Ponta Delgada *Portugal*, METEOR-Berichte, doi:10.2312/cr_m161, 2020.

Rose, T., Crewell, S., Löhnert, U., and Simmer, C.: A network suitable microwave radiometer for operational monitoring of the cloudy atmosphere, Atmos Res, 75, 183–200, doi:10.1016/j.atmosres.2004.12.005, 2005.

Schäfer, S., Ehrlich, A., Luebke, A., et al.: Cloud mask derived from airborne KT19 measurements during the EUREC4A field campaign, doi:10.25326/162, AERIS, 2021a.

Schäfer, S., Ehrlich, A., Luebke, A., et al.: Two-dimensional cloud mask and cloud fraction with 1 Hz temporal resolution derived from VELOX during the EUREC4A field campaign, doi:10.25326/163, AERIS, 2021b.

Stevens, B., Ament, F., Bony, S., et al.: A High-Altitude Long-Range Aircraft Configured as a Cloud Observatory: The NARVAL Expeditions, Bull. Am. Meteorol. Soc., 100, 1061 – 1077, doi:10.1175/BAMS-D-18-0198.1, 2019.

Stevens, B., Bony, S., Farrell, D., and 290 co-authors: EUREC^{4}A, Earth Syst. Sci. Data Discuss., 2021, 1–78, doi:10.5194/essd-2021-18, 2021.

Wendisch, M., Müller, D., Schell, D., and Heintzenberg, J.: An airborne spectral albedometer with active horizontal stabilization, J Atmos Oceanic Technol, 18, 1856–1866, doi:10.1175/1520-0426(2001)018<1856:AASAWA>2.0.CO;2, 2001.

Wendisch, M., Poschl, U., Andreae, M. O., et al.: Acridicon-chuva campaign: Studying tropical deep convective clouds and precipitation over Amazonia using the New German research aircraft HALO, Bull Am Meteorol Soc, 97, 1885–1908, doi:10.1175/BAMS-D-14-00255.1, 2016.

Contrasting cloud properties in the trade wind region of Barbados in the dry and wet season

Roschke, J.[1], **Emmanouilidis, A.**[1]

[1] *Institut für Meteorologie, Stephanstraße 3, 04103 Leipzig,*
E-mail: jr55riqa@studserv.uni-leipzig.de,
E-mail: alexandros.emmanouilidis@uni-leipzig.de

Summary: A statistical analysis is provided in order to describe the macro- and microphysical properties of clouds over the Barbados. Data from the Cloudnet target classification product are analyzed for February and October 2013 and 2015 over the Barbados cloud observatory. The months February and October are taken to be representative for the dry and the wet season over Barbados. Hydrometeor fraction from the Cloudnet target classification and from a combination of cloud radar and ceilometer data are presented. Moreover, results of the distribution of the first layer of detected cloud base height from the ceilometer are presented. Additionally, the analysis for hydrometeor fraction and cloud base height are carried out for the measurements on board the Research Vessel Meteor during the EUREC^{4}A field campaign and compared to the observations over the Barbados cloud observatory in February 2020. The strongest seasonal variation of the vertical distribution of the Cloudnet classification targets appears between 3 and 9 km. The maximum occurrence of the first detected cloud base height is found at higher altitudes during the dry season compared to the wet season. The vertical distribution of hydrometeor fraction shows a bimodal distribution and is largest during the wet season. In general, the seasonal variation of the distribution of the Cloudnet targets, hydrometeor fraction and cloud base height between 0 and 3 km is less pronounced compared to heights above 3 km.

Zusammenfassung: Diese Studie enthält eine statistische Analyse der makro- und mikrophysikalischen Eigenschaften von Wolken über dem "Barbados Cloud Observatory". Es wurden Daten aus dem "Cloudnet target classification"-Produkt aus den Monaten Februar und Oktober für die Jahre 2013 und 2015 analysiert. Die Monate Februar und Oktober gelten als charakteristisch für die Trocken- und die Regenzeit. Der Hydrometeor-Anteil aus der Cloudnet Target Classification und aus der Kombination von Wolkenradar und Ceilometer-Daten wurden ermittelt. Die Verteilung der ersten Schicht der detektierten Wolkenbasishöhe aus den Ceilometer-Daten wurde abgeleitet. Zusätzlich wurden die Analysen für den Hydrometeor-Anteil und die Wolkenbasishöhe zwischen den Messungen an Bord des Forschungsschiffes Meteor während der EUREC^{4}A-Feldkampagne und den Beobachtungen über dem "Barbados Cloud Observatory" für Februar 2020 verglichen. Die Ergebnisse dieser Untersuchung zeigen, dass die stärkste saisonale Variation der vertikalen Verteilung des "Cloudnet target classification"-Produktes zwischen 3 und 9 km auftritt. Das maximale Auftreten der ersten detektierten Wolkenbasishöhe wird in der Trockenzeit in größeren Höhen gefunden als in der Regenzeit. Wolkenanteil und Hydrometeor-Anteil zeigen eine bimodale Verteilung und sind in

der Regenzeit am größten. Im Allgemeinen ist die saisonale Variation des Wolkenanteils, des Hydrometeor-Anteils und der Wolkenbasishöhe zwischen 0 und 3 km gering.

1 Introduction

Understanding patterns of cloudiness and advancing investigations of clouds are central to increase the confidence in fundamental aspects of climate change. However, much uncertainty still exists about the physical properties of clouds especially of those found within the trade wind regions (Stevens et al., 2016). Surveys such as that conducted by Medeiros and Nuijens (2016) have shown that clouds over Barbados are representative of clouds in the broader tropics. Thus, enhancing the knowledge about clouds over Barbados broadens the understanding of clouds within the trade wind region and improves their representation in climate models. A suitable location to observe clouds over Barbados is the Barbados Cloud Observatory (BCO), which is located on the island's eastern coast next to the Caribbean Sea. The observatory is equipped with ground-based remote sensing instruments that form the basis of Cloudnet (Stevens et al., 2016).
A statistical analysis of data from the Cloudnet target classification, cloud radar and ceilometer is presented to resolve the micro- and macrophysical properties of clouds over the BCO. In particular, the vertical distribution of Cloudnet classification targets, hydrometeor fraction (HF) and the first layer of the detected cloud base height (cbh^1) are compared from the dry to the wet season over Barbados. Finally, HF is compared between the instruments over the BCO and from the Research Vessel Meteor (R/V Meteor) during the EUREC^{4}A (Elucidating the role of clouds-circulation coupling in climate) field campaign, which took place in early 2020 (Bony et al., 2017).

2 Instrumentation and Methods

The data analyzed in this study are taken from the Cloudnet target classification, ground-based cloud-radar and ceilometer over the BCO. These data differ in their resolution and time period covered due to instrument exchanges. The years 2013 and 2015 were selected for the seasonal comparison out of the available Cloudnet data over the BCO (2011 until 2017) because they show the most continuous data coverage in February and October. Furthermore, an unrealistically high proportion of low clouds were misclassified as aerosols and insects by the Cloudnet algorithm in 2016. For this reason, the data from 2016 were not included in the analysis. Data from cloud radar and ceilometer are chosen for the same years. The months February and October are taken to be representative for the dry and the wet season as proposed from previous research by Stevens et al. (2016). Orientated on definitions provided by Stevens et al. (2016), low level clouds are defined as clouds located from 0 to 3 km. The mid-levels are defined as the height range from 3 to 9 km and the high-levels from 9 to 15 km. Heights below 1 km are referred to as near the lifting condensation level (near LCL). The methods used to derive HF and cbh^1 are based on studies of Stevens et al. (2016) and Nuijens et al. (2014). All data source and the methods that were applied to the data are described in the following sections.

2.1 Cloudnet data products

The Cloudnet project was started in 2001[1] in order to provide information about the physical state of the atmosphere from a synergy of ground-based remote sensing observations. The Cloudnet target classification product enables the identification of the physical phase of hydrometeors (Illingworth et al., 2007). Core instruments of a Cloudnet observation site are a cloud radar and a ceilometer. The measurements of these instruments are analyzed in combination with thermodynamic profiles of a model by the Cloudnet algorithms (Illingworth et al., 2007). In general, the ceilometer is used to identify the base of liquid water clouds. Liquid droplets are assigned when a threshold value is exceeded in the ceilometer signal followed by a characteristic decrease in signal above the cloud base. The cloud top is detecteed by the radar signal in case the ceilometer backscatter is not extinguished. Falling targets are assigned between cloud base and the highest pixel below cloud top when the radar signal decreases with height and the radar reflectivity exceeds −30 dBZ. Additionally, all radar echos in the profile are classified as falling in the case that rain is detected at the ground. Ice particles are assigned when falling targets are observed and the wet bulb temperature is below 0 °C. In the case that falling targets have been detected and additionally the wet bulb temperature is above 0 °C, the profile is categorized as containing precipitation. The height of the melting layer is derived either from the model data or when a sharp increase in the Doppler velocity is observed. A detailed description of the Cloudnet target classification algorithm can be found in Hogan and O'Connor (2004). An example of the Cloudnet classification product for the 25th of February 2015 is presented in Fig.1 (a) and after selecting the targets relevant for this study in (b). HF is calculated by taking the sum of all targets in each height bin (30 m).

In this study the original resolution of 30 m and 15 s is maintained. Profiles are analyzed for containing "Cloud droplets only", "Drizzle–rain and cloud droplets", "Ice and supercooled droplets", "Ice" and "Drizzle or rain." "Cloud droplets only" and "Drizzle-rain and cloud droplets" are combined to the category "Liquid droplets". The data from the Cloudnet target classification are processed with "pyLARDA", an algorithm designed by Bühl et al. (2018) simplifying the handling of the Cloudnet data.

2.2 Ceilometers

The Jenoptik CHM 15k(X) ceilometer measures at 1064 nm with a range resolution of 30 m and a temporal resolution of 30 s until April 2015 and 10 s since April 2015. The first cloudy point detected by the ceilometer is taken to be the cloud-base height (cbh^1). The ceilometer detects cbh^1 using a vertical gradient method explained in detail by Nuijens et al. (2014). A time range of 456 h was chosen to ensure an equal amount of data for the seasonal comparison. In this study, vertical profiles of cbh^1 are analyzed up to 4 km. Cloud-base height occurrence is derived by taking 50 m bins. Rain events are not excluded within the estimation of cloud base height. The ceilometer on board the R/V Meteor is a Jenoptik system ceilometer like over the BCO.

[1] https://cloudnet.fmi.fi

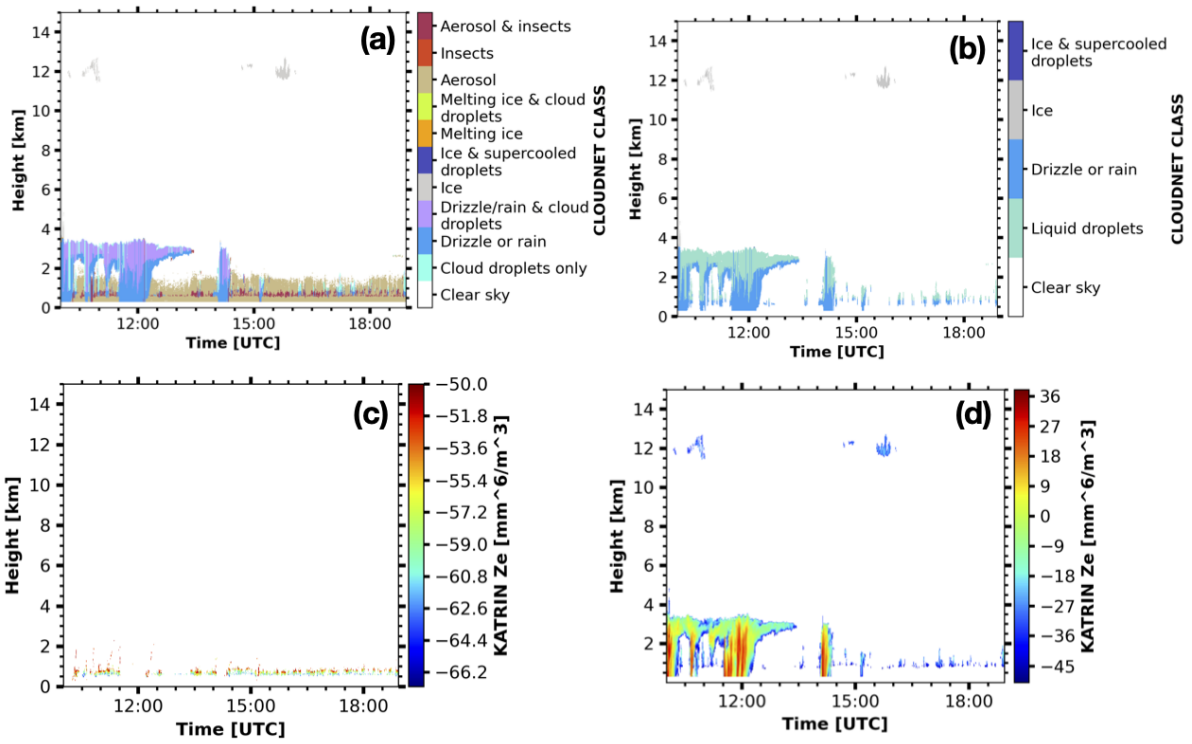

Figure 1: *The example output of the Cloudnet classification product over the BCO on the 25th of February 2015 is displayed. The unprocessed Cloudnet output (a) and the same scenario after selecting the relevant targets for the study in (b) are presented. The equivalent radar reflectivity* $-65\,\mathrm{dBZ} < Z_e < -50\,\mathrm{dBZ}$ *from KATRIN during the same time is displayed in (c) and with a threshold of* $-50\,\mathrm{dBZ}$ *in (d).*

2.3 Cloud radars

The cloud radars KATRIN and CORAL from the BCO operate at 35.5 GHz. KATRIN was replaced by CORAL in April 2015 which is still ongoing. Profiles from KATRIN are taken every 30 s with a range resolution of 30 m. Since KATRIN operated from January 2011 to mid-May 2011 and October 2011 in an alternating vertical pointing and scanning mode, the data from 2011 is excluded from the analysis (Nuijens et al., 2014). CORAL measures with a resolution of 10 s and 30 m. Additionally, data from the RPG 94 GHz polarized cloud radar LIMRAD94 on board the R/V Meteor were analyzed.
Hydrometeor fraction is estimated by combining radar and ceilometer data as proposed by Bony et al. (2017). All radar signals detected above the cbh^1 account for the hydrometeor fraction. Due to differences in the instrument resolutions, the data is averaged with a temporal resolution of 30 s and spacial resolution of 30 m as displayed in Fig.2. Each radar signal where the equivalent radar reflectivity Z_e exceeds $-50\,\mathrm{dBZ}$ is defined as a true hydrometeor return as proposed by Klingebiel et al. (2019) to ensure that haze echos are excluded. Comparing Fig.1 (a) and (c), weak radar signals between $-65\,\mathrm{dBZ} < Z_e < -50\,\mathrm{dBZ}$ are classified as "Aerosols and insects" by the Cloudnet algorithm and are excluded in the analysis. Following methods from previous research by Nuijens et al. (2015a) all returns below cbh^1 indicating drizzle are excluded.
An example of hourly mean HF resolved for each season in 2015 can be seen in Fig.7. The vertical distribution of monthly mean HF is presented for the dry and the wet season

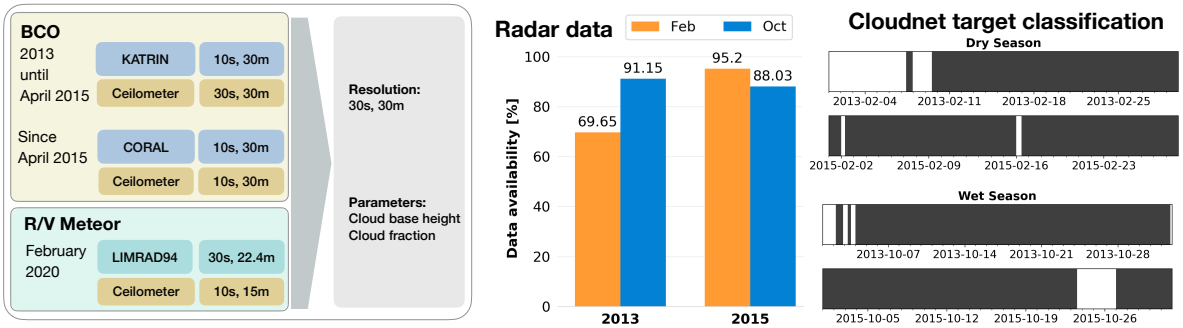

Figure 2: *Resolution and data availability of the relevant instruments used to derive cloud fraction and cloud base height at the BCO and R/V Meteor. The data from the different instruments are averaged on a common grid with a resolution of* 30 s *and* 30 m. *The radar data availability at the BCO is presented on the right for February and October in 2013 and 2015.*

in 2015 (the original resolution was maintained). For the statistics no data are excluded even though the radar data coverage is not equal every time. Interpretations of monthly mean HF have to be made under consideration of this fact.

3 The vertical distribution of cloud

A statistical analysis of the vertical distribution of the targets from the Cloudnet data, cbh[1] and HF from the Cloudnet data and from the combination of radar and ceilometer data are presented. The method deriving HF is applied on the measurements on board the R/V Meteor and compared to the observations over the BCO in February 2020.

3.1 Cloudnet target classification

Cloudnet target classification distributions are shown in Fig.3 partitioned into Liquid droplets (1), Drizzle or rain (2), Ice (3) and Ice and supercooled droplets (4) for the dry and the wet season. Liquid droplets (1) occurred more frequent at 780 m (8.8 %) during the dry season compared to the wet season at 750 m (7.2 %) . This supports findings of Nuijens et al. (2014) who pointed out that clouds start to form in higher altitudes during the dry season compared to the wet season. Liquid droplets (1) show a second peak at 1.8 km during the dry season and a weaker peak at 1.5 km during the wet season, potentially indicating deeper and more developed cumuli with stratiform outflow. Nuijens et al. (2014) also assigned the second peak in profile of HF to stratiform cloud layers which are located close to the trade inversion. Also, these results seem to be consistent with research from Lamer et al. (2015) who point out a higher occurrence of stratiform layers during the dry season and a considerable absence of precipitating boundary layer clouds during the wet season in 2013 over the BCO.
Drizzle or rain (2) occurred most often at 540 m during both seasons. Consequently, a noticeable amount of Drizzle or rain (2) during the dry season can be contributed to be originated from shallow cumuli and those with stratiform like outflow. This also supports evidence from previous observations such as Nuijens et al. (2009), Vogel et al. (2016),

Rauber et al. (2007) and Short and Nakamura (2000) who showed that precipitation from shallow cumulus occurs often. Short and Nakamura (2000) also mentioned that the intensity of warm rain from shallow clouds increases as they grow deeper and that shallow cumulus producing rainfall typically extend up to 2 km. Accordingly, it can be assumed that a high proportion of the precipitation was caused by clouds contributing to the maximum in Liquid droplets (1) in 1.8 km.

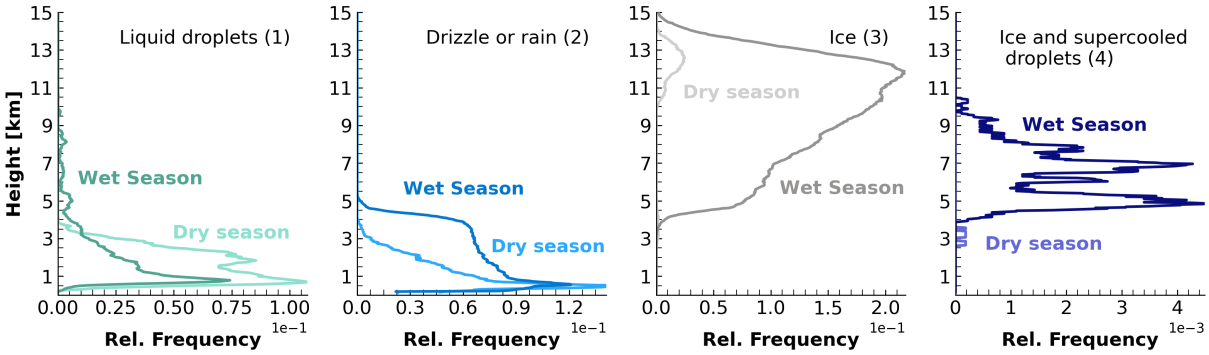

Figure 3: *Relative Frequencies of Cloudnet target classification for the targets Liquid droplets (1) , Drizzle or rain (2), Ice (3), and Ice and supercooled droplets (4) during dry and wet season. Data for dry and wet season are summed up for February and October (2013 and 2015) respectively.*

Ice (3) in Fig.3 showing a higher occurrence during the wet season compared to the dry season. Indeed, the occurrence of cirrus clouds is related to the presence of deep convective clouds which dominate during the wet season as mentioned by Sassen et al. (2009). The sharp decrease in Ice (3) occurrence below 5 km marks the average height at which ice starts to melt during the wet season, also indicated by the minimum in the distribution of HF in Fig.6 (a) at 4.3 km (Melting ice from the original Cloudnet target classification is excluded in the analysis). Short and Nakamura (2000) refers to the influence of the melting level on the statistics of the storm height. Accordingly, the 0 °C isotherm is located at an average height of 5 km in the tropics. Melting ice, which appears as an area of increased reflectivity in the radar signal below 0 °C isotherm was not included in the statistics and therefore appears as a minimum in the vertical distribution of HF.
Ice and supercooled droplets (4) were rarely observed compared to the other Cloudnet targets but significantly more frequent during the wet season compared to the dry season. Moreover, the distribution of Ice and supercooled droplets (4) indicates, that mixed phase clouds containing combination of the targets (1), (3) and (4) were more frequent during the wet season.

An overview of the height ranges at which the respective targets occurs mostly in relation to each other is presented in Fig.4. The monthly target proportion corresponds to the mean frequency of occurrence (for the height ranges near LCL, low, mid, high and total) of all targets shown in Fig.4. The results show that only Liquid droplets (1) and Drizzle or rain (2) are present near the LCL and within low levels during both seasons. The proportion of Drizzle or rain (2) increases during the wet season near the LCL and in the low levels. Concluding from this, the total observed precipitation must not only result from clouds in the low levels but also from deep convective clouds which increase the

frequency of occurrence of Drizzle or rain (2) above and below 3 km during the wet season.
What stands out is that the highest seasonal variation of the target proportions occurs within the mid-levels. The ratio change can be explained by the increase in total target occurrence mainly due to the increase in Ice (3) occurrence during the wet season. Moreover, the ratio of Liquid droplets (1) to Drizzle or rain (2) changes with the former dominating in the dry season and the latter dominating over Liquid droplets (1) during the wet season. The targets Liquid droplets (1) and Drizzle or rain (2) dominate over Ice (3) and Ice and supercooled droplets (4) over the total height range during the dry season. Moreover, the target proportion changes during the wet season with Ice (3) dominating because of deep convective clouds which are more commonly observed during the wet season as the comparison in 7 indicates.. The ratio of Drizzle or rain (2) to Liquid droplets (1) changes with (2) being greater than (1) during the wet season.

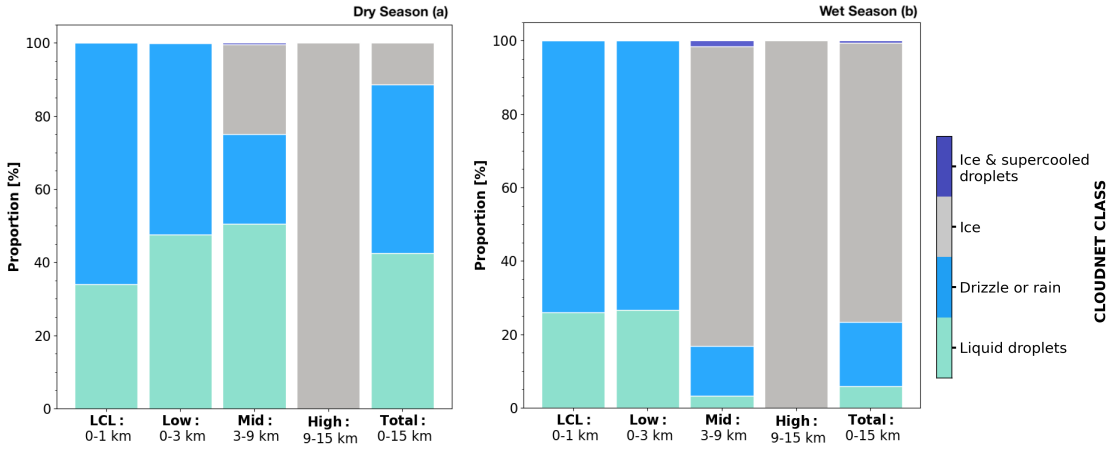

Figure 4: *Proportion of Cloudnet classification targets relative to each other for different height ranges for the dry (a) and wet (b) season.*

3.2 Cloud-base height distribution

The maximum occurrence in cbh^1 detected by the ceilometer in Fig. 5 is located below the LCL (<1 km). During the dry season this peak is found at 746±100 m and during the wet season at 646±100 m. The peak during the dry season is located at a similar height compared to the maxima in Liquid droplet (1) occurrence. However, the results from the Cloudnet target classification indicate that low level liquid clouds are more frequent during the dry season compared to the wet season which seems to be contradictory to the findings in cbh^1 occurrence showing larger frequencies during the wet season. The higher occurrence in cbh^1 during the wet season detected by the ceilometer is suggested to be overestimated due to heavier rain events during the wet season which can distort the ceilometer signal (Nuijens et al., 2014). Compared to the dry season, the results of cbh^1 from the ceilometer correspond more with the Cloudnet target classification results despite precipitating targets (Drizzle or rain (2)) being frequently observed. However, the ceilometer is able to detect cbh^1 during light rain events which are suggested to be occurred more often during the dry season. Consequently, the results in cloud base height are less accurate during the wet season compared to the dry season. However, the

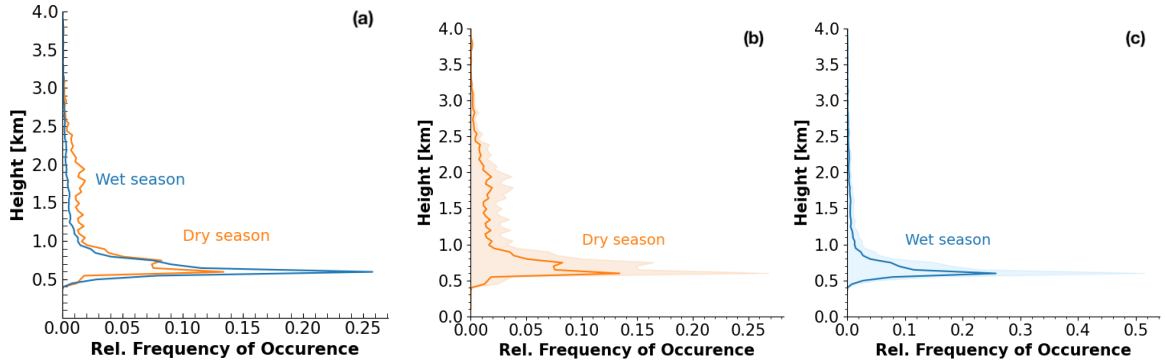

Figure 5: *Relative frequency of occurrence of cloud base height (*50 m *bins) provided by the ceilometer over the BCO (a) with shaded areas showing the standard deviation for each distribution during the dry (b) and wet (c) season.*

spread in height between the two peaks reflects the range in LCL from the dry to the wet season as indicated in the previous section. Clouds start to form at higher altitudes during the dry season compared to the wet season. Thus, the bases of clouds during the dry season are located higher up (Nuijens et al., 2015b). cbh^1 becomes less frequent above 1 km with the hint of a second maximum between 1 and 1.5 km which might reflect the presence of clouds with stratiform outflows (Nuijens et al., 2015b). Above 1.5 km cbh^1 is becoming less frequent which confirms findings presented by Nuijens et al. (2014) and Nuijens et al. (2015b).

3.3 Cloud fraction

Fig. 6 (a) represents the HF estimated from the Cloudnet target classification by taking the sum over the four targets presented within this study. In general, the occurrence of low level clouds is less variable during the seasons compared to mid and high levels. Total HF is larger during the wet season compared to the dry season with the seasonal variability being more pronounced on mid and high levels. The vertical distribution of HF in (a) and (b) is bimodal in both seasons which confirms earlier findings by Stevens et al. (2016). The seasonality of clouds over the BCO is related to the migration of the ITCZ which produces circulation shifts and large changes in cloudiness (Stevens et al., 2016). Large scale subsidence during the dry season suppresses the development of deeper clouds which explains why mid and high level clouds are less frequent during the dry season. The higher frequency of clouds in the mid and high levels during the wet season is caused by upward motion that favors the formation of deep convective clouds (Nuijens et al., 2015a). Furthermore, the atmosphere is more humid through a deeper layer during the wet season which is why HF is on average higher.
The low level total HF occurrence from the Cloudnet data shows a peak at 630 m (21 %) during the dry season which indicates the presence of Drizzle or rain (2) as described in the previous section. Findings by Nuijens et al. (2015a) suggest that the cloud base is located where the profile in low levels of HF maximizes. This idea is supported in the second peak at 840 m (19 %) during the dry season and at 750 m (17 %) during the wet season which are located at a similar height as most cloud bases and also of the maximum occurrence of Liquid droplets (1). Thus, it is suggested that these peaks reflect

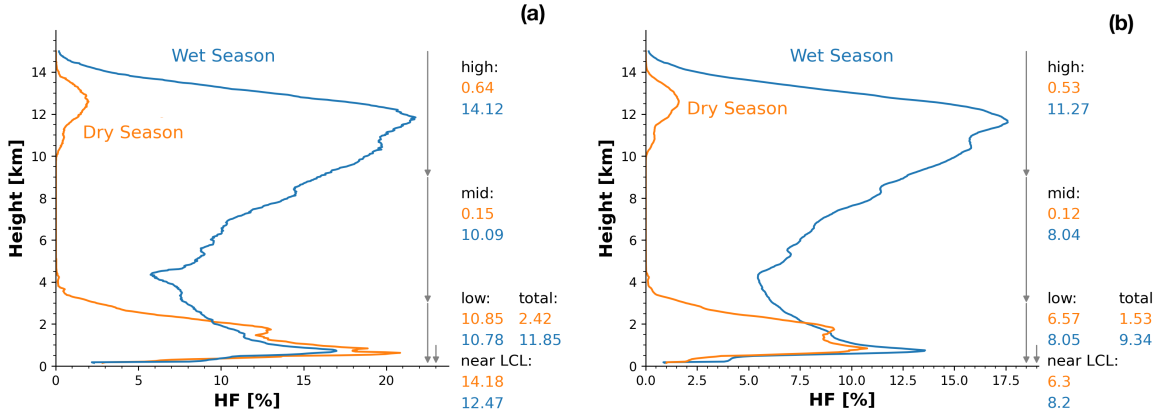

Figure 6: *Vertical profiles of hourly mean hydrometeor fraction (HF) from the Cloudnet target classification (a) and derived combining cloud radar and ceilometer data (rain is not excluded) (b). Means over the height levels (near LCL: 0-*1 km*, low: 0-*3 km*, mid: 3-*9 km*, high: 9-*15 km*, total: 0-*15 km*) during both seasons are presented.*

shallow clouds rather than Drizzle or rain (2). The first maximum in Fig.6 b is found at the same height during the dry season but with a smaller occurrence in HF (11 %). The lower occurrence in Fig. 6b must result from the chosen threshold in the radar return. Lowering the threshold would include more optically thin clouds or drizzle that is falling from cloud bases and evaporates in the sub-cloud layer. Consequently, lowering the threshold would result in larger frequencies of HF in the low levels as indicated by Nuijens et al. (2014). Moreover, Nuijens et al. (2015a) suggest that the first low level peak in HF is related to the presence of shallower trade-cumuli. On average, the peak within the low levels during the wet season is located at smaller altitudes because of higher relative humidity in the atmosphere. This influences the cloud formation process to start at lower altitudes (lower LCL) during the wet season than during the dry season. Also, rain events that were not filtered out and are more common during the wet season might have led to an overestimation of HF (Nuijens et al., 2015a).
In comparison to the changes in HF through all height levels, HF does not vary much at low levels from the dry to the wet season supporting the findings by Stevens et al. (2016). The second peak during the dry season in Fig. 6b is located at 1.7 km with an occurrence of 9 % corresponding to the height were the second peak in low level Liquid droplets (1) and cbh^1 is found. Also the hint of this second maximum can be seen in the distribution of HF during the wet season. This supports the theory of Nuijens et al. (2015a) who pointed out that deeper cumulus clouds with tops near the trade inversion are common during the dry season. Furthermore, it is assumed by Nuijens et al. (2015a) that deep convective cloud systems suppress cloud formation in their near surroundings during the wet season. As a result, deep convective clouds are less frequently surrounded by smaller cumuli near the trade inversion during the wet season (Nuijens et al., 2015a). HF decreases through the mid-levels during the dry season showing a second peak in high levels during the dry season which reflects high level cirrus clouds. HF during the wet season decreases from a second maximum near the LCL through the mid-levels and increases with height above 4.2 km were the average melting layer was indicated as in previous results in the distribution of the Cloudnet targets.

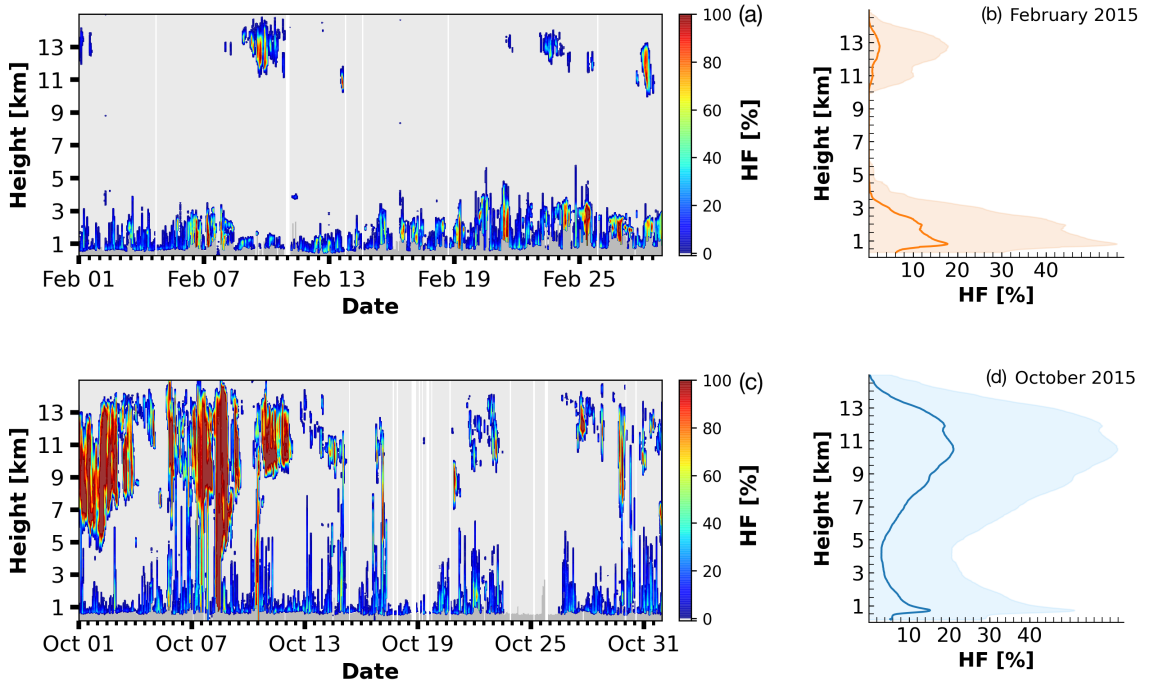

Figure 7: *Vertical profile of hourly mean hydrometeor fraction (HF) derived by combining CORAL Cloud radar and ceilometer data for February (dry season) (a) and October (wet season) (c) 2015 over the BCO. Note that white bars occur when data gaps are present and grey corresponds to clear sky. Vertical profile of monthly mean cloud fraction (the original resolution is maintained) for the dry (b) and wet season (d) in 2015 over the BCO with the estimated standard deviation.*

As an example of the distribution of clouds over a month hourly mean HF (taken to increase the readability of the figure) are presented in Fig. 7 for February and October 2015 (representative for dry and wet season). Deep convective clouds can be seen especially during the first half of the month in October. Furthermore, it can be seen that the distribution of low clouds does not change much over the dry and wet seasons. However, during the dry season, more low-level clouds with increased HF are evident, especially in the second half of the month. Additionally to the previous results, this indicates that deeper clouds are more common during the dry season than during the wet season.

Fig. 8 provides an overview about the distribution of monthly mean HF during February 2020 on board the R/V Meteor and the BCO. Averaged hourly HF do not reflect the distribution over the BCO typical during the dry season which is due to the maximum in HF in the mid-levels, which appears to be uncharacteristic for the dry season in comparison to previous findings over the BCO. This is suggested to be caused by the amount of data which is included in the analysis. Moreover, the increase in HF within the mid-levels can be attributed to the event between the 14th and 17th February. The first maximum is located at 872 m in the low levels with a lower frequency than the second one at 1.7 km above the R/V Meteor. Over the BCO, the first maximum is located in 811 m and the second one at the same altitude as above the R/V Meteor. The second

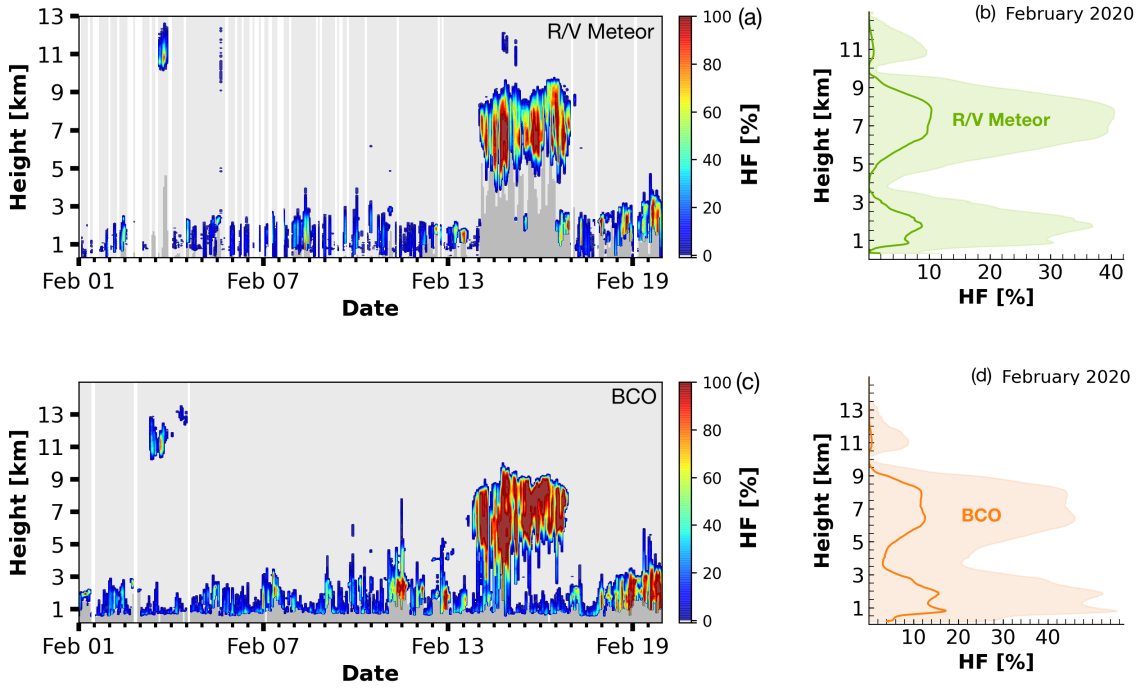

Figure 8: *Vertical profile of hourly mean hydrometeor fraction (HF) in February 2020 on board the R/V Meteor (a) and over the BCO (c). Note that white bars occur when data gaps are present and grey corresponds to clear sky. Vertical profile of mean hydrometeor fraction (original resolution maintained) over the BCO (b) and on board the R/V Meteor (d) with the estimated standard deviation.*

peak over the BCO is more than twice as compared to the low level maximum from the R/V Meteor. An explanation might be the difference in the radars operating on 94 GHz (with corresponding wavelength 3.2 mm) over the R/V Meteor and on 35.5 GHz (with corresponding wavelength 8.6 mm) over the BCO. The signal on smaller wavelengths is more attenuated by large hydrometeors like drizzle or rain compared to measurements on larger wavelengths (Görsdorf et al., 2015). Consequently, the radar over the R/V Meteor misses larger particles located below the cloud bases and shallow cumuli located near the LCL. Thus, it might be possible that the 94 GHz radar underestimates HF near the LCL. In contrast, the radar over the BCO successfully detects large liquid droplets or drizzle located near the LCL which explains the higher occurrence in HF on these levels.

4 Conclusions & Outlook

This work contributes to existing knowledge of clouds in the trade wind region by providing insights into the distribution of macro- and microphysical properties of clouds over the Barbados cloud observatory (BCO). Data from February were taken to be representative for the dry season and data from October for the wet season. The present study is one of the first attempts to examine the micro- and macro-physical properties of clouds from the Cloudnet target classification product over the BCO. Two years (2013 and 2015) were analyzed from a seven year data set of the Cloudnet target classification product to resolve the vertical distribution of cloud properties. The chosen Cloudnet targets are Liquid Droplets (1), Drizzle or rain (2), Ice (3) and Ice and supercooled droplets (4). HF was estimated combining cloud radar (Ka-band, KATRIN and CORAL) and ceilometer data from the BCO. A comparison of HF estimated from the Cloudnet data and the combination from radar and ceilometer data from the BCO were carried out. Furthermore HF was estimated combining cloud radar (W-band cloud radar LIMRAD94) and ceilometer data on board the R/V Meteor and over the BCO for the dry season in February 2020.

The results of this investigation show that the strongest seasonal variation of the Cloudnet classification targets appears on the mid-levels. While Liquid droplets (1) dominate during the dry season, the proportion of Ice (3) is significantly increased on the mid-levels during the wet season. The proportion of Liquid droplets (1) also decreases during the wet season in the mid-levels. Low clouds show little variability over the BCO, which is supported in the vertical distributions of Liquid Droplets (1) and Drizzle or rain (2) that do not change much from the dry to the wet season. The occurrence in Drizzle or rain (1) shows that precipitation originating from low clouds appears with nearly the same frequency over the seasons. However, the proportion of Drizzle or rain (2) increases during the wet season as precipitation from deep convective clouds contributes to an increase in the distribution of HF within the mid-levels.
The maximum occurrence of cbh^1 during the dry season at 746±100 m is found at higher altitudes compared to the wet season at 646±100 m. The maxima in HF at the lower levels, indicating the presence of shallow cumuli, are located at 840 m altitude during the dry season and at 750 m altitude during the wet season. The differences compared to the results in cbh^1 can be related to difference in the ceilometer sensitivity thresholds which determine how many thin clouds near cbh^1 are detected (Nuijens et al., 2009). Moreover, different range resolutions also influence the distribution of the low level maxima. Thereby, 50 m bins were chosen in the statistics for cbh^1 and the height resolution in the calculations for HF of 30 m was maintained.
HF shows a bimodal distribution and is overall largest during the wet season over the BCO. The highest seasonal variation appears within the mid and high levels. On the low levels HF does not vary much over the seasons. The second peak in HF is located near the trade inversion at 1.7 km and is more pronounced during the dry season compared to the wet season. Additionally, the results of cbh^1 show a second maximum located at 1.5 km which is linked to the presence of more developed cumuli with stratiform outflow. Deep convective clouds occur often during the wet season, which, according to Nuijens et al. (2014), suppress cumuli near the trade inversion between 1.5 and 2 km.

The transferability of these results is subject to certain limitations. For instance, the statistics were qualified by the available data. Each year displays data gaps during different times of the months. Taking more data into account would result in more accurate statistics and profiles of all variables and targets. Besides the gaps in data availability, the estimation of HF was mainly aggravated by varying instrument settings of the ceilometer and the exchange of the radar in April 2015. Due to that, the data had to be interpolated on a common range and time resolution. Moreover, the distribution of HF

is influenced by the chosen threshold of the radar and the ceilometer. A lower threshold in the radar will include smaller particles and will mostly influence the distribution of HF on the low levels. By comparing findings from the BCO to the findings from the R/V Meteor it has to be considered that the radars operate at different sensitivities (94 GHz for the R/V Meteor and 35.5 GHz over the BCO). Consequently, the radar on board the R/V Meteor underestimates the amount of low level clouds in comparison to the radar operating at the BCO. Another source of uncertainty is that rain was not filtered out within the procedure. The instruments do not provide accurate information when rain is present. Results from Nuijens et al. (2014) indicate that including rain increases the distribution of HF at most levels but do not change the shape of the cloud profile and its variability with time. Furthermore, the classification of hydrometeors in Cloudnet can lead to erroneous profiles in liquid water if the radar signal is dominated by larger particles like rain and the ceilometer signal is attenuated (Hogan and O'Connor, 2004). Also, an unusually high occurrence of aerosols and insects was observed in the Cloudnet data in 2016. In this case, most shallow cumuli were misclassified as aerosols and insects. The misclassification is likely related to a weak signal from the ceilometer and a missing radar signal necessary to detect falling particles and liquid water droplets.

Despite these promising results, questions remain and ideas advancing future work emerged. First of all the statistics could be improved by implementing more data. The ceilometer at the BCO measured almost continuously. Time series and long term means of cbh[1] could contribute to confirm previous findings. Other variables such as cloud cover which is a popular derived parameter in studies could be statistically analyzed and compared to previous work. Furthermore, profiles of humidity, temperature and other meteorological parameters could help describing the environment as they influence cloud formation and development. It could be tested if the time period of the investigation was representative for the climate over Barbados or explains the occurrence of unusual events. In addition, the frequency of occurrence of different hydrometeors as a function of the temperature and humidity observed inside clouds could improve the representation of microphysical properties and their dependency on temperature and humidity. Moreover, the Cloudnet target classification product provides more parameters like liquid water content, ice water content and effective radius of the detected particles which are important properties to describe cloud properties. Era interim data could resolve the seasonal cycle by providing the parameter vertical pressure velocity. This parameter shows at what time of the year the dry or wet season appears. On that basis, data from more months could be included to the respective season and in return more accurate statistics could be realized. Data from a micro rain radiometer could help to exclude rain events. Furthermore, a micro rain radiometer is a commonly used instrument in combination with radar and ceilometer data to derive cloud fraction as conducted in previous studies by Nuijens et al. (2014). An equal combination of instruments in deriving parameters such as cloud fraction would assist to make the results more comparable to previous findings over the BCO.

All in all, this study might advance future investigations and either improve existing methods or help to improve instrument settings resolving the vertical distribution of clouds. In return, this will help to produce more accurate parameterization schemes of clouds in climate models. As clouds contribute to the largest uncertainties in climate sensitivity, it is necessary to support further investigations to expand data sets of meteorological parameters and to improve forecast models.

References

Bony, S., Stevens, B., Ament, F., et al.: EUREC 4 A: a field campaign to elucidate the couplings between clouds, convection and circulation, Surveys in Geophysics, 38, 1529–1568, 2017.

Bühl, J., Radenz, M., Schimmel, W., and Vogl, T.: pyLARDA, URL `https://lacros-tropos.github.io/larda-doc/html/index.html#`, 2018.

Görsdorf, U., Lehmann, V., Bauer-Pfundstein, M., et al.: A 35-GHz polarimetric Doppler radar for long-term observations of cloud parameters—Description of system and data processing, Journal of Atmospheric and Oceanic Technology, 32, 675–690, 2015.

Hogan, R. J. and O'Connor, E. J.: Facilitating cloud radar and lidar algorithms: the Cloudnet Instrument Synergy/Target Categorization product, Cloudnet documentation, 2004.

Illingworth, A., Hogan, R., O'connor, E., et al.: Cloudnet: Continuous evaluation of cloud profiles in seven operational models using ground-based observations, Bulletin of the American Meteorological Society, 88, 883–898, 2007.

Klingebiel, M., Ghate, V. P., Naumann, A. K., et al.: Remote sensing of sea salt aerosol below trade wind clouds, Journal of the Atmospheric Sciences, 76, 1189–1202, 2019.

Lamer, K., Kollias, P., and Nuijens, L.: Observations of the variability of shallow trade wind cumulus cloudiness and mass flux, Journal of Geophysical Research: Atmospheres, 120, 6161–6178, 2015.

Medeiros, B. and Nuijens, L.: Clouds at Barbados are representative of clouds across the trade wind regions in observations and climate models, Proceedings of the National Academy of Sciences, 113, E3062–E3070, 2016.

Nuijens, L., Stevens, B., and Siebesma, A. P.: The environment of precipitating shallow cumulus convection, Journal of the Atmospheric Sciences, 66, 1962–1979, 2009.

Nuijens, L., Serikov, I., Hirsch, L., Lonitz, K., and Stevens, B.: The distribution and variability of low-level cloud in the North Atlantic trades, Quarterly Journal of the Royal Meteorological Society, 140, 2364–2374, 2014.

Nuijens, L., Medeiros, B., Sandu, I., and Ahlgrimm, M.: The behavior of trade-wind cloudiness in observations and models: The major cloud components and their variability, Journal of Advances in Modeling Earth Systems, 7, 600–616, 2015a.

Nuijens, L., Medeiros, B., Sandu, I., and Ahlgrimm, M.: Observed and modeled patterns of covariability between low-level cloudiness and the structure of the trade-wind layer, Journal of Advances in Modeling Earth Systems, 7, 1741–1764, 2015b.

Rauber, R. M., Stevens, B., Ochs III, H. T., et al.: Rain in shallow cumulus over the ocean: The RICO campaign, Bulletin of the American Meteorological Society, 88, 1912–1928, 2007.

Sassen, K., Wang, Z., and Liu, D.: Cirrus clouds and deep convection in the tropics: Insights from CALIPSO and CloudSat, Journal of Geophysical Research: Atmospheres, 114, 2009.

Short, D. A. and Nakamura, K.: TRMM radar observations of shallow precipitation over the tropical oceans, Journal of Climate, 13, 4107–4124, 2000.

Stevens, B., Farrell, D., Hirsch, L., et al.: The Barbados Cloud Observatory: Anchoring investigations of clouds and circulation on the edge of the ITCZ, Bulletin of the American Meteorological Society, 97, 787–801, 2016.

Vogel, R., Nuijens, L., and Stevens, B.: The role of precipitation and spatial organization in the response of trade-wind clouds to warming, Journal of Advances in Modeling Earth Systems, 8, 843–862, 2016.

Tethered balloon broadband radiation profiles during MOSAiC

Lonardi, M.[1], Ehrlich, A.[1], Wendisch, M.[1]

[1] *University of Leipzig, Leipzig Institute for Meteorology (LIM), Leipzig, 04103, Germany,*
E-mail: michael.lonardi@uni-leipzig.de

Summary: The Multidisciplinary drifting Observatory for the Study of the Arctic Climate (MOSAiC), held between 2019 and 2020, represented a major highlight for Arctic research. The Leipzig Institute for Meteorology (LIM) and the Institute for Tropospheric Research (TROPOS) contributed to MOSAiC in Summer 2020 by deploying the Balloon-bornE moduLar Utility for profilinG the lower Atmosphere (BELUGA). During four weeks of measurements, BELUGA provided a comprehensive data set characterizing the atmosphere thermodynamical conditions, turbulence, broadband radiation and aerosol particles. The major scientific goal of the LIM project is to measure profiles of broadband radiation to investigate the impact of clouds, temperature and humidity on heating rates profiles in the Arctic atmospheric boundary layer.

Zusammenfassung: Das Forschungsprojekt "Multidisciplinary drifting Observatory for the Study of the Arctic Climate" (MOSAiC), welches zwischen Herbst 2019 und Herbst 2020 stattfand, ist ein Meilenstein der internationalen Arktisforschung. Das Leipziger Institut für Meteorology (LIM) und das Insitut für Troposphärenforschung (TROPOS) nahmen im Sommer 2020 an der MOSAiC Expedition teil. Während einer Messzeit von vier Wochen, wurde das Fesselballonmessystem "Balloon-bornE moduLar Utility for profilinG the lower Atmosphere" (BELUGA) zu Erprobung der unteren Atmosphäre eingesetzt. Die Messungen lieferten einen umfangreichen Datensatz, welcher die Profile von thermodynamischen Parametern, Turbulenz, Breitbandstrahlung und Aerosol Partikel charakterisiert. Ein wichtiges Ziel der nun folgenden Auswertung der Messdaten ist die Analyse der Profile der Nettostrahlungsflüsse. Aus Änderungen des Nettostrahlungsfluss lassen sich Profile der atmosphärischen Heizraten ableiten. Insbesondere kann damit der Einfluss von Wolken auf die Thermodynamik in der arktischen atmosphärischen Grenzschicht untersucht werden.

1 Overview of the MOSAiC campaign

The ice camp based Multidisciplinary drifting Observatory for the Study of the Arctic Climate (MOSAiC, https://mosaic-expedition.org/) was one of the most extensive and relevant scientific expeditions of 2019-2020 (Brainard, 2019). The expedition is highlighted by its unique multidisciplinary approach, its internationality involving scientific institutes from 20 nations and its long duration (Fig. 1). The extraordinary logistical effort to conduct such a complex campaign was significantly increased, when in early 2020 the COVID-19 pandemic started. It represented a challenge to rearrange the exchange of the scientific crews and the schedule of MOSAiC. Despite this unfortunate

event, MOSAiC continued until its planned end in October 2020, providing a wealth of observations that will feed the whole Arctic academic community in the next decade.

In addition, the MOSAiC ice floe quickly crossed the central Arctic, ending up northwest of Svalbard as early as May 2020. As a result, the number of legs of MOSAiC was reduced from 6 to 5. The first two legs occurred in winter 2019 as planned. Leg 3 was extended until early June 2020. Leg 4 was delayed to June-August (from April-June) and leg 5 concluded the campaign. For the crew exchange between legs 3 and 4, the MOSAiC ice floe had to be abandoned for about four weeks. Only some instruments remained on the floe for continuous autonomous measurements. The camp was then re-established during the melting season in mid June 2020. As the ice floe reached the marginal sea ice zone and was close to break up, the camp was dismissed in late July 2020, after about 300 days of extensive survey. For the final leg of MOSAiC, in August-September 2020, a new location was used to re-establish the camp. An ice floe close to the North Pole was chosen to cover the central Arctic freezing season. A publication describing MOSAiC in detail is planned by Rex et al.

All LIM activities under the umbrella of $(AC)^3$ (ArctiC Amplification: Climate Relevant Atmospheric and SurfaCe Processes and Feedback Mechanisms) are described by Brückner et al. (2020). Tethered balloon observations originally were scheduled for the field during the original legs 4 and 5, and two airborne campaigns were planned for spring and autumn. Operations had to be adapted to the developing situation. The planned spring deployment of the tethered balloon was moved to summer (new leg 4), while its leg 5 activities had to be cancelled. Also the airborne spring campaign was cancelled. The second airborne campaign took place in autumn 2020. Unfortunately, at this time, RV Polarstern already left the original ice camp and moved further north, out of reach for the research aircrafts Polar 5 and 6.

2 BELUGA deployment

After 18 days of quarantine and 18 days of navigation between Bremerhaven and Svalbard, the combined balloon team from LIM and TROPOS boarded RV Polarstern on 5 June 2020. Having concluded the bunker operations in the harbour of Longyearbyen, RV Polarstern headed back to the original MOSAiC ice floe. During the transit, the balloon team worked together with the ATMOS team on the preparation of the laboratories and instruments for the upcoming work on the ice. Once the MOSAiC ice floe was reached, it was scouted for the onset of a new camp. Before tethered balloon operations could be started, instruments for the continuous measurement of atmosphere, ocean and ice were deployed in selected locations. The balloon team helped in building the shared infrastructure. Then the balloon site (Balloon town) was set up about 260 m from the starboard side of RV Polarstern. The balloon team also significantly contributed for the whole length of leg 4 to the 6-h radiosounding routine, as well as to polar bear guarding activities needed for safety on the ice.

Balloon town consisted of a tent to house the instruments, the 12-meter-long tethered balloon "BELUGA" (Balloon-bornE moduLar Utility for profilinG the lower Atmosphere, Egerer et al., 2019) and a winch with a deflection pulley used to operate it (Fig. 2). The 90 m^3 balloon was routinely inflated at RV Polarstern with the help of other scientists (Fig. 3). For safety reasons, the Helium was stored on the ship. The scientific

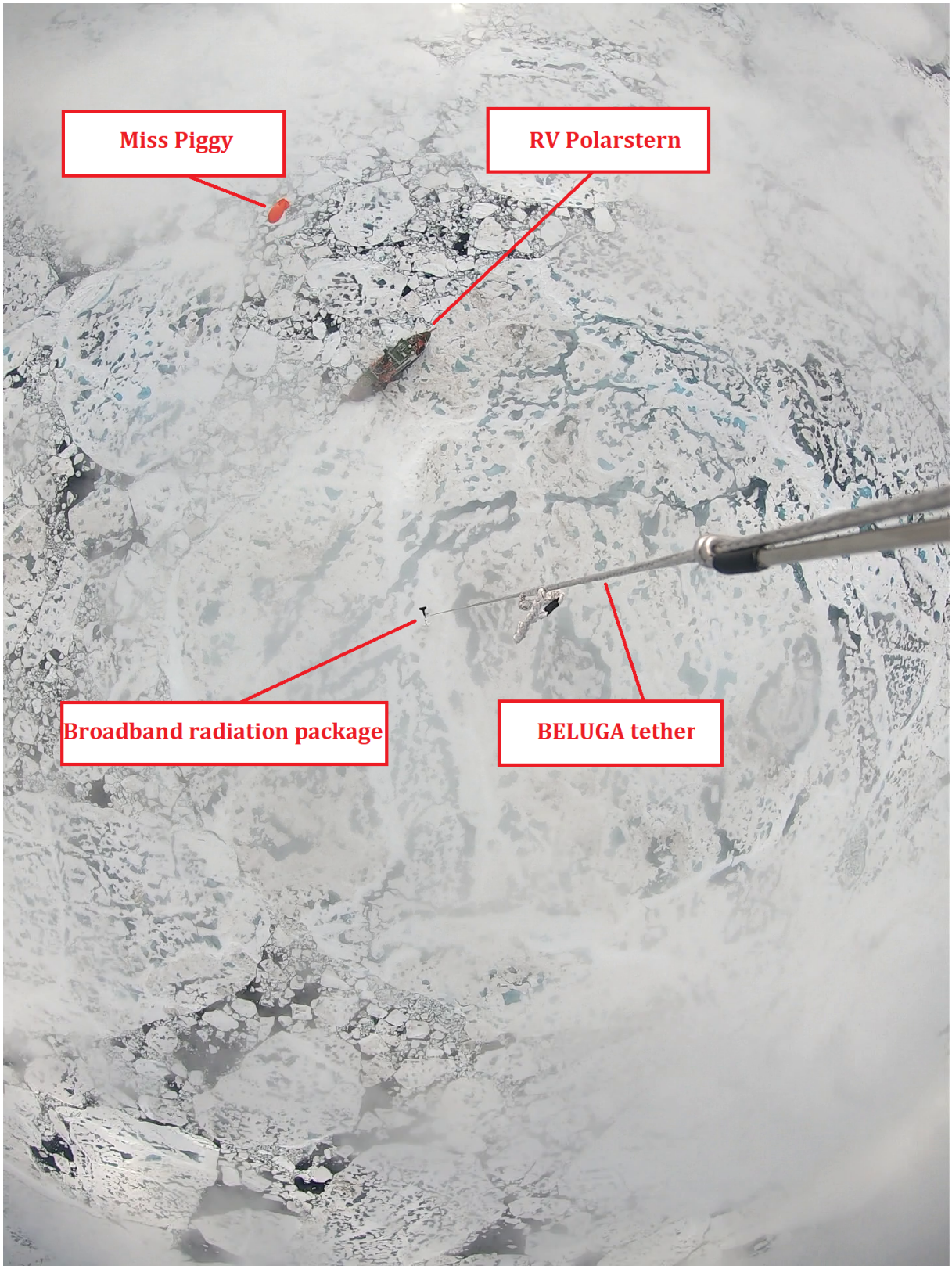

Figure 1: *Aerial view of MOSAiC. RV Polarstern, Miss Piggy balloon and the MOSAiC ice floe seen by a camera on BELUGA from about 600 m.*

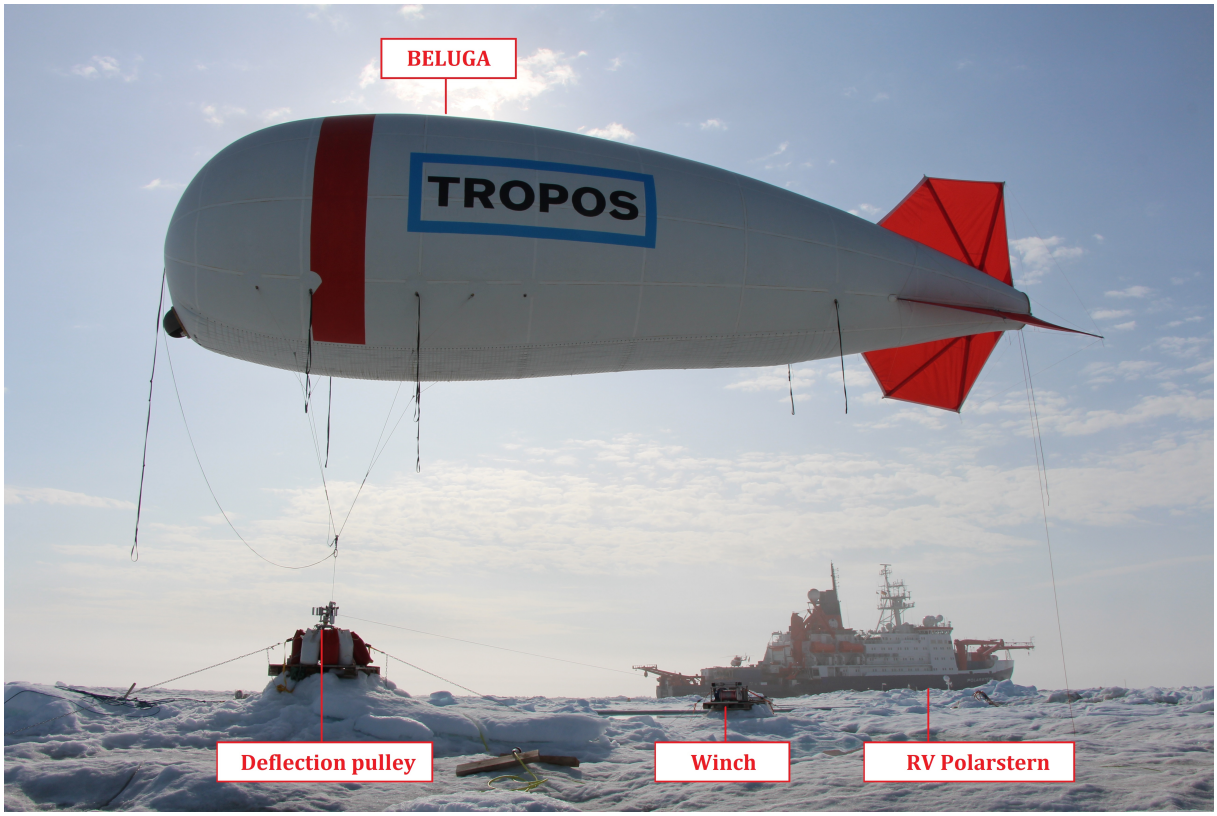

Figure 2: *BELUGA ground setup. The balloon is seen together with the winch and the deflection pulley for the tether. The tent for the storage of the instruments is not shown. In the background, RV Polarstern.*

observation schedule, conducted between 29 June and 29 July, aimed to profile the Arctic atmospheric boundary layer up to 1500 m using a set of probes mounted on the tether holding the balloon. The payload was modular, allowing to combine different instruments. These included a standard meteorology probe (StdMet), the broadband radiation package (BP) and the ultrasonic anemometer package (UP) described by Egerer et al. (2019), the newly developed Cubic Aerosol Measurement Platform (CAMP) for the study of aerosol, and the Video Ice Particle Sampler (VIPS) to characterize cloud particles. Profiles provide high resolution datasets due to the climbing speeds of about 0.5-1 ms^{-1}.

Due to strong winds and logistical constraints, including polar bears encounters (Wendisch et al., 2020), the operation of the balloon was intermittent during the first part of the campaign. Most of the profiles were obtained between 19-27 July. In total, 33 flights up to an average height of about 1000 m were obtained during the campaign. All instruments worked reliably for most of the time without large data gaps. Not all instrument payloads could be operated simultaneously due to the weight limitations of BELUGA. The daily combination of instrumentation was selected compromising between permanent routine measurements and specific measurements related to the given meteorological conditions. The operation time of VIPS, which purpose was to measure cloud ice particles, was significantly reduced due to the low amount of cloud ice observed in the summer season. BELUGA profiles represent different atmospheric scenarios, including cloudy and cloudless cases, as well as distributions of aerosol advected from various source regions.

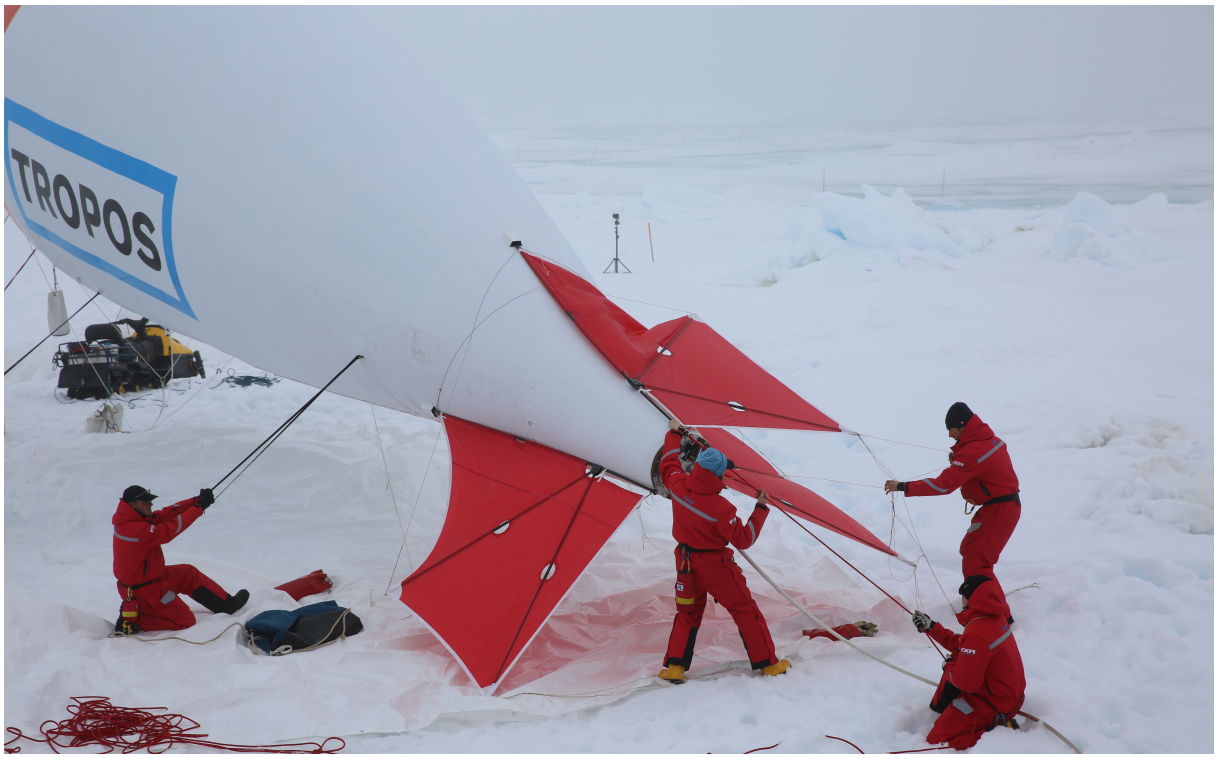

Figure 3: *The complexity of the preparation and maintenance of BELUGA required the help from several volunteers during the whole deployment period. During these operations, the balloon was secured with ropes to a snowmobile and controlled by the volunteers. Credits AWI/Grosfeld.*

3 Broadband radiation measurements

The measurement and analysis of broadband radiation profiles was the major scientific focus of LIM contributions to BELUGA. A total of 18 flights (36 profiles) were obtained using the broadband radiation package BP. Profiles always include data from StdMet and, depending on the scenario, are coupled with aerosol, turbulence or cloud microphysical properties. The observations include 4 cloudless and 14 cloudy cases, further divided into 6 cases of single-layer and 8 of multi-layer cloud cover. Every BP profile includes measurements of the four radiative flux densities (upward and downward terrestrial and solar irradiance). Based on these four components, profiles of net irradiances and the resulting radiative heating rates, as well as broadband albedo, were calculated. These profiles are being analysed at LIM to quantify the role of cloud top cooling and cloud base warming/cooling on the Arctic atmospheric boundary layer structure.

4 Summary & Outlook

MOSAiC provided one year of almost continuous observations of atmospheric, oceanic, sea ice, and biological processes in the central Arctic by a diversity of measurement methods. An overview of the atmospheric measurements will be provided by Shupe et al. (manuscript in preparation). Profiles of broadband radiation using the tethered balloon platform BELUGA were one part of the summer phase of MOSAiC. BELUGA

data obtained during the campaign, and its processing, are described in a publication planned by Pilz et al. Due to its peculiarity, the data management of BELUGA data during MOSAiC is planned to be described as a case study by Immerz et al. A scientific overview planned by Lonardi et al. provides an integrated analysis of general thermodynamical conditions, clouds, turbulence, broadband radiation and aerosol on three days with a similar cover of liquid water single layer clouds . Further studies are planned to explore the full depth of data observed during the four weeks of operation of BELUGA during MOSAiC. A detailed analysis will be conducted to quantify the sensitivity of broadband radiation and heating rates profiles to cloud microphysics and macrophysical conditions. However, the rather short time period of the BELUGA deployment during MOSAiC covers only a limited range of meteorological conditions. In particular typical Arctic mixed-phase clouds could not be observed during the summer. Therefore it is planned to extend the BELUGA observations by two campaigns in Ny-Ålesund, scheduled for autumn 2021 and spring 2022. The deployments will allow for the inclusion of mixed-phase clouds, typically present during those seasons as shown by Nomokonova et al. (2019).

References

Brainard, J.: What's coming up in 2019, Science (New York, N.Y.), 363, 8–10, doi:10.1126/science.363.6422.8, URL https://www.sciencemag.org/lookup/doi/10.1126/science.363.6422.8, 2019.

Brückner, M., Lonardi, M., Ehrlich, A., Wendisch, M., Jäkel, E., Schäfer, M., Quaas, J., and Kalesse, H.: Multidisciplinary drifting Observatory for the Study of Arctic Climate (MOSAiC): Overview of LIM Contributions, Wiss. Mitteil. Inst. f. Meteorolo. Univ. Leipzig, 58, 11–19, URL https://nbn-resolving.org/urn:nbn:de:bsz:15-qucosa2-743813, 2020.

Egerer, U., Gottschalk, M., Siebert, H., Ehrlich, A., and Wendisch, M.: The new BELUGA setup for collocated turbulence and radiation measurements using a tethered balloon: First applications in the cloudy Arctic boundary layer, Atmospheric Measurement Techniques, 12, doi:10.5194/amt-12-4019-2019, 2019.

Nomokonova, T., Ebell, K., Löhnert, U., Maturilli, M., Ritter, C., and O'Connor, E.: Statistics on clouds and their relation to thermodynamic conditions at Ny-Ålesund using ground-based sensor synergy, Atmospheric Chemistry and Physics, 19, doi:10.5194/acp-19-4105-2019, 2019.

Wendisch, M., Brückner, M., and Lindemann, S.: (AC)^3 newsletter, issue 10, URL http://www.ac3-tr.de/wp-content/uploads/2020/12/newsletter_winter_2020_v1.pdf, 2020.

Ionospheric delayed response to solar EUV radiation variations based on model simulations and satellite observations

Vaishnav, R.[1], Jacobi, Ch.[1], Schmölter, E.[2], Berdermann, J.[2], Codrescu, M.[3]

[1] *Institute for Meteorology, Universität Leipzig, Stephanstr. 3, 04103 Leipzig, Germany, E-mail: rajesh_ishwardas.vaishnav@uni-leipzig.de*
[2] *German Aerospace Center, Kalkhorstweg 53, 17235 Neustrelitz, Germany*
[3] *Space Weather Prediction Centre, National Oceanic and Atmospheric Administration, Boulder, Colorado, USA*

Summary: We investigate the ionospheric response to solar extreme ultraviolet (EUV) variations using the ionospheric total electron content (TEC) provided by the International GNSS Service (IGS) and the Coupled Thermosphere Ionosphere Plasmasphere Electrodynamics (CTIPe) model, together with the solar EUV flux measured by the Solar Dynamics Observatory (SDO) EUV Variability Experiment (EVE). The study was conducted with data observed over European, Australian and South African stations from 2011 to 2013. Our results show differences in the TEC response to solar EUV over southern and Northern Hemispheric stations. The modeled TEC is consistent with the observed TEC over South African station, while it shows an underestimation with respect to the observed TEC over European stations.

The ionospheric delay estimated with the modeled TEC agrees with the delay estimated for observed TEC. The mean delay for the observed TEC is about 17.3 hours, while it is 16.4 hours for the modeled TEC. The mean correlation with the solar flux measured by SDO EVE is always higher in the case of the model-simulated TEC than for the observed TEC.

Zusammenfassung: Wir untersuchen die ionosphärische Reaktion auf solare extreme ultraviolette (EUV) Schwankungen unter Verwendung des ionosphärischen Gesamtelektronengehalts (TEC) des International GNSS Service (IGS) und simuliert vom CTIPe-Modell (Coupled Thermosphere Ionosphere Plasmasphere Electrodynamics) gegen den vom Solar Dynamics Observatory (SDO) EVE gemessenen solaren EUV-Fluss. Die Studie verwendet Daten aus den Jahren 2011 bis 2013 an europäischen, australischen und südafrikanischen Stationen. Unsere Ergebnisse zeigen eine unterschiedliche TEC-Reaktion über Stationen der südlichen und nördlichen Hemisphäre. Der modellierte TEC stimmt mit dem beobachteten TEC über südafrikanischen Stationen überein, während er eine Unterschätzung in Bezug auf den beobachteten TEC über europäischen Stationen zeigt.

Darüber hinaus stimmt die unter Verwendung von modellsimuliertem TEC geschätzte ionosphärische Verzögerung mit dejenigen für beobachteten TEC überein. Eine durchschnittliche Verzögerung für den beobachteten TEC beträgt etwa 17,3 Stunden, während der modellierte TEC 16,4 Stunden beträgt. Darüber hinaus ist die mittlere Korrelation mit EUV-Beobachtungen bei modelliertem TEC stärker als bei beobachtetem TEC.

1 Introduction

The Sun emits electromagnetic radiation in a wide spectral range, including ultraviolet/extreme ultraviolet (UV/EUV) radiation, which affects the thermosphere-ionosphere (T-I) system as these spectral ranges are absorbed in the T-I, leading to ionization and thus, the formation of the ionosphere. UV and EUV radiation varies on different time scales, including the prevailing 11-year cycle and, on shorter time scales, the 27-day solar rotation period. The EUV/UV radiation is responsible for the ionization and photodissociation of major neutrals, in particular atomic oxygen, molecular nitrogen, and molecular oxygen, and in this way contributes to the vertical and horizontal distribution of electron density. Solar EUV radiation has only been observed continuously since the launch of the TIMED / SEE mission in 2002 (Woods et al., 2000; Woods, 2005), see also the review by Schmidtke (2015). Therefore, it is often represented by solar proxies, the most prominent one being the F10.7 index (Tapping, 2013).

The influence of solar radiation on the T-I system has been extensively studied by many researchers (e.g. Kutiev et al., 2013; Jacobi et al., 2016; Vaishnav et al., 2018, 2019a). The state of the ionosphere is characterized by different parameters, including the total electron content (TEC, given in units of 1 TECU = 10^{16} electrons m^{-2}), i.e., the vertically integrated electron density. Otherwise, used parameters are the peak electron density (NmF2, cm^{-3}) and the corresponding height (hmF2, km). Unglaub et al. (2011, 2012) used the EUV-TEC proxy from combined EUV spectra observed by TIMED-SEE and SDO-EVE to study the ionospheric response. Solar activity plays a significant role in the ionospheric effect on solar variability (Vaishnav et al., 2021a). Vaishnav et al. (2019b) suggested that during solar cycle (SC) 23, the correlation between solar proxies and ionospheric TEC was stronger than during SC 24. This is likely due to the longer lifetime of active regions during SC 23. The wavelet variance estimation method suggests that the variance is more significant during SC 23 than during SC 24.

Several authors have reported an ionospheric delay of about one day with respect to solar EUV radiation or solar proxies on the time scale of the 27-day solar rotation period (e.g. Jakowski et al., 1991; Min et al., 2009; Jacobi et al., 2016; Schmölter et al., 2018; Vaishnav et al., 2018, 2019a). In recent years, the delay has been more accurately estimated due to the availability of high-resolution EUV measurements and has been reported to be about 17 hours, modified by latitude and season (Schmölter et al., 2018; Schmölter et al., 2020; Vaishnav et al., 2021b). Initial attempts to model the delay were made by Jakowski et al. (1991), who used a one-dimensional numerical model between 100 and 250 km altitude with simplifying assumptions to investigate the physical mechanism of ionospheric delay. They proposed that a delay of about 2 days in atomic oxygen at 180 km altitude occurs due to photodissociation of molecular oxygen and transport processes.

Preliminary investigation by Vaishnav et al. (2018) also showed the possible role of transport processes in ionospheric delay using the Coupled Thermosphere Ionosphere Plasmasphere Electrodynamics (CTIPe, Fuller-Rowell and Rees (1983); Codrescu et al. (2012)) model simulations. In addition, Ren et al. (2018) suggested a possible contribution of photochemical and electrodynamic processes in the ionospheric delayed response using the Thermosphere Ionosphere Electrodynamics-General Circulation Model (TIE -GCM) simulations. The delay is due to the different response times between the quasi-

instantaneous ionization and the slower recombination in the ionospheric F region.

Vaishnav et al. (2021b) investigated the ionospheric delay and showed good agreement between the estimated delay between the model-simulated TEC and the observed TEC with the flux measured by Solar Dynamics Observatory (SDO) in the extreme ultraviolet (EUV) Variability Experiment (EVE). The average delay for the observed (modeled) TEC is 17(16) hours. The average delay calculated for the observed and modeled TEC is 1 and 2 hours longer, respectively, for the Southern Hemisphere than for the Northern Hemisphere. Schmölter et al. (2020) also showed the latitudinal and seasonal variations in the ionospheric delay and also discussed the possible role of geomagnetic activity. In addition, Vaishnav et al. (2021a) discussed the possible contribution and role of eddy diffusion in the delayed ionospheric response. They showed that eddy diffusion is one of the important sources directly affecting the ionospheric delay. Increasing eddy diffusion leads to a decrease in ionospheric delay.

The present study aims to analyse the TEC variations of the ionosphere in the Northern and Southern Hemispheres during moderate solar activity phases in SC 24, 2011 to 2013. This analysis uses GNSS data over European, Australian and South African stations. The observed TEC properties are compared with the model-simulated TEC. In Section 2, we present our data sources and the CTIPe model used for the analyses. In Section 3, we investigate the variability of TEC, a possible relationship with the F10.7 index, and the periodicity estimation. In Section 4, we summarize our conclusions.

2 Data sources and numerical model used

2.1 TEC observations

In this paper, we use TEC, extracted from the International GNSS Service (IGS) TEC maps provided by NASA's CDDIS (Noll, 2010), which have a time resolution of 1 hour and a latitude and longitude resolution of $2.5^\circ \times 5^\circ$ (Hernández-Pajares et al., 2009). The GNSS data collected were used from grid points near different stations in the Northern and Southern Hemispheres. The stations used from Europe are Arnstein and Rome in the Northern Hemisphere. For the Southern Hemisphere region, Bloemfontein in South Africa and Canberra in Australia were selected. We used the nearest grid points in TEC maps available near the ground stations, weighted more by observations and less by the model used in TEC map generation to fill temporal and spatial gaps.

Figure 1 shows a map depicting the study sites used to calculate the ionospheric delay in the Northern and Southern Hemispheres.

2.2 Solar EUV radiation

To investigate the influence of solar EUV radiation on the variability of the ionosphere, both solar EUV flux observations and solar proxies are often used. The SDO-EVE instrument provides a continuous high-resolution spectra with a wavelength range of 0.1 to 120 nm, a spectral resolution of 0.1 nm, and a temporal resolution of 20s (Woods et al., 2010; Pesnell et al., 2011). The high-resolution observations provided by SDO were used here on an hourly basis to calculate an ionospheric delay in TEC.

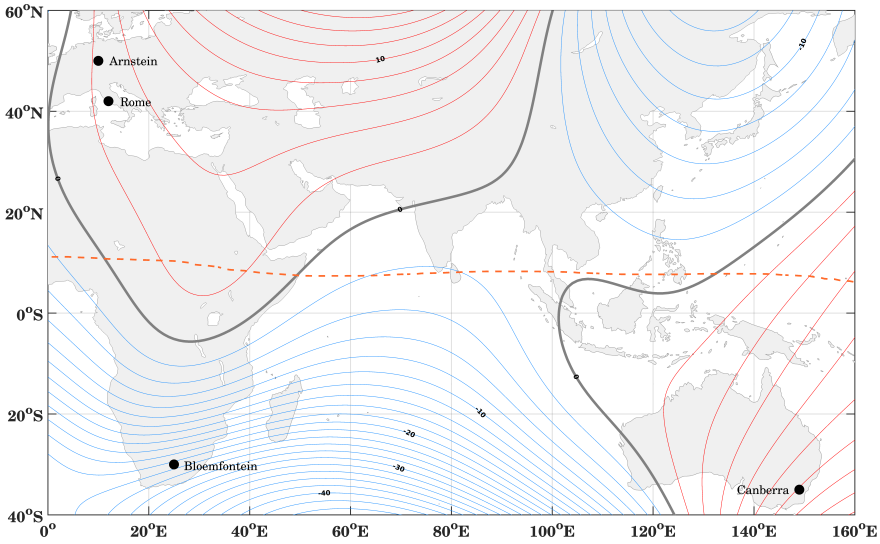

Figure 1: *Map depicting the study locations: European (Arnstein and Rome), South African (Bloemfontein) and Australian (Canberra) GPS stations. The Earth's magnetic field is shown by the geomagnetic equator (orange dashed line) and magnetic declination (blue, red, and black lines). The magnetic field data were taken from the World Magnetic Model (NASA, 2014).*

2.3 CTIPe Model

The CTIPe model is a global, three-dimensional, numerical, physics-based coupled thermosphere-ionosphere-plasmasphere model that self-consistently solves the primitive continuity, momentum, and energy equations to calculate the wind components, global temperature, and neutral composition, and is further used to calculate plasma production, loss, and transport. The model consists of four components, namely (a) a neutral thermosphere model (Fuller-Rowell and Rees, 1980), (b) a convection model for the mid- and high-latitude ionosphere (Quegan et al., 1982), (c) a plasmasphere and low-latitude ionosphere model (Millward et al., 1996), and (d) an electrodynamic model (Richmond et al., 1992). The calculations are performed at a resolution of 2°/18° in latitude/longitude. In the vertical direction, the atmosphere is divided into 15 logarithmic pressure levels at intervals of one scale height, starting with a lower boundary at 1 Pa (about 80 km altitude) to over 500 km altitude at pressure level 15. External inputs are required to run the model, such as solar UV and EUV radiation, the Weimer electric field, TIROS /NOAA Aurora precipitation, and tidal forcing from the Whole Atmosphere Model (WAM). The F10.7 index is used as a solar proxy to calculate ionization, heating, and oxygen dissociation processes in the ionosphere. Detailed information on CTIPe can be found in Codrescu et al. (2008, 2012).

3 Results

3.1 TEC variations at moderate solar activity of solar cycle 24

The behavior of the T-I system varies greatly depending on the conditions of solar activity. Figure 2 shows the averaged midday (11:00-13:00 LT) variations in TEC from 2011

Table 1: *Geographic latitudes and longitudes of European (Arnstein and Rome), South African (Bloemfontein), and Australian (Canberra) GPS stations and the nearest CTIPe model grid points used to investigate the TEC variations delayed ionospheric response.*

Station	Geog. Lat (°)	Geog. Long (°)	CTIPe Geog. Lat (°)	CTIPe Geog. Lon (°)
Arnstein	50	10	50	18
Rome	41.8	12.5	42	18
Bloemfontein	-30	25	-30	18
Canberra	-35.3	149	-36	144

to 2013 during SC 24. The figure shows the comparison between the observed TEC (red) and the modeled TEC (blue) simulated with the EUVAC flux model for Arnstein, Rome, Canberra and Bloemfontein. The integrated SDO EVE flux (1-120 nm) is shown on the second y-axis of figure 2a.

The variation of the TEC level during the different seasons and the varying solar activity can be seen in the time series. The ionospheric electron density distribution is mainly controlled by photoionization, dissociation, and transport processes, as well as loss through recombination processes. Variations in the observed TEC vary with location, such as Southern Hemisphere and Northern Hemisphere.

Figures 2(a) show that there are continuously pronounced 27-day cycles in the SDO EVE flux in 2012. This type of regular variation in the solar observations provides us an opportunity to study the corresponding ionospheric variations. The observed TEC variations over the Arnstein site are larger during the spring season and smaller during the winter season. Compared to the observed TEC, the modeled TEC is underestimated during the spring and summer periods, while it is in good agreement during the winter season. The overall level of TEC is lower compared to the other study stations. The discrepancy between the modeled and observed TEC is higher during the spring and summer seasons. Above this site, the modeled TEC mostly underestimates the observed TEC.

Compared to the TEC level at Arnstein, TEC shows opposite characteristics at Rome (Figure 2(b)). Above this site, the modeled TEC overestimates the observed TEC during the winter months, while it shows underestimation during the summer months. The observed TEC in Arnstein and Rome is comparable, but the modeled TEC is higher in Rome. This is due to the fact that maximum ionization occurs at the equator and in low latitude regions. The TEC value decreases towards high latitudes. Therefore, the TEC values are higher in Rome than in Arnstein.

Figure 2(c) shows the TEC level during 2011-2013 over the Australian station Canberra. Here, the maximum of TEC is observed during March-April (autumn) and November (spring) in 2011. Over this site, the modeled TEC is in good agreement with the observed TEC during the spring months. During the autumn and winter months, the observed TEC is underestimated by the modeled TEC.

Figure 2(d) shows the variations over the South African station Bloemfontein. The modeled TEC shows an overestimation compared to the observed TEC during the spring

season. Except during the spring months, the modeled TEC level is in good agreement with the observed TEC level during midday over Bloemfontein. It can be seen that the TEC levels are almost the same depending on the moderate solar activity conditions during the study period.

In general, TEC levels vary latitudinally and longitudinally depending on the time of year both in the Northern and at Southern Hemisphere. The TEC simulated by the CTIPe model agrees better with the Southern Hemispheric stations than with the Northern Hemispheric stations. The spatial distribution of TEC depends on the ionization of neutrals, transport processes, and recombination, which varies with latitude and longitude. The variations in TEC are not only controlled by solar irradiance, but there are other factors such as local dynamics, or geomagnetic activities due to solar wind variations that also affect the ionospheric state (Abdu, 2016).

The TEC values over Southern Hemispheric stations are higher than the Northern Hemispheric values and the TEC values change faster from the southern to the Northern Hemisphere values, causing the annual anomaly (Romero-Hernandez et al., 2018).

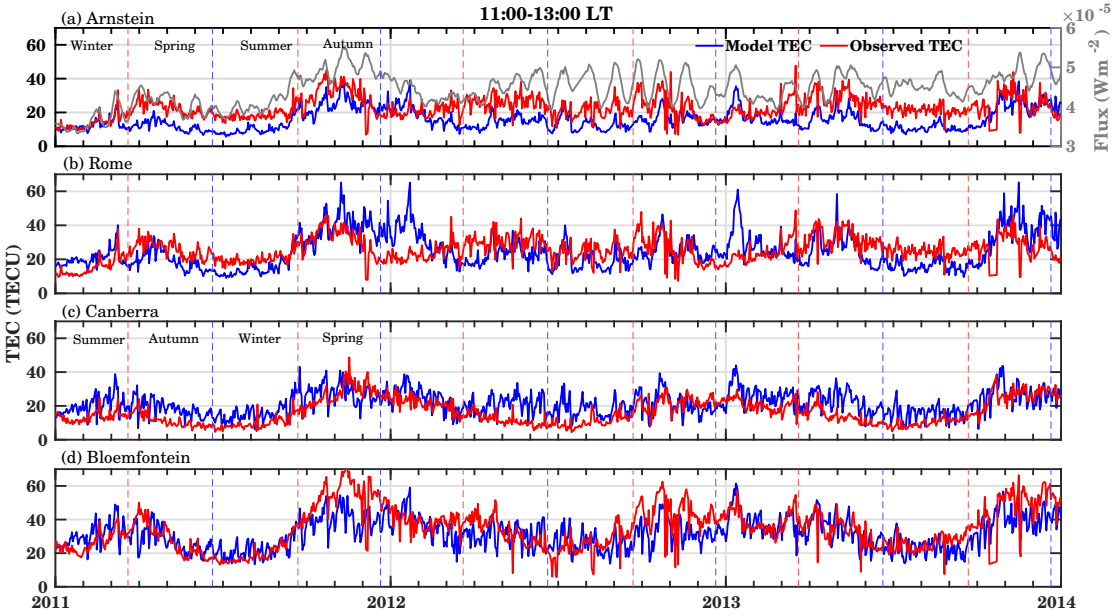

Figure 2: *Comparison between observed TEC and model-simulated TEC at midday (11:00-13:00 LT) for different locations: (a) Arnstein, (b) Rome, (c) Canberra, and (d) Bloemfontein. The gray curve in panel (a) represents the integrated SDO EVE flux (1-120 nm).*

3.2 Periodicity estimation

To investigate the oscillatory behavior in the time series of TEC across all stations, the continuous wavelet transfer method (CWT) was used. The CWT captures the impulsive events at the same times they occur in the time series (Percival and Walden, 2000). However, the CWT also examines the low-frequency features of the data that are hidden in the time series. Several authors have reported the oscillatory behavior of solar and ionospheric parameters using the wavelet method (e.g. Vaishnav et al., 2018). The solar activity varies on different time scales from minutes to 11-year solar cycle and beyond.

Recently, Vaishnav et al. (2021b) used the CWT technique to study the periodicity during 2011 to 2013 for low, mid, and high latitudes. Here, we use a similar technique to examine the dominant periods over our study locations, as shown in Table 1. The uninterpreted data of daily observed and modeled TEC during 2011 to 2013 are used to analyze the periodic behavior of the T-I system.

Here we will examine and compare the different temporal patterns of observed and modeled global TEC. Figure 3 shows the continuous wavelet spectra of the model-simulated and observed TEC for different stations from 2011 to 2013. The white line represents the corresponding time series used to calculate the CWT.

The top panel (a-c) and bottom panel (d-f) of Figure 3 show the CWT of modeled TEC and observed TEC, respectively, over three different sites, as mentioned in the figure title. The most dominant period observed in the modeled TEC is 16-32 days in 2012 across all stations. During this study period, 16-32 day periodicity has been observed in the F10.7 index, e.g., by Vaishnav et al. (2021b). This dominant period is weaker in 2011 and 2013. During this period, the influence of other dynamical processes in the ionosphere (e.g., lower atmospheric forcing) is stronger. A very weak 27-day periodicity was observed in these years. The 27-day periodicity is stronger in the winter season. Pancheva et al. (1991) suggested a possible cause for the 27-day variation in the lower ionosphere (D region), which is often caused by dynamical forcing, especially in the winter season under conditions of low solar activity.

Especially over Bloemfontein and Canberra there is a dominance of the period range of 8-16 days. In addition, another strong region is visible in the 128-256 day period range, representing the semi-annual oscillations in both the modeled and observed TEC. The semi-annual oscillation is most dominant during our study period. Compared to the modeled TEC, the 27-day periodicity is weaker in the observed TEC, as shown in Figure 3(d-f). The dominant period is observed only during the September-October months of each year. The 64-128-day periodicity is not observed in the observations, but is seen in the modeled TEC.

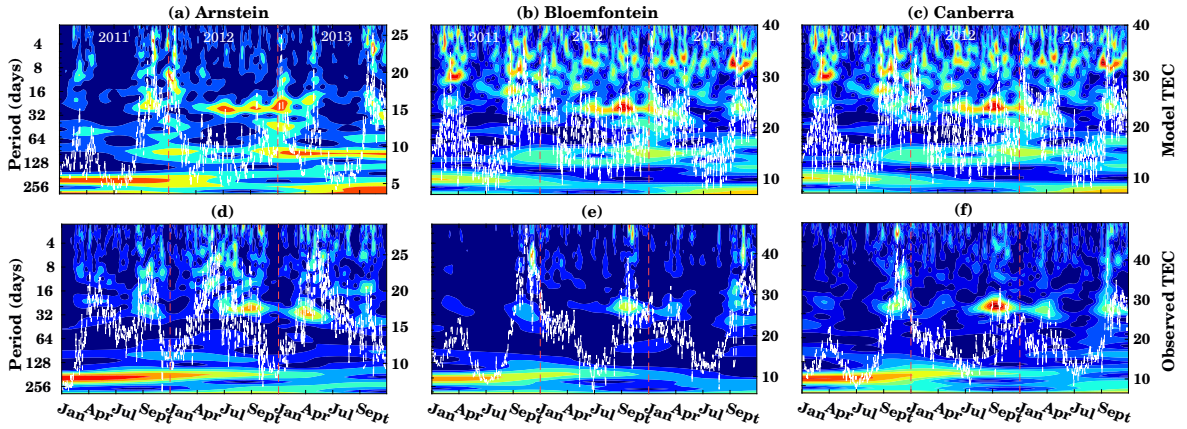

Figure 3: *Continuous wavelet spectra of modeled TEC (a-c) and observed TEC (d-f) for Arnstein, Bloemfontein and Canberra. The white lines show the corresponding time series.*

3.3 Cross-correlation and delay estimation

The delayed response of the ionosphere to solar EUV observations and solar proxies has been studied by several authors and they reported an ionospheric delay of about 1-2 days (Jakowski et al., 1991; Jacobi et al., 2016; Vaishnav et al., 2019a). Using the high-resolution SDO EVE and GOES EUV fluxes against TEC, a more accurate ionospheric delay of about 17 hours was reported (Schmölter et al., 2020). The observed delay is also confirmed by numerical physics-based models (Ren et al., 2018; Vaishnav et al., 2018, 2021b).

Figure 4 shows the cross-correlation and a corresponding ionospheric delay calculated using observed and modeled TEC with the integrated SDO EVE flux in the wavelength range from 1 to 120 nm over the study sites listed in Table 1. The modeled TEC, used for these analyses, was simulated using the EUVAC solar flux model within CTIPe and the F10.7 index as a solar proxy to calculate the input spectra. Here, the cross-correlation and lag are calculated for each month from 2011 to 2013.

The results over the Northern Hemispheric stations are shown in Figure 4 (a-b). The upper panel shows the correlation coefficient, and the corresponding lower panel shows the ionospheric delay. The trend for the correlation coefficient over both European sites calculated for observed TEC is similar, which is also true for the ionospheric lag. This is consistent with similar results from Schmölter et al. (2020).

We compare the correlation coefficient and ionospheric delay calculated with the observed TEC with the simulated model TEC. The correlation coefficients generally agree over Arnstein and are only slightly higher than the observed values. Similar variations are seen over Rome. The bottom panel of the figure 4 (a-b) shows the corresponding ionospheric delay. Here, the ionospheric delay from the observations at both locations is almost similar, and the average ionospheric delay during this study period is about 15-19 hours. The minimum delay from the observations is about 6 hours in August 2012 TEC, while from the model simulation TEC it has a delay of 22 hours. In general, the ionospheric delay calculated from the modeled TEC is in good agreement over the European sites. Of particular note is the annual decrease in delay during the winter season reported by Schmölter et al. (2020), which is well reproduced by the model.

Figure 4(c) shows the correlation coefficient and ionospheric delay over the Australian station Canberra. Here the model correlation coefficient is generally slightly higher than the observed one. The lower panel shows the ionospheric delay. The ionospheric delay calculated from the model simulation TEC agrees with the observed one, but the difference is slightly larger in 2011, and amounts to about 5 hours. The seasonal characteristics show the same tendency as those of the stations from Northern Hemisphere, but the scatter is larger.

A similar characteristic is observed at the South African station (Figure 4(d)). The ionospheric delay in the model-simulated TEC is very small, about 5 hours for November 2012.

An average ionospheric delay for the observed TEC is about 17.3 hours and 16.4 hours for the modeled TEC across all stations. An average difference between the Northern and Southern Hemispheric stations is about 1 hour for the observed TEC, while it is 2 hours for the modeled TEC. Our analysis shows that the ionospheric delay is longer in the case of the observed Southern Hemisphere than in the case of the modeled TEC,

while the model shows an opposite characteristic with a difference of about 2 hours. Moreover, the cross-correlation analysis shows that the mean correlation in the case of the modeled TEC is about 0.2, while it is 0.1 in the case of the observed TEC against the solar flux measured by SDO EVE. This indicates that in the real observations the ionospheric behavior is not only controlled by the solar activity, but also other factors, e.g. meteorological influences, play a significant role. During some months even a negative correlation was observed both in the model and in the observations. This negative correlation indicates the influence of local dynamics. The correlation coefficients at the Southern Hemispheric stations are generally higher than at the Northern Hemispheric stations.

In general, the ionospheric delay seen in the observed TEC is successfully reproduced by the CTIPe model simulated TEC and is about 17 hours. The seasonal variability of the delay is also captured by the model. Vaishnav et al. (2021b) examined the delayed ionospheric response at 15°E and found that the average delay calculated for observed and modeled TEC is 1 and 2 hours longer for Southern Hemisphere than for Northern Hemisphere. The ionospheric delay is related to the change in the ratio of atomic oxygen to molecular nitrogen, as suggested by Ren et al. (2018).

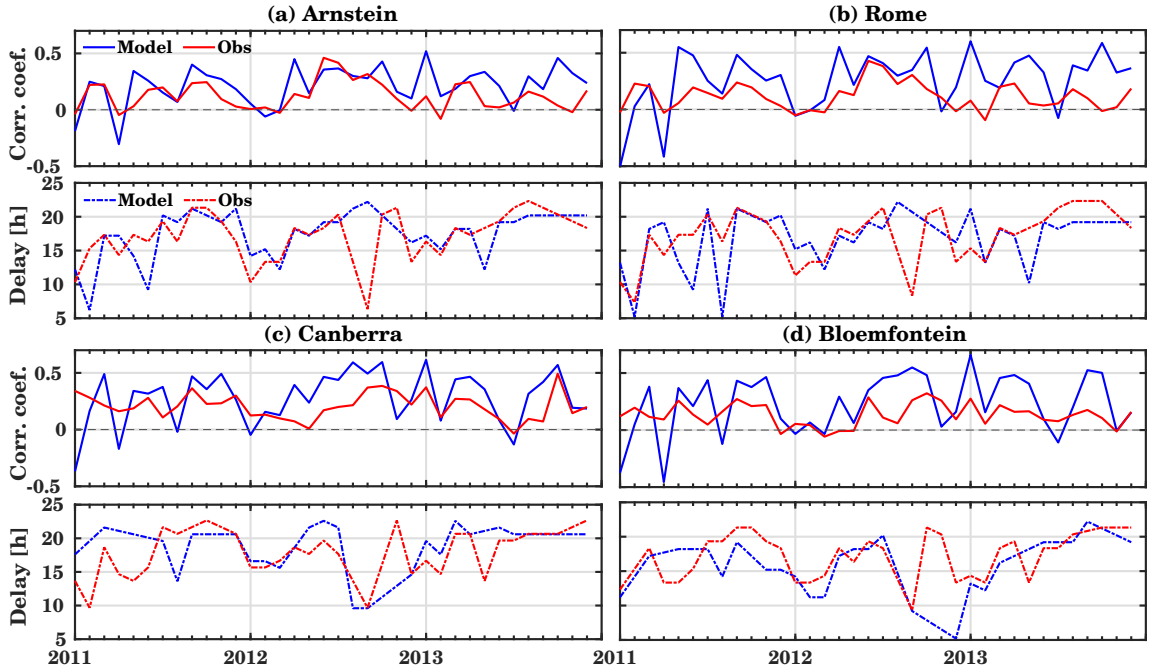

Figure 4: *Time series of correlation coefficients and delay estimations for different locations (a) Arnstein, (b) Rome, (c) Canberra and (d) Bloemfontein using observed and model simulated TEC with solar EUV flux from SDO EVE.*

4 Conclusions

We analyzed the ionospheric TEC from TEC maps provided by the International GNSS Service (IGS) and simulated it with the CTIPe model against the solar EUV flux measured by the SDO EVE satellite and its trend during 2011-2013 over European, Australian and South African stations. The modeled TEC is in agreement with the observed

TEC over South African, while it shows an underestimation with respect to the observed TEC over European stations.

In addition, the ionospheric delay estimated with the model TEC agrees with the delay estimated for observed TEC. The mean delay for the observed TEC is about 17.3 hours, while it is 16.4 hours for the modeled TEC. Moreover, the mean correlation with the solar flux measured by SDO EVE is always higher in the case of modeled TEC than observed TEC.

Acknowledgements IGS TEC maps have been kindly provided via NASA through ftp://cddis.gsfc.nasa.gov/gnss/products/ionex/. SDO-EVE data have been provided by the Laboratory for Atmospheric and Space Physics (LASP) through http://lasp.colorado.edu/eve/data_access/evewebdata (LASP, 2018a). Daily F10.7 index can be downloaded from http://lasp.colorado.edu/lisird/data/noaa_radio_flux/ (LASP, 2018b). The study has been supported by Deutsche Forschungsgemeinschaft (DFG) through grants nos. JA 836/33-1 and BE 5789/2-1.

References

Abdu, M. A.: Electrodynamics of ionospheric weather over low latitudes, Geoscience Letters, 3, doi:10.1186/s40562-016-0043-6, 2016.

Codrescu, M. V., Fuller-Rowell, T. J., Munteanu, V., Minter, C. F., and Millward, G. H.: Validation of the Coupled Thermosphere Ionosphere Plasmasphere Electrodynamics model: CTIPE-Mass Spectrometer Incoherent Scatter temperature comparison, Space Weather, 6, doi:10.1029/2007sw000364, 2008.

Codrescu, M. V., Negrea, C., Fedrizzi, M., et al.: A real-time run of the Coupled Thermosphere Ionosphere Plasmasphere Electrodynamics (CTIPe) model, Space Weather, 10, doi:10.1029/2011sw000736, 2012.

Fuller-Rowell, T. and Rees, D.: Derivation of a conservation equation for mean molecular weight for a two-constituent gas within a three-dimensional, time-dependent model of the thermosphere, Planetary and Space Science, 31, 1209–1222, doi:10.1016/0032-0633(83)90112-5, 1983.

Fuller-Rowell, T. J. and Rees, D.: A Three-Dimensional Time-Dependent Global Model of the Thermosphere, Journal of the Atmospheric Sciences, 37, 2545–2567, doi:10.1175/1520-0469(1980)037<2545:atdtdg>2.0.co;2, 1980.

Hernández-Pajares, M., Juan, J. M., Sanz, J., et al.: The IGS VTEC maps: a reliable source of ionospheric information since 1998, Journal of Geodesy, 83, 263–275, doi:10.1007/s00190-008-0266-1, 2009.

Jacobi, C., Jakowski, N., Schmidtke, G., and Woods, T. N.: Delayed response of the global total electron content to solar EUV variations, Advances in Radio Science, 14, 175–180, doi:10.5194/ars-14-175-2016, 2016.

Jakowski, N., Fichtelmann, B., and Jungstand, A.: Solar activity control of ionospheric and thermospheric processes, Journal of Atmospheric and Terrestrial Physics, 53, 1125–1130, doi:10.1016/0021-9169(91)90061-B, 1991.

Kutiev, I., Tsagouri, I., Perrone, L., et al.: Solar activity impact on the Earth's upper atmosphere, Journal of Space Weather and Space Climate, 3, A06, doi:10.1051/swsc/2013028, 2013.

LASP: EVE Data, available at: `http://lasp.colorado.edu/eve/data_access/evewebdata`, last access: 15 August 2018, 2018a.

LASP: F10.7 index, available at: `http://lasp.colorado.edu/lisird/data/noaa_radio_flux/`, last access: 15 August 2018, 2018b.

Millward, G., Moffett, R., Quegan, S., and Fuller-Rowell, T.: A coupled thermosphere-ionosphere-plasmasphere model (CTIP), STEP handbook on ionospheric models, pp. 239–279, 1996.

Min, K., Park, J., Kim, H., et al.: The 27-day modulation of the low-latitude ionosphere during a solar maximum, Journal of Geophysical Research: Space Physics, 114, 1–8, doi:10.1029/2008JA013881, 2009.

NASA: Shapefiles for declination and inclination of the World Magnetic Model, available at: ftp://ftp.ngdc.noaa.gov/geomag/wmm/wmm2015/shapefiles/2015/, last access: 15 August 2018, 2014.

Noll, C. E.: The crustal dynamics data information system: A resource to support scientific analysis using space geodesy, Advances in Space Research, 45, 1421–1440, doi:10.1016/j.asr.2010.01.018, 2010.

Pancheva, D., Schminder, R., and Laštovička, J.: 27-day fluctuations in the ionospheric D-region, Journal of Atmospheric and Terrestrial Physics, 53, 1145–1150, doi:10.1016/0021-9169(91)90064-e, 1991.

Percival, D. B. and Walden, A. T.: Wavelet Methods for Time SeriesAnalysis, Cambridge University Press, doi:10.1017/cbo9780511841040, 2000.

Pesnell, W. D., Thompson, B. J., and Chamberlin, P. C.: The Solar Dynamics Observatory (SDO), Solar Physics, 275, 3–15, doi:10.1007/s11207-011-9841-3, 2011.

Quegan, S., Bailey, G. J., Moffett, R. J., et al.: A theoretical study of the distribution of ionization in the high-latitude ionosphere and the plasmasphere: first results on the mid-latitude trough and the light-ion trough, Journal of Atmospheric and Terrestrial Physics, 44, 619–640, doi:10.1016/0021-9169(82)90073-3, 1982.

Ren, D., Lei, J., Wang, W., et al.: Does the Peak Response of the Ionospheric F2 Region Plasma Lag the Peak of 27-Day Solar Flux Variation by Multiple Days?, Journal of Geophysical Research: Space Physics, pp. 1–11, doi:10.1029/2018JA025835, 2018.

Richmond, A. D., Ridley, E. C., and Roble, R. G.: A thermosphere/ionosphere general circulation model with coupled electrodynamics, Geophysical Research Letters, 19, 601–604, doi:10.1029/92GL00401, 1992.

Romero-Hernandez, E., Denardini, C. M., Takahashi, H., et al.: Daytime ionospheric TEC weather study over Latin America, Journal of Geophysical Research: Space Physics, doi:10.1029/2018ja025943, 2018.

Schmidtke, G.: Extreme ultraviolet spectral irradiance measurements since 1946, History of Geo- and Space Sciences, 6, 3–22, doi:10.5194/hgss-6-3-2015, 2015.

Schmölter, E., Berdermann, J., Jakowski, N., Jacobi, C., and Vaishnav, R.: Delayed response of the ionosphere to solar EUV variability, Advances in Radio Science, 16, 149–155, doi:10.5194/ars-16-149-2018, 2018.

Schmölter, E., Berdermann, J., Jakowski, N., and Jacobi, C.: Spatial and seasonal effects on the delayed ionospheric response to solar EUV changes, Annales Geophysicae, 38, 149–162, doi:10.5194/angeo-38-149-2020, 2020.

Tapping, K. F.: The 10.7 cm solar radio flux (F10.7), Space Weather, 11, 394–406, doi:10.1002/swe.20064, 2013.

Unglaub, C., Jacobi, C., Schmidtke, G., Nikutowski, B., and Brunner, R.: EUV-TEC proxy to describe ionospheric variability using satellite-borne solar EUV measurements: First results, Advances in Space Research, 47, 1578–1584, doi:10.1016/j.asr.2010.12.014, 2011.

Unglaub, C., Jacobi, C., Schmidtke, G., Nikutowski, B., and Brunner, R.: EUV-TEC proxy to describe ionospheric variability using satellite-borne solar EUV measurements, Advances in Radio Science, 10, 259–263, doi:10.5194/ars-10-259-2012, 2012.

Vaishnav, R., Jacobi, C., Berdermann, J., Schmölter, E., and Codrescu, M.: Ionospheric response to solar EUV variations: Preliminary results, Advances in Radio Science, 16, 157–165, doi:10.5194/ars-16-157-2018, 2018.

Vaishnav, R., Jacobi, C., and Berdermann, J.: Long-term trends in the ionospheric response to solar extreme-ultraviolet variations, Annales Geophysicae, 37, 1141–1159, doi:10.5194/angeo-37-1141-2019, 2019a.

Vaishnav, R., Jacobi, C., Berdermann, J., Codrescu, M., and Schmölter, E.: Ionospheric response to solar variability during solar cycles 23 and 24, Rep. Inst. Meteorol. Univ. Leipzig, 57, 97–106, URL https://nbn-resolving.org/urn:nbn:de:bsz:15-qucosa2-741822, 2019b.

Vaishnav, R., Jacobi, C., Berdermann, J., Codrescu, M., and Schmölter, E.: Role of eddy diffusion in the delayed ionospheric response to solar flux changes, Annales Geophysicae, 39, 641–655, doi:10.5194/angeo-39-641-2021, 2021a.

Vaishnav, R., Schmölter, E., Jacobi, C., Berdermann, J., and Codrescu, M.: Ionospheric response to solar

extreme ultraviolet radiation variations: comparison based on CTIPe model simulations and satellite measurements, Annales Geophysicae, 39, 341–355, doi:10.5194/angeo-39-341-2021, 2021b.

Woods, T., Bailey, S., Eparvier, F., et al.: TIMED Solar EUV experiment, Physics and Chemistry of the Earth, Part C: Solar, Terrestrial & Planetary Science, 25, 393–396, doi:10.1016/s1464-1917(00)00040-4, 2000.

Woods, T. N.: Solar EUV Experiment (SEE): Mission overview and first results, Journal of Geophysical Research, 110, doi:10.1029/2004ja010765, 2005.

Woods, T. N., Eparvier, F. G., Hock, R., et al.: Extreme Ultraviolet Variability Experiment (EVE) on the Solar Dynamics Observatory (SDO): Overview of Science Objectives, Instrument Design, Data Products, and Model Developments, Solar Physics, 275, 115–143, doi:10.1007/s11207-009-9487-6, 2010.

Tidal signatures in sporadic E occurrence rates: migrating and nonmigrating components

Jacobi, Ch.[1], Lilienthal, F.[1], Yamazaki, Y.[2], Sobhkhiz-Miandehi, S.[2], Arras, C.[3]

[1] *Institute for Meteorology, Leipzig University, Stephanstr. 3, 04103 Leipzig, Germany, E-mail: jacobi@uni-leipzig.de*
[2] *Helmholtz Centre Potsdam German Research Centre for Geosciences - GFZ, Section 2.3: Geomagnetism, Telegrafenberg, 14473 Potsdam, Germany*
[3] *Helmholtz Centre Potsdam German Research Centre for Geosciences - GFZ, Section 1.1: Space Geodetic Techniques, Telegrafenberg, 14473 Potsdam, Germany*

Summary: We analyze sporadic E (E_S) occurrence rates (OR) obtained from ionospheric GPS radio occultation measurements by the FORMOSAT-3/COSMIC constellation. Maximum OR are seen at 95 – 105 km altitude. Midlatitude E_S are mainly due to wind shear in the presence of tides, and the strongest signals are the migrating diurnal and semidiurnal components. Especially in the Southern Hemisphere, nonmigrating components such as a diurnal westward wave 2 and a semidiurnal westward wave 1 are also visible, especially at high latitudes. Near the equator, a strong diurnal eastward wavenumber 3 component and a semidiurnal eastward wavenumber 2 component occur in summer and autumn. Terdiurnal and quarterdiurnal components are weaker than the diurnal and semidiurnal ones.

Zusammenfassung: Wir untersuchen Auftrittsraten sporadischer E-Schichten (E_S), die aus ionosphärischen GPS-Radiookkultationsmessungen von FORMOSAT-3 / COSMIC bestimmt wurden. Maximale Auftrittsraten treten in 95 – 105 km Höhe auf. E_S in mittleren Breiten sind hauptsächlich auf Windscherung durch Gezeiten zurückzuführen, und die stärksten Signale sind eine westwärts wandernde Tages- und Halbtageskomponente. Insbesondere in der Südhemisphäre sind auch nichtmigrierende Komponenten wie eine ganztägige westwärts wandernde Welle der Wellenzahl 2 und eine halbtägige westwärts wandernde Welle der Wellenzahl 1 sichtbar. In der Nähe des Äquators treten im Sommer und Herbst eine starke ostwärts wandernde ganztägige Komponente der Wellenzahl 3 und eine ostwärts wandernde halbtägige Komponente der Wellenzahl 2 auf. Dritteltägige und vierteltägige Komponenten sind schwächer als die ganz- und halbtägigen.

1 Introduction

Sporadic E (E_S) layers are thin clouds of accumulated ions in the lower ionosphere. They are most frequently found during the summer season at middle latitudes (e.g., Arras et al., 2008). E_S are generally formed at heights between 90 km and 120 km. Their occurrence can be described through the wind shear theory (Whitehead, 1961), which describes the

interaction between the metallic ion concentration, the Earth's magnetic field, and the vertical shear of the neutral wind (e.g., Gong et al., 2014; Fytterer et al., 2014).

The dynamics of the lower thermosphere at time scales up to one day are mainly influenced by solar tides, with periods of a solar day and its harmonics (e.g., Forbes, 1995). Tidal amplitudes usually maximize around or above 120 km, where they are of the order of magnitude of the mean wind. Shorter period tidal waves often have smaller amplitudes, so that, on a global scale, the major diurnal variability of lower thermosphere winds is due to the diurnal tide (DT, Pancheva et al., 2002), the semidiurnal tide (SDT, Jacobi et al., 1999; Pancheva et al., 2002), and, to a lesser degree, also to the terdiurnal tide (TDT, Beldon et al., 2006; Liu et al., 2019). Note, however, that at higher midlatitudes the DT wind amplitudes become small compared with SDT ones during most of the year. Owing to its smaller amplitude, the quarterdiurnal tide (QDT) has been analyzed less frequently in the past, but more recently has attained increasing attention (Liu et al., 2015; Azeem et al., 2016; Jacobi et al., 2018a, 2019; Guharay et al., 2018).

Solar tides are a major source of vertical wind shear, and the tidal contribution to the overall wind shear is frequently larger than the one of the background wind. Therefore, tide-like structures are also expected in E_S occurrence rates. Consequently, tides are generally accepted to be the major driver of E_S (Mathews, 1998), and they lead to the downward moving tidal signatures in ionosonde registrations (e.g., Haldoupis et al., 2006; Haldoupis, 2012). Analyzing GPS E_S observations together with meteor radar wind measurements at Collm (51.3°N, 13.0°E), a clear correspondence of E_S and negative wind shear maximums has been found for the SDT (Arras et al., 2009), TDT (Fytterer et al., 2013), and QDT (Jacobi et al., 2019), but not for the DT (Jacobi and Arras, 2019). Fytterer et al. (2014) and Jacobi et al. (2019) compared GPS E_S radio occultations (RO) and modeled wind shear. They demonstrated the similarity of the TDT and QDT in E_S and wind shear on a global scale. Resende et al. (2018a) modeled the connection of E_S and tides, although focusing on the equatorial region, where electric field effects become more important than at middle latitudes.

Comparisons of E_S and wind shear have frequently been performed based on local wind measurements (Arras et al., 2009; Fytterer et al., 2013; Jacobi et al., 2019; Jacobi and Arras, 2019). These observations cannot distinguish between migrating and non-migrating tidal components. To reveal the migrating E_S tidal components only, these results were compared with E_S sampled in local time at all longitudes. This approach showed good correspondence for Northern Hemisphere (NH) stations, where the migrating tidal component is obviously dominating.

Using frequency-wavenumber analysis, it is possible to analyze also non-migrating tidal components from global fields. Therefore, in the following, we present analyses of migrating but also non-migrating tides seen in E_S OR, which are based on FORMOSAT-3/COSMIC GPS RO observations. We will use the following notation: The period is represented by the letter D, S, T, Q for diurnal, semidiurnal, terdiurnal, and quarterdiurnal, respectively. This is followed by W or E for westward or eastward, and an integer representing the zonal wavenumber. So DW1 represents the diurnal westward migrating tide of zonal wavenumber 1, SE2 stands for the semidiurnal eastward wavenumber 2 component, and so forth.

Note that the correspondence between the wind shear and the E_S diurnal variability is much weaker for the DT than for the SDT, TDT, and QDT. This is owing to the fact

that a diurnal E_S variation is not only due to wind shear, but also owing to background ionization, which is much stronger during daytime. Strictly speaking, it is therefore incorrect to interpret the diurnal E_S variation as a DT signature. For a consistent description, we nevertheless refer to the diurnal E_S signature as a DT.

2 Sporadic E analysis

We make use of ionospheric RO measurements by the FORMOSAT-3/COSMIC constellation, which performs observations in both the neutral and ionized atmosphere (Anthes et al., 2008) though a constellation of six low-Earth orbiting (LEO) satellites. During each occultation, signals of the rising or setting GPS satellites are received by a LEO satellite. When the signals pass the atmosphere/ionosphere of the Earth, they are influenced in particular by the ionospheric electron density, which causes refraction and degradation of the GPS waves. This effect can be utilized to obtain information about the ionosphere. Observation of the neutral atmosphere is also possible, but this is not the topic of this study. Detailed information on the RO technique principles is provided by Hajj et al. (2002) and Kursinski et al. (1997).

In this study the Signal-to-Noise (SNR) profiles of the GPS L1 phase measurements are used according to Arras and Wickert (2018). The SNR is very sensitive to vertical variations of the electron density, and these occur within an E_S layer. These vertically localized electron density variations lead to phase fluctuations of the GPS signal, which can be observed as changes in the received signal strength (Hajj et al., 2002). In order to avoid influences from the different basic signal power values on the further data analysis, every SNR profile is normalized first. In the case of the absence of ionospheric disturbances, the SNR value is almost constant at altitudes above 35 km. The SNR standard deviation profile is considered to be disturbed when it exceeds an empirically found threshold of 0.2. If large standard deviation values are concentrated within a thin layer of less than 10 km vertical extent, we assume that the respective SNR profile includes the signature of an E_S layer. The height where the SNR value deviates most from the mean of the SNR profile is considered as the altitude of the E_S layer. This has been validated by comparisons with ionosonde E_S observations. (Arras and Wickert, 2018; Resende et al., 2018b).

The following analysis is based on observations from 2007 to 2017. The number of occultations and the number of observed E_S are each binned into a 4-dimensional grid of $5° \times 10° \times 1\text{km} \times 1\text{h}$ (latitude $\times$ longitude $\times$ altitude $\times$ time), calculated within partly overlapping boxes of 10° (latitudes, 20° (longitude), 10 km (altitude) and 1 h, respectively, and as 3-monthly (seasonal) means. E_S OR are then calculated as the number of E_S divided by the number of occultations in each bin. Note that the OR of an individual bin is set to zero if there are less than five occultations within this bin.

3 Global distribution of Sporadic E

Figure 1 shows the 2007 - 2017 mean zonal mean and seasonal mean E_S OR for December–February (DJF), and June–August (JJA). The distributions are similar to those shown by Fytterer et al. (2014); Jacobi et al. (2019) obtained from a more limited dataset.

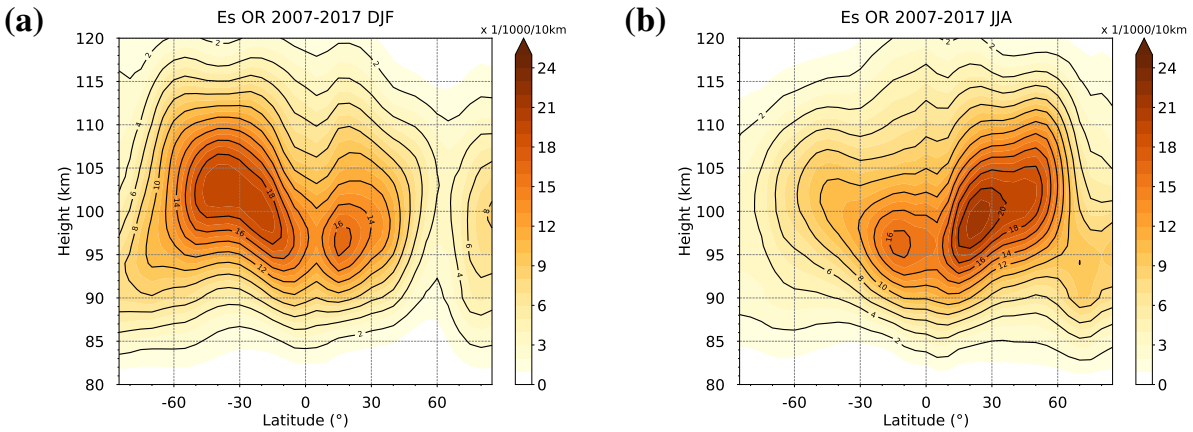

Figure 1: *Zonal and seasonal mean E_S occurrence rates in a 10 km vertical window each for (a) DJF, (b) JJA. Data are averages over* 2007 - 2017.

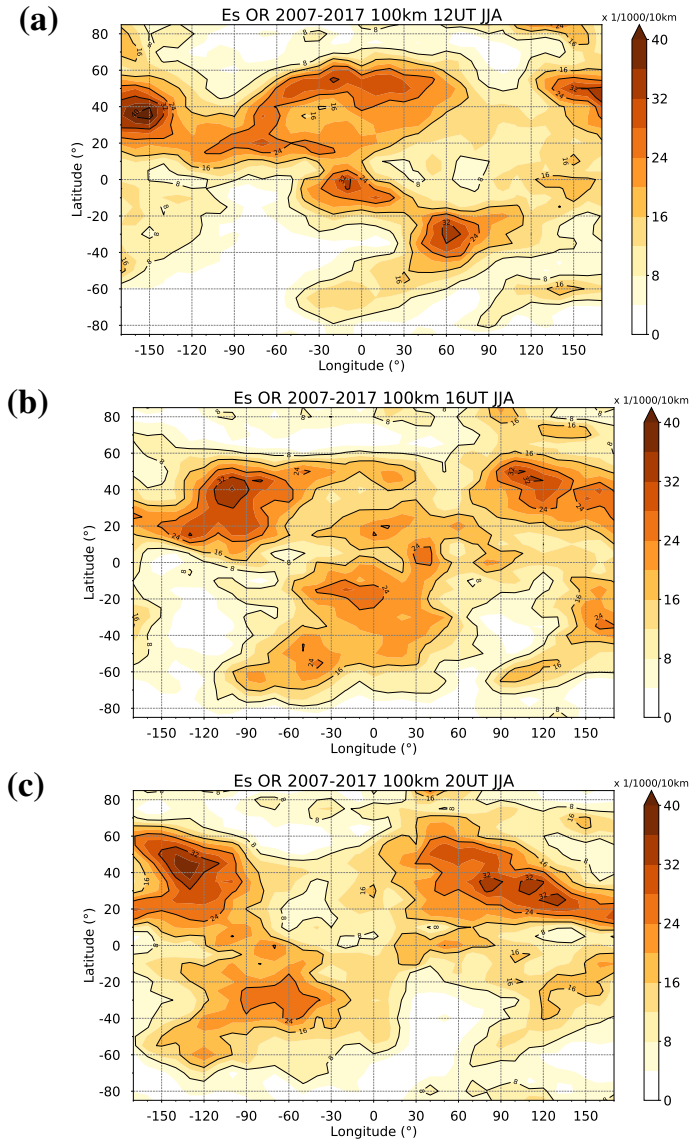

Figure 2: *Global distribution of JJA mean E_S occurrence rates at 95 – 105 km for (a) 12 UT, (b) 16 UT, (c) 20 UT.*

Maximum OR are found at altitudes slightly between 95 km and 105 km. OR maximize in summer, which is thought to be owing to increased meteor influx during that season (Haldoupis et al., 2007). The summer maximum is more pronounced in the NH, which is due to the weaker magnetic field within the South Atlantic Anomaly (e.g., Arras et al., 2008; Chu et al., 2014; Arras and Wickert, 2018). Near the equator, E_S OR are small, owing to the horizontal magnetic field at the magnetic equator, which does not allow the electrons to follow the vertically moving ions (e.g., Arras et al., 2008, 2010; Arras and Wickert, 2018).

As an example of the diurnal variability of JJA mean E_S, Figure 2 presents latitude-longitude sections of OR in an 10 km height window centered at 100 km, for three different universal times differing by 4 hrs each. The data have been sampled in windows of 10° latitude and 20° longitude. The strong summer signal is visible between 10 and 20°N, and it exhibits a clear wavenumber 2 signature at midlatitudes. This structure is moving westward with time, and obvious is the signature of the migrating SW2. The SW2 is also visible in the Southern Hemisphere (SH). At the equator, the semidiurnal signal is only weakly visible.

4 Spectral distribution of tidal components

In order to analyze the tidal components in the long-term diurnal E_S signal, we performed frequency-wavenumber (f-k) analyses that have been based on gridded data that have again been sampled in boxes of 10° times 20° in latitude and longitude, resp., and 10 km in height. Again, we analyze results in windows centered at 100 km. Figure 3 presents f-k spectra at 30°N, while the spectra for 30°S are shown in Figure 4.

In the NH, the main signal is due to the DW1 and SW2. In winter, OR are small

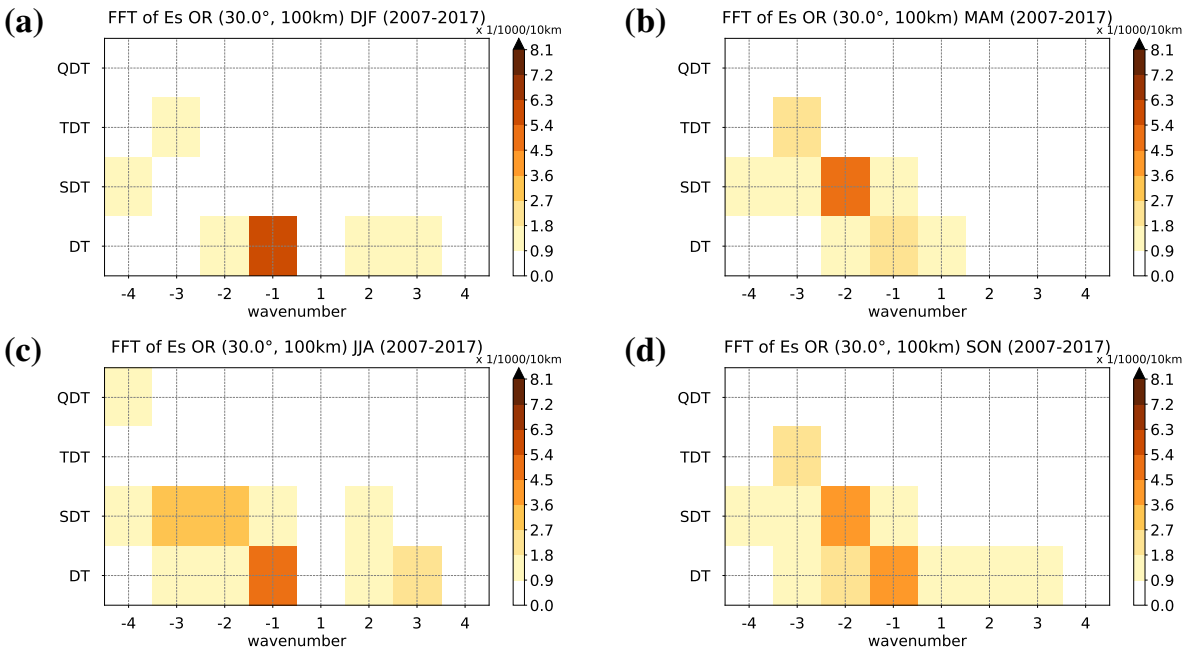

Figure 3: *Wavenumber-frequency spectra of E_S OR at 30°N in the 95 – 105 km height window for (a) DJF, (b) MAM, (c) JJA, and (d) SON.*

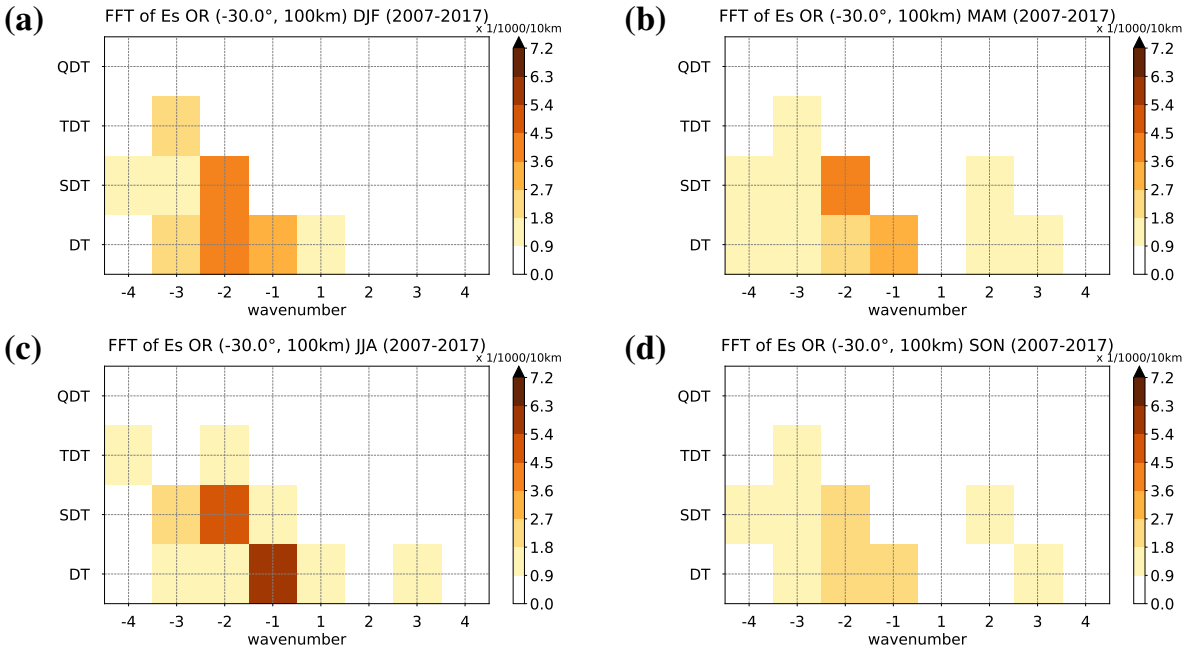

Figure 4: *As in Fig. 3, but at 30°S.*

and only a DW1 is visible. During equinoxes, a TW3 also appears, which reflects the seasonal cycle of the TDT with maximums in autumn/spring and winter (Jacobi et al., 2018a; Lilienthal et al., 2018). The QW4 is weak and only visible in summer. The only relevant non-migrating component is a SW3 signature in summer.

In the SH at 30°S, more non-migrating components show up. In addition to a winter (JJA) SW3, there is a distinct DW2 in all seasons except for winter. The stronger non-migrating components may be owing to the distinct non-zonal structure of overall E_S OR through the South Atlantic Anomaly.

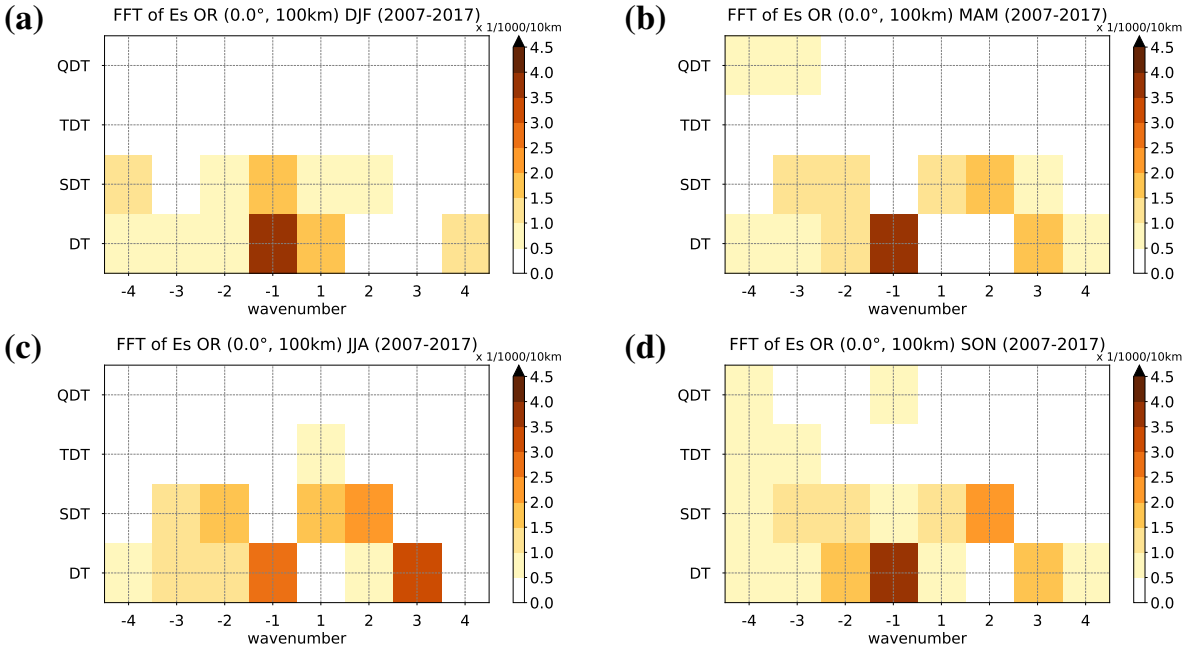

Figure 5: *As in Fig. 3, but at the equator.*

The spectral distribution at the equator shown in Figure 5 differs from the one at midlatitudes. The DW1 is strongest in most months, but during NH summer (JJA) and equinoxes, a clear DE3 is visible, with amplitudes partly larger than the DW1. The DE3 is accompanied by a SE2 during these months. The SE2 is stronger than the rather weak SW2 at the equator. There are several other non-migrating components, namely a DE1 and a SW1 in NH winter (DJF), a SE1 in JJA, and a DW2 in SON. These components may partly be due to the non-zonal structure of the background E_S, especially at the South American Anomaly. TDT and QDT signatures are weak at the equator.

The latitudinal distributions of DT and SDT spectra are shown in Figures 6 and 7. Figure 6 also shows that in the NH the migrating DW1 dominates, in all seasons, while in the SH there is also a DW2 as already visible in Figure 4. At the equator, the DE3 is visible. Note that there is a strong DW1 signature at high latitudes, which is not connected with tidal activity, but due to the action of magnetospheric electric fields (Kirkwood and Nilsson, 2000). The SDT (Figure 7) in the NH is, as is the case with the DT, mainly due to the migrating SW2, except for a summer SW3, which is also seen in the SH summer. In the SH, also the non-migrating SW1 is visible during most of the year.

The latitudinal distributions of TDT and QDT spectra are shown in Figures 8 and 9. Their amplitudes are much weaker than the DT and SDT ones. For the TDT, again the migrating TW3 dominates, but there is a considerable activity of non-migrating components, in particular a TW2, but in some seasons and at some latitudes also a TW4, TW1, and TE1. The QDT is more irregular. The migrating QW4 dominates in most months, but there is also a distinct QW3, QW2, and other components.

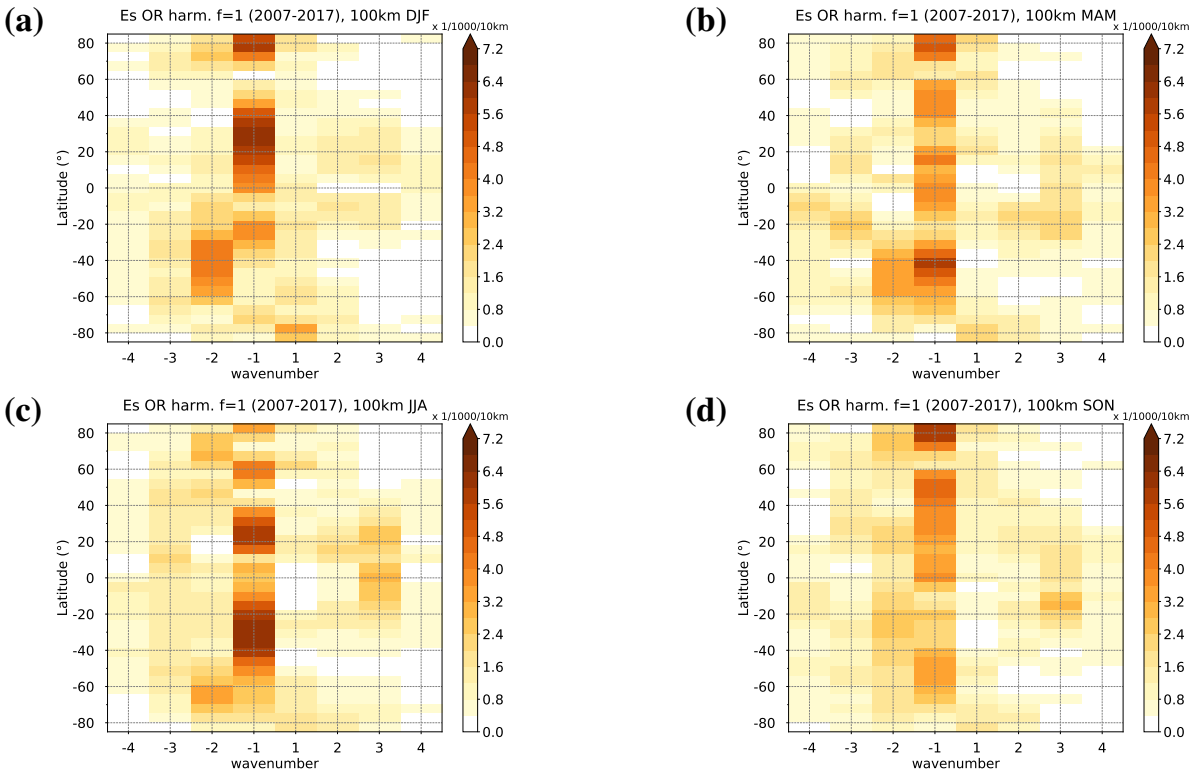

Figure 6: *Global distribution of DT wavenumber spectra of E_S OR in the 95 – 105 km height window for (a) DJF, (b) MAM, (c) JJA, and (d) SON.*

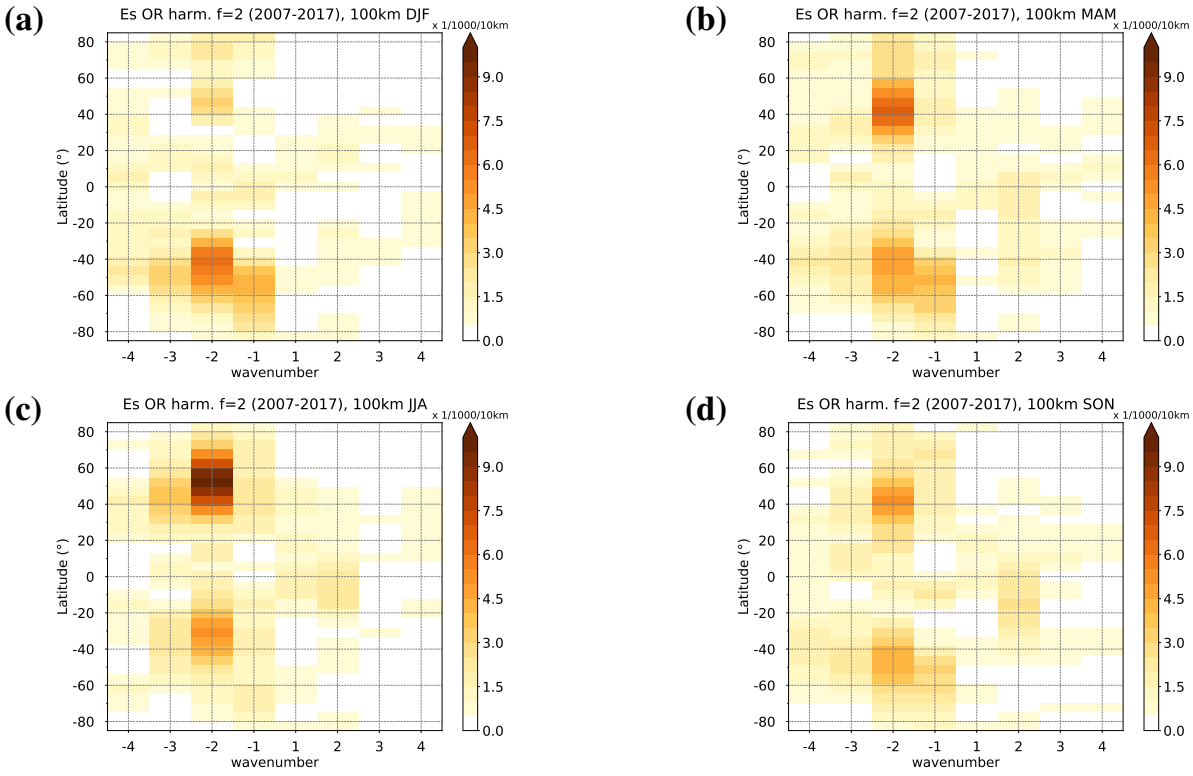

Figure 7: *As in Fig. 6 but for the SDT.*

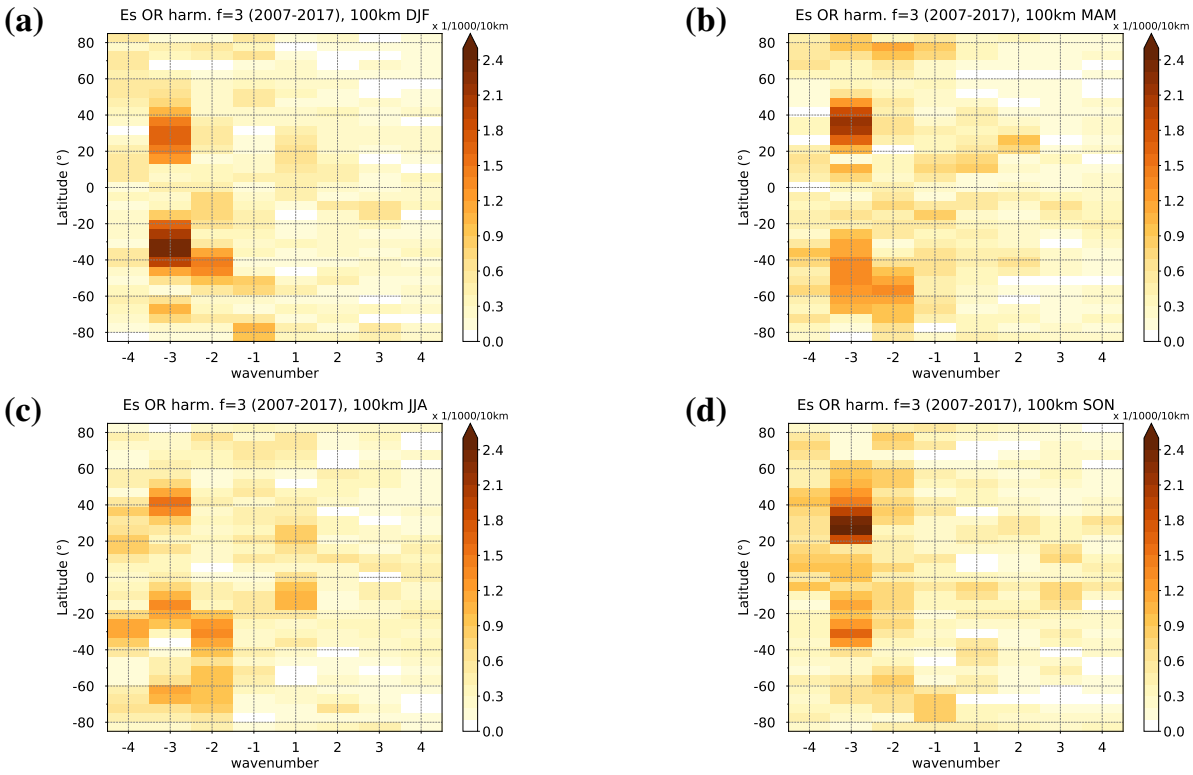

Figure 8: *As in Fig. 6 but for the TDT.*

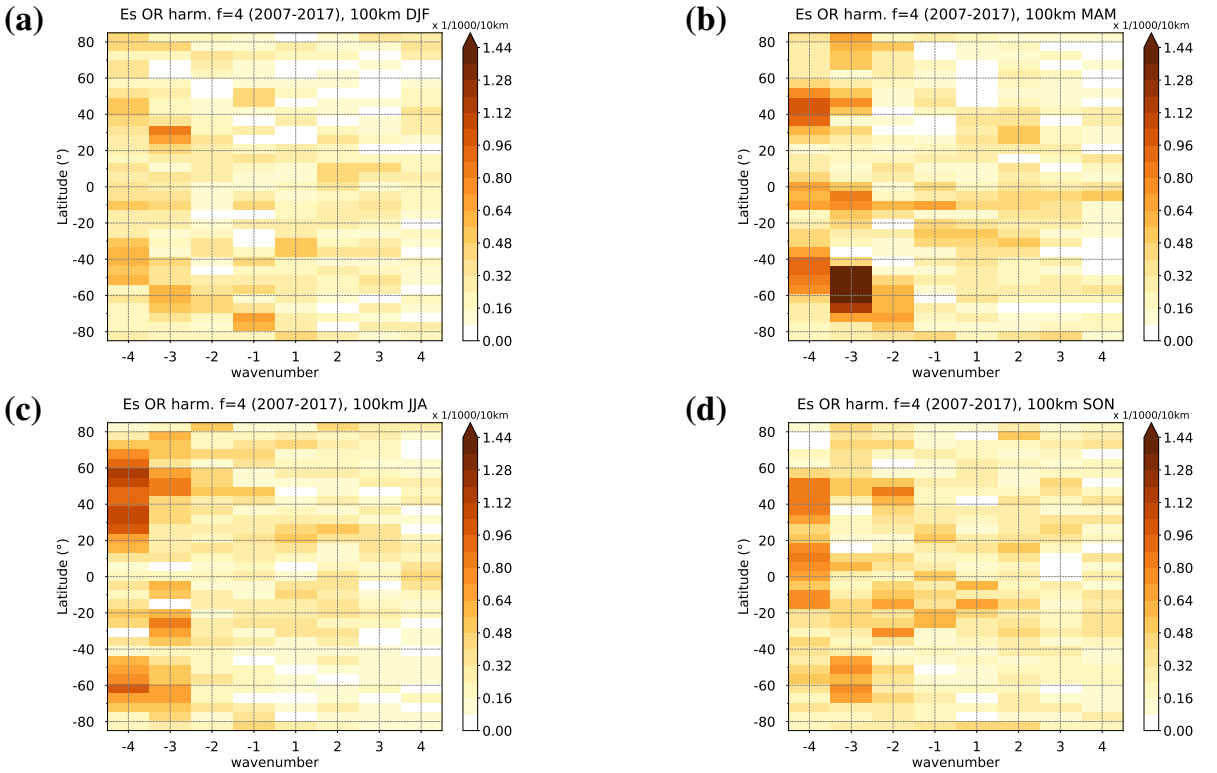

Figure 9: *As in Fig. 6 but for the QDT.*

5 Conclusions & Outlook

We analyzed E_S OR obtained from ionospheric GPS RO. Maximum OR are seen at 95 – 105 km altitude. The strongest signals are due to the migrating DW1 and SW2. Especially in the SH, non-migrating components such as a DW2 and a SW1 are also visible, especially at higher latitudes. Near the equator, a strong DE3 and also a SE2 occur in summer and autumn. Terdiurnal and quarterdiurnal components are weaker than the diurnal and semidiurnal ones.

Note that the amplitudes of OR oscillations, or tidal components in OR, are determined by the tidal activity and the corresponding wind shear, but also by the background ionization of metallic ions. The latter, in particular produces a DW1 signature, but this is not connected with shear, as has been shown by phase comparisons by Jacobi et al. (2018a). Furthermore, the seasonal cycle and global structure of E_S amplitudes also reflect the respective background OR, which are determined by meteor influx (Haldoupis et al., 2007; Jacobi et al., 2013). Removing the background variability by normalizing OR amplitudes by the OR background (e.g., Fytterer et al., 2014; Jacobi et al., 2019) frequently leads to a stronger correspondence of the wind and E_S amplitude distributions.

Acknowledgements: The provision of FORMOSAT-3/COSMIC data by University Corporation for Atmospheric Research is gratefully acknowledged. CJ and FL acknowledge support by Deutsche Forschungsgemeinschaft through grant JA 836/34-1.

References

Anthes, R. A., Bernhardt, P. A., Chen, Y., et al.: The COSMIC/FORMOSAT-3 Mission: Early Results, Bull. Amer. Meteorol. Soc., 89, 313–334, doi:10.1175/BAMS-89-3-313, 2008.

Arras, C. and Wickert, J.: Estimation of ionospheric sporadic E intensities from GPS radio occultation measurements, J. Atmos. Sol.-Terr. Phys., 171, 60 – 63, doi:10.1016/j.jastp.2017.08.006, 2018.

Arras, C., Wickert, J., Beyerle, G., et al.: A global climatology of ionospheric irregularities derived from GPS radio occultation, Geophys. Res. Lett., 35, doi:10.1029/2008GL034158, 2008.

Arras, C., Jacobi, C., and Wickert, J.: Semidiurnal tidal signature in sporadic E occurrence rates derived from GPS radio occultation measurements at higher midlatitudes, Ann. Geophys., 27, 2555–2563, doi:10.5194/angeo-27-2555-2009, 2009.

Arras, C., Jacobi, C., Wickert, J., Heise, S., and Schmidt, T.: Sporadic E signatures revealed from multi-satellite radio occultation measurements, Adv. Radio Sci., 8, 225–230, doi:10.5194/ars-8-225-2010, 2010.

Azeem, I., Walterscheid, R. L., Crowley, G., Bishop, R. L., and Christensen, A. B.: Observations of the migrating semidiurnal and quaddiurnal tides from the RAIDS/NIRS instrument, J. Geophys. Res.: Space Physics, 121, 4626–4637, doi:10.1002/2015JA022240, 2016.

Beldon, C., Muller, H., and Mitchell, N.: The 8-hour tide in the mesosphere and lower thermosphere over the UK, 1988–2004, J. Atmos. Sol.-Terr. Phys., 68, 655–668, doi:10.1016/j.jastp.2005.10.004, 2006.

Chu, Y. H., Wang, C. Y., Wu, K. H., et al.: Morphology of sporadic E layer retrieved from COSMIC GPS radio occultation measurements: Wind shear theory examination, J. Geophys. Res.: Space Physics, 119, 2117–2136, doi:10.1002/2013JA019437, 2014.

Forbes, J. M.: Tidal and Planetary Waves, pp. 67–87, American Geophysical Union (AGU), doi:10.1029/GM087p0067, 1995.

Fytterer, T., Arras, C., and Jacobi, C.: Terdiurnal signatures in sporadic E layers at midlatitudes, Adv. Radio Sci., 11, 333–339, doi:10.5194/ars-11-333-2013, 2013.

Fytterer, T., Arras, C., Hoffmann, P., and Jacobi, C.: Global distribution of the migrating terdiurnal tide seen in sporadic E occurrence frequencies obtained from GPS radio occultations, Earth Planets Space, 66, 1–9, doi:10.1186/1880-5981-66-79, 2014.

Gong, Y., Zhou, Q., and Zhang, S.: Numerical and observational study of ion layer formation at Arecibo, in: XXXIth URSI General Assembly, Beijing, China, pp. 1–4, doi:10.1109/URSIGASS.2014.6929732, 2014.

Guharay, A., Batista, P. P., Buriti, R. A., and Schuch, N. J.: On the variability of the quarter-diurnal tide in the MLT over Brazilian low-latitude stations, Earth Planets Space, 70, 140, doi:10.1186/s40623-018-0910-9, 2018.

Hajj, G., Kursinski, E., Romans, L., Bertiger, W., and Leroy, S.: A technical description of atmospheric sounding by GPS occultation, J. Atmos. Sol.-Terr. Phys., 64, 451 – 469, doi:10.1016/S1364-6826(01)00114-6, 2002.

Haldoupis, C.: Midlatitude Sporadic E. A Typical Paradigm of Atmosphere-Ionosphere Coupling, Space Sci. Rev., 168, 441–461, doi:10.1007/s11214-011-9786-8, 2012.

Haldoupis, C., Meek, C., Christakis, N., Pancheva, D., and Bourdillon, A.: Ionogram height–time–intensity observations of descending sporadic E layers at mid-latitude, J. Atmos. Sol.-Terr. Phys., 68, 539 – 557, doi:10.1016/j.jastp.2005.03.020, 2006.

Haldoupis, C., Pancheva, D., Singer, W., Meek, C., and MacDougall, J.: An explanation for the seasonal dependence of midlatitude sporadic E layers, J. Geophys. Res.: Space Physics, 112, doi:10.1029/2007JA012322, 2007.

Jacobi, C. and Arras, C.: Tidal wind shear observed by meteor radar and comparison with sporadic E occurrence rates based on GPS radio occultation observations, Advances in Radio Science, 17, 213–224, doi:10.5194/ars-17-213-2019, 2019.

Jacobi, C., Portnyagin, Y., Solovjova, T., et al.: Climatology of the semidiurnal tide at 52–56°N from ground-based radar wind measurements 1985–1995, J. Atmos. Sol.-Terr. Phys., 61, 975 – 991, doi:https://doi.org/10.1016/S1364-6826(99)00065-6, 1999.

Jacobi, C., Arras, C., and Wickert, J.: Enhanced sporadic E occurrence rates during the Geminid meteor

showers 2006-2010, Advances in Radio Science, 11, 313–318, doi:10.5194/ars-11-313-2013, 2013.

Jacobi, C., Geißler, C., Lilienthal, F., and Krug, A.: Forcing mechanisms of the 6 h tide in the mesosphere/lower thermosphere, Adv. Radio Sci., 16, 141–147, doi:10.5194/ars-16-141-2018, 2018a.

Jacobi, C., Arras, C., Geißler, C., and Lilienthal, F.: Quarterdiurnal signature in sporadic E occurrence rates and comparison with neutral wind shear, Annales Geophysicae, 37, 273–288, doi:10.5194/angeo-37-273-2019, 2019.

Kirkwood, S. and Nilsson, H.: High-latitude Sporadic-E and other Thin Layers – the Role of Magnetospheric Electric Fields, Space Science Reviews, 91, 579–613, doi:10.1023/A:1005241931650, 2000.

Kursinski, E. R., Hajj, G. A., Schofield, J. T., Linfield, R. P., and Hardy, K. R.: Observing Earth's atmosphere with radio occultation measurements using the Global Positioning System, J. Geophys. Res.: Atmospheres, 102, 23 429–23 465, doi:10.1029/97JD01569, 1997.

Lilienthal, F., Jacobi, C., and Geißler, C.: Forcing mechanisms of the terdiurnal tide, Atmospheric Chemistry and Physics, 18, 15 725–15 742, doi:10.5194/acp-18-15725-2018, 2018.

Liu, H., Tsutsumi, M., and Liu, H.: Vertical Structure of Terdiurnal Tides in the Antarctic MLT Region: 15-Year Observation Over Syowa (69°S, 39°E), Geophysical Research Letters, 46, 2364–2371, doi:https://doi.org/10.1029/2019GL082155, 2019.

Liu, M., Xu, J., Yue, J., and Jiang, G.: Global structure and seasonal variations of the migrating 6-h tide observed by SABER/TIMED, Sci. China Earth Sci., 58, 1216–1227, doi:10.1007/s11430-014-5046-6, 2015.

Mathews, J.: Sporadic E: current views and recent progress, J. Atmos. Sol.-Terr. Phys., 60, 413 – 435, doi:10.1016/S1364-6826(97)00043-6, 1998.

Pancheva, D., Mitchell, N., Hagan, M., et al.: Global-scale tidal structure in the mesosphere and lower thermosphere during the PSMOS campaign of June–August 1999 and comparisons with the global-scale wave model, J. Atmos. Sol.-Terr. Phys., 64, 1011 – 1035, doi:https://doi.org/10.1016/S1364-6826(02)00054-8, 2002.

Resende, L. C. A., Batista, I. S., Denardini, C. M., et al.: The influence of tidal winds in the formation of blanketing sporadic e-layer over equatorial Brazilian region, J. Atmos. Sol.-Terr. Phys., 171, 64 – 71, doi:https://doi.org/10.1016/j.jastp.2017.06.009, 2018a.

Resende, L. C. A., Arras, C., Batista, I. S., et al.: Study of sporadic E layers based on GPS radio occultation measurements and digisonde data over the Brazilian region, Ann. Geophys., 36, 587–593, doi:10.5194/angeo-36-587-2018, 2018b.

Whitehead, J.: The formation of the sporadic-E layer in the temperate zones, J. Atmos. Terr. Phys., 20, 49 – 58, doi:10.1016/0021-9169(61)90097-6, 1961.

Determination of radiation couplings in climate change simulations: Analysis with two different linearization methods

Martin, A.[1,*]**, Quaas, J.**[1]

[1]) *Institute for Meteorology, Stephanstr. 3, 04103 Leipzig,*
E-Mail: a.martin@mpic.de
[*]) *Now at: Max-Planck-Institut for Chemistry, Hahn-Meitner-Weg 1, 55128 Mainz*

Zusammenfassung: In dieser Arbeit werden zwei Linearisierungsmethoden zur Bestimmung von Strahlungskopplungen in Klimaänderungssimulationen verglichen. Die individuellen Feedbackparameter werden mit der Partial Radiative Perturbation (PRP)-Methode und der Kernel Methode basierend auf CMPI6 Daten des Max-Planck-Instituts Earth System Model in Low Resolution (MPI-ESM-LR) mit vierfacher CO_2-Konzentration berechnet. Für die Berechnung der Feedbacks wurde das eigenständige ECHAM6 Strahlungsmodul genutzt. Neben regionalen Besonderheiten der einzelnen Rückkopplungsparameter, zeigen sich die größten Unterschiede im Oberflächenalbedo Feedback. Wasserdampf, Lapses-Rate und Planck Feedback weisen eine vergleichsweise geringe Methodenabhänigkeit auf. Dies kann auch im Vergleich mit vorherigen Studien verifiziert werden. Zusätzlich wird gezeigt, dass die Verwendung von mehrjährigen Monatsmittelwerten den Rechenaufwand bei nur geringem Genauigkeitsverlust reduziert.

Summary: In this paper two linearization methods for the determination of radiation couplings in climate change simulations are compared. Individual feedback parameters are calculated using the partial radiative perturbation (PRP) method and kernel-technique based on CMIP6 data of the Max Planck Institute Earth System Model at Low Resolution (MPI-ESM-LR) model with quadrupled CO_2 concentration. The applied kernels were computed separately for two directions using the same radiation module as for the PRP method, providing the opportunity to compare both based on the same data basis. The largest disagreements between methods were found for the surface albedo feedback, followed by the water vapor feedback, lapse-rate feedback and Planck feedback, whereas the differences of the last three mentioned are minor. Nevertheless, the found results are within the range of former studies. Beside regional features of the individual feedback parameters, an overall good agreement between the PRP and kernel approach is observed. Additionally, it is shown that the use of multiyear monthly averages reduces the computational expense with only a small loss in accuracy, compared to calculations based on yearly monthly averages.

1 Introduction

Climate and the earth's atmospheric composition are continuously changing. Thus, the analysis and simulation of changes in atmospheric composition is of great importance

to obtain possible impacts on the global climate. In this context, the fraction of greenhouse gases in the atmosphere plays a significant role. Consequently, many studies have been conducted on the effect of increased CO_2 levels and their impact on global surface temperature. The change in mean global surface temperature due to a doubling in CO_2 within the atmosphere is the so-called equilibrium climate sensitivity. Currently, the fifth Assessment Report of the Intergovernmental Panel on Climate Change (IPCC AR5) estimates the equilibrium climate sensitivity (ECS) in the range of $3.2 \pm 1.3\,^{\circ}\mathrm{C}$ (Flato et al. 2013). The variability of the ECS is strongly related to physical adjustment processes, so-called climate feedbacks. The characterization of those climate feedbacks, in terms of order of magnitude and sign are especially relevant for global climate model evaluations. In the following the PRP method and the radiative kernel technique are applied to identify possible method dependent biases in the determination of radiation couplings.

2 Feedbacks and data description

2.1 Feedbacks

Feedback mechanisms are described as responses to changes in the radiative budget at the top of the atmosphere (TOA) due to external forcing processes (Thorsen et al. 2018).

In general the climate system can be visualized as a box, with TOA as box edge, in which physical laws like energy conservation apply. Observed long enough, the climate system reaches equilibrium, when the TOA net radiation flux $R_{\mathrm{net}}(t \to \infty)$ reaches zero. Considering smaller time scales, the radiation flux differs from zero. This can be due to several external forcing processes ΔF, which increase or dampen energy transport in and out of the system. External forcings are for example changes in greenhouse gas concentration, surface albedo, aerosol composition or a changing solar radiation (Bony et al. 2006). The changes of the TOA radiative flux due to changes in surface temperature T_{S}, resulting in variation of processes depending on temperature, are defined as climate feedbacks, which occur to restore the equilibrium state within the climate system, leading to $\Delta R = \Delta F + \lambda \Delta T_{\mathrm{S}}$ (Thorsen et al. 2018). They can be quantified using a climate feedback factor λ_{X}, where X stands for a certain physical property of the climate system, like surface albedo A, temperature T, water vapor WV or clouds CL. The total feedback factor λ is the sum of all specific feedback factors, with additional separation of λ_{T} into the lapse-rate feedback λ_{LR}, describing the rate of temperature decrease with height and the Planck feedback λ_{PL}, depending on surface longwave (LW) emission (Klocke, Quaas, and Stevens 2013):

$$\lambda = \underbrace{\lambda_{\mathrm{T}}}_{=\lambda_{\mathrm{PL}}+\lambda_{\mathrm{LR}}} + \lambda_{\mathrm{WV}} + \lambda_{\mathrm{CL}} + \lambda_{\mathrm{A}}. \tag{1}$$

λ (in units of $\mathrm{W\,m^{-2}\,K^{-1}}$) is defined as the change of radiation ΔR depending on surface temperature change ΔT_{S} and can be approximated as follows:

$$\lambda = \frac{\partial R}{\partial T_{\mathrm{S}}} = \sum_{\mathrm{X}} \frac{\partial R}{\partial X}\frac{\partial X}{\partial T_{\mathrm{S}}} + \phi(\partial^2) \approx \sum_{\mathrm{X}} \lambda_{\mathrm{X}} = \sum_{\mathrm{X}} \frac{\partial R}{\partial X}\frac{\partial X}{\partial T_{\mathrm{S}}}, \tag{2}$$

with indicated interactions between different feedbacks $\phi(\partial^2)$ and individual feedback parameters λ_X (Klocke, Quaas, and Stevens 2013). The new equilibrium is reached when $\Delta R = 0$, with ΔT_S for the equilibrium state is referred to as equilibrium climate sensitivity (ECS). In the following study particularly the surface albedo, Planck, lapse-rate and water vapor feedback are analyzed to determine potential biases between the PRP and kernel method.

Surface albedo The albedo of a specific surface is generally defined as its fraction of incoming radiation, reflected by the surface. It strongly depends on land use, snow cover or ice shield thickness and extent. Those soil and water surface properties are coupled to atmospheric and oceanic dynamics due to latent heat or freshwater transports. A change in the outgoing surface radiation and, thus a change in surface albedo, occurs by transformation of the surface properties. Apart from changes in land use, this is mostly associated with changes in snow cover and ice shield thickness in the high latitudes, due to temperature changes. Surface properties can vary on a locally small scale, making the parametrization of the surface albedo a challenging factor within GCMs (Bony et al. 2006). The surface albedo feedback is considered to be the weakest one compared to the others listed below, with a model mean of $0.3 \pm 0.1\,\mathrm{W\,m^{-2}\,K^{-1}}$, estimated by the IPCC AR5 (Flato et al. 2013). It is a positive feedback, leading to rising surface temperature, due to increased CO_2 concentration (Cess et al. 1991; Randall et al. 1994) and hence intensifies polar amplification (Bony et al. 2006).

Planck The Planck feedback is a component of the temperature feedback and often referred to as 'zero feedback', since it represents the earth's LW emission to space only depending on T_S. The earth's emission can be described using the Planck blackbody radiation law where $R = \varepsilon\sigma T_S^4$ with emissivity ε and the Stefan-Boltzmann constant σ. Using this formulation, the Planck feedback parameter for the global mean surface temperature of 288 K can be obtained by $\lambda_{PL} = -4\varepsilon\sigma T_S^3 = -3.4\,\mathrm{W\,m^{-2}\,K^{-1}}$. It follows that for an increase in incoming radiation of $1\,\mathrm{W\,m^{-2}}$, the surface temperature increases by 0.294 K. For the multi-model mean of the IPCC AR5 the Planck feedback was estimated as $3.2 \pm 0.1\,\mathrm{W\,m^{-2}\,K^{-1}}$ (Flato et al. 2013). It is the strongest negative feedback reducing the effect of global warming.

Lapse-rate The lapse-rate describes the negative temperature change with altitude. It strongly affects the LW emission of the earth's atmosphere. The lapse-rate in tropical regions can be approximated by the moist adiabatic profile, since it is driven by convective processes (Boucher et al. 2013). In those regions, rising saturated air parcels condensate and release latent heat, which is partly compensated by adiabatic cooling. This leads to a small change of temperature with altitude, less energy absorption within the atmosphere and thus a strongly negative lapse-rate feedback. In extra tropical regions (or areas of sinking motion) the lapse-rate change is harder to approximate (Boucher et al. 2013), also because of larger temperature decrease with altitude. Hence, more energy is absorbed within the atmosphere compared to the Tropics, leading to a positive lapse-rate feedback resulting in an amplification of the greenhouse effect. The IPCC AR5 multi-model mean of the global lapse-rate feedback is $-0.6 \pm 0.4\,\mathrm{W\,m^{-2}\,K^{-1}}$, thus it is dominated by the tropical responses and reduces the effect of global warming due to increased CO_2 emission (Flato et al. 2013).

Water vapor The water vapor feedback estimated by the IPCC AR5 multi model mean to $1.6 \pm 0.3\,\mathrm{W\,m^{-2}\,K^{-1}}$ is the strongest positive climate feedback (Flato et al. 2013). In-

creased CO_2 emission enhances the earth's greenhouse effect, and thus global warming. Consequently, rising temperatures increase specific humidity and the ability of water uptake within the atmosphere. This physical process is based on the Clausius-Clapeyron equation which relates the saturation vapor pressure to temperature for fixed relative humidity. If constant relative humidity is supposed, it is assumed that changes in relative humidity are much smaller than changes in the saturation mixing ratio for water vapor. Therefore, changes in the specific humidity are predominantly driven by changing saturation water vapor mixing ratio (Boucher et al. 2013). For example, the saturation mixing ratio for water vapor increases almost exponentially with temperature depending on altitude with 6 to $10\,\%\,K^{-1}$ close to the surface and up to $17\,\%\,K^{-1}$ in higher altitudes (Boucher et al. 2013). An increased amount of water vapor in the earth's atmosphere, means an increased greenhouse gas concentration and consequently rising temperature.

2.2 Data

The Coupled Model Intercomparison Project (CMIP) is a collection of experimental data generated by different global climate models in a standardized format. The current phase 6 contains the Diagnostic, Evaluation and Characterization of Klima (DECK) experiments and the CMIP historical simulations, whereby the DECK experiments are done using specific forcings, boundary conditions, initialization procedures, minimum length of runs and provide a baseline for performing many of the CMIP6 experiments (Eyring et al. 2016). The selected model MPI-ESM-LR is a combination of the atmospheric general circulation model ECHAM6 (Stevens et al. 2013), the land model JSBACH (Reick et al. 2013) and the ocean general circulation model MPIOM (Jungclaus et al. 2013) including the model for marine biogeochemistry HAMOCC (Ilyina et al. 2013) in low resolution (LR). Compared to ECHAM5, ECHAM6 provides a new radiation scheme and albedo calculation, in which the short-wave (SW) scheme has been replaced by the SW rapid radiation transfer model GCMs depending on solar zenith angle over open water, melt points on sea ice and snow cover (Roeckner et al. 2012). The horizontal resolution of the used ECHAM6 is T63/1.9 ° and it is vertically divided in 47 hybrid sigma pressure levels. The multi-century Pre-Industrial Control simulation (*piControl*), a coupled atmosphere- and ocean circulation DECK experiment, is used as a control run. The CO_2 concentration is prescribed and the minimum period of calculation is 500 years, starting from 1850, representing the conditions before the industrial revolution. The abruptly quadrupling CO_2 simulation (*abrupt4xCO_2*) is used as the perturbed run. It is developed to characterize the climate system's response to greenhouse gas forcing and also part of the DECK experiments in CMIP6 (Eyring et al. 2016). Therefore, only the CO_2 concentration is abruptly quadrupled in 1850 compared to the *piControl* simulation and then held constant, while all other parameters stay the same as in the control run. Preprocessing of the CMIP6 data was done by calculating the monthly averages of the daily data associated with cloud forcing (CFday) and combining them with the remaining required variables from monthly atmospheric data (Amon) and monthly atmospheric chemistry and aerosol data (AERmon) in one data file, including a land-sea mask, a glacier mask, surface pressure and geopotential data.

3 Partial radiative perturbation method

The partial radiative perturbation PRP method is based on the assumption that the TOA radiation R can be calculated depending on several atmospheric variables that have a significant feedback on the earth's energy budget such as water vapor WV, temperature T, surface albedo A and cloud properties CL, leading to $R = R(WV,T,CL,A)$ (Wetherald and Manabe 1988). The TOA radiation is calculated in two directions using the ECHAM6 standalone radiation model developed by the Max Planck Institute for Meteorology (MPI-M) in Hamburg and the Deutsche Wetterdienst (DWD) in Germany. To derive the TOA radiative imbalance ΔR, R is calculated for two different climate states, a control climate simulation ($piControl$) and a perturbed climate state ($abrupt4x\mathrm{CO}_2$). For the forward direction R is calculated using all variables, except the one of interest from the control run. The variable of interest is instead taken from the perturbed run. For example the difference in TOA radiation for water vapor can be written as $\delta R_{\mathrm{WV_{fwrd}}} = R(WV_{\mathrm{pert}}, T_{\mathrm{ctrl}}, CL_{\mathrm{ctrl}}, A_{\mathrm{ctrl}}) - R(WV_{\mathrm{ctrl}}, T_{\mathrm{ctrl}}, CL_{\mathrm{ctrl}}, A_{\mathrm{ctrl}})$. Likewise, the backward PRP TOA radiation can be obtained by using only the variable of interest from the control run and the remaining variables from the perturbed run leading to $\delta R_{\mathrm{WV_{bwrd}}} = R(WV_{\mathrm{ctrl}}, T_{\mathrm{pert}}, CL_{\mathrm{pert}}, A_{\mathrm{pert}}) - R(wv_{\mathrm{pert}}, T_{\mathrm{pert}}, CL_{\mathrm{pert}}, A_{\mathrm{pert}})$ for water vapor. To minimize biases due to the assumption of temporal uncorrelation between all fields, the TOA radiation is averaged over both directions (forward and backward) leading to the two-sided PRP results (Eq. 3) (Colman and McAvaney 1997; B. Soden, Broccoli, and Hemler 2004).

$$\delta R_{\mathrm{X_{2sides}}} = \frac{\delta R_{\mathrm{X_{fwrd}}} - \delta R_{\mathrm{X_{bwrd}}}}{2}. \tag{3}$$

With $\overline{\Delta T_{\mathrm{S}}}$, the temporally and spatially averaged surface temperature change between both runs λ_{X} can be estimated as:

$$\lambda_{\mathrm{X}} = \frac{\partial R}{\partial X}\frac{\partial X}{\partial T_{\mathrm{S}}} \approx \frac{\delta R_{\mathrm{X}}}{\delta X}\frac{\delta X}{\overline{\Delta T_{\mathrm{S}}}}, \tag{4}$$

With $\overline{\Delta T_{\mathrm{S}}} = \langle T_{\mathrm{S_{4xCO2}}}(x,y,t) - T_{\mathrm{S_{piCrtl}}}(x,y,t)\rangle = 4.65\,\mathrm{K}$. The PRP method has the advantage of estimating the responses of specific variables on the TOA radiative imbalance leading to straightforward interpretable results. However, this method is highly computational expensive, since it requires a large amount of processing and memory capacity (B. Soden, Broccoli, and Hemler 2004; Block and Mauritsen 2013).

4 Radiative kernel method

Radiative kernels are implemented comparably to the PRP method. Instead of taking the relevant variable from the perturbed climate simulation, only an incremental change of the variable is implemented, depending on the direction of the radiative flux calculation (Held and Brian Soden 2000; Brian Soden and Held 2006). The radiative kernels K_{X} are defined as:

$$K_{\mathrm{X}} = \frac{\partial R_{\mathrm{X}}(x,y)}{\partial X} \approx \frac{\delta R_{\mathrm{X}}(x,y)}{\delta X}, \tag{5}$$

Whereby $\delta R_{\mathrm{X}} = R(X+\delta X, Y) - R(X,Y)$, depending on the incremental change in the variable of interest δX. For the water vapor kernel the amount of water vapor corresponding to a positive temperature change of 1 K is used to perturb the specific humidity of the control climate state and the amount of water vapor corresponding to a negative temperature change of 1 K is used to perturb the specific humidity of the perturbed climate state (B. J. Soden et al. 2008; Klocke, Quaas, and Stevens 2013). The surface albedo kernel is calculated using a change of 1% in the surface albedo, and the temperature kernels are computed by changing the Temperature by 1 K (B. J. Soden et al. 2008; Klocke, Quaas, and Stevens 2013). The different feedback parameters can then be calculated by multiplying the kernel with ΔX and dividing by $\overline{\Delta T_{\mathrm{S}}}$ (Sec. 3):

$$\lambda_{\mathrm{X}} = \frac{\overline{\delta R_{\mathrm{X}}(x,y)}}{\overline{\Delta T_S}} = \frac{\overline{K_{\mathrm{X}}(x,y)\cdot\Delta X(x,y)}}{\overline{\Delta T_S}}, \tag{6}$$

with $\Delta X(x,y,z,t) = X_{\mathrm{4xCO2}}(x,y,z,t) - X_{\mathrm{piCrtl}}(x,y,z,t)$, representing the respective change in X between the perturbed and control climate. Vertical resolved variables (e.g. water vapor or temperature) need to be perturbed in each altitude level and the results are vertically integrated, which is done by summing over the model levels:

$$\delta R_{\mathrm{X}}(x,y,z,t) = \sum_z \frac{\delta R_{\mathrm{X}}(x,y,z,t)}{\delta X(x,y,z,t)} \cdot \Delta X(x,y,z,t) = \sum_z K_{\mathrm{X}}(x,y,z,t)\cdot\Delta X(x,y,z,t). \tag{7}$$

In the case of temperature, this is done only within the troposphere, to mask out the effect of stratospheric adjustment (Tomassini et al. 2013). The pressure at tropopause level depending on latitude *lat* was approximated as $p(z_{\mathrm{trop}}) = 100\,\mathrm{hPa} + 200\,\mathrm{hPa}\cdot|lat|\cdot 90^{\circ -1}$.

5 Results and discussion

In the following chapter, the results of the feedback determination using the PRP and kernel method are presented, discussed and compared to former studies (tab. 1). First, the results of the differently performed temporal averages are analyzed to justify the application of a multiyear monthly average mean dataset. Backward calculations for the PRP as well as the kernel method are generally multiplied with -1 to make them comparable to calculations in forward direction. Fig. 1 shows the feedback factor results obtained for yearly data of monthly averages λ_{PRP} (green) and the multiyear monthly averages over 39 years $\lambda_{PRP_{39yrs}}$ (orange). The zonal distributions are similar and the largest differences can be obtained for the water vapor feedback with $\Delta\lambda_{\mathrm{2sides}} \approx 0.022\,\mathrm{W\,m^{-2}\,K^{-1}}$ (fig. 1d). Since the found differences are assumed to be small compared to the feedback factor results, the simplification was applied and the kernels were calculated using multiyear monthly averages.

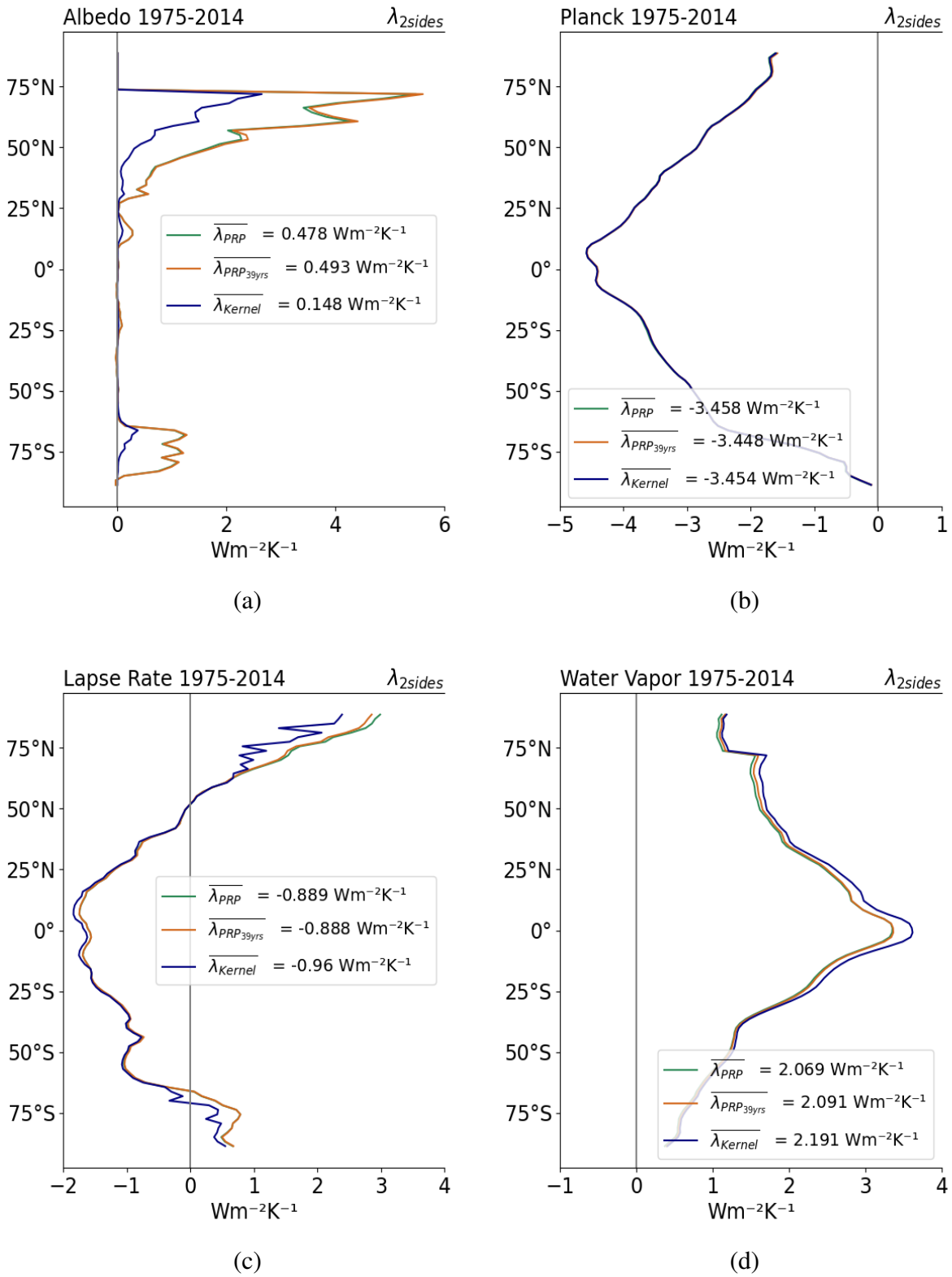

Figure 1: *Zonal averages of the individual feedback parameters for each year (green) and multiyear monthly averages (orange) using the PRP method and the results of the kernel method (blue), based on multiyear monthly averages. Including the surface albedo (a), Planck (b), lapse-rate (c) and water vapor (d) feedback in* $\mathrm{W\,m^{-2}\,K^{-1}}$ *based on multiyear monthly averages.*

Table. 1: *Comparison of resulting feedback parameters in* $\mathrm{W\,m^{-2}\,K^{-1}}$ *for the PRP and kernel method based on CMIP6 data and the MPI-ESM-LR model. Additionally, values of former studies of Klocke, Quaas, and Stevens (2013) based on ECHAM5 data, Rieger, Dietmüller, and Ponater (2017) and the IPCC AR5 kernel results for CMIP5 data and the MPI-ESM-LR model (Flato et al. 2013).*

Method	Direction	λ_A	λ_{PL}	λ_{LR}	λ_{WV}	$\sum\lambda$
PRP	forward	0.51	-3.693	-0.894	2.089	-1.988
	backward	0.475	-3.203	-0.882	2.092	-1.518
	two-sided	0.493	-3.448	-0.888	2.091	-1.752
Kernel	forward	0.199	-3.368	-0.804	1.701	-2.272
	backward	0.096	-3.541	-1.116	2.681	-1.88
	two-sided	0.148	-3.454	-0.96	2.191	-2.075
PRP Klocke et al. (2013)	forward	0.22	-3.23	-0.61	1.76	-1.86
	backward	0.16	-3.17	-0.23	1.79	-1.45
	two-sided	0.19	-3.23	-0.42	1.78	-1.68
Kernel Klocke et al. (2013)	forward	0.17	-3.08	-0.68	2.08	-1.51
PRP Rieger et al. (2017)	two-sided	0.23	-3.11	-0.86	2.01	-1.73
Kernel IPCC AR5 (2013)	forward	0.3	-3.3	-0.9	1.8	-2.1

5.0.1 Surface albedo feedback

The results of the 39-year average albedo feedback parameter (λ_A) calculations are shown as global distributions and zonal averages in fig. 1a and fig. 2. For both methods λ_A in units of $\mathrm{W\,m^{-2}\,K^{-1}}$ reaches its maximum value over land and sea ice in the polar regions. In lower latitudes and oceanic regions λ_A is close to zero. For the PRP method the forward calculation λ_{fwrd} with global averages of $0.51\,\mathrm{W\,m^{-2}\,K^{-1}}$ is slightly larger than the backward calculation λ_{bwrd} with $0.475\,\mathrm{W\,m^{-2}\,K^{-1}}$ (tab. 1). The two-sided PRP method yields a total albedo feedback of $0.493\,\mathrm{W\,m^{-2}\,K^{-1}}$. Forward and backward runs agree well. The kernel method with increased surface albedo of 1 % in the control run leads to a global average feedback parameter λ_{fwrd} of $0.199\,\mathrm{W\,m^{-2}\,K^{-1}}$. For decreased of surface albedo in the perturbed run, λ_{bwrd} is $0.096\,\mathrm{W\,m^{-2}\,K^{-1}}$, leading to a global average λ_{2sides} of $0.148\,\mathrm{W\,m^{-2}\,K^{-1}}$, which is displayed in fig. 5b. Comparing both methods as in fig. 1a, stronger results are retrieved with the PRP method than with the kernel approach. The kernel results are within the range of former studies, as listed in tab. 1, while the PRP results are larger than the outcomes of for example Klocke, Quaas, and Stevens 2013 and Rieger, Dietmüller, and Ponater 2017. Those disagreements could be due to differences in ECHAM6 compared to ECHAM5, used by Klocke, Quaas, and

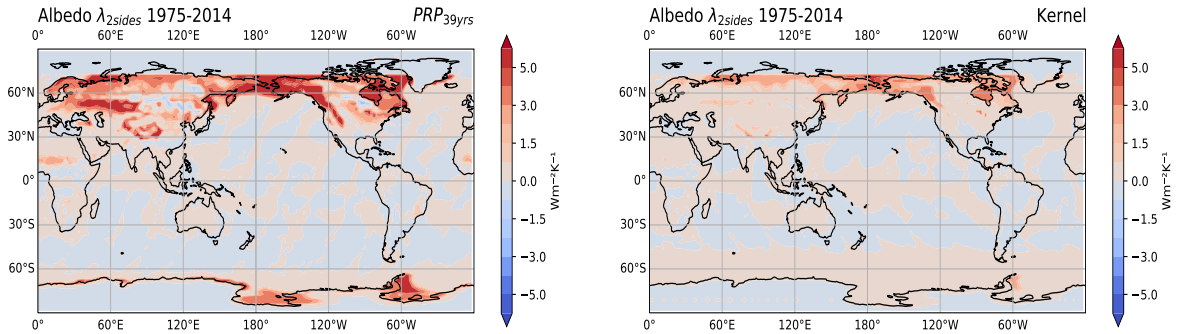

(a) (b)

Figure 2: *Comparison of the surface albedo feedback factor* λ_A *in* $\mathrm{W\,m^{-2}\,K^{-1}}$ *calculated using the PRP method (a) and the Kernel method (b). Spatially resolved as global distributions and based on multiyear monthly averages.*

Stevens 2013. Stevens et al. (2013) point out that in the radiation scheme of ECHAM6, the couplings between melt ponds and sea ice are not properly implemented, leading to and error dampening the effect of melt ponds. This artificially downsizes the surface albedo feedback. The results of Rieger, Dietmüller, and Ponater (2017) based on ECHAM6 data and the ECHAM6 radiation module retrieved a two-sided surface albedo feedback of $0.23\,\mathrm{W\,m^{-2}\,K^{-1}}$, which is closer to the feedback obtained in this study. The IPCC AR5 presents a surface albedo feedback of $0.3\,\mathrm{W\,m^{-2}\,K^{-1}}$ for a forward kernel calculation based on MPI-ESM-LR data, which is larger than the forward kernel results in this work ($0.199\,\mathrm{W\,m^{-2}\,K^{-1}}$). The same can be stated for the results of Block and Mauritsen (2013) with $0.48 \pm 0.03\,\mathrm{W\,m^{-2}\,K^{-1}}$. This leads to the assumption that the kernel method in this study generally underestimates the surface albedo feedback, which could be due to its high local variability or the implementation bug in the ECHAM6 radiation module, as described in Stevens et al. (2013), which strengthening the underestimation of the surface albedo feedback. The kernel method uses additionally a stronger linearization than the PRP method, assuming a linear change of the surface albedo with ΔT_S by 1%. Since the surface albedo depends on several factors, such as geometric pattern of the snow surface, solar zenith angle or snow characteristics, its change is strongly non-linear (Pirazzini 2004). Small changes in surface temperature around the freezing point of water can lead to huge differences in albedo, while changes beyond this range won't cause such great difference. Difficulties in the parametrization of small scale differences in the surface properties as described in Sec. 2.1, causing large model differences lead to an uncertainty in the magnitude of the surface albedo feedback. Nevertheless, studies agree in its positive sign (Bony et al. 2006), which is also observed in this study.

5.0.2 Planck feedback

Fig. 3 shows the global distribution of the Planck feedback parameter λ_{PL} and fig. 1b the zonal averages resulting from both methods. The two-sided PRP result λ_{2sides} is $-3.448\,\mathrm{W\,m^{-2}\,K^{-1}}$ with $\lambda_{fwrd} = -3.693\,\mathrm{W\,m^{-2}\,K^{-1}}$ and $\lambda_{bwrd} = -3.203\,\mathrm{W\,m^{-2}\,K^{-1}}$ (tab. 1). The kernel method yields a λ_{2sides} of $-3.454\,\mathrm{W\,m^{-2}\,K^{-1}}$.

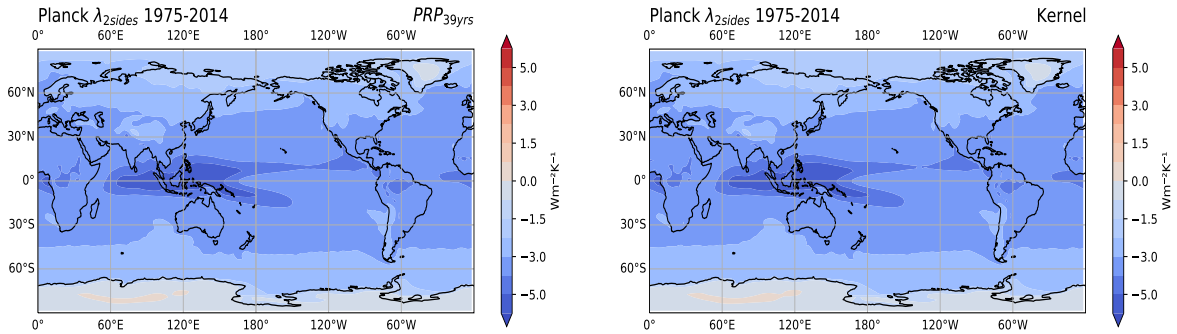

(a) (b)

Figure 3: *Comparison of the Planck feedback factor* λ_P *in* $\mathrm{W\,m^{-2}\,K^{-1}}$ *calculated using the PRP method (a) and the Kernel method (b). Spatially resolved as global distributions and based on multiyear monthly averages.*

The forward calculation, with an incremental increase of 1 K in the control run, gives slightly weaker results of $-3.368\,\mathrm{W\,m^{-2}\,K^{-1}}$ than the backward calculation, with a decrease of 1 K in the perturbed run $-3.541\,\mathrm{W\,m^{-2}\,K^{-1}}$ (tab. 1). The global distributions agree well with smallest values at the low latitudes where the surface temperature is lowest (fig. 3a and 3b). Comparing the two-sided PRP results to the results of Klocke, Quaas, and Stevens (2013) with $-3.23\,\mathrm{W\,m^{-2}\,K^{-1}}$ and Rieger, Dietmüller, and Ponater (2017) with $-3.11\,\mathrm{W\,m^{-2}\,K^{-1}}$, both show slightly weaker values for the Planck feedback. The same can be observed for the forward kernel results. The IPCC AR5 estimates the Planck feedback to $-3.3\,\mathrm{W\,m^{-2}\,K^{-1}}$ and Klocke, Quaas, and Stevens (2013) to $-3.08\,\mathrm{W\,m^{-2}\,K^{-1}}$. Although the results of the Planck feedback calculated using the PRP and kernel technique are slightly stronger than the Planck feedback estimated in former studies, they agree well with each other and the Planck feedback according to the Stefan-Boltzmann law. It is confirmed that the Planck feedback is the strongest negative feedback. Hence, it contributes significantly to LW cooling.

5.0.3 Lapse-rate feedback

Fig. 4 displays the global distribution of the lapse-rate feedback λ_{LR}. The geographical distributions of the Kernel and PRP calculations are generally similar and show minimal values for low latitudes and maximal values for high latitudes ranging from $-2.0\,\mathrm{W\,m^{-2}\,K^{-1}}$ to $4.0\,\mathrm{W\,m^{-2}\,K^{-1}}$ for the PRP method (fig. 4a) and $-2.0\,\mathrm{W\,m^{-2}\,K^{-1}}$ to $3.0\,\mathrm{W\,m^{-2}\,K^{-1}}$ for the kernel method (fig. 4b) with minimal values around Greenland. The zonal average for the forward PRP λ_{fwrd} of $-0.894\,\mathrm{W\,m^{-2}\,K^{-1}}$ is slightly larger than the average for the backward PRP λ_{bwrd} of $-0.882\,\mathrm{W\,m^{-2}\,K^{-1}}$ leading to the two-side PRP average $\lambda_{2\mathrm{sides}}$ of $-0.888\,\mathrm{W\,m^{-2}\,K^{-1}}$ as listed in tab. 1 . λ_{fwrd} for the temperature kernel with increased air temperature by 1 K gives an lapse-rate feedback of $-0.804\,\mathrm{W\,m^{-2}\,K^{-1}}$ and $-1.116\,\mathrm{W\,m^{-2}\,K^{-1}}$ for the perturbed climate state λ_{bwrd} with decreased T_{air} by 1 K. This yields to $\lambda_{2\mathrm{sides}}$ of $-0.96\,\mathrm{W\,m^{-2}\,K^{-1}}$. The comparison of both method results (fig. 1c) shows higher absolute values of the PRP technique compared to the kernel technique.

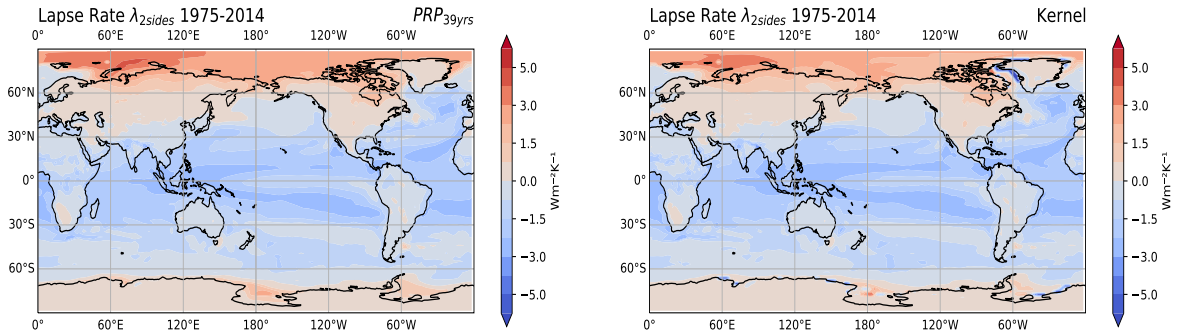

(a) (b)

Figure 4: *Comparison of the lapse-rate feedback factor* λ_{LR} *in* $\mathrm{W\,m^{-2}\,K^{-1}}$ *calculated using the PRP method (a) and the Kernel method (b). Spatially resolved as global distributions and based on multiyear monthly averages.*

The strongest variability is found in the polar regions using the kernel technique, leading to the assumption of more complex processes in those areas. Positive values of λ_{LR}, as observed in the extratropics (or areas of sinking motion) amplify the effect of global warming, due to an increased greenhouse effect (Held and Brian Soden 2000). Negative values of λ_{LR}, as observed in the Tropics, indicate a stronger decrease of temperature with height resulting in an increased LW emission back to space. The global average indicates a stronger tropical response than extra-tropical response, resulting in an overall negative lapse-rate feedback. Although the results of the PRP and kernel technique in this study agree well, there are slight differences to Klocke, Quaas, and Stevens (2013) with results of with $-0.42\,\mathrm{W\,m^{-2}\,K^{-1}}$ (tab. 1). A good agreement can be found for the PRP results of Rieger, Dietmüller, and Ponater (2017), who estimated $\lambda_{2\mathrm{sides}}$ to $-0.86\,\mathrm{W\,m^{-2}\,K^{-1}}$. Since Rieger, Dietmüller, and Ponater (2017) used the same dataset as in this study, this finding is not unexpected. For the forward kernel, the difference between Klocke, Quaas, and Stevens (2013) with an lapse-rate feedback parameter of $-0.68\,\mathrm{W\,m^{-2}\,K^{-1}}$ and this work with $-0.804\,\mathrm{W\,m^{-2}\,K^{-1}}$ is lower and comparable to the results of the IPCC AR5 with $-0.90\,\mathrm{W\,m^{-2}\,K^{-1}}$. Overall, the lapse-rate feedback compared to former studies using the same dataset, is slightly weaker for the kernel method and slightly stronger for the PRP method (tab. 1). The difference between both methods is largest in the high latitudes with stronger kernel results. This could be due to differences in surface warming and stronger coupling between the surface and free troposphere in the low latitudes compared to the high latitudes (Brian Soden and Held 2006). Since the temperature change with altitude within the troposphere can be approximated by $6.5\,\mathrm{K\,km^{-1}}$ (Held and Brian Soden 2000), a linearization is reasonable within the Tropics but needs further investigation for the extra Tropics.

5.0.4 Water vapor feedback

The water vapor feedback is displayed in fig. 5 with consistently positive values. The PRP and kernel global distribution do not differ much and have their maximum values in the equatorial region declining towards the poles, with minimal values in the Southern Hemisphere. The forward PRP yields to a feedback parameter of $2.089\,\mathrm{W\,m^{-2}\,K^{-1}}$ and

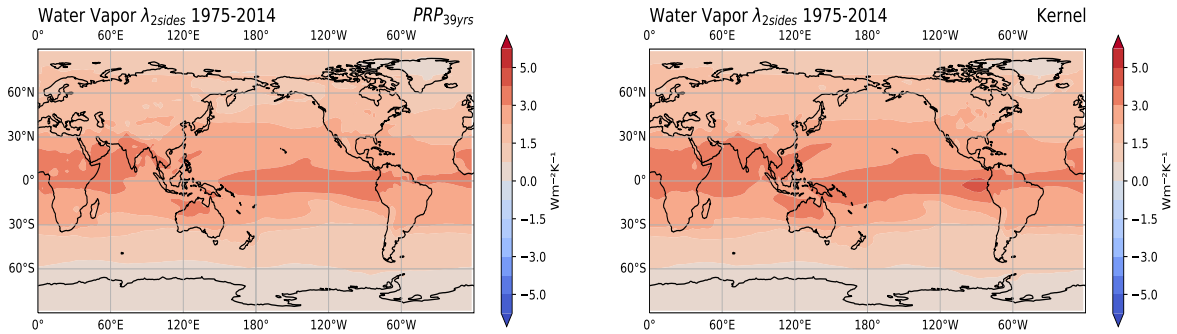

(a) (b)

Figure 5: *Comparison of the water vapor feedback factor* λ_{LR} *in* $\mathrm{W\,m^{-2}\,K^{-1}}$ *calculated using the PRP method (a) and the Kernel method (b). Spatially resolved as global distributions and based on multiyear monthly averages.*

the backward PRP to $2.092\,\mathrm{W\,m^{-2}\,K^{-1}}$ resulting in the two-sided PRP of $2.091\,\mathrm{W\,m^{-2}\,K^{-1}}$ (tab. 1). For the kernel method, the forward calculation, for which the specific humidity was increased by the amount corresponding to 1 K warming, differ more than the backward calculation, with decreased specific humidity corresponding to 1 K cooling. The global average for λ_{fwrd} gives $1.701\,\mathrm{W\,m^{-2}\,K^{-1}}$ and for λ_{bwrd} $2.681\,\mathrm{W\,m^{-2}\,K^{-1}}$, resulting in a two-sides kernel feedback parameter $\lambda_{2\mathrm{sides}}$ of $2.191\,\mathrm{W\,m^{-2}\,K^{-1}}$ (tab. 1). Since $\lambda_{2\mathrm{sides}}$ of the kernel method is similar to the PRP $\lambda_{2\mathrm{sides}}$ the decorrelation between both climate states by averaging over both directions seems reasonable. The current IPCC AR5 estimates the water vapor feedback factor to $1.8\,\mathrm{W\,m^{-2}\,K^{-1}}$ and Block and Mauritsen (2013) to $1.79 \pm 0.08\,\mathrm{W\,m^{-2}\,K^{-1}}$ for the MPI-ESM-LR and the forward kernel. These values are close to the forward kernel estimated in this study with $1.701\,\mathrm{W\,m^{-2}\,K^{-1}}$. The PRP results are within the same range as Rieger, Dietmüller, and Ponater (2017), as seen in tab. 1, but stronger than the results of Klocke, Quaas, and Stevens (2013). The water vapor feedback is the second strongest feedback. Furthermore, based on the Clausius-Clapeyron equation, the water vapor feedback is driven by changes in the saturation vapor pressure depending on temperature. An increase in global CO_2 concentration leads to rising global mean temperature, which in turn, enhances the ability of the atmosphere to take up water vapor. Since water vapor is a trace gas, more solar radiation is absorbed and the greenhouse effect is enhanced (Flato et al. 2013). Changes in specific humidity can be approximated by the change of saturation vapor pressure if relative humidity stays constant (Boucher et al. 2013). This yields to an exponential relationship between specific humidity and T_{S} according to the Clausius-Clapeyron relation. Even though the relation between surface temperature change and specific humidity change is not exactly linear, both linearizations (kernel and PRP) give reasonable results, compared to each other and to former studies.

6 Conclusion

Within this study, the determination of radiation couplings in climate change simulations has been analyzed using the PRP and kernel method based on MPI-ESM-LR data. The

results of the surface albedo, Planck, lapse-rate and water vapor feedback are within the range of previous studies and, hence, provide an example for the potential linearization of the feedback quantification. They also provide a general overview of regions strongly affected by an increased global CO_2 concentration. Furthermore, the effect of differently performed temporal averages has been investigated. It was found that the feedback factors calculated using a multiyear mean show only minimal differences to the results based on yearly data. This achievement provides the possibility to minimize computational expense. The strongest disagreement between both methods can be observed for the surface albedo feedback which is positive and the weakest among feedbacks (tab. 1). Since the surface albedo change is a strongly nonlinear process, especially in the temperature range of 260 K to 293 K in which the transition from ice covered surface to water takes place, the kernel technique generally underestimates the effect of the surface albedo feedback. This leads to less reliable model results compared to the more complex calculations of the PRP method. Regarding the Planck feedback, the strongest negative feedback, both methods agree well. It is slightly larger compared to former studies but corresponds to the Planck feedback of $-3.4\,\mathrm{W\,m^{-2}\,K^{-1}}$ for a global mean surface temperature of 288 K estimated from the Stefan-Boltzmann law. The lapse-rate feedback, which is on average negative, shows a fluctuation in polar regions using the kernel method. Apart from those, the PRP and kernel method results agree well and correspond to the IPCC AR5 results. It contributes to weakening of surface warming due to increased global CO_2 concentration. Both water vapor feedback results agree well with former studies. It is the strongest positive feedback, contributing to a temperature increase due to the strong greenhouse effect of water vapor. Despite the non-linear relationship between specific humidity and surface temperature, both methods give similar results and, thus, they are acceptable tools to determine the water vapor feedback. The disagreements between the forward and backward calculations for both methods are mostly compensated by the two-sided average. Thus, the application of both directions to minimize biases due to correlation within fields are found to be reasonable also for the kernel method. Once the kernels are calculated, they can be utilized for different climate perturbations without renewed radiative transfer calculations. This is a clear advantage of the kernel method. However, this advantage may compromise accuracy, as observed for the surface albedo and the lapse-rate feedback in polar regions. Decreasing computational effort due to the usage of multiyear monthly averages is possible. To receive more reliable results, the implementation bug in radiation scheme of ECHAM6 reported by (Stevens et al. 2013) needs to be corrected. Also, Polar regions must be given special attention, due to several complex coupling processes affecting the lapse-rate feedback. To confirm the results of this study further investigations are needed.

References

Block, K. and T. Mauritsen (2013). "Forcing and feedback in the MPI-ESM-LR coupled model under abruptly quadrupled CO2". In: *Journal of Advances in Modeling Earth Systems* 5, pp. 676–691. DOI: https://doi.org/10.1002/jame.20041.

Bony, Sandrine et al. (2006). "How Well Do We Understand and Evaluate Climate Change Feedback Processes?" In: *Journal of Climate* 19, pp. 3445–3482. DOI: 10.1175/JCLI3819.1.

Boucher, O. et al. (2013). "Clouds and Aerosols". In: *Climate Change 2013: The Physical Science Basis. Contribution of Working Group I to the Fifth Assessment Report of the Intergovernmental Panel on*

Climate Change. Ed. by T.F. Stocker et al., pp. 571–658. DOI: 10.1017/CBO9781107415324.016.

Cess, Robert et al. (1991). "Interpretation of Snow-Climate Feedback as Produced by 17 General Circulation Models". In: *Science (New York, N.Y.)* 253, pp. 888–92. DOI: 10.1126/science.253.5022.888.

Colman, R. A. and B. J. McAvaney (1997). "A study of general circulation model climate feedbacks determined from perturbed sea surface temperature experiments". In: *Journal of Geophysical Research: Atmospheres* 102, pp. 19383–19402. DOI: 10.1029/97JD00206.

Eyring, Veronika et al. (2016). "Overview of the Coupled Model Intercomparison Project Phase 6 (CMIP6) experimental design and organization". In: *Geoscientific Model Development* 9, pp. 1937–1958. DOI: 10.5194/gmd-9-1937-2016.

Flato, G. et al. (2013). "Evaluation of Climate Models". In: *Climate Change 2013: The Physical Science Basis. Contribution of Working Group I to the Fifth Assessment Report of the Intergovernmental Panel on Climate Change*. Ed. by T.F. Stocker et al., pp. 741–866. DOI: 10.1017/CBO9781107415324.020.

Held, Isaac and Brian Soden (2000). "Water Vapor Feedback and Global Warming". In: *Annual Review of Energy and The Environment* 25, pp. 441–475. DOI: 10.1146/annurev.energy.25.1.441.

Ilyina, Tatiana et al. (2013). "Global ocean biogeochemistry model HAMOCC: Model architecture and performance as component of the MPI-Earth system model in different CMIP5 experimental realizations". In: *Journal of Advances in Modeling Earth Systems* 5, pp. 287–315. DOI: 10.1029/2012MS000178.

Jungclaus, J. et al. (2013). "Characteristics of the ocean simulations in the Max Planck Institute Ocean Model (MPIOM) the ocean component of the MPI-Earth system model". In: *Journal of Advances in Modeling Earth Systems* 5. DOI: 10.1002/jame.20023.

Klocke, Daniel, Johannes Quaas, and Bjorn Stevens (2013). "Assessment of different metrics for physical climate feedback". In: *Climate Dynamics* 41. DOI: 10.1007/s00382-013-1757-1.

Pirazzini, Roberta (2004). "Surface albedo measurements over Antarctic sites in summer". In: *Journal of Geophysical Research: Atmospheres* 109. DOI: https://doi.org/10.1029/2004JD004617.

Randall, D. et al. (1994). "Analysis of snow feedbacks in 14 general circulation models". In: *Journal of Geophysical Research* 99, pp. 20757–. DOI: 10.1029/94JD01633.

Reick, C. et al. (2013). "Representation of natural and anthropogenic land cover change in MPI-ESM". In: *Journal of Advances in Modeling Earth Systems* 5. DOI: 10.1002/jame.20022.

Rieger, V.S., S. Dietmüller, and M. Ponater (2017). "Can feedback analysis be used to uncover the physical origin of climate sensitivity and efficacy differences?" In: *Climate Dynamics*. DOI: 10.1007/s00382-016-3476-x.

Roeckner, Erich et al. (2012). "Impact of melt ponds on Arctic sea ice in past and future climates by MPI-ESM". In: *Journal of Advances in Modeling Earth Systems* 4. DOI: 10.1029/2012MS000157.

Soden, B., A. Broccoli, and R. Hemler (2004). "On the Use of Cloud Forcing to Estimate Cloud Feedback". In: *Journal of Climate* 17. DOI: 10.1175/1520-0442(2004)017<3661:OTUOCF>2.0.CO;2.

Soden, Brian and Isaac Held (2006). "An Assessment of Climate Feedbacks in Coupled Ocean–Atmosphere Models". In: *Journal of Climate* 19. DOI: 10.1175/JCLI3799.1.

Soden, Brian J. et al. (2008). "Quantifying Climate Feedbacks Using Radiative Kernels". In: *Journal of Climate* 21, pp. 3504–3520. DOI: 10.1175/2007JCLI2110.1.

Stevens, Bjorn et al. (2013). "Atmospheric component of the MPI-M Earth System Model: ECHAM6". In: *Journal of Advances in Modeling Earth Systems* 5, pp. 146–172. DOI: 10.1002/jame.20015.

Thorsen, Tyler J. et al. (2018). "Observation-Based Decomposition of Radiative Perturbations and Radiative Kernels". In: *Journal of Climate* 31, pp. 10039–10058. DOI: 10.1175/JCLI-D-18-0045.1.

Tomassini, Lorenzo et al. (2013). "The respective roles of surface temperature driven feedbacks and tropospheric adjustment to CO2 in CMIP5 transient climate simulations". In: *Climate Dynamics* 41. DOI: 10.1007/s00382-013-1682-3.

Wetherald, R. T. and S. Manabe (1988). "Cloud Feedback Processes in a General Circulation Model". In: *Journal of Atmospheric Sciences* 45, pp. 1397–1416. DOI: 10.1175/1520-0469(1988)045<1397:CFPIAG>2.0.CO;2.

Forschungsbericht 2020
Bearbeitete Forschungsprojekte

Institut für Meteorologie

Direktor Prof. Dr. M. Wendisch

Allgemeine Meteorologie; Manfred Wendisch
AG Atmosphärische Strahlung

Koordination des Schwerpunktprogramms 1294 "Atmosphären- und Erdsystemforschung mit dem Forschungsflugzeug HALO (High Altitude and Long Range Research Aircraft)"
HALO coordination project

Schlagworte: flugzeuggetragene Forschung

Projektleiter: M. Wendisch (m.wendisch@uni-leipzig.de)
Professor Dr. Joachim Curtius, Goethe-Universität Frankfurt am Main, Institut für Atmosphäre und Umwelt

Projektmitarbeiter: Anja Schwarz, Jörg Schmidt

Projektbeginn: 2010
Projektende: 2021

Beschreibung
Das Ziel des Antrages ist die zentrale Koordination des SPP 1294 'Atmosphären- und Erdsystemforschung mit HALO' (HALO: HighAltitude and Long Range Research Aircraft, Hochfliegendes und weitreichendes Forschungsflugzeug). Das Projekt dient der Förderung der Zusammenarbeit und Kommunikation innerhalb der HALO Missionsteams und den individuellen Projektpartnern, die im SPP eingebunden sind. Die drei Koordinatoren (M. Wendisch, Universität Leipzig; J. Curtius, Universität Frankfurt am Main; M. Scheinert, Technische Universität Dresden) vertreten den SPP gegenüber der DFG, dem Wissenschaftlichen Lenkungsausschuss (WLA) für HALO, dem HALO Projektteam des Deutschen Zentrums für Luft- und Raumfahrt (DLR-FX) und der Öffentlichkeit. Der DFGAnteil an den Missionskosten wird an der Universität Leipzig zentral verwaltet. Die Finanzmittel für Maßnahmen zur Förderung der Gleichstellung werden verwaltet, und die Ausbildung der jungen Wissenschaftler wird koordiniert. Monatliche Telefonkonferenzen der drei Koordinatoren, jährlich Statusseminare und thematische Workshops werden organisiert. Spezielle Sitzungen auf internationalen Konferenzen und Veröffentlichungen von Spezialausgaben in internationalen Zeitschriften werden initiiert und befördert. Die SPP Internet-Seite wird überarbeitet, fortlaufend aktualisiert und gewartet. Um die Arbeit der Koordinatoren zu unterstützen, werden eine halbe Position eines Wissenschaftlichen Administrators und eine Stelle für einen HALO Nutzerkoordinator beantragt.

Description
The goal of this proposal is the central coordination of the SPP 1294 'Atmospheric and Earth System Research with HALO' (HALO: High Altitude and Long Range Research Aircraft). The project

serves the promotion of cooperation and communication among the HALO mission teams and the individual project participants involved in the SPP. The three coordinators (M. Wendisch, University of Leipzig; J.Curtius, University of Frankfurt am Main; M. Scheinert, Dresden University of Technology) represent the SPP at the DFG, the scientific steering committee of HALO (WLA: Wissenschaftlicher Lenkungsausschuss), the HALO project team of the German Aerospace Center (DLR-FX), and the public. The DFG share of the mission costs will be centrally administered by the University of Leipzig. The funds for measures to promote gender equality are managed, and the training of young researchers is coordinated. Monthly teleconferences of the three coordinators, annual status seminars, and topical workshops will be organized. Special sessions at international conferences and publications of special issues are initiated and pursued. The SPP web page will be revised, continuously updated, and maintained. To support the three coordinators in conducting these tasks, funding of a half-time position of a Scientific Administrator and a HALO User Coordinator is applied for.

Weiterführung: ja

Mittelgeber: DFG WE 1900/24-1, Projekt number 179953493 and Projekt number 316646266

Kampagnenantrag für die HALO-(AC)³ Mission: Arktische Luftmassentransformationen während Warmlufteinschüben und Kaltluftausbrüchen
Umbrella Proposal for the HALO-(AC)³ Mission: Arctic Air-Mass Transformations During Warm Air Intrusions and Marine Cold Air Outbreaks

Schlagworte: flugzeuggetragene Forschung

Projektleiter: M. Wendisch (m.wendisch@uni-leipzig.de)

Projektmitarbeiter: ...

Projektbeginn: 2020
Projektende: 2023

Beschreibung
Das Ziel des Antrages ist die zentrale Koordination des SPP 1294 'Atmosphären- und Erdsystemforschung mit HALO' (HALO: HighAltitude and Long Range Research Aircraft, Hochfliegendes und weitreichendes Forschungsflugzeug). Das Projekt dient der Förderung der Zusammenarbeit und Kommunikation innerhalb der HALO Missionsteams und den individuellen Projektpartnern, die im SPP eingebunden sind. Die drei Koordinatoren (M. Wendisch, Universität Leipzig; J. Curtius, Universität Frankfurt am Main; M. Scheinert, Technische Universität Dresden) vertreten den SPP gegenüber der DFG, dem Wissenschaftlichen Lenkungsausschuss (WLA) für HALO, dem HALO Projektteam des Deutschen Zentrums für Luft- und Raumfahrt (DLR-FX) und der Öffentlichkeit. Der DFG-Anteil an den Missionskosten wird an der Universität Leipzig zentral verwaltet. Die Finanzmittel für Maßnahmen zur Förderung der Gleichstellung werden verwaltet, und die Ausbildung der jungen Wissenschaftler wird koordiniert. Monatliche Telefonkonferenzen der drei Koordinatoren, jährlich Statusseminare und thematische Workshops werden organisiert. Spezielle Sitzungen auf internationalen Konferenzen und Veröffentlichungen von Spezialausgaben in internationalen Zeitschriften werden initiiert und befördert. Die SPP Internet-Seite wird

überarbeitet, fortlaufend aktualisiert und gewartet. Um die Arbeit der Koordinatoren zu unterstützen, werden eine halbe Position eines Wissenschaftlichen Administrators und eine Stelle für einen HALO Nutzerkoordinator beantragt.

Description
So far, observations of air-mass transformations in the Arctic have mostly been conducted from a fixed local position. Only few aircraft-based samplings of air-mass properties over a limited regional area have been reported. This Eulerian point of view does not permit the observations of air-mass modifying processes along their meridional pathway, which are required for model validations. Therefore, we propose a quasi-Lagrange approach following air-masses to and from the Arctic to observe the air-mass transformation processes during warm air intrusions and cold air outbreaks, whereby we focus on warm air intrusions, which have been observed much less frequently in the past. This quasi-Lagrange approach requires a long-endurance airborne facility, which may carry the necessary equipment for the observations. HALO with its exceptional endurance and high lifting capacity is most suited for these observations.

Weiterführung: ja

Mittelgeber: DFG Projekt number 442647689

Einfluss der Eisphase auf den Strahlungsantrieb von Wolken: Messungen und Representation in numerischen Wettervorhersagemodellen
Influence of ice phase on radiative forcing of clouds: Observations and representation in numerical weather prediction models

Schlagworte: flugzeuggetragene Messungen, Wolken, Strahlungsantrieb, Eisphase

Projektleiter: M. Wendisch (m.wendisch@uni-leipzig.de)

Projektmitarbeiter: Kevin Wolf

Projektbeginn: 2016
Projektende: 2020

Beschreibung
Methoden der flugzeuggetragenen passiven Fernerkundung mit Hilfe spektraler, solarer und reflektierter Strahldichten werden zur Ableitung der thermodynamischen Phase, der optischen Dicke und des Partikeleffektivradius von Wolken während der HALO Missionen NARVAL-II und NAWDEX angewendet. Insbesondere werden die horizontalen und vertikalen Verteilungen der thermodynamischen Phasen in unterschiedlichen Wolkentypen untersucht. Die Kombination mit anderen HALO-Fernerkundungsinstrumenten einschließlich Radar und Mikrowellensensoren ist geplant. Gleichzeitige Messungen der Wolkenalbedo werden durchgeführt und zur Analyse der Abhängigkeit des Strahlungsantriebs von Wolken-makrophysikalischen und mikrophysikalischen Eigenschaften verwendet. Auf der Basis von breitbandigen und spektralen Strahlungsgrößen dient die gemessene spektrale Wolkenalbedo zur Bewertung von Ergebnissen des ECMWF Integrated Forecast System (IFS). In mehreren Schritten werden 1D und 3D Strahlungstransfermodelle zusammen mit Beobachtungen verwendet, um die Unsicherheiten in der ECMWF-Vorhersage zu

identifizieren. Unsicherheiten in Bezug auf das Strahlungsschema und die simulierten Wolkeneigenschaften werden separiert.

Description
The airborne passive solar remote sensing of spectral reflected radiance will be applied to derive cloud thermodynamic phase, optical thickness, and particle effective radius during the HALO Missions NARVAL-II and NAWDEX. In particular, cloud thermodynamic phase and its horizontal and vertical distribution in different cloud types will be investigated. Combination with other remote sensing instruments of HALO including active radar and passive microwave sensors is planned. Simultaneous measurements of cloud top albedo will be derived and used to analyse the dependence of cloud radiative forcing on cloud macrophysical and microphysical properties. Measured spectral cloud top albedo will be employed to evaluate the ECMWF Integrated Forecast System (IFS) on the basis of broadband and spectral radiative quantities. In different steps, 1D and 3D radiative transfer models will be utilized in combination with the observations to identify and quantify uncertainties in IFS forecasts and analysis fields. Uncertainties due to the radiations scheme and simulated cloud properties will be separated.

Weiterführung: nein bzw. ja, im unten folgenden Fortsetzungsprojekt

Mittelgeber: DFG, SPP 1294, Projekt number 316500630

Einfluss der Eiskristallform auf den Strahlungseffekt von arktischen Zirren: Messungen und Repräsentation in numerischen Wettervorhersagemodellen
Influence of the ice crystal shape on radiative effects of Arctic cirrus: Observations and representation in numerical weather prediction models

Schlagworte: flugzeuggetragene Messungen, Wolken, Strahlungsantrieb, Eisphase

Projektleiter: M. Wendisch (m.wendisch@uni-leipzig.de)

Projektmitarbeiter: Johannes Röttenbacher

Projektbeginn: 2021
Projektende: 2023

Beschreibung
Flugzeuggetragenen Messungen der solaren und thermisch-infraroten atmosphärischen Strahlung sollen verwendet werden, um den Strahlungseffekt von Zirren in hohen Breiten zu quantifizieren und dessen Repräsentation in numerische Wettervorhersagemodellen zu evaluieren. Diese Zielstellung basierend auf den Erkenntnissen des vorangegangenen Projektes, in dem eine hohe Sensitivität des Strahlungsschemas im ECMWF Integrated Forecast System (IFS) bezüglich der Parametrisierung der Strahlungseigenschaften von Eiskristallen nachgewiesen werden konnte. Für arktischen Zirrus muss diese Analyse auf das Strahlungsbudget im thermisch-infraroten Wellenlängenbereich erweitert werden, da in der Arktis (Polarnacht), die solare Strahlung einen geringen bis nicht-vorhanden Anteil am Energiebuget ausmacht. Das Projekt ist in den HALO Missionen Cirrus-HL (High Latitude) und HALO-(AC)^3 (ArctiC Amplification: Climate Relevant Atmospheric and SurfaCe Processes, and Feedback Mechanisms) eingebunden. Beide Missionen

nutzen das Forschungsflugzeug HALO, um arktische Wolken mit neuesten aktiven und passiven Fernerkundungsmethoden sowie in situ Messungen der Wolkeneigenschaften zu charakterisieren. In diesem Projekt werden Messungen der von den Wolken reflektierten solaren und der emittierten thermisch-infraroten Strahlung durchgeführt. Dazu wird ein neues breitbandiges Radiometersystem, ein spektrales Albedometer und ein abbildendes Infrarotkamera verwendet, um das Strahlungsbudget oberhalb und unterhalb der Zirren zu quantifizieren. Basierend auf diesen Messungen, wird der Strahlungseffekt der Zirren berechnet und in Abhängigkeit der Wolkeneigenschaften analysiert. Besonders wird hier untersucht, in wie weit sich typisch arktische Randbedingungen wie das reflektierende Meereis und langlebige niedrige Wolken auf den Strahlungseinfluss der Zirren auswirken. Des Weiteren wird untersucht, wie diese Strahlungseffekte von arktischen Zirren in numerischen Wettervorhersagemodellen repräsentiert werden. Dazu werden die im Modell vorhergesagten Strahlungseffekte mit den Messungen verglichen. In mehreren Schritten, werden Strahlungstransfermodellen mit unterschiedlichen Parametrisierungen der Strahlungseigenschaften von Eiskristall verwendet, um die Unsicherheiten in Bezug auf das Strahlungsschema und die prognostizieren Wolkeneigenschaften zu separieren.

Description

Based on the sensitivity of the ECMWF radiation scheme to the parametrization of ice crystal radiative properties observed in the completed project for ice clouds in mid-latitudes, the continuation of the project aims to extends this model evaluation for the radiative effects of cirrus in high-latitudes. For Arctic cirrus, the analysis needs to be extended to the thermal-infrared radiation budget, which dominates due to the lag of solar radiation and depends on cloud altitude, thickness and ice crystal properties. Therefore, the project is embedded in the proposed HALO missions Cirrus-HL (High Latitude) and HALO-(AC)^3 (ArctiC Amplification: Climate Relevant Atmospheric and SurfaCe Processes, and Feedback Mechanisms), which both aim to investigate Arctic clouds by state of the art airborne remote sensing (active and passive) and cloud microphysical in situ observations.Within this project, measurements of the cloud-reflected solar and emitted thermal infrared radiance and irradiance with a new broadband radiometer system, a spectral albedometer, and a thermal-infrared imager are proposed to quantify the radiative energy budget above and below Arctic cirrus. Based on the observations, the cirrus radiative effect will be derived and evaluated with respect to its dependence on cloud macrophysical and microphysical properties, and the special Arctic environment (sea ice, persistent low clouds). We will evaluate how well the cirrus and their radiative effects are represented in numerical weather prediction models. The comparison will be performed in the observational space of irradiances and radiances instead of cloud properties. Therefore, the output of the numerical weather prediction (NWP) models will be converted by radiative transfer models into the observed radiation quantities. Operational and experimental radiation schemes will be tested and compared to the observed radiation quantities to identify the reasons of potential differences between model and observation. The airborne observations and the radiative transfer simulations will be used to corroborate the hypothesis: “The radiative effects of Arctic cirrus, which significantly depend on their macrophysical and microphysical properties such as the ice crystal shape, can be used to validate numerical weather prediction models.” To address this hypothesis, the proposed study will focus on five specific science questions: (A) How variable are the radiative effects by Arctic cirrus on different horizontal scales (e.g., contrail cirrus, cirrus in air mass transformation)? (B) How strong the radiative effects depend on the presence of sea ice and low clouds? (C) Do observed ice crystal shapes of Arctic cirrus lead to a significant change of cloud radiative effects? (D) Do NWP models realistically represent the radiative effects of Arctic cirrus? (E) Can we use spectral solar and thermal-infrared radiation measurements to constrain potential uncertainties of NWP models?

Weiterführung: ja

Mittelgeber: DFG, SPP 1294, Projekt number 316500630

SFB/Transregio 172 „Arktische Verstärkung“
Zentrale Dienstleistungen, Verwaltung und Koordinierung (Z01)
Central services, administration and coordination (Z01)

Schlagworte: Arktis.

Projektleiter:
M. Wendisch (m.wendisch@uni-leipzig.de)
Prof. Dr. Susanne Crewell, Universität zu Köln, Institut für Geophysik und Meteorologie
Prof. Dr. Justus Notholt, Universität Bremen, Institut für Umweltphysik

Projektmitarbeiter: Dr. Marlen Brückner

Projektbeginn: 2016
Projektende: 2023

Beschreibung
Innerhalb des TR 172 Antrages werden Mittel für die zentrale Koordinierung beantragt. Dieses Teilprojekt dient dazu, die Kooperationen und Kommunikation im Verbund unter den einzelnen wissenschaftlichen Projekten und Clustern zu fördern. Aus diesem Grund werden monatliche Videokonferenzen, halbjährliche Meetings, jährliche wissenschaftliche Konferenzen, als auch spezielle Workshops organisiert und durchgeführt. Die Mittel für Gleichstellungsmaßnahmen werden dazu verwendet um junge Wissenschaftler/innen in Zusammenarbeit mit lokalen Graduiertenschulen zu trainieren. Die internationale Präsenz des TR 172 wird etabliert. Eine Internetseite wird erstellt und implementiert. Die logistische Organisation und wissenschaftliche Planung von intensiven Messkampagnen innerhalb des TR 172 werden durch das Projekt Z01 unterstützt. Öffentlichkeitsarbeit zwischen den verschiedenen Partnern wird organisiert und koordiniert.

Description
Funds for the central coordination of TR 172 are requested within this proposal. The project serves the promotion of cooperation and communication among the individual scientific projects and clusters. Monthly video conferences, biannual general assemblies, annual scientific conferences, as well as topical workshops will be organized and conducted. The funds for measures to promote gender equality are managed the training of young researchers is coordinated, in collaboration with local graduate schools. The international visibility of TR 172 will be fostered. A web page will be set up and maintained. The logistic organization and scientific planning of the extensive observational campaigns within TR 172 will be supported by project Z01. Public outreach activities will be organized and coordinated between the different partners.

Weiterführung: ja

Mittelgeber: DFG, TRR 172, Projekt number 268020496

SFB/Transregio 172 „Arktische Verstärkung“
Modul integriertes Graduiertenkolleg (MGK*)
Integrated Research Training Group (MGK*)

Schlagworte: Arktis.

Projektleiter:
M. Wendisch (m.wendisch@uni-leipzig.de)
Prof. Dr. Susanne Crewell, Universität zu Köln, Institut für Geophysik und Meteorologie
Prof. Dr. Justus Notholt, Universität Bremen, Institut für Umweltphysik

Projektmitarbeiter: Dr. Marlen Brückner

Projektbeginn: 2020
Projektende: 2023

Beschreibung
Ziel des Projektes ist es eine Integrated Research Training Group (IRTG) innerhalb von (AC) 3 einzurichten, um junge Forscher (Doktoranden und Postdocs) bei der Entwicklung ihrer wissenschaftlichen Unabhängigkeit zu unterstützen und sie auf den Arbeitsmarkt in Wissenschaft, in verschiedenen Bereichen der Industrie, oder in der wissenschaftlichen Verwaltung vorzubereiten. Das im Rahmen der IRTG geplante Qualifizierungsprogramm wird dazu beitragen, das Wissen und die Fähigkeiten junger Forscher zu vertiefen und ihre Unabhängigkeit zu fördern.

Description
The project will establish an Integrated Research Training Group (IRTG) within (AC)3 to support young researchers (Phd students and Postdocs) in their development of scientific independence, and prepare them for positions in academia, industry, in various fields, or in administration. The qualification programme planned within the IRTG will help to deepen their knowledge and skills of young researchers and promote their independence.

Weiterführung: ja

Mittelgeber: DFG, TRR 172, Projekt number 268020496

SFB/Transregio 172 „Arktische Verstärkung“
Fesselballongetragene Messungen des Energiebudgets in der wolkenbedeckten Zentralarktis (A02)
Tethered balloon-borne energy budget measurements in the cloudy central Arctic (A02)

Schlagworte: Arktis, ballongetragene Messungen, Energiebilanz, Strahlungsabkühlung.

Projektleiter: M. Wendisch (m.wendisch@uni-leipzig.de)
Dr. Holger Siebert, Leibniz-Institut für Troposphärenforschung e.V. (TROPOS)

Projektmitarbeiter: Michael Lonardi

Projektbeginn: 2016
Projektende: 2023

Beschreibung
Während der Expedition MOSAiC im Frühsommer (April bis Juni) 2020 werden fesselballongetragene Messungen von einer Eisschollenstation analysiert. Basierend auf den gewonnenen Messungen werden wir typische Werte und Profile von Turbulenz, Strahlung, Aerosolpartikeln und wolkenmikrophysikalische Eigenschaften während der Entstehung von stratiformen Grenzschichtwolken in der Zentralarktis sammeln. Wir fokussieren uns hier auf lokale Aspekte der bewölkten Grenzschicht auf die Arktische Verstärkung, wobei auch entfernte Prozesse wie Advektion berücksichtigt werden.
Description
Tethered balloon-borne measurements from an ice-floe camp during the MOSAiC expedition in early summer (April-June) 2020 will be analysed. On the basis of the collected data we will quantify typical values and profiles of turbulence, radiation, aerosol particle and cloud microphysical properties during the life-time of stratiform ABL clouds in the central Arctic. Here we focus on local aspects of the cloudy ABL on Arctic amplification, although remote processes such as advection will also be considered.

Weiterführung: ja

Mittelgeber: DFG, TRR 172, Projekt number 268020496

SFB/Transregio 172 „Arktische Verstärkung“
Einfluss von tiefen Wolken auf die arktische atmosphärische Grenzschichtturbulenz und -Strahlung (A03)
Impact of low-level clouds on Arctic atmospheric boundary layer turbulence and radiation (A03)

Schlagworte: Arktis, flugzeuggetragene Messungen, Energiebilanz, Strahlungsabkühlung.

Projektleiter: M. Wendisch (m.wendisch@uni-leipzig.de)
Dr. Christof Lüpkes, Alfred-Wegener-Institut Helmholtz-Zentrum für Polar- und Meeresforschung

Projektmitarbeiter: Sebastian Becker

Projektbeginn: 2016
Projektende: 2023

Beschreibung (Deutsch- Pflicht; <2000 Zeichen)
Um den Einfluss von atmosphärischen Grenzschichtwolken auf die Arktische Verstärkung zu verstehen, sind detaillierte Studien der wolkenbedingten Prozesse, welche die arktische Grenzschicht und das Energiebudget beeinflussen, unabdingbar. Wir schlagen zwei Hauptziele für die zweite Phase vor. Ersteres bezweckt ein besseres Verständnis des Einflusses der Jahreszeit auf Wolken und deren verbundene Grenzschichtprozesse und das Energiebudget. Zweites Ziel beinhaltet die Untersuchung der Wolken während eines Lagrangeschen Luftmassentransports. Um

diese Ziele zu erreichen, werden drei Messkampagnen mit den Polar5/6 Flugzeugen sowie mit HALO (High Altitude and Long Range Research Aircraft) durchgeführt.

Description
To understand the role of atmospheric boundary layer clouds in Arctic amplification, detailed studies of cloud–related processes influencing the ABL and the atmospheric energy budget are indispensable. We propose two major goals for phase II. The first one aims at a better understanding of the seasonal dependence of the cloud impact on the ABL processes and energy budget. The second objective includes to investigate the changing cloud impact during Lagrangian air mass transports. To reach these goals, we will perform three campaigns using the AWI Polar 5/6 aircraft and the High Altitude and Long Range Research Aircraft (HALO).
Weiterführung: ja

Mittelgeber: DFG, TRR 172, Projekt number 268020496

SFB/Transregio 172 „Arktische Verstärkung“
Einfluss von Bodenheterogenität auf den Strahlungsantrieb und Ableitung von Aerosol- und Wolkeneigenschaften in der Arktis (C01)
Influence of surface heterogeneity on radiative forcing and retrieval of aerosol and cloud properties in the Arctic (C01)

Schlagworte: Arktis, flugzeuggetragene Messungen, Eis- und Schneealbedo, BRDF

Projektleiter: M. Wendisch (m.wendisch@uni-leipzig.de)
Dr. Georg Heygster (bis 12/2019), Universität Bremen, Institut für Umweltphysik (IUP)
Dr. Marcel Nicolaus (Seit 01/2020), Alfred-Wegener-Institut Helmholtz-Zentrum für Polar- und Meeresforschung
Dr. Gunnar Spreen, (seit 01/2020), Universität Bremen, Institut für Umweltphysik Abteilung für Erdfernerkundung

Projektmitarbeiter: Dr. Evelyn Jäkel
Projektbeginn: 2016
Projektende: 2023

Beschreibung
Die Bodenheterogenität und zeitliche Entwicklung der Bodeneigenschaften des Arktischen Ozeans beeinflussen den Strahlungsenergietransfer durch die Kopplung von Atmosphäre, Meereis und Ozean im arktischen Klimasystem. Strahlungseffekte durch Interaktionen dieser Komponenten sind nicht gut verstanden, allerdings können sie eine entscheidende Rolle im arktischen Klimasystem spielen. Wir werden Flugzeugmessungen der vorangegangenen Kampagnen ACLOUD, PAMARCMiP, und AFLUX analysieren und neue Messungen während MOSAiC und HALO-(AC) hoch 3 sammeln. Zusätzlich werden wir Satellitendaten (MERIS, Sentinel-3) für unsere Analyse verwenden.

Description
The spatial heterogeneity and temporal evolution of surface properties of the Arctic Ocean influence the radiative energy transfer through the coupled compartments (atmosphere, sea ice, open ocean) of the Arctic climate system. Radiative effects of interactions between these

components are not well studied, however, they may play an important role in the Arctic climate system. We will analyse airborne data from the previous ACLOUD, PAMARCMiP, and AFLUX campaigns, and collect new measurements during the planned MOSAiC and HALO-(AC) observations. In addition, we will use satellite data (MERIS, Sentinel-3) in our analysis.

Weiterführung: ja

Mittelgeber: DFG, TRR 172, Projekt number 268020496

SFB/Transregio 172 „Arktische Verstärkung“
Charakterisierung von arktischen Mischphasenwolken durch flugzeuggetragene in-situ Messungen und Fernerkundung (B03)
Characterization of Arctic mixed-phase clouds by airborne in-situ measurements and remote sensing (B03)

Schlagworte: Arktis, flugzeuggetragene Messungen, Mischphasenwolken.

Projektleiter: Dr. André Ehrlich (a.ehrlich@uni-leipzig.de)
Professor Dr. Susanne Crewell, Universität zu Köln, Institut für Geophysik und Meteorologie
Professor Dr. Andreas Macke, Leibniz-Institut für Troposphärenforschung e.V. (TROPOS)

Projektmitarbeiter: Elena Ruiz, Marcus Klingebiel
Projektbeginn: 2016
Projektende: 2023

Beschreibung
Dieses Teilprojekt kombiniert flugzeuggetragene Fernerkundung der Vertikalsäule und den Strahlungseffekt von Wolken mittels in-situ mikrophysikalischen Messungen von Wolken- und Aerosolpartikeln. Da die vorangegangenen Kampagnen lediglich Momentaufnahmen der arktischen Bedingungen geliefert haben, werden wir diese Messungen mit zwei weiteren Kampagnen ausbauen, um die saisonalen und regionalen Unterschiede von Wolken- und Aerosoleigenschaften und deren Beitrag zur Arktischen Verstärkung systematisch zu untersuchen. Die beobachteten Wolken- und Aerosoleigenschaften werden untereinander verlinkt und für unterschiedliche Aspekte kategorisiert, um Änderungen der Aerosol-Wolken-Wechselwirkung unter verschiedenen Bedingungen zu identifizieren, welche mehr oder weniger häufig bedingt durch die Arktische Verstärkung zu beobachten sind.

Description
We aim to combine airborne remote sensing of the vertical column and the radiative impact of clouds with in–situ microphysical measurements of cloud and aerosol properties. As the completed campaigns represent only a snapshot of Arctic conditions, we aim to extend these measurements by two major campaigns to systematically investigate seasonal and regional differences of cloud and aerosol properties and their contribution to Arctic amplification. The observed cloud and aerosol properties will be linked to each other and categorized for different issues to identify changes of aerosol-cloud interaction under different conditions, which are expected to occur more/less frequently due to Arctic amplification.
Weiterführung: ja

Mittelgeber: DFG, TRR 172, Projekt number 268020496

SFB/Transregio 172 „Arktische Verstärkung“
Analyse und Vorhersage des Transports und der Transformation von Arktischen Luftmassen (Warmlufteinschübe und Kaltluftausbrüche)
Analysis and forecast of transport and transformation of Arctic air masses (warm air intrusions, cold air outbreaks)

Schlagworte: Arktis, Luftmassentransport.

Projektleiter: Dr. Michael Schäfer (michael.schaefer@uni-leipzig.de)

Projektmitarbeiter: Benjamin Kirbus

Projektbeginn: 2020
Projektende: 2023

Beschreibung
Im Frühjahr 2022 werden Messungen mit dem deutschen Forschungsflugzeug HALO (High Altitude and Long Range Research Aircraft) im Rahmen von HALO- (AC) ³ (www.halo-spp.de) durchgeführt. Ziel sind Fernerkundungsmessungen, um die Auswirkungen von Wolken auf atmosphärische Grenzschichtprozesse und den Energiehaushalt in der Arktis zu untersuchen. Mit HALO wollen wir einen Lagrange-Ansatz verfolgen, um dasselbe Wolkensystem innerhalb von mehreren Tagen zu untersuchen und die Entwicklung der eingebetteten Wolken zu charakterisieren. In diesem Zusammenhang sind Warmlufteinschübe und Kaltluftausbrüche von besonderem Interesse. Sie bleiben in der Regel mehrere Tage bestehen und können große Mengen an Wärme und Feuchtigkeit über große Entfernungen in die Arktis oder aus der Arktis transportieren, wodurch die Wolkenmorphologie auf ihrem Weg beeinflusst wird. Um die Wolkenbildung / -entwicklung entlang solcher Transportwege von Anfang an zu erfassen, müssen Warmlufteinbrüche und Kaltluftausbrüche rechtzeitig vorhergesagt werden. Der Kern dieses Projekts besteht darin, ein Prognosetool zu entwickeln, es während der HALO- (AC) 3-Kampagne anzuwenden und anschließend zu validieren. Darüber hinaus werden die Luftmasseneigenschaften, die Wolkenentwicklung und ihr Einfluss auf die Strahlungseigenschaften analysiert.

Description
In spring 2022 airborne remote sensing in the Arctic will be used to study the cloud impact on atmospheric boundary layer processes and the energy budget. The measurements will be performed using the German research aircraft HALO (High Altitude and Long range research aircraft) within the framework of HALO-(AC)³ (www.halo-spp.de). With HALO, we aim to follow a Lagrangian approach to sample the same cloud system in the course of several days to investigate the embedded cloud evolution. In this regard, warm air intrusions and cold air outbreaks are of special interest. They usually persist for several days and are capable to transport large amounts of heat and moisture over huge distances into the Arctic or out of it, influencing the cloud morphology on its way. To capture the cloud formation/evolution along such transport paths from the very beginning, it is necessary to forecast warm air intrusions and cold air outbreaks in time. The core of this project is to develop a forecast tool, apply it during the HALO-(AC)3 campaign, and

to validate it afterwards. Furthermore, the air-mass characteristics, the cloud evolution, and their influence on radiative properties will be evaluated.

Weiterführung: ja

Mittelgeber: Universität Leipzig, Doktorandenförderung

SFB/Transregio 172 „Arktische Verstärkung“
Evaluierung der ECMWF und ICON Vorhersagequalität von arktischen Wolkeneigenschaften mit Hilfe von flugzeuggetragenen Messungen
Evaluation of ECMWF and ICON forecast quality of cloud properties using airborne dropsonde and cloud measurements in the Arctic

Schlagworte: Arktis, flugzeuggetragene Messungen, Mischphasenwolken.

Projektleiter: Dr. Michael Schäfer (michael.schaefer@uni-leipzig.de)

Projektmitarbeiter: Hanno Müller

Projektbeginn: 2021
Projektende: 2024

Beschreibung
In den letzten Jahren hat sich die Leistung numerischer Wettervorhersagemodelle wie ECMWF oder ICON stetig verbessert. Ihre horizontale und vertikale Auflösung wurde erhöht, während die Unsicherheit ihrer vorhergesagten Parameter und die erforderliche Rechenzeit verringert werden konnten. Daher wurden solche Modelle zu einem wertvollen Instrument, um das Auftreten verschiedener Wolkentypen in bestimmten synoptischen Situationen zu untersuchen, was insbesondere in arktischen Regionen mit spärlichen lokalen Beobachtungen von entscheidender Bedeutung ist. Darüber hinaus helfen die Modelle in wissenschafltich interessante synoptische Situationen zu identifizieren und unterstützen die Planung geeigneter Flugmuster zur Untersuchung von arktischen Wolken. In früheren Kampagnen (ACLOUD, AFLUX oder MOSAiC-ACA) wurden zahlreiche Dropsonden- und Wolkenmessungen (in-situ, Fernerkundung) erfasst. Das Ziel dieses Projekts ist es, diese Daten zu verwenden, um die ECMWF- und ICON-Prognosequalität von Wolkeneigenschaften in der Arktis in unterschiedlichen synoptischen Situationen zu bewerten.
Es sind Profildaten von Temperatur und Luftfeuchtigkeit aus Dropsonde-Messungen zu verwenden, die während mehrerer Forschungsflüge nördlich von Spitzbergen in früheren Kampagnen erfasst wurden. Zusätzliche Kamera-, Radar- und Lidar-Messungen stehen zur Verfügung, um die Wolkensituation während der Flüge zu charakterisieren. Die Ergebnisse sollen zu einer quantitativen Bewertung der Vorhersagequalität von EZMW und ICON führen, die 2022 in weiteren Luftkampagnen wie HALO- (AC) 3 getestet wird.

Description
During the past years, the performance of numerical weather prediction models like ECMWF or ICON improved steadily. Their horizontal and vertical resolution have been increased, while the uncertainty of their predicted parameters and the required computational time could be reduced. Therefore, such models became a valuable tool to investigate the occurrence of different cloud

types in specific synoptic situations, which is crucial especially in Arctic regions, where local observations are sparse. Furthermore, in such regions, they help to identify interesting upcoming cloud situations and to design most suited flight patterns for airborne campaigns. During past campaigns (ACLOUD, AFLUX, or MOSAiC-ACA) numerous dropsonde and cloud (in-situ, remote sensing) measurements have been collected. The objective of this project is to use these data to evaluate the ECMWF and ICON forecast quality of cloud properties in the Arctic in different synoptic situation.
Profile data of temperature and humidity from dropsonde measurements shall be used, which were captured during several research flights North of Svalbard during past campaigns. Additional image data, radar, and lidar measurements are available to further characterize the cloud situation during the flights. The results shall lead to a quantitative evaluation of the prediction quality of ECMWF and ICON, which will be tested during further airborne campaigns like HALO-(AC)3 in 2022.

Weiterführung: ja

Mittelgeber: Universität Leipzig, Doktorandenförderung

Entwicklung von tropischer hochreichender Konvektion abgeleitet aus bodengebundenen abbildenden Spektroradiometermessungen
Evolution of tropical deep-convective clouds derived from ground-based imaging spectroradiometer measurements

Schlagworte: Konvektive Wolken, atmosphärische Strahlung, bodengebundene Fernerkundung

Projektleiter: M. Wendisch (m.wendisch@uni-leipzig.de)
Projektmitarbeiter: Kátia Mendes de Barro (katia.mendes_de_barros@uni-leipzig.de)

Projektbeginn: 2017
Projektende: 2020

Beschreibung
Im Rahmen des Projekts soll aus bodengebundenen Wolkenseitenmessungen der reflektierten Strahlung mittels eines abbildenden Spektrometersystems von tropischer hochreichender Konvektion auf das Vertikalprofil der mikrophysikalischen Eigenschaften der Wolke geschlossen werden. Damit soll die vertikale Entwicklung von hochreichender Konvektion, die eine wesentliche klimarelevante Rolle spielt, unter Berücksichtigung des Einflusses von Aerosolpartikeln und von thermodynamischen Bedingungen auf das Tropfenwachstum charakterisiert werden. Die geplanten Messungen sollen auf einem 320 m hohen Messturm (ATTO: Amazonian Tall Tower Observatory), der kürzlich im brasilianischen Regenwald errichtet wurde, stattfinden. ATTO ist mit Messgeräten ausgestattet, die meteorologische, chemische und Aerosolparameter liefern. Die Messregion bietet ideale Beobachtungsbedingungen mit klar definierten Jahreszeiten (Regen- und Trockenzeit), täglicher Konvektion und variablen Aerosolbedingungen. Aus den Messungen eines neuen abbildenden Spektrometersystems, SPIRAS (SPectral Imaging Radiation System) sollen Vertikalprofile der thermodynamischen Phase und der Partikelgröße mit hoher zeitlicher und räumlicher Auflösung und mit Hilfe von adaptierten Verfahren unter Verwendung von dreidimensionalen Strahlungstransportsimulationen abgeleitet werden. Damit sollen vertikale Bereiche, die das Tropfenwachstum beschreiben (Diffusion, Koaleszenz, Mischphasenbereich und

Vereisung), identifiziert werden. Zusätzliche Messungen einer Infrarotkamera und eines scannenden Depolarisations-Lidars werden für die Höhen- und Temperaturbestimmung der beobachteten Wolkenelemente herangezogen. Zusätzlich werden die Polarisationsmessungen des Lidars zur Bestimmung der thermodynamischen Phase verwendet, um den wichtigen Phasenübergang zu identifizieren. Mit Hilfe der gewonnenen Daten werden außerdem Annahmen (Effektivradius als konservative Wolkeneigenschaft) wie sie von Ableitungsverfahren zur Bestimmung von mikrophysikalischen Wolkenprofilen aus Satellitenmessungen gemacht werden, überprüft.

Description
Specifically, the project will derive the vertical profile of microphysical properties of tropical deep-convective clouds (DCC) from ground-based measurements of reflected radiation from cloud sides by an imaging spectroradiometer system. This general objective is to characterize the vertical evolution of DCCs, which play an important role in the Earths climate system. The evolution will be studied with respect to the impact of aerosol and thermodynamic conditions on the cloud particle growth. The planned measurements will be performed on the new Amazonian Tall Tower Observatory (ATTO), of 320 m height situated in the Amazon Basin near the equator. ATTO is equipped with instruments to measure micrometeorological and atmospheric chemical variables, as well as aerosol properties. It provides ideal observation conditions with clear seasons (wet and dry season), and daily occurrence of DCCs in a highly variable environment with respect to concentrations and types of aerosol particles. The new imaging spectroradiometer system, SPIRAS (SPectral Imaging Radiation System), will be used to derive vertical profiles of thermodynamic phase and cloud effective radius with high temporal and spatial resolution by means of adapted methods based on three-dimensional radiative transfer simulations. In this way vertical zones characterizing the droplet growth (diffusion, coalescence, mixed-phase, and glaciation) will be identified. Auxiliary measurements by an infrared camera and a scanning depolarization Lidar will be used to estimate the height and the temperature of the observed cloud element. Additionally, polarization measurements by Lidar will support the retrieval of the thermodynamic phase which is important to identify the phase transition. By means of the data obtained we will validate assumptions (effective particle radius as conservative cloud property) of retrieval methods for satellite-based observations to derive microphysical profiles.

Weiterführung: nein

Mittelgeber: DFG WE 1900/34-1, Projekt number 310366544

Fernerkundung und Strahlungsantrieb von Inhomogenen Passatwind-Cumuli
Remote Sensing and Radiative Forcing of Inhomogeneous Trade-Wind Cumuli

Schlagworte: Passatwind-Cumuli, atmosphärische Strahlung, flugzeuggetragene Fernerkundung

Projektleiter: M. Wendisch (m.wendisch@uni-leipzig.de)
Projektmitarbeiter: Samkeyat Shohan, Anna Luebke

Projektbeginn: 2019
Projektende: 2022

Beschreibung
Das Hauptziel des Projektes besteht in der Quantifizierung des großskaligen Strahlungsantriebes von flachen Passatwind Cumulus-Wolken als Funktion der makro- und mikrophysikalischen Wolkeneigenschaften, der räumlichen Anordnung der Wolken, und der mesoskaligen Vertikalbewegung. Wir kombinieren makro-, mikrophysikalische und Strahlungseigenschaften von Passatwindwolken, welche von flugzeuggetragenen Fernerkundungsbeobachtungen und in-situ Strahlungsmessungen abgeleitet werden. Diese Messungen werden an Bord von HALO (High Altitude and Long Range Research Aircraft) während der Messkampagne EUREC4A (ElUcidating the Role of Cloud-Circulation Coupling in ClimAte) östlich von Barbados im Februar 2020 gewonnen. Um die relevanten Wolken- und Strahlungsdaten ableiten zu können, werden wir die Instrumentierung von HALO erweitern durch (i) eine multispektrale thermisch-infrarote Kamera, und (ii) auf- und abwärts gerichtete, halbräumliche Breitband-Pyranometer und Pyrgeometer. Die breitbandigen Radiometer werden solare und terrestrische Strahlungsflussdichtemessungen liefern, um den atmosphärischen Strahlungshaushalt in Flughöhe zu quantifizieren. Die thermisch-infrarote Kamera wird die Helligkeitstemperatur in verschiedenen Spektralbändern mit hoher räumlicher (5 Meter) und zeitlicher (20 Hz) Auflösung bestimmen. Diese Geräte wurden noch nicht auf HALO eingesetzt. Deshalb besteht ein wichtiger Teil des vorgeschlagenen Arbeitsplanes in intensiven Tests und Kalibrierungen der neuen Geräte und der Entwicklung von Software zur Handhabung und Auswertung der Daten. Die thermisch-infrarote Kamera wird verwendet, um Wolkenprodukte abzuleiten. Dies umfasst Felder der Temperatur am Wolkenoberrand, Flüssigwasserpfad und Effektivradien. Die Felder werden statistisch analysiert, um den Bedeckungsgrad, den Grad der Organisation, und die Wolkengrößenverteilung zu erhalten. Die Daten werden mit atmosphärischen Parametern (Temperatur-/Feuchteprofile, Hintergrundaerosol, großskalige Divergenz) korreliert. Die Beobachtungen mit den Breitband-Radiometern werden in Kombination mit den Feldern der Wolkeneigenschaften, die von den Messungen mit der thermisch-infraroten Kamera abgeleitet werden, analysiert. Die Quantifizierung des Wolken-Strahlungsantriebes für unterschiedliche Wolkenbedeckungen sowie Wolkenoberkantentemperaturen wird zeigen, wie empfindlich der Wolken-Strahlungsantrieb im Hinblick auf makroskopische Eigenschaften und die Anordnung der Passatwolken ist. Eine Parametrisierung dieser Empfindlichkeiten hilft bei der Beschreibung von Passatwind-Wolken in numerischen Wettervorhersage- und globalen Klimamodellen.

Description
The core objective of the project is to quantify the large-scale radiative forcing of shallow trade-wind cumuli as a function of the cloud macrophysical and microphysical properties, the cloud spatial organization, and the mesoscale vertical motion. We will combine macrophysical, microphysical, and radiative properties of trade-wind cumuli obtained from airborne remote sensing cloud observations and in situ irradiance measurements aboard the High Altitude and Long Range Research Aircraft (HALO) during the EUcidating the Role of Cloud-Circulation Coupling in ClimAte (EUREC4A) campaign east of Barbados in February 2020.To retrieve the relevant cloud and radiation data, we will extend the instrumentation of HALO by (i) a multi-wavelength thermal infrared (IR) imager, and (ii) pairs of upward and downward looking, hemispheric broadband pyranometers and pyrgeometers. These broadband radiometers will provide solar and terrestrial irradiance measurements to quantify the atmospheric radiation budget at flight level. The thermal IR imager will map the cloud top brightness temperatures at different thermal IR spectral bands with high spatial (5 m) and temporal (20 Hz) resolution. The instruments were not operated on HALO yet. Therefore, a crucial part of the proposed work plan is related to extensive tests and calibrations of the new instruments and developing tools for handling and post processing the

data. The thermal IR imager will be used to develop an IR-based cloud product, providing maps of cloud top temperature, cloud liquid water path and cloud effective droplet size. The maps will be analysed statistically to obtain the cloud fraction, degree of clustering, and cloud size distributions. The data will be correlated with atmospheric parameters (temperature/humidity profiles, background aerosol, large-scale divergences). The observations of the broadband radiometers will be analysed in combination with the maps of cloud properties derived from the thermal IR imager. Quantifying the cloud radiative forcing for scenes of trade-wind cumuli with different cloud fraction, degree of clustering, and cloud top temperatures will indicate how sensitive the cloud radiative forcing is with respect to the macroscopic properties and organization of trade-wind cumuli. Parameterizing this sensitivity provides a tool to evaluate the representation of trade-wind cumuli in numerical weather prediction models and global climate models.

Weiterführung: ja

Mittelgeber: DFG Projekt Nummer 422897361

Anwendung von Eisoberflächen- und Strahlungsdaten in der Luft basierend auf MOSAiCBeobachtungen für Oberflächenalbedoparametrisierungen der zentralen Arktis
Application of airborne ice surface and radiation data based on MOSAiC observations for surface albedo parameterizations of the central Arctic (ALIBABA)

Schlagworte: Arktis, Oberflächenalbedo, hubschraubergetragene Messungen, MOSAiC

Projektleiter: M. Wendisch (m.wendisch@uni-leipzig.de)
Projektmitarbeiter: Tim Sperzel

Projektbeginn: 2021
Projektende: 2024

Beschreibung
Das Ziel des Projekts ALIBABA ist die direkte Anwendung der fluggestützten Strahlungs- und Kameradaten, die mit der Hubschrauber-Schleppsonde „HELiPOD“ während MOSAiC erhoben werden. Damit soll der Einfluss von Wolken-Inhomogenitäten auf die Eigenschaften der Rückstreuung solarer Strahlung von arktischen Eisflächen quantifiziert werden. Es werden verschiedene Skalen von 0.25 km bis 10 km betrachtet, die für regionale Klimamodelle und die horizontale Auflösung von Satelliten charakteristisch sind. Für diese räumlichen Skalen stellen die Oberflächen-Reflexionseigenschaften oft eine Mischung von verschiedenen Oberflächen-Arten dar, wie z.B. offenes Wasser, pures Eis, mit Schnee bedecktes Eis -und Schmelztümpel. Dreidimensionale (3D) Strahlungstransportsimulationen sollen mit den Messungen der komplexen Oberflächen-Reflexionseigenschaften kombiniert werden. Die Albedo und die direktionale Reflexion der individuellen Oberflächenarten sollen aus den großflächigen Beobachtungen unter Berücksichtigung der von Einstrahlungsänderungen (Wolkenbedeckung, Sonnenstand) abgeleitet werden. Dadurch soll die zeitliche Entwicklung der Reflexionseigen-schaften der verschiedenen Oberflächenarten über einen längeren Zeitraum dokumentiert werden (MOSAiC-Messungen Mai bis August 2020). Damit können Parametrisierungen der Oberflächen-Albedo für Klimamodelle wie HIRHAM-NAOSIM und ICON evaluiert und verbessert werden.

Description
The aim of the project ALIBABA is the direct application of the airborne radiation and camera data obtained with the helicopter borne meteorological sonde “Helipod” during MOSAiC (Multi-disciplinary drifting Observatory for the Study of Arctic Climate). The data are used to quantify the impact of cloud inhomogeneity on the solar reflection properties of Arctic surfaces on typical spatial scales (0.25 – 10 km) covered by regional climate models and satellite footprint sizes. For such spatial scales, the surface reflection properties may feature a mixture of different surface types such as open water, bare ice, snow covered ice, and melt ponds. Three-dimensional (3D) radiative transfer modeling will be combined with measurements of such complex surface reflection properties. The subtype albedo and directional reflection will be extracted from areal surface observations considering effects of illumination changes (cloud occurrence, solar zenith angle). By that, the temporal evolution of the individual subtypes of reflection properties during the course of MOSAiC (May – August 2020) will be documented. That will help to evaluate and improve the surface albedo parameterization scheme of climate models such as HIRHAM-NAOSIM and ICON.

Weiterführung: ja

Mittelgeber: BMBF Projekt Nummer 232101570

Theoretische Meteorologie; Johannes Quaas
AG Wolken und globales Klima

Probabilistic attribution of extreme precipitation to aerosol perturbations (PATTERA)

Schlagworte: Attribution, Klima-Extremereignisse, Aerosol-Konvektions-Wechselwirkung

Projektleiter:
Koordinator: Andreas Hense, Universität Bonn (ahense@uni-bonn.de)
J. Quaas (johannes.quaas@uni-leipzig.de)

Projektmitarbeiter:
Dr. Ribu Cherian (ribu.cherian@uni-leipzig.de)

Projektbeginn: 1.3.2020
Projektende: 28.2.2023

Beschreibung
Der Klimawandel wirkt sich insbesondere über Änderungen in Extermereignissen auf die Gesellschaft aus; hierbei stellen Extremniederschläge und Blitzeinschläge aus hochreichender Konvektion (Gewitter) besondere Gefahren dar. Anthropogene Änderungen der Atmosphärenzusammensetzung können Veränderungen in solchen Ereignissen bewirken. Anders als Treibhausgase und globale Erwärmung haben Emissionen von Aerosolpartikeln möglicherweise

einen unmittelbaren Einfluss auf Konvektion. Das Projekt PATTERA wird (i) die Einflüsse von Aerosolen auf Konvektion, wie sie im ICON-Atmosphärenmodell simuliert werden, evaluieren, wobei vorhandene hochaufgelöste Simulationen, Multi-Modell-Ensembles und bodengebundene Beobachtungen als Referenz genutzt werden. Es wird weiterhin (ii) mit dem Ansatz probabilistischer Ursachenzuordnung (attribution; Ensemblesimulation tatsächlicher und hypothetischer – faktischer und kontrafaktischer – Bedingungen) die Auswirkungen von anthropogenen Aerosolen auf Extremniederschlag und Blitze untersuchen. In einer möglichen zweiten Phase können diese Untersuchungen auf die globale Skala ausgeweitet werden.

Weiterführung: ja

Mittelgeber: BMBF

Contrast between hemispheres in aerosol impact on cloud erosion (CHANCE)

Schlagworte: Neuseeland, Aerosol-Wolken-Wechselwirkungen, Hemisphärischer Unterschied

Projektleiter:
Koordinator: J. Quaas (johannes.quaas@uni-leipzig.de)
Gilles Bellon, University of Auckland (gilles.bellon@auckland.ac.nz)

Projektmitarbeiter:
Dr. Hailing Jia (hailing.jia@uni-leipzig.de)

Projektbeginn: 1. 4. 2020
Projektende: 31.3.2022

Beschreibung
Die Frage, wie anthropogene Verschmutzungspartikel, sogenannte Aerosole, Wolken, und dadurch die Energiebilanz des Erdsystems beeinflussen, ist eine der wichtigsten Fragen bezüglich der Physik des Klimawandels. Hierbei spielen vor allem niedrige Wolken eine Rolle, und der wichtigste Wolkentyp bezüglich des Einflusses auf die Strahlung sind Stratokumuluswolken. Besonders interessant und mit besonders großer Unsicherheit behaftet ist dabei, inwiefern Stratokumulus auf einen anfänglichen Anstieg der Wolkentröpfchenkonzentration, Nd, aufgrund der anthropogenen Aerosolemissionen, reagieren (Wolkenanpassungen). Dabei sind zwei gegenläufige Senkenprozesse zu untersuchen: (i) Wolkenauflösung via Niederschlagsbildung – höhere Nd führen zu verzögerter Niederschlagsbildung, längerer Wolkenlebensdauer und damit zu einem stärkeren abkühlenden Effekt der Wolken. (ii) Wolkenauflösung durch turbulente Mischung mit der Umgebung und Tröpfchenverdunstung. Bei höhrerer Nd verdunsten die Tröpfchen durch größeres Oberfläche-Volumen-Verhältnis schneller – der gegenteilige Effekt. CHANCE baut auf neuen, komplementären Entwicklungen in Neuseeland und Deutschland auf: Neue Ansätze für die Darstellung und Untersuchung des Wolkenlebenszyklus anhand von hochaufgelösten Modelle (Auckland/NZ) sowie die führende universitäre Rolle in den Entwicklungen des ICON-Atmosphärenmodells (Leipzig/D). Dies ermöglicht wolkenauflösende – mit realistischer Darstellung der Wolkensenkenprozesse – bis globale Simulationen. CHANCE verbindet die Modellierung mit eingehenden Analysen von Beobachtungsdaten insbesondere von Satelliten und wird Stratokumulus für eine große Bandbreite an Wetterbedingungen und Aerosolkonzentrationen in den beiden unterschiedlichen

Hemisphären simulieren; die beiden Wolkenauflösungsprozesse eingehend analysieren; die Modelle prozessorientiert mit Satellitendaten evaluieren und damit Modellverbesserungen vorschlagen; und schließlich den Aerosol-Wolken-Strahlungsantrieb quantifizieren.

Weiterführung: ja

Mittelgeber: BMBF

---

innovative MachIne leaRning to constrain Aerosol-cloud CLimate Impacts (iMIRACLI)

Schlagworte: Aerosol-Wolken-Wechselwirkungen, Maschinelles Lernen, Datenwissenschaften

Projektleiter:
Koordinator: Philip Stier, Universität Oxford (philip.stier@physics.ox.ac.uk)
J. Quaas (johannes.quaas@uni-leipzig.de)

Projektmitarbeiter:
Jessenia Gonzalez Villarreal (jessenia.gonzalezv@uni-leipzig.de)
Julien Lenhardt (julien.lenhardt@uni-leipzig.de)

Projektbeginn: 1.1.2020
Projektende: 31.12.2023

Beschreibung
Climate change is one of the most urgent problems facing mankind. Implementation of the Paris climate agreement relies on robust scientific evidence. Yet, the uncertainty of non-greenhouse gas forcing associated with aerosol-cloud interactions limits our constraints on climate sensitivity. Radically new ideas are required. While the majority of radiative forcing estimates are model based, model uncertainties remain too large to achieve the required uncertainty reductions. The quantification of aerosol cloud climate interactions in Earth Observation data is thus one of the major challenges of climate science. Progress has been hampered by i) the difficulty to disentangle aerosol effects on clouds and climate from their covariability with confounding factors, ii) retrieval issues, iii) a very low signal-to-noise ratio and on the other hand computationally, due to the scale of the “big” datasets (100s of Tb) and their heterogeneity.
Such “big data” challenges are not unique to climate science but occur across a wide range of data sciences. However, innovative techniques and tools developed by the data mining and machine learning community have not yet found their way into climate sciences and climate scientists are currently not trained to capitalise on these advances.
This Marie Curie ITN will train the next generation of climate & data scientists through synergies between climate research and modern data sciences. Its innovative training plan will match students (and supervisors) from climate and data backgrounds, provide them with training in state of the art data and climate science techniques which will be applied to key uncertainties in current climate research. Partners from the data-science and space industry will be closely involved in the projects and provide real-world training opportunities in a commercial context. This will produce a new generation of climate and data scientists, ideally trained for employment in science or commercial data applications.

Weiterführung: ja

Mittelgeber: Europäische Union, Horizon 2020, Marie Curie Innovative Training Network

---

Advancing the Science for Aviation and ClimAte (ACACIA)

Schlagworte: Einfluss von Flugverkehr auf Klima, Aerosol – Wolken – Wechselwirkungen, Kondensstreifen

Projektleiter:
Koordinator: Robert Sausen, Deutsches Zentrum für Luft- und Raumfahrt, Institut für Physik der Atmosphäre (Robert.Sausen@dlr.de)
J. Quaas (johannes.quaas@uni-leipzig.de)

Projektmitarbeiter: Sajedeh Marjani (sajedeh.marjani@uni-leipzig.de)

Projektbeginn: 1.1.2020
Projektende: 31.12.2022

Beschreibung
Non-CO2 emissions of aviation may impact climate as much as aviation's carbon dioxide (CO2) emissions do. However, the impact the non-CO2 effects (e.g., ozone and methane from NOx emissions, contrails, indirect aerosol effects) is associated with much larger uncertainties, some of these effects might result in a relatively large cooling. ACACIA has four aims for scientifically based and internationally harmonised policies and regulations for a more climate-friendly aviation system. (1) We will improve scientific understanding of those impacts that have the largest uncertainty, in particular, the indirect effect of aviation soot and aerosol on clouds. (2) We will identify needs for international measurement campaigns to constrain our numerical models and theories with data and we will formulate several design options for such campaigns. (3) Putting all aviation effects on a common scale will allow providing an updated climate impact assessment. Uncertainties will be treated in a transparent way, such that trade-offs between different mitigation strategies can be evaluated explicitly. This helps our final aim (4) to provide the knowledge basis and strategic guidance for future implementation of mitigation options, giving robust recommendations for no-regret strategies for achieving reduced climate impact of aviation. To this end, ACACIA brings together research across scales (from plume to global scale), from the laboratory experiments to global models, and it proceeds from fundamental physics and chemistry to the provision of recommendations for policy, regulatory bodies, and other stakeholders in the aviation business. Additionally, ACACIA will cooperate with international partners, both research institutions and organisations.

Weiterführung: ja

Mittelgeber: Europäische Union, Horizon2020

Copernicus Atmospheric Monitoring Service 74 - Radiative Forcings

Schlagworte: Aerosol-Strahlungsantrieb, Reanalyse, Aerosol-Wolken-Wechselwirkungen

Projektleiter:
Koordinator: Nicolas Bellouin, Universität Reading (n.bellouin@reading.ac.uk)
J. Quaas (johannes.quaas@uni-leipzig.de)

Projektmitarbeiter: Ph D Johannes Mülmenstädt (johannes.muelmenstaedt@uni-leipzig.de)

Projektbeginn: 1.1.2016
Projektende: 31.7.2020

Beschreibung
Ziel dieses Services des COPERNICUS Atmospheric Monitoring Service ist die Bereitstellung einer Diagnostik für den anthropogenen Strahlungsantrieb durch verschiedene Mechanismen auf Basis der Reanalyse der Atmosphärenzusammensetzung. Beitrag der Uni Leipzig ist hierbei der Strahlungsantrieb durch Aerosol-Wolken-Wechselwirkungen.

Weiterführung: ja

Mittelgeber: Europäische Union, COPERNICUS-Programm, COPERNICUS Atmospheric Monitoring Service (Subcontractor der Uni Reading)

Modellierung von Aerosolen und Aerosol-Wolken-Wechselwirkungen in der Arctis (D02)
Modelling aerosols and aerosol-cloud interactions in the Arctic (D02)

Schlagworte: Arktischer Klimawandel, Aerosol-Wolken-Wechselwirkungen, Modellierung

Projektleiter: Johannes Quaas, Universität Leipzig (johannes.quaas@uni-leipzig.de)

Projektmitarbeiterin:
Iris Papakonstantinou-Presvelou (i.presvelou@uni-leipzig.de)
Jan Kretzschmar (jan.kretzschmar@uni-leipzig.de)
Projektbeginn: 1.1.2016
Projektende: 31.12.2023

Beschreibung
In diesem Beitrag zum SFB/Transregio $(AC)^3$ soll mit Hilfe von globaler Modellierung in Kombination mit verschiedenen Beobachtungen der Einfluss anthropogener Aerosole auf den arktischen Klimawandel untersucht werden. In Kooperation mit dem Leibniz-Institut für Troposphärenforschung liegt hierbei der Schwerpunkt auf dem Meridionaltransport der Aerosole (TROPOS) und der Wechselwirkung von Aerosol mit Wolken (LIM).

Weiterführung: ja

Mittelgeber: Deutsche Forschungsgemeinschaft (DFG) TRR 172 $(AC)^3$

Arktische Rückkopplungsprozesse in Klimamodellen (E01)
Assessment of Arctic feedback processes in climate models (E01)

Schlagworte: Arktischer Klimawandel, Feedbacks, Modellierung

Projektleiter: Johannes Quaas, Universität Leipzig (johannes.quaas@uni-leipzig.de)

Projektmitarbeiterin:
Olivia Linke (olivia.linke@uni-leipzig.de)
Karoline Block (karoline.block@uni-leipzig.de)

Projektbeginn: 1.1.2016
Projektende: 31.12.2023

Beschreibung
In diesem Beitrag zum SFB/Transregio $(AC)^3$ sollen mit Hilfe von globaler Modellierung in Kombination mit verschiedenen Beobachtungen die verschiedenen Klima-Feedback-Mechanismen quantifiziert und in den Klimamodellen evaluiert werden. Spezielles Augenmerk ist hierbei in Kooperation mit der Uni Köln auf dem Wolken-Feedback.

Weiterführung: ja

Mittelgeber: Deutsche Forschungsgemeinschaft (DFG) TRR 172 $(AC)^3$

Aerosol-Wolke-Niederschlag-Wechselwirkungen über Gebieten von Emissionsquellen
Aerosol-cloud-rainfall interactions over emission source regions

Schlagworte: Aerosol-Wolken-Niederschlagswechselwirkungen, Solar dimming

Projektleiter:
Koordinator: Dr. Ribu Cherian, Universität Leipzig (ribu.cherian@uni-leipzig.de)

Projektmitarbeiter: Dr. Ribu Cherian (ribu.cherian@uni-leipzig.de)

Projektbeginn: 15.3.2017
Projektende: 14.3.2020

Beschreibung (Deutsch)
Aerosol-Wolken-Wechselwirkungen stellen einen der wesentlichen Unsicherheitsfaktoren bei Verständnis und Quantifizierung der geographischen Verteilung von Wolken- und Niederschlagseigenschaften, aber auch des Strahlungsantriebs des globalen Klimawandels dar. Die grundlegende Idee des Projekts ist es, regional unterschiedliche Trends in anthropogenenen Emissionen von Aerosolen zu nutzen, um deren Einfluss auf Trends in Wolken-, Niederschlags- und Strahlungsgrößen zu bestimmen. Hierzu sollen verschiedene Szenarien in Multi-Klimamodell-

Ensembles ("historische" Simulationen mit allen Strahlungsantrieben und "Aerosol"-Simulationen mit allen Antrieben außer anthropogenem Aerosol) analysiert werden und mit Beobachtungsdaten verglichen werden. Konkret werden vier Fragen untersucht:
(i) Welche Beziehung besteht zwischen regionalen Trends in Aerosolemissionen und Wolken-Strahlungs-Effekten? - Diese Studien analysieren Simulationen aus dem Multi-Modell-Ensemble.
(ii) Wie erfolgreich reproduzieren die Modelle beobachtete Trends? Hier werden die Klimamodelle mit Beobachtungsdaten verglichen.
(iii) Welchen Einfluss haben Emissionstrends für Aerosole und resultierende Strahlungsantriebe auf die atmosphärische Zirkulation? Simulationen mit dem Aerosol-Klima-Modell ECHAM6-HAM2 sollen für drei Zeitscheiben durchgeführt und analysiert werden.
(iv) Welche Rolle spielen Emissionstrends für Änderungen in Extremniederschlägen in Südost-Asien? - Mit speziellen Simulationen sollen die verschiedenen Hypothesen getestet werden.

Beschreibung (Englisch)

The basic idea of the project is to use regionally different trends in anthropogenic emissions of aerosols to determine their impact on trends in cloud, precipitation and radiation levels.

Weiterführung: nein

Mittelgeber: Deutsche Forschungsgemeinschaft (DFG) (Eigene Stelle), CH 1881/1-1

Atmosphären-Modelldaten: Datenqualität, Kurationskriterien und DOI-Branding
Atmospheric model data: data quality, curation criteria, and doi-branding

Projektleiter: Prof. Dr. Johannes Quaas (johannes.quaas@uni-leipzig.de)
Projektmitarbeiter:
Jan Kretzschmar (jan.kretzschmar@uni-leipzig.de)
Dr. Johannes Mülmenstädt (johannes.muelmenstaedt@uni-leipzig.de)

Projektbeginn: 1.6.2019
Projektende: 31.05.2022

Beschreibung
Der Austausch und die Interpretation von Klimamodelldaten sind weit über die Klimaforschungsgemeinschaft hinaus von Bedeutung, werden jedoch aktuell durch das Fehlen übergreifender qualitätssichernder Maßnahmen und abgestimmter Kurationskriterien erschwert. In der Meteorologie und Klimaforschung bereits etablierte Datenqualitäts- und Datenkurationsstandards zur Gewährleistung effektiver Teil- und Nachnutzbarkeit der Forschungsdaten finden primär in großen, international koordinierten Modellvergleichsstudien (MIPs, z.B. Coupled Model Intercomparison Project - CMIP) ihre Anwendung. In diesem Vorhaben werden diese auf CMIP fußenden Standards und Konventionen im Austausch mit den Fachcommunities systematisch in weiteren Bereichen der Meteorologie und Klimaforschung angepasst: Zum einen an die Bedürfnisse kleinerer MIPs, für die eine volle CMIP-Adaptierung nicht sinnvoll erscheint und zu aufwändig ist. Zum anderen in der Stadtklimaforschung mit ihren sehr hochauflösenden Daten, einem Forschungsbereich ohne etablierten Datenstandard. Die Ergebnisse werden in der Praxis auf existierende Atmosphärenmodelldaten angewendet (Datenaufbereitung

sowie Langzeitarchivierung) und auf ihre universelle Nutzbarkeit hin evaluiert. Die Ergebnisse etablieren zudem auf weitere Bereiche der Klimaforschung anwendbare Blaupausen für Kurationskriterien und Standardisierungen, die eine Reproduzierbarkeit und Prüfbarkeit signifikant erhöhen und darüber hinaus eine interdisziplinäre Nachnutzung von Klimamodelldaten unterstützen. Darüber hinaus wird, um Nachnutzern die Auswahl von Forschungsdaten zu erleichtern, zum einen eine fachspezifische Erweiterung des DataCite Metadatenschemas vorgenommen. Eine zwingend mit einem DOI-Branding verbundene, für Nutzer deutlich sichtbare, anspruchsvollere Qualitätsprüfung für disziplinspezifische Daten und Kurationsprozesse stärkt die Wertigkeit der DataCite DOIs und erhöht das Vertrauen bei der Nachnutzung. Zum anderen wird im Sinne der FAIR-Prinzipien ein maschinenlesbares Fachvokabular auf Basis von DCAT (W3C Data Catalog Vocabulary) bereitgestellt. Eine nachhaltige Anwendung des universellen Datenstandards, der Prozesse zur Kuratierung und Qualitätssicherung sowie auch die Vergabe fachspezifischer DataCite DOI's werden durch die Angebote der beiden beteiligten Infrastrukturdienstleister dauerhaft gesichert und die Etablierung über den Bereich der Meteorologie und Klimaforschung hinaus ermöglicht. Die Verbindung von national und international stark vernetzten Partnern aus der Klimaforschung (Universität Hamburg, Universität Leipzig) mit einem Infrastrukturbetreiber aus der Klimaforschung (DKRZ) sowie der Zentralen Fachbibliothek für Technik und Naturwissenschaften (TIB) im AtMoDat-Konsortium bürgt für eine hochwertige, alle Aspekte dieses Vorhabens abdeckende Kompetenz und eine weitreichende, nachhaltige Aufnahme der Ergebnisse in diesem Forschungsgebiet. AtMoDat ist darüber hinaus fachübergreifend Impulsgeber für Verbesserungen im Forschungsdatenmanagement.

Weiterführung: ja

Mittelgeber: BMBF Bundesministerium für Bildung und Forschung, 16QK02B

Besser bestimmes Aerosolforcing für verbesserte Klimaprojektionen (FORCES)
Constrained aerosol forcing for improved climate projections (FORCES)

Projektleiter: Prof. Dr. Johannes Quaas(johannes.quaas@uni-leipzig.de)
Projektmitarbeiter: Dr. Dipu Sudhakar (dipu.sudhakar@uni-leipzig.de)
Dr. Tom Goren (tom.goren@uni-leipzig.de)

Projektbeginn: 1.10.2019
Projektende: 30.09.2023

Beschreibung (Deutsch)
FORCES strebt eine bessere Quantifikation des Klimaantriebs durch Aerosole an, mit dem Ziel, Klimavorhersagen zu verbessern.

Beschreibung (Englisch)
FORCES aims at constraining the aerosol-climate forcing in order to improve climate projections.

Weiterführung: ja

Mittelgeber: Europäische Union

Besser bestimmte Unsicherheit für multi-dekadische Klimavorhersagen (CONSTRAIN)
Constraining uncertainty of multi decadal climate projections (CONSTRAIN)

Projektleiter: Prof. Dr. Johannes Quaas (johannes.quaas@uni-leipzig.de)
Projektmitarbeiterin: Dr. Karoline Block (karoline.block@uni-leipzig.de)

Projektbeginn: 1.6.2019
Projektende: 30.05.2023

Beschreibung (Deutsch)
Verschiedene unsichere Aspekte in multi-dekadischen Klimavorhersagen werden in CONSTRAIN besser bestimmt, darunter effektiver Strahlungsantrieb und transiente Klimasensitivität.

Beschreibung (Englisch)
Several uncertain aspects for multi-decadal climate projections will be constrained in CONSTRAIN, among which the effective radiative forcing and transient climate sensitivity.

Weiterführung: ja

Mittelgeber: Europäische Union

FOR 2820 Teilprojekt: Einfluss von Vulkanen auf Wolken (VolCloud)
FOR 2820 Teilprojekt: Cloud response to Volcanic eruptions (VolCloud)

Projektleiter: Prof. Dr. Johannes Quaas (johannes.quaas@uni-leipzig.de)
Projektmitarbeiterin: Mahnoosh Haghighatnasab (mahnoosh.haghighatnasab@uni-leipzig.de)

Projektbeginn: 1.3.2019
Projektende: 28.02.2022

Beschreibung (Deutsch)
Wolken spielen eine Schlüsselrolle für die Energiebilanz der Erde. Sie reagieren auf Änderungen in Aerosolen auf verschiedene Weise, und diese Reaktionen sind jeweils einerseits mit großen Unsicherheiten behaftet und andererseits potentiell sehr relevant in ihrer Auswirkung auf Energiebilanz und Klima. (i) Flüssigwasserwolken werden von Aerosol, das als Wolkenkondensationskeim (CCN) dient, verändert. Die Tröpfchenkonzentration wird vergrößert, und dies hat Veränderungen von mikrophysikalischen Wolken- und Niederschlagsprozessen einerseits, und Wolkendynamik (etwa das Einmischen von trockener Umgebungsluft) andererseits zur Folge. Hierbei ist es vor allem wichtig, die Änderung von Bedeckungsgrad und Flüssigwasserweg der Wolken zu quantifizieren. (ii) Eis- und Mischphasenwolken werden, je nach Eisbildungsmechanismus, durch CCN, aber auch Eiskeime verändert. Veränderungen der komplexen Wolken- und Niederschlagsprozesse sind die Folge. (iii) Die Störung der Energiebilanz bedeutet Änderungen in thermodynamischen Profilen und Zirkulation durch schnelle Anpassungen, auf die Wolken wiederum reagieren. Es ist die Summe aus den ursprünglichen

Wolkenänderungen und diesen Anpassungen, aus denen sich die effektive Änderung der Strahlungsbilanz zusammensetzt. (iv) Wird hochreichende Konvektion beeinflusst, können Gewitter sich intensivieren, und der Transport zwischen Troposphäre und Stratosphäre kann verändert werden. Dies hat möglicherweise bedeutende Auswirkungen auf die Zirkulation und das Klima. Diese Fragestellungen sind besonders im Kontext von Vulkanausbrüchen relevant: (a) ein Vulkanausbruch bedeutet eine vergleichsweise gut definierte und gegebenenfalls bedeutende Störung des atmosphärischen Aerosols, aus exogener Quelle. Die Beobachtung der Wolkenreaktion auf einen Vulkanausbruch ist daher eine einzigartige Gelegenheit, um Aerosol-Wolken-Niederschlags- Wechselwirkungen zu untersuchen. (b) Die Reaktion der Wolken beeinflusst die Auswirkung des Vulkanausbruchs auf die Strahlung. Es ist daher essentiell, die Wolkenreaktion angemessen zu quantifizieren, um die Klimawirkung zu beurteilen. VolCloud geht diese Fragen und Herausforderungen an, indem drei verschiedene Typen von Vulkanausbrüchen in der Vergangenheit untersucht werden (eine massive Änderung des troposphärischen Sulfats durch den Holuhraun; eine Eruption, die auch Eiskeime emittiert hat, von Eyjafjallajökull; sowie die größte von Satelliten beobachtete Eruption, Mt. Pinatubo). Hierbei werden Modellsimulationen mit detaillierter Darstellung von Wolken und Aerosol mit Wolkensystem-auflösender Diskretisierung (ICON-NWP-ART, 2 km Auflösung) in Kombination mit Satellitebeobachtung aus passiver und – soweit verfügbar – aktiver Fernerkundung. VolCloud arbeitet eng mit den anderen VolImpact-Projekten zusammen, wobei insbesondere die Möglichkeiten der höheraufgelösten, aber beschränkteren Simulationen einerseits und der gröber aufgelösten, aber globalen Simulationen einerseits ausgewertet werden.

Beschreibung (Englisch)

Clouds are a key modulator of the Earth energy budget. They respond to perturbations in aerosol in various ways, and all these pathways are uncertain yet of potentially very large importance when assessing the impact of the aerosol perturbation on the Earth energy budget and on climate. (i) Liquid-water clouds respond to the perturbation in aerosols serving as cloud condensation nuclei (CCN). Cloud droplet number concentration is perturbed, and this entails perturbations to cloud- and precipitation microphysical processes, but also to cloud dynamics responses (e.g. altered entrainment rates of dry air into the clouds). The most relevant question is how cloud fraction and cloud liquid water paths respond to this perturbation. (ii) Ice- and mixed- phase clouds respond to both CCN and ice nucleating particle concentration changes, depending on the ice formation mechanism. Modifications of intricate cloud and precipitation processes follow. (iii) The change in the energy budget leads to alterations in thermodynamic profiles and in atmospheric circulation via rapid adjustments, and clouds respond to these as well. It is the sum of the initial cloud perturbation and these adjustments that composes the effective perturbation of the Earth energy budget. (iv) When deep convective clouds are altered, thunderstorms may become more intense, and transport from the troposphere into the stratosphere may be altered, with strong consequences for circulation and climate. These questions are particularly relevant when considered in the context of volcanic eruptions for two reasons: (a) the volcanic eruption is a relatively well-defined and occasionally strong perturbation to the atmospheric aerosol concentration that is exogenous to the atmosphere system. The observation of the cloud response to volcanic eruption thus is a unique opportunity to study the aerosol- cloud-precipitation interactions. (b) the cloud response may strongly modulate, and likely enhance, the radiative impact of a volcanic eruption. It is thus crucial to adequately quantify the cloud response, in order to assess the climate response. VolCloud will address these questions and challenges by investigating three different types of past volcanic eruptions (a massive sulfur perturbation to the troposphere, Holuhraun; an eruptive perturbation that also emitted INP, Eyjafjallajökull; and the largest eruption in the satellite era, Mt. Pinatubo) using model simulations with a detailed cloud

and aerosol representation, resolving cloud systems (ICON-NWP-ART at 2 km resolution), in combination with satellite observations from passive and – where available – active remote sensing. VolCloud intensely collaborates with the other projects within VolImpact, reaching out to what can be learned from simulations at finer but in extent more limited, and coarser but global scale.

Weiterführung: ja

Mittelgeber: DFG Deutsche Forschungsgemeinschaft ,QU 311/23-1

Klimamodell-PArametrisierungen – Revision mit Hilfe von RAdar (PARA)
Climate model PArameterizations informed by RAdar (PARA)

Projektleiter: Prof. Dr. Johannes Quaas (johannes.quaas@uni-leipzig.de)
Projektmitarbeiterin: Sabine Hörnig (sabine.hoernig@uni-leipzig.de)

Projektbeginn: 1.1.2019
Projektende: 31.12.2021

Beschreibung (Deutsch)
Die adäquate Darstellung diabatischer Wolken- und Niederschlagsprozesse ist eine besondere Herausforderung für Klimamodelle, da diese räumlich nicht aufgelösten Prozesse mittels subskaliger Parameterisierungen repräsentiert werden. Diese müssten mit Hilfe von Beobachtungen und/oder prozessauflösenden Simulationen erstellt und evaluiert werden. Radarpolarimetrie liefert die am Besten geeingeten Beobachtungen für die Wolken- und Niederschlagsmikrophysik dank der Ableitung mikrophysikalischer Zustandsgrößen und der Prozesserkennung. In der ersten Phase von PROM wird das Projekt PARA die räumliche Heterogenität des Eiswassergehalts sowie die Niederschlagsbildung über de Eisphase betrachten; in der zweiten Phase wird die Betrachtung von Mischphasenprozessen wie Bereifung, und die Rolle der Variabilität der Partikelanzahlkonzentration hinzukommen. PARA betrachtet dabei mit Hilfe von polarimetrischen Radarbeobachtungen und der Evaluierung und Revision der Parametrisierungen im ICON-Klimamodell die vier Prozesse, die für die Bestimmung von aus der Eisphase gebildeten Niederschlag am Boden relevant sind: (i) die Eisbildung und die räumliche Heterogenität des Eiswassergehalts auf bezüglich des ICON-GCM subskaligen Dimensionen, (ii) die Rolle dieser Variabilität für die Schneebildung durch den Aggregationsprozess, (iii) das Schmelzen von Schnee bei Temperaturen über 0°C, und (iv) die Verdunstung von Regen unterhalb der Schmelzschicht.

Beschreibung (Englisch)
An adequate representation of moist diabatic processes in clouds and precipitation in climate models is challenging, because these spatially unresolved processes are subject to sub-grid parameterizations, which must be informed by observations and/or models resolving these processes. Radar polarimetry provides most suitable observations on cloud and precipitation microphysics via microphysical retrievals and process fingerprints. PARA will focus in Phase I of PROM on ice water content heterogeneity and precipitation generation via the ice phase and concentrate on mixed-phase processes including riming and the role of particle number concentration variability in Phase II. PARA will investigate four processes both by polarimetric radar

retrievals and the evaluation and revision of their representation in the ICON general circulation model: (i) ice generation and spatial heteorogeneity of ice water content at ICON-GCM sub-grid scales, (ii) the role of both in snow formation like aggregation, (iii) melting of snow falling through the 0°C isotherm, and (iv) evaporation of rain below the melting layer.

Weiterführung: ja

Mittelgeber: DFG Deutsche Forschungsgemeinschaft, QU 311/21-1

Hochatmosphäre, Christoph Jacobi
Upper Atmosphere

Large-scale dynamical impacts on regional Arctic climate change
Der Einfluss großräumiger Dynamik auf regionale arktische Klimaänderungen

Schlagworte: Arktische Verstärkung, Klimavariabilität

Projektleiter:
Prof. Dr. Christoph Jacobi (jacobi @ rz.uni-leipzig.de), Prof. Dr. Johannes Quaas (johannes.quaas @ uni-leipzig.de)

Projektmitarbeiter: Daniel Mewes

Projektbeginn: 1.1.2016
Projektende: 31.12.2023

Beschreibung
Das Projekt umfasst die Wechselwirkung zwischen der variablen großskaligen Zirkulation und regionalen arktischen Klimaänderungen und der Diagnose der arktischen Verstärkung auf regionaler Skala als Reaktion auf Variationen großskaliger Zirkulation in der Vergangenheit sowie in Klimaszenarien zukünftigen Klimwandels. Es werden hierzu Reanalysedaten und CMIP5-Modellergebnisse herangezogen und eigene Modellsimulationen durchgeführt. Die Kopplung von Troposphäre und Stratosphäre als wichtiger Bestandteil der Variabilität der polaren Atmosphäre wird auch mit numerischen Simulationen untersucht.

Weiterführung: ja

Mittelgeber: Deutsche Forschungsgemeinschaft, SFB-Transregio 172

Effeke lokalen Schwerewellenantriebs auf die mittlere Atmosphäre

Middle atmosphere effects of localized gravity wave forcing (MATELO)

Schlagworte: Schwerewellen, mittlere Atmosphäre, residuelle Zirkulation, Globale Navigationssatellitensysteme, planetare Wellen

Projektleiter:
Prof. Dr. Christoph Jacobi (jacobi @ rz.uni-leipzig.de)

Projektmitarbeiter:
N. Samtleben

Projektbeginn: 1.1.2017
Projektende: 31.3.2020

Beschreibung
Das Projekt beinhaltet eine Studie der Auswirkungen einer begrenzten Region erhöhter atmosphärischer interner Schwerewellenaktivität und Schwerewellenrechens auf die mittlere Atmosphäre. Die Charakteristik solch einer Region, ihre räumlich und zeitliche Variabilität und Verbindung zu anderen Klimaparametern wird anhand von GPS Radiookkultationsanalysen untersucht. Es werden Algorithmen zur dreidimensionalen Analyse der Wellenreibung und der Brewer-Dobson-Zirkulation (BDC) verwendet; als Datengrundlage dienen Simulationen mit einem mechanistischen Zirkulationsmodell der mittleren Atmosphäre und Reanalysedaten. Die dreidimensionaler Variabilität der BDC und die Rolle lokalisierter erhöhte Schwerewellenaktivität wird so untersucht. Weiterhin wird die Anregung und folgende Ausbreitung planetarer Wellen durch eine Region erhöhter Schwerewellenaktivität untersucht. Die Auswirkungen auf die Polarregionen (mittlere Zirkulation, Präkonditionierung, winterliche Stratosphärenerwärmungen) und auf die äquatoriale Stratosphäre (Einfluss auf Tropopausenbrüche und Stratosphäre-Troposphäre-Austausch) werden untersucht. Weiterhin wird der Einfluss lokalisierten Schwerewellenbrechens auf die mittlere Zirkulation der Mesosphäre analysiert, insbesondere im Hinblick auf stationäre Wellen, und ihre Variabilität. Das Projekt ist eine Kooperation zwischen dem LIM und dem Department Atmosphärenphysik, Karls-Universität Prag.

Weiterführung: nein

Mittelgeber: Deutsche Forschungsgemeinschaft (DFG JA 836/32-1)

6-stündige Gezeiten in den mittleren Atmosphäre (QuarTA)
Quarterdiurnal tide in the middle atmosphere (QuarTA)

Schlagworte: mittlere Atmosphäre; Gezeiten; Ionosphäre

Projektleiter:
Prof. Dr. Christoph Jacobi (jacobi @ rz.uni-leipzig.de)

Projektmitarbeiter:
C. Geißler

Projektbeginn: 1.2.2017
Projektende: 31.3.2020

Beschreibung
Die Dynamik der Mesosphäre und unteren Thermosphäre wird zu großen Teilen von solaren Gezeiten dominiert. Eine davon ist die 6-stündige Gezeit (quarterdiurnal tide, QDT), die unter anderem in sporadischen E-Schichten und mit Hilfe von Radar- und Satellitenmessungen beobachtet wurde. Während allerdings die ganztägigen, halbtägigen, und auch 8-stündigen Gezeiten vergleichsweise gut dokumentiert und untersucht sind, sind Beobachtungen und Analysen der - weniger starken aber nichtsdestoweniger als ein Bestandteil der dynamischen Prozesse in ihrer Gesamtheit zu sehenden - 6-stündigen Komponente bislang selten. Um diese Lücke zu schließen, werden innerhalb des QuarTA-Projekts die 6-stündigen Gezeiten und ihre Antriebsmechanismen im Detail untersucht. Die Klimatologie der Gezeiten wir mit Hilfe von Meteorradarwindmessungen, vor allem der Langzeitreihe in Collm, ergänzt durch weitere Radarmessungen, erstellt. Die globale Verteilung der Gezeitenamplituden wird mit Hilfe von Ionosonden- und GPS-Radiookkultationsmessungen sporadischer E-Schichten untersucht, und die Beobachtungen in Verbindung mit Windscherungen aus Radarmessungen und numerischen Simulationen interpretiert. Um Einblick in die hauptsächlichen Anregungsmechanismen der 6-stündigen Gezeiten zu erhalten, wird ein nichtlineares mechanistisches Zirkulationsmodell, welches auch die Anregung durch Absorption solarer Strahlung enthält, verwendet. Hierbei wird, einzeln und in Kombination, die Anregung der 6-stündigen Gezeit durch Absorption solarer Strahlung und durch nichtlineare Wechselwirkung von Gezeiten in den Simulationen ausgeschaltet, so dass die Hauptantriebsquelle erkennbar wird. Innerhalb des QuarTA-Projekts wird daher, durch die Kombination von Beobachtungen und Modellsimulationen, ein vertiefter Einblick in die Klimatologie und die Anregung der 6-stündigen Gezeiten ermöglicht, der bislang noch nicht in ausreichendem Maße gegeben ist.

Weiterführung: nein

Mittelgeber: Deutsche Forschungsgemeinschaft (DFG JA 836/34-1)

Verzögerte Antwort der Ionosphäre auf Variationen des solaren EUV (DRIVAR)
Delayed response of the ionosphere to solar EUV variability (DRIVAR)

Schlagworte: Ionosphäre, solare Variabilität

Projektleiter:
Prof. Dr. Christoph Jacobi (jacobi @ rz.uni-leipzig.de)

Projektmitarbeiter:
R. Vaishnav

Projektbeginn: 1.5.2017
Projektende: 30.11.2021

Beschreibung

Das ionosphärische Plasma reagiert auf Änderungen der ionosphärischen EUV und UV-Strahlung auf der Zeitskala der solaren Rotation mit einer Verzögerung von 1-2 Tagen. Es wird angenommen, dass diese Verzögerung auf Transportprozesse von der unteren Ionosphäre in die F-Region zurück zu führen ist, doch wurden bislang nur begrenzte Modelluntersuchungen durchgeführt, um diesen Zusammenhang zu belegen. Innerhalb von DRIVAR sollen die Prozesse, die für die ionosphärische Verzögerung verantwortlich sind, durch umfassende Datenanalyse und Modellierung untersucht werden. Verschiedene solare Proxies sowie spektral aufgelöste EUV- und UV-Flüsse aus Satellitenmessungen werden verwendet und zusammen mit ionosphärischen Parametern analysiert, welche aus GPS-Radiookkultationsmessungen, Ionosondenmessungen und GPS-Gesamtelektronenmessungen stammen. Letztere haben sowohl den Vorteil einer globalen Abdeckung als auch einer z.T. räumlich hoher Auflösung. Die ionosphärsche Verzögerung wird auf verschiedenen Zeitskalen ionosphärischer Variation (Tage, solare Rotation, saisonal) untersucht, und regionale Abhängigkeiten werden analysiert. Wegen des komplexen Charakters der involvierten Prozesse in der Thermosphäre und Ionosphäre werden Experimente mit numerischen Modellen benötigt, um die der Verzögerung zugrundeliegenden Prozesse physikalisch zu untersuchen. Wir verwenden das Coupled Thermosphere Ionosphere Plasmasphere Electrodynamics (CTIPe), um die Verzögerung zu simulieren und führen Sensitivitätsstudien durch um die zur ionosphärischen Verzögerung führenden Prozesse im Detail zu analysieren. Die Ergebnisse von DRIVAR werden zu einem verbesserten Verständnis ionosphärischer Prozesse führen und werden insbesondere in der Vorhersage ionosphärischer Variabilität Anwendung finden, z.B. bei der Analyse und Vorhersage von GNSS- Positionsfehlern.

Weiterführung: ja

Mittelgeber: Deutsche Forschungsgemeinschaft (DFG JA 836/33-1)

Nicht-zonale Strukturen der Dynamik der Mesosphäre/unteren Thermosphäre in mittleren Breiten (NOSTHEM)
Non-zonal Structures of Mesosphere/lower Thermosphere Dynamics at Middle Latitudes (NOSTHEM)

Schlagworte: mittlere Atmosphäre; Radarmessungen

Projektleiter:
Prof. Dr. Christoph Jacobi (jacobi @ rz.uni-leipzig.de)

Projektmitarbeiter:
F. Lilienthal

Projektbeginn: 1.9.2018
Projektende: 31.8.2022

Beschreibung
In NOSTHEM sollen zonale Unterschiede des mittleren Windes, Gezeitenparameter, planetarer Wellen und Schwerewellen in der Mesosphäre und unteren Thermosphäre untersucht und erklärt werden. Ihr Einfluss auf die Repräsentativität einzelner Messungen für ein zonales Mittel von mittlerem Wind und Wellen wird bestimmt werden. Dies soll eine quantitative Einschätzung der

Unsicherheiten von mittlerer Klimatologie, Langzeittrends und Maßen für die Variabilität auf der Basis einzelner Messungen ermöglichen. Der Beitrag nicht-zonaler Strukturen auf die mittlere Zirkulation und ihre Variabilität wird bestimmt. Hemisphärische Analysen von Wellen und Zirkulation in der unteren und mittleren Atmosphäre werden verwendet, um deren Rolle bei der Bildung longitudinaler Unterschiede zu klären. Dies wird auch die Frage beantworten, ob die schon seit langem beobachteten Unterschiede des mesosphärischen Windes über Mittel- und Osteuropa signifikant sind und wenn ja, welche Prozesse zu deren Auftreten beitragen.
In NOSTHEM werden Beobachtungen zweier praktisch identischer VHF-Meteorradare auf ähnlicher geographischer Breite, aber mit 36° Längenunterschied herangezogen. Daher kann daraus der Beitrag nicht-zonaler Strukturen zur lokalen Klimatologie und Variabilität ermittelt werden. Um ein umfassendes hemisphärisches Bild zu erhalten, werden die lokalen Radarmessungen durch Satellitenbeobachtungen und Reanalysedaten ergänzt, sowie numerische Simulationen mit einem Zirkulationsmodell der mittleren Atmosphäre durchgeführt.
Die Hauptziele von NOSTHEM sind (1) eine quantitative Darstellung von Ähnlichkeiten und Unterschieden der mesosphärischen/thermosphärischen Zirkulation an zwei Längengraden, (2) eine Erweiterung dieser Analyse durch hemisphärische Daten und (3) eine Quantifizierung der Rolle von Wellen bei der Ausprägung der Zirkulation an einzelnen Orten. Als Endziel werden nicht-zonale Strukturen und ihre Gründe und die zu ihnen führenden Prozesse geklärt, und auch Hinweise für die Interpretation von Klimatologie und Variabilität an einzelnen Orten in Bezug auf die gesamthemisphärische Dynamik gegeben.
NOSTHEM wird als Kooperation des Instituts für Meteorologie, Universität Leipzig und des radiophysikalischen Departments, Universität Kasan gemeinsam durchgeführt.

Weiterführung: ja

Mittelgeber: Deutsche Forschungsgemeinschaft (DFG JA 836/38-1)

Wellenkopplung der mittleren und oberen Atmosphäre: Jahr-zu-Jahr-Variabilität und Langzeittrends (VACILT)
Wave coupling processes of the middle and upper atmosphere: Interannual and long-term variability (VACILT)

Schlagworte: mittlere Atmosphäre; Hochatmosphäre, Langzeittrends

Projektleiter:
Prof. Dr. Christoph Jacobi (jacobi @ rz.uni-leipzig.de)

Projektmitarbeiter:
A. Kuchar

Projektbeginn: 1.5.2019
Projektende: 30.6.2022

Beschreibung
Die langfristigen Änderungen in der Hochatmosphäre werden durch dynamische Prozesse der darunterliegenden Schichten beeinflusst. Diese meteorologischen Einflüsse werden vor allem durch Wellen hervorgerufen, die sich von der unteren Atmosphäre in die Thermosphäre

ausbreiten. Indem sie Energie und Impuls transportieren, modifizieren sie thermosphärische und ionosphärische Parameter. Wellen in der Atmosphäre werden nicht nur vom Zustand der unteren und mittleren Atmosphäre beeinflusst, sondern weisen auch Langzeittrends auf. Daher trägt nicht nur die bekannte Abkühlung durch die Zunahme von Treibhausgasen zu langfristigen Änderungen in der Thermosphäre bei, sondern auch Trends der Wellenaktivität, so dass eine umfassende Beschreibung hochatmosphärischer Variabilität auch Trends der Wellen beinhalten muss.
Um die Auswirkung von Wellen auf die Kopplung von mittlerer und oberer Atmosphäre zu quantifizieren, zielt das Projekt VACILT auf die Beobachtung und Simulation von Wellen, sowie die Quantifizierung ihrer Variabilität und die Analyse ihrer Auswirkungen auf die Thermosphäre. Dazu werden langfristige (> 30 Jahre) Radarbeobachtungen herangezogen und Ergebnissen einer Langzeitsimulation mit dem GAIA-Erdsystemmodell gegenübergestellt, welche wiederum durch Beobachtungen thermosphärischer Parameter gestützt werden.
Die GAIA-Analysen erlauben es, die Auswirkungen atmosphärischer Wellen in der Thermosphäre zu quantifizieren und mit der Variabilität der atmosphärischen Zirkulation in Verbindung zu bringen. Die Ergebnisse werden mit Hilfe von Sensitivitätsstudien unter Verwendung eines mechanistischen Zirkulationsmodells gestützt.
Die Ziele von VACILT sind demnach die folgenden: (1) Quantifizierung der Variabilität der Wellen in der mittleren Atmosphäre auf der Basis von Radarbeobachtungen und GAIA-Analysen (2) quantitative Bestimmung der Auswirkung von Wellenkopplung auf die Hochatmosphäre und (3) die umfassende Analyse des Beitrags von Wellen auf Trends in der Thermosphäre/Ionosphäre, gegenüber dem Beitrag von Treibhausgasen und deren Änderung. Das Erreichen dieser Ziele wird die Rolle von Wellen auf die Thermosphäre/Ionosphäre klären, und hat damit direkte Anwendung z.B. in der Vorhersage der Genauigkeit von Kommunikations-/Navigationssignalen.
VACILT ist ein gemeinsames Projekt der Universität Leipzig mit dem Leibniz-Institut für Atmosphärenphysik, Kühlungsborn und dem Department of Earth and Planetary Sciences, Universität Kyushu, Japan. Damit können die Ressourcen der jeweiligen Partner, nämlich Radarbeobachtungen und mechanistische Modelle auf deutscher, Erdsystemmodellierung und thermosphärischer Satellitenanalysen auf japanischer Seite, optimal kombiniert werden.

Weiterführung: ja

Mittelgeber: Deutsche Forschungsgemeinschaft (DFG JA 836/43-1)

Junior-Professorin Dr. Heike Kalesse

Fernerkundung; Heike Kalesse
AG Fernerkundung der Atmosphäre und das Arktische Klimasystem

---

Bodengebundene Fernerkundung der Atmosphäre zur Verbesserung der Charakterisierung mikrophysikalischer Wolkeneigenschaften sowie der Leistungsprognose erneuerbarer Energien

Ground-based remote sensing of the atmosphere for improving the characterization of microphysical cloud properties and for improving the load prediction of renewable energies

Schlagworte: bodengebundene Fernerkundung, erneuerbare Energien, Wolkenretrieval, DACAPO-PESO

Projektleiter: H. Kalesse (heike.kalesse@uni-leipzig.de), A. Ehrlich (a.ehrlich@uni-leipzig.de), M. Schäfer (michael.schaefer@uni-leipzig.de), M. Wendisch (m.wendisch@uni-leipzig.de)
Projektmitarbeiter: AP1: M. Lochmann (moritz.lochmann@uni-leipzig.de), AP2: W. Schimmel (willi.schimmel@uni-leipzig.de), AP3: J.Stapf (johannes.stapf@uni-leipzig.de)

Projektbeginn: 1.9.2018
Projektende: 31.8.2021

Beschreibung
Die bodengebundene Fernerkundung der Atmosphäre dient sowohl der Grundlagenforschung von Wolken und Niederschlag, als auch im operationellen Dienst der Wettervorhersage als ein wichtiger Baustein für die Leistungsprognose erneuerbarer Energien. Innerhalb dieses Projekts gibt es zwei Hauptzielstellungen: Zum einen wird analysiert werden, wie künstliche neuronale Netze (KNN) zur Leistungsprognose von Photovoltaik- und Windkraftanlagen optimiert werden können, wenn zusätzliche Daten von Wetterstationen und bodengebundenen Fernerkundungsmessungen implementiert werden. Zum anderen sollen in zwei weiteren Teilprojekten für Wolkenbeobachtungen Ableitungsalgorithmen (Retrievals) weiterentwickelt werden, um die Bestimmung von Wolkeneigenschaften zu verbessern und zu erweitern. Dabei stehen Messgerätesynergien zur Ableitung der Wolkentröpfchenkonzentration sowie die Entwicklung anwendungsspezifischer KNN zur Charakterisierung der Verteilung von Flüssigwasser in Mischphasenwolken im Vordergrund.

Das Projekt ist in drei Arbeitspakete unterteilt:
AP1: Test des Einflusses zusätzlicher Messdaten von Wetterstationen und aus der bodengebundenen Fernerkundung auf die Leistungsprognose von PV- und Windkraft-Anlagen mittels künstlicher Neuronaler Netze (KNN)

AP2: Entwicklung eines auf Wolkenradar- und Lidar basierendem KNN zur Detektion von Flüssigwasser in Wolken

AP3: Entwicklung einer auf synergistischen Fernerkundungsmessungen basierenden Methode zur Ableitung der Wolkentröpfchenkonzentration

Description
Ground-based remote sensing of the atmosphere serves both, the basic research of clouds and precipitation, and in the operational service of weather forecasting as an important building block for the power prognosis of renewable energies. Within this project there are two main objectives: Firstly, it will be analysed how artificial neural networks (ANN) can be optimized for power forecasting of Photovoltaics (PV) and wind turbines, if additional data from weather stations and ground-based remote sensing measurements are implemented. On the other hand, in two further subprojects for cloud observations, retrieval algorithms will be developed to improve and extend the determination of cloud properties. The focus will be on instrument synergies for the derivation of cloud droplet concentrations and the development of application-specific ANN for the characterization of the distribution of liquid water in mixed-phase clouds.

The project is divided into three work packages:
AP1: Testing the influence of additional measurement data from weather stations and ground-based remote sensing on the power prognosis of PV and wind power plants using artificial neural networks (ANN)
AP2: Development of a cloud radar and lidar based ANN for detection of liquid water in clouds
AP3: Development of a cloud droplet concentration retrieval based on synergistic remote sensing observations

Weiterführung: ja

Mittelgeber: ESF - Sächsische Aufbaubank (SAB), Antragsnummer : 100339509

PICNICC - Durch CCN und INP beeinflusste Polarimetrie in Zypern und Chile – Abschätzung von hemisphärischen Kontrasten in radarpolarimetrischen Größen und deren Beziehung zu Unterschieden in der Aerosolbelastung
Polarimetry Influenced by CCN aNd INP in Cyprus and Chile (PICNICC):
An assessment of hemispheric cloud polarimetric contrasts and its relation to differences in aerosol load

Schlagworte: Radarpolarimetrie, DACAPO-PESO, Wolkenmikrophysik, Aerosol-Wolken-Wechselwirkung

Projektleiter: H. Kalesse (heike.kalesse@uni-leipzig.de)
Dr. P. Seifert, Leibniz Institut für Troposphärenforschung (TROPOS)
Projektmitarbeiter:
Prof. J. Quaas (johannes.quaas@uni-leipzig.de)
Teresa Vogl (teresa.vogl@uni-leipzig.de), A. Teissiere (TROPOS)

Projektbeginn: 1.11.2018
Projektende: 31.12.2021

Beschreibung
Das Verständnis von mikrophysikalischen Wachstumsprozessen in Mischphasenwolken wie Aggregation und Bereifung beruht auf einer gründlichen Charakterisierung der in der Wolke vorhandenen Flüssigphase. In dieser Studie wird eine einzigartige Messmöglichkeit mit einer erweiterten Fernerkundungsinstrumentensuite genutzt, die polarimetrische Radarbeobachtungen bei mehreren Wellenlängen auf der Nord- und Südhalbkugel beinhaltet, um die Millimeterwellenlängen-Radarpolarimetrieforschung für mikrophysikalische Prozessstudien voranzubringen. Die übergeordnete Hypothese, die in diesem Projekt untersucht wird, ist, dass Mischphasen-Wolkenprozesse anfällig für Aerosolstörungen sind. Wir postulieren, dass:
A) Die Aggregation wird bei hohen Aerosolbelastungen und damit verbundenen höheren INP (Ice Nucleating Particle)-Konzentrationen häufiger erfolgen, da höhere Eiskristallkonzentrationen die Aggregation begünstigen.
B) Bereifung von Eiskristallen wird häufiger auftreten, wenn aufgrund einer Knappheit von INP anhaltende unterkühlte Flüssigkeitsschichten auftreten.
Um diese Hypothesen anzugehen, wird die Häufigkeit des Auftretens von Aggregation und Bereifung in mehrjährigen Datensätzen charakterisiert, die bei Feldexperimenten in der Aerosol-

Lasten-Atmosphäre über Limassol, Zypern und der unberührten Region Punta Arenas, Chile, erhalten wurden und werden. Die beobachtete Reaktion von Mischphasen-Wolkenprozessen auf Aerosolstörungen wird im Zusammenhang mit einer Modellsensitivitätsstudie von Simulationen mit einer wolkensystemauflösenden (1 km) Version des ICON-NWP für die gesamten Beobachtungszeiträume für regionale Bereiche um die Beobachtungsstandorte in Zypern und Chile gestellt, die von Radar-Fortsimulationen begleitet werden.

Description
Understanding mixed-phase cloud processes such as aggregation and riming relies on a thorough characterization of the liquid phase present in the cloud. For this study we propose to use a unique measurement opportunity with an extended remote-sensing instrument suite including triple-frequency polarimetric radar observations on the Northern and Southern hemisphere to bring forward millimeter wavelength radar polarimetry research for microphysical process studies. The overarching hypothesis that we would like to study within this project is that mixed-phase cloud processes are susceptible to aerosol perturbations. We postulate that
A) Aggregation will be more frequent for high aerosol loads and associated higher ice nucleating particle (INP) concentrations because higher ice crystal concentrations favor aggregation.
B) Riming will be more frequent where sustained supercooled liquid layers occur due to a scarcity of INP.
To address these hypotheses, we will characterize the frequency of occurrence of aggregation and riming in multi-year datasets obtained during institutional-funded field experiments in the aerosol-burden atmosphere above Limassol, Cyprus and the pristine region of Punta Arenas, Chile. For that purpose, we will make slanted linear depolarization (SLDR) polarimetric observations with a Ka-band radar a versatile technique for classification of hydrometeors in mixed-phase clouds.
The observed response of mixed-phase cloud processes to aerosol perturbations will be put in context to a model sensitivity study of simulations with a cloud-system-resolving (1 km) version of the ICON-NWP for the entire observation periods for regional domains around the observations sites in Cyprus and Chile that are accompanied by radar forward simulations.

Weiterführung: ja

Mittelgeber: DFG KA 4162/2-1 innerhalb **Mittelgeber:** DFG

Einfluss von Wasserrinnen im Meereis und Polynyas auf arktische Wolkeneigenschaften – B07
(Influence of sea ice leads or polynyas on Arctic cloud properties – B07)

Schlagworte: Arktische Verstärkung, Arktische Wolken, bodengebundene Fernerkundung von Wolken

Projektleiter: H. Kalesse (heike.kalesse@uni-leipzig.de)
Projektmitarbeiter:
Pablo Saavedra-Garfias (pablo.saavedra@uni-leipzig.de)

Projektbeginn: 01.01.2020
Projektende: 31.12.2023

Beschreibung
Die winterliche Meereisbedeckung ist charakterisiert durch verschiedenste Brüche unterschiedlichsten Levels. Wasserrinnen und Polynyas führen zu erheblichen Wärme- und Feuchteflüssen vom relativ warmen Ozean zur kalten Atmosphäre. Damit beeinflussen sie die Struktur der atmosphärischen Grenzschicht, Wolkenbedeckung und das Energiebudget an der Oberfläche und ebenfalls den chemischen Austausch zwischen Atmosphäre und Ozean. Um den Einfluss von Meereisrinnen und Polynyas auf Wolken zu quantifizieren, werden mikro- und makrophysikalische Eigenschaften von bodennahen Wolken während auflandigen Winden in Anwesenheit von Meereisrinnen oder Polynyas verglichen mit Wolken während auflandigen Wind über einer geschlossenen Eisdecke.

Description
The wintertime Arctic sea ice area is characterised by different degrees of fracturing. Leads and polynyas result in a substantial heat and moisture flux from the relatively warm ocean to the cold atmosphere. They thus alter the atmospheric boundary layer structure, cloud cover, and the surface energy budget and also affect atmosphere-ocean chemical exchanges. To quantify the influence of leads or polynyas on clouds, the micro- and macrophysical properties of surface-coupled clouds during onshore winds in the presence of leads or polynyas will be compared to clouds observed during onshore winds in closed sea-ice conditions.

Weiterführung: ja

Mittelgeber: Projektnummer 268020496 innerhalb von TRR 172 „Arktische Verstärkung (AC)^3“

Ein neuartiger Retrievalansatz zur Ableitung troposphärischer Temperatur- und Feuchteprofile unter allen Wetterbedingungen für eine verbesserte Quantifizierung von Verdunstungsraten

(A novel synergistic retrieval approach to enable tropospheric temperature and humidity profiling under all weather conditions for an improved quantification of evaporation rates)

Schlagworte: Instrumentensynergie, bodengebundene Fernerkundung, Niederschlag, Neuronale Netze, optimale Schätzung, Wasserdampfprofile, Temperaturprofile, Verdunstungsraten, Abkühlungsraten

Projektleiter: A. Foth (andreas.foth@uni-leipzig.de)
Projektmitarbeiter: A. Foth (andreas.foth@uni-leipzig.de)

Projektbeginn: 1.4.2020
Projektende: 31.03.2023

Beschreibung
Die ständige Weiterentwicklung und Verbesserung der Wetter- und Klimamodelle stellt die Fernerkundung der Atmosphäre vor große Herausforderungen. Für die Evaluierung der Modelle werden immer besser aufgelöste Messungen und Methoden benötigt. Herkömmliche Ansätze scheitern hier vor allem an fehlenden kontinuierlichen Beobachtungen der Temperatur und Feuchte bei allen Wetterbedingungen und insbesondere bei Regen. Ein Windprofiler ist allerdings auch bei solchen Bedingungen in der Lage Vertikalinformationen der Temperatur- und

Feuchtegradienten zu messen. Der hier vorgeschlagene neuartige Ansatz aus einer Synergie aus Windprofiler (inklusive Radio Acoustic Sounding System), Ramanlidar, Mikrowellenradiometer und Wolkenradar ermöglicht eine automatisierte und kontinuierliche Erstellung von Temperatur- und Feuchteprofilen sogar bei Niederschlägen.

Langzeitbeobachtungen an Meteorologischen Observatorium in Lindenberg werden genutzt, um aussagekräfige Statistiken über die Verdunstungs- und Abkühlungsraten zu erstellen. Die Ergebnisse werden für verschiedene Bedingungen wie stratiformen und konvektiven Niederschlag und für verschiedenen Jahreszeiten evaluiert. Dies wird den Modellieren helfen, die Parametrisierungen der Verdunstungsraten in kleinskaligen Modellen zu evaluieren.

Description
Steady improvements of weather and climate models are challengeing for remote sensing of the atmosphere. For the evaluation of the models highly resolved measurements and methods are necessary. Usual approaches fail due to the lack of continuous observation of temperature and humidity profiles during all weather conditions, especially during precipitation. A wind profiling radar enables the measurement vertical profiles of temperature and humidity gradients. The novel approach based on synergy between eind profiling radar (with Radio Acoustic Sounding System), Raman lidar, microwave radiometer, and cloud radarenables an automated and continuous observation of temperature and humidity profiles even during precipitation. The used variational approach (optimal estimation) provides a robust tool for the combination of different instruments including the uncertainties of the single systems.

Longterm observation at the meterological observatory Lindenberg will be used to estimate robust statistics about evaporation and cooling rates. The results will be evaluated for differenet conditions as stratiform or convective precipitation or for different seasons. The outcome will help modellers to evaluate the parametrizations of evaporation rates in small-scale models.

Weiterführung: ja

Mittelgeber: Deutsche Forschungsgemeinschaft (DFG FO 1285/2-1)

Aerosole und Wolken, Matthias Tesche
Aerosols and Clouds

Partikel in Aerosol-Wolken Wechselwirkungen: Schichtung, Konzentration und Wolkenlebenszyklus

Particles in Aerosol Cloud Interactions: stratification, CCN/INP concentrations, and Cloud lifecycle (PACIFIC)

Schlagworte: Aerosol-Wolken-Wechselwirkungen, Satellitenfernerkundung, Wolkenverfolgung, Wolken- und Eiskeime

Projektleiter:
Dr. Matthias Tesche (matthias.tesche@uni-leipzig.de)

Projektmitarbeiter:
Dr. Peter Bräuer, Dr. Torsten Seelig, Fani Alexandri, Goutam Choudhury, Felix Müller

Projektbeginn: 01.01.2019
Projektende: 31.12.2022

Beschreibung
Aerosolpartikel sind von herausragender Bedeutung für die Bildung von Wolken, da sie als Wolkenkondensationskerne in Flüssigwasserwolken and als Eiskeime in eisenthaltenden Wolken wirken. Veränderungen der Aerosolkonzentration in der Atmosphäre beeinflussen die Reflektivität, die Entwicklung, die Wasserphase, die Lebenszeit und die Regenrate von Wolken. Diese Prozesse werden als Aerosol-Wolken-Wechselwirkungen bezeichnet. Obwohl ihr Einfluss auf das Klima der Erde seit Jahrzenten einen Schwerpunkt der Atmosphärenforschung bildet, ist unser derzeitiger Wissensstand, so wie er im letzten Bericht des Weltklimarates zusammengefasst wurde, dass Aerosol-Wolken-Wechselwirkungen die größte Unsicherheit zu unserem Verständnis des Klimawandels beiträgt.
PACIFIC wird unser Verständnis von Aerosol-Wolken-Wechselwirkungen durch zwei Innovationen verbessern: (1) die Charakterisierung der für diese Prozesse relevanten Aerosolpartikel und (2) die Untersuchung der zeitlichen Veränderung der Eigenschaften von Wolken im Verlauf ihres Lebenszyklus. Untersuchungen von Aerosol-Wolken-Wechselwirkungen mit Geräten auf polarumlaufenden Satelliten sind auf Wolkenbeobachtungen zu festen Zeiten beschränkt. Die für solche Studien benötigte Information der Anzahl vorhandener Wolkenkondensationskerne wird derzeit aus säulenintegrierten optischen Aerosoleigenschaften abgeschätzt. Eine ähnliche Methodik zur Abschätzung der Konzentration von Eiskeimen existiert nicht, da deren Eigenschaften von der Art und Größe der Partikel abhängen. Daher sind zur Zeit keinen Studien von Aerosol-Wolken-Wechselwirkungen auf eisenthaltende Wolken basierend auf Fernerkundungsmessungen möglich. Die quantitative Abschätzung der Bedeutung von Aerosolen in Aerosol-Wolken-Wechselwirkungen verlangt, dass Informationen über die räumliche Verteilung von Wolkenkondensationskernen und Eiskeimen vorhanden sind. Das Projekt strebt an bisher nicht erhältliche Informationen über die Konzentration von Wolkenkondensationskernen und Eiskeimen aus weltraumgetragenen Lidarmessungen zu erlangen. Dessweiteren wird die Entwicklung von Wolken vor und nach der Punktbeobachtung mir polarumlaufenden Geräten dadurch charakterisiert, dass diese Wolken in zeitlich aufgelösten Beobachtungen von geostationären Geräten verfolgt werden. Die neuartige Information wird dann zum Studium der Effekte von Wolkenkondensationskernen und Eiskeimen auf die Helligkeit, den Flüssig- und Eiswassergehalt, die Tropfen- und Eiskristallgröße, die Entwicklung, die Wasserphase und die Regenrate von Wolken in verschiedenen Wolkenregimen verwendet. Besonderes Augenmerk wird dabei auf eine umfassende Berücksichtigung der meteorologischen Rahmenbedingungen gelegt werden. Die Ergebnisse von PACIFIC sind von Bedeutung für die Untersuchung und Verbesserung des Verhaltens von Klimamodellen.

Description:
Atmospheric aerosol particles are of great importance for cloud formation in the atmosphere because they are needed to act as cloud condensation nuclei (CCN) in liquid-water clouds and as ice nucleating particles (INP) in ice-containing clouds. Changes in aerosol concentration affect the

albedo, development, phase, lifetime and rain rate of clouds. These aerosol-cloud interactions (ACI) and the resulting climate effects have been in the focus of atmospheric research for several decades. Nevertheless, the IPCC still concludes that ACI cause the largest uncertainty in assessing climate change as they are understood only with medium confidence.
PACIFIC will improve our understanding of ACI by enhancing the representation of the aerosols relevant for cloud processes and by quantifying temporal changes in cloud properties throughout the cloud life cycle. ACI studies using polar-orbiting sensors are limited to snap-shot observations of clouds. CCN concentrations for assessing ACI are currently estimated from column- integrated optical aerosol parameters. There is no such proxy of INP concentrations for remote-sensing studies of aerosol effects on cold clouds as INP activity depends on aerosol type and size. Quantifying the role of aerosols in ACI requires knowledge of the spatial and vertical distribution of CCN and INP. The project aims to obtain unprecedented insight in CCN and INP concentrations from spaceborne lidar data. In addition, the development of clouds before and after the snap-shot view of polar-orbiting sensors is characterised by tracking those clouds in time-resolved geostationary observations. This novel information will be used to study the effects of CCN and INP on the albedo, liquid and ice water content, droplet and crystal size, development, phase and rain rate of clouds within different regimes carefully accounting for the meteorological background. The findings of PACIFIC are crucial for assessing and improving the performance of climate models.

Weiterführung: ja

Mittelgeber: Bundesministerium für Bildung und Forschung (BMBF) und Deutscher Akademischer Austauschdienst (DAAD), MOPGA-GRI Senior Research Grant PACIFIC (57429422)

Publikationen
LIM 2020

Autor_Name	Vorname	weitere Autoren	Titel	ID, DOI Publikationsort
Carlsen	**Tim**	Birnbaum, G., **Ehrlich, A.**, Helm, V., **Jäkel, E.**, Schäfer, M., and **Wendisch, M.**	Parameterizing anisotropic reflectance of snow surfaces from airborne digital camera observations in Antarctica,	doi:10.5194/tc-14-3959-2020 The Cryosphere, 14, 3959–3978 (2020)
Cohen	Judah	Zhang, X., Francis, J., Jung, T., Kwok, R., Overland, J., Ballinger, T., Bhatt, U.S., Chen, H. W., Coumou, D., Feldstein, S., Handorf, D., Henderson, G., Ionita, M., Kretschmer, M., Laliberte, F., Lee, S., Linderholm, H. W., Maslowski, W., Peings, Y., Pfeiffer, K., Rigor, I., Semmler, T., Stroeve, J., Taylor, P.C., Vavrus, S., Vihma, T., Wang, S., **Wendisch, M.**, Wu, Y., and Yoon, J.	Divergent consensuses on Arctic amplification influence on midlatitude severe winter weather	doi:10.1038/s41558-019-0662-y Nat. Clim. Chang., 10, 20–29 (2020)
Donth	**Tobias**	**Jäkel, E., Ehrlich, A.**, Heinold, B., Schacht, J., Herber, A., Zanatta, M., and **Wendisch, M.**	Combining atmospheric and snow layer radiative transfer models to assess the solar radiative effects of black carbon in the Arctic	doi:10.5194/acp-20-8139-2020 Atmos. Chem. Phys., 20, 8139–8156 (2020)
Ehrlich	**André**	**Schäfer, M., Ruiz-Donoso, E., and Wendisch, M.**	Airborne Remote Sensing of Arctic Clouds	doi:10.1007/978-3-030-38696-2_2 In: Kokhanovsky A. (eds) Springer Series in Light Scattering, Volume 5, 39-66 (2020)
Hartmann	Markus	K. Adachi, O. Eppers, C. Haas, A. Herber, R. Holzinger, A. Hünerbein, **E. Jäkel,** C. Jentzsch, M. Pinxteren, H. Wex, S. Willmes, and F. Stratmann	Wintertime airborne measurements of ice nucleating particles in the high Arctic: a hint to a marine, biogenic source for Ice Nucleating	doi:10.1029/2020GL087770 Geophys. Res. Lett., 47, e2020GL087770 (2020)

			Particles	
Holanda	Bruna A.	Pöhlker, M. L., Walter, D., Saturno, J., Sörgel, M., Ditas, J., Ditas, F., Schulz, C., Franco, M. A., Wang, Q., **Donth, T.,** Artaxo, P., Barbosa, H. M. J., Borrmann, S., Braga, R., Brito, J., Cheng, Y., Dollner, M., Kaiser, J., Klimach, T., Knote, C., Krüger, O. O., Fütterer, D., Lavrič, J. V., Ma, N., Machado, L. A. T., Ming, J., Morais, F., Paulsen, H., Sauer, D., Schlager, H., Schneider, J., Su, H., Weinzierl, B., Walser, A., **Wendisch, M.,** Ziereis, H., Zöger, M., Pöschl, U., Andreae, M. O., and Pöhlker, C.	Influx of African biomass burning aerosol during the Amazonian dry season through layered transatlantic transport of black carbon-rich smoke	doi:10.5194/acp-20-4757-2020 Atmos. Chem. Phys., 20, 4757–4785 (2020)
Kokhanovsky	Alexander	Tomasi, C., Smirnov, A., Herber, A., Neuber, R., **Ehrlich, A.**, Lupi, A., Petkov, B. H., Mazzola, M., Ritter, C., Toledano, C., Carl, R., Vitale, V., and Holben, B., Zielinski, T., Bélanger, S., Larouche, P., Kinne, S., Radionov, V., **Wendisch, M.**, Tackett, J. L., and Winker, D. M.	Remote Sensing of Arctic Atmospheric Aerosols	doi:10.1007/978-3-030-33566-3_9 in: Kokhanovsky A., Tomasi C. (eds) Physics and Chemistry of the Arctic Atmosphere, 505-589, Springer Polar Sciences. Springer, Cham (2020)
Li	Li	Li, Z., Chang, W., Ou, Y., Goloub, P., Li, C., Li, K., Hu, Q., Wang, J., and **Wendisch, M.**	Aerosol solar radiative forcing near the Taklimakan Desert based on radiative transfer and regional meteorological simulations during the Dust Aerosol Observation-Kashi campaign	doi:10.5194/acp-20-10845-2020 Atmos. Chem. Phys., 20, 10845–10864 (2020)
Mei	Fan	Wang, J., Comstock, J. M., Weigel, R., Krämer, M., Mahnke, C., Shilling, J. E., Schneider, J., Schulz, C., Long, C. N., **Wendisch, M.**, Machado, L. A. T., Schmid, **B., Krisna**, T., Pekour, M., Hubbe, J., Giez, A., Weinzierl, B., Zoeger, M., Pöhlker, M. L.,	Comparison of Aircraft Measurements during GoAmazon2014/5 and ACRIDICON-CHUVA	doi:10.5194/amt-13-661-2020 Atmos. Meas. Tech., 13, 661–684 (2020)

		Schlager, H., Cecchini, M. A., Andreae, M. O., Martin, S. T., de Sá, S. S., Fan, J., Tomlinson, J., Springston, S., Pöschl, U., Artaxo, P., Pöhlker, C., Klimach, T., Minikin, A., Afchine, A., and Borrmann, S.		
Nakoudi	Konstantina	Ritter, C., Böckmann, C., Kunkel, D., Eppers, O., Rozanov, V., Mei, L., Pefanis, V., **Jäkel, E.**, Herber, A.; Maturilli, M.; Neuber, R.	Does the Intra-Arctic Modification of Long-Range Transported Aerosol Affect the Local Radiative Budget? (A Case Study)	doi:10.3390/rs12132112 Remote Sens., 12(13), 2112 (2020)
Pohl	Christine	Istomina, L., Tietsche, S., **Jäkel, E., Stapf, J.,** Spreen, G., and Heygster, G.	Broadband albedo of Arctic sea ice from MERIS optical data	doi:10.5194/tc-14-165-2020 The Cryosphere, 14, 165–182 (2020)
Pohl	Christine	Rozanov, V. V., **Wendisch, M.**, Spreen, G., and Heygster, G.	Impact of the near-field effects on radiative transfer simulations of the bidirectional reflectance factor and albedo of a densely packed snow layer	doi:10.1016/j.jqsrt.2019.106704 J. Quant. Spectrosc. Radiat. Transf., 241, 106704 (2020)
Polonik	Pascal	Knote, C., Zinner, T., Ewald, F., Kölling, T., Mayer, B., Andreae, M. O., Jurkat-Witschas, T., Klimach, T., Mahnke, C., Molleker, S., Pöhlker, C., Pöhlker, M. L., Pöschl, U., Rosenfeld, D., Voigt, C., Weigel, R., and **Wendisch, M.**	The challenge of simulating the sensitivity of the Amazonian clouds microstructure to cloud condensation nuclei number concentrations	doi:10.5194/acp-20-1591-2020 Atmos. Chem. Phys., 20, 1591–1605 (2020)
Stapf	**Johannes**	**Ehrlich, A., Jäkel, E.**, Lüpkes, C., and **Wendisch, M.**	Reassessment of shortwave surface cloud radiative forcing in the Arctic: Consideration of surface-albedo–cloud interactions	doi:10.5194/acp-20-9895-2020 Atmos. Chem. Phys., 20, 9895–9914 (2020)
Sun	**Bin**	**Jäkel, E., Schäfer, M., and Wendisch, M.**	A Biased Sampling Approach to Accelerate Backward Monte Carlo Atmospheric Radiative Transfer Simulations and its	doi:10.1016/j.jqsrt.2019.106690 J. Quant. Spectrosc. Radiat. Transfer, 240, 106690 (2020)

			Application to Arctic Heterogeneous Cloud and Surface Conditions	
Ruiz-Donoso	**Elena**	**Ehrlich, A., Schäfer, M., Jäkel, E.**, Schemann, V., Crewell, S., Mech, M., Kulla, B. S., Kliesch, L.-L., Neuber, R., and **Wendisch, M.**	Small-scale structure of thermodynamic phase in Arctic mixed-phase clouds observed by airborne remote sensing during a cold air outbreak and a warm air advection event	doi: 10.5194/acp-20-5487-2020 Atmos. Chem. Phys., 20, 5487–5511 (2020)
Wolf	**Kevin**	**A. Ehrlich,** M. Mech, R. J. Hogan, and **M. Wendisch**	Evaluation of ECMWF Radiation Scheme Using Aircraft Observations of Spectral Irradiance above Clouds	doi:10.1175/JAS-D-19-0333.1 J. Atmos. Sci., 77 (8), 2665–2685 (2020)
Gavrilov	Nikolai M.	**Ch. Jacobi**	Multi-year changes in the mesoscale waves according to the data of drift and radio-meteor measurements at Collm, Germany	doi: 10.1117/12.2574804 Proc. SPIE 11560, 26th International Symposium on Atmospheric and Ocean Optics, Atmospheric Physics, 115607X (12 November 2020)
Geißler	**Christoph**	**Ch. Jacobi**, and **F. Lilienthal**	Forcing mechanisms of the migrating quarterdiurnal tide	doi: 10.5194/angeo-38-527-2020 Ann. Geophys., 38, 527–544 (2020)
Heale	Christopher J.	K. Bossert, S. L. Vadas, L. Hoffmann, A. Dörnbrack, G. Stober, J. B. Snively, and **Ch. Jacobi**	Secondary gravity waves generated by breaking mountain waves over Europe	doi: 10.1029/2019JD031662 J. Geophys. Res: Atmospheres, 125, e2019JD031662 (2020)
Jones Jr.	McArthur	D. E. Siskind, D. P. Drob, J.P. McCormack, J. T. Emmert, M. S. Dhadly, H. E. Attard, M. G. Mlynczak, P. G. Brown, G. Stober, A. Kozlovsky, M. Lester, and **Ch. Jacobi**	Coupling from the middle atmosphere to the exobase: Dynamical disturbance effects on light chemical species	doi: 10.1029/2020JA028331 J. Geophys. Res.: Space Physics, 125, e2020JA028331 (2020)
Joshi	Vaidehi	S, Sharma, K. N. Kumar, N. Patel, P. Kumar, H. Bencherif, P. Ghosh, C. Jethva and **R. Vaishnav**	Analysis of the middle atmospheric ozone using SABER observations: a study over mid-	doi: 10.1007/s00382-020-05124-6 Clim. Dyn., 54, 2481-2492 (2020)

			latitudes in the northern and southern hemispheres	
Kuchař	**Ales**	P. Sacha, R. Eichinger, **Ch. Jacobi,** P. Pisoft, and H. E. Rieder	On the intermittency of orographic gravity wave hotspots and its importance for middle atmosphere dynamics	doi: 10.5194/wcd-1-481-2020 Weather Clim. Dynam., 1, 481–495 (2020
Lilienthal	**Friederike**	E. Yiğit, **N. Samtleben**, and **Ch. Jacobi**	Variability of gravity wave effects on the zonal mean circulation and migrating terdiurnal tide as studied with the middle and upper atmosphere model (MUAM2019) using a whole atmosphere nonlinear gravity wave scheme	doi: 10.3389/fspas.2020.588956 Front. Astron. Space Sci.,7, 588956 (2020)
Merzlyakov	Eugeny	T. Solovyova, A. Yudakov, D. Korotyshkin, **Ch. Jacobi**, and **F. Lilienthal**	Amplitude modulation of the semidiurnal tide based on MLT wind measurements with a European/Siberian meteor radar network in October - December 2017	doi: 10.1016/j.asr.2020.04.036 Adv. Space Res., 66, 631-645 (2020)
Merzlyakov	Eugeny	T. Solovyova, A. Yudakov, D. Korotyshkin, **Ch. Jacobi**, and **F. Lilienthal**	Some features of the day-to-day MLT wind variability in winter 2017-2018 as seen with a European/Siberian meteor radar network,	doi: 10.1016/j.asr.2019.12.018 Adv. Space Res., 65, 1529-1543 (2020)
Mewes	**Daniel**	**Ch. Jacobi**	Horizontal temperature fluxes in the Arctic in CMIP5 model results analyzed with Self-Organizing Maps	doi: 10.3390/atmos11030251 Atmosphere, 11(3), 251 (2020)
Rodrigues de Araújo	Luciana	L. M. Lima, P.P . Batista, and C**h. Jacobi**	Behaviour of monthly tides from meteor radar winds at 22.7°S during declining phases	doi: 10.1016/j.jastp.2020.105298 J. Atmos. Sol.-Terr. Phys., 205, 105298

			of 23 and 24 solar cycles	(2020)
Samtleben	**Nadja**	**A. Kuchař**, P. Šácha, P. Pišoft, and **Ch. Jacobi**	Mutual Interference of local gravity wave forcings in the stratosphere	doi: 10.3390/atmos11111249 Atmosphere, 11, 1249 (2020)
Samtleben	**Nadja**	**A. Kuchař**, P. Šácha, P. Pišoft, and **Ch. Jacobi**	Impact of local gravity wave forcing in the lower stratosphere on the polar vortex stability: Effect of longitudinal displacement	doi: 10.5194/angeo-38-95-2020 Ann. Geophys., 38, 95-108 (2020)
Schmölter	Erik	J. Berdermann, N. Jakowski, and **Ch. Jacobi**	Spatial and seasonal effects on the delayed ionospheric response to solar EUV changes	doi: 10.5194/angeo-38-149-2020 Ann. Geophys., 38, 149–162 (2020)
Vaishnav	**Rajesh**	**Ch. Jacobi**	Ionospheric response to the 25-26 August 2018 intense geomagnetic storm	https://nbn-resolving.org/urn:nbn:de:bsz:15-qucosa2-741226 Rep. Inst. Meteorol. Univ. Leipzig, 58, 1-10 (2020)
Bellouin	Nicolas	**J. Quaas**, **E. Gryspeerdt**, S. Kinne, P. Stier, D Watson-Parris, O. Boucher, K.S. Carslaw, M. Christensen, A.-L. Daniau, J.-L. Dufresne, G. Feingold, S. Fiedler, P. Forster, A. Gettelman, J. M. Haywood, F. Malavelle, U. Lohmann, T. Mauritsen, D.T. McCoy, G. Myhre, **J. Mülmenstädt**, D. Neubauer, A. Possner, M. Rugenstein, Y. Sato, M. Schulz, S. E. Schwartz, **O. Sourdeval**, T. Storelvmo, V. Toll, D. Winker, and B. Stevens	Bounding global aerosol radiative forcing of climate change	doi:10.1029/2019RG000660 Rev. Geophys., 58, e2019RG000660 (2020)
Bellouin	Nicolas	W. H. Davies, K. P. Shine, **J. Quaas, J. Mülmenstädt**, P. M. Forster, C. Smith, L. Lee, L. Regayre, G. Brasseur, N. Sudarchikova, I. Bouarar, O. Boucher, and G. Myhre	Radiative forcing of climate change from the Copernicus reanalysis of atmospheric composition	doi:10.5194/essd-12-1649-2020 Earth Syst. Sci. Data, 12, 1649-1677 (2020)

Block	**Karoline**	**F. A. Schneider, J. Mülmenstädt, M. Salzmann, and J. Quaas**	Climate models disagree on the sign of total radiative feedback in the Arctic	doi:10.1080/16000870.2019.1696139 Tellus A, 72, 1-14 (2020)
Cherian	**Ribu**	**J. Quaas**	Trends in AOD, clouds and cloud radiative effects in satellite data and CMIP5 and CMIP6 model simulations over aerosol source regions	doi:10.1029/2020GL087132 Geophys. Res. Lett., 47, e2020GL087132 (2020)
Costa-Surós	Montserrat	**O. Sourdeval**, C. Acquistapace, H. Baars, C. C. Henken, C. Genz, J. Hesemann, C. Jimenez, M. König, **J. Kretzschmar**, N. Madenach, C. I. Meyer, R. Schrödner, P. Seifert, F. Senf, M. Brueck, G. Cioni, J. F. Engels, K. Fieg, K. Gorges, R. Heinze, P. K. Siligam, U. Burkhardt, S. Crewell, C. Hoose, A. Seifert, I. Tegen, and **J. Quaas**	Detection and attribution of aerosol-cloud interactions in large-domain large-eddy simulations with the ICOsahedral Non-hydrostatic model	doi:10.5194/acp-20-5657-2020 Atmos. Chem. Phys., 20, 5657-5678 (2020)
Ganske	Anette	D. Heydebreck, H. Höck, A. Kraft, and **J. Quaas,** and A. Kaiser	A Short Guide to Increase FAIRness of Atmospheric Model Data	doi:10.1127/metz/2020/1042 Meteorol. Z., 29, 483-491 (2020)
Gryspeerdt	**Edward**	**J. Mülmenstädt**, A. Gettelman, F. F. Malavelle, H. Morrison, D. Neubauer, D. G. Partridge, P. Stier, T. Takemura, H. Wang, M. Wang, and K. Zhang	Surprising similarities in model and observational aerosol radiative forcing estimates	doi:10.5194/acp-20-613-2020 Atmos. Chem. Phys., 20, 613-623 (2020)
Krämer	**Martina**	M. C. Rolf, N. Spelten, A. Afchine, D. Fahey, E. Jensen, S. Khaykin, T. Kuhn, P. Lawson, A. Lykov, L. L. Pan, M. Riese, A. Rollins, F. Stroh, T. Thornberry, V. Wolf, S. Woods, P. Spichtinger, **J. Quaas**, and O. Sourdeval	A microphysics guide to cirrus – Part 2: Climatologies of clouds and humidity from observations	doi:10.5194/acp-20-12569-2020 Atmos. Chem. Phys., 20, 12569-12608 (2020)
Kretzschmar	**Jan**	J. Stapf, D. Klocke, **M. Wendisch**, and **J. Quaas**	Employing airborne radiation and cloud microphysics observations to improve cloud representation in ICON at	doi:10.5194/acp-20-13145-2020 Atmos. Chem. Phys., 20, 13145-13165 (2020)

			kilometer-scale resolution in the Arctic	
Lauer	**Melanie**	**K. Block, M. Salzmann, and J. Quaas**	CO_2-forced changes of Arctic temperature lapse-rates in CMIP5 models	doi:10.1127/metz/2020/0975 Met. Z., 29, 79-93 (2020)
Metzner	**Enrico P.**	**M. Salzmann,** and R. Gerdes	Arctic Ocean surface energy flux and the cold halocline in future climate projections	doi:10.1029/2019JC015554 J. Geophys. Res. Oceans, 125, e2019JC015554 (2020)
Mülmenstädt	**Johannes**	**C. Nam, M. Salzmann, J. Kretzschmar,** T. S. L'Ecuyer, U. Lohmann, P.-L. Ma, G. Myhre, D. Neubauer, P. Stier, K. Suzuki, M. Wang, and **J. Quaas**	Reducing the aerosol forcing uncertainty using observational constraints on warm rain processes	doi:10.1126/sciadv.aaz6433 Science Adv., 6, eaaz6433 (2020)
Rickels	Wilfried	M. Quaas, K. Ricke, **J. Quaas**, J. Moreno-Cruz, and S. Smulders	Who turns the global thermostat and by how much?	doi:10.1016/j.eneco.2020.104852 Energy Economics, 91, 104852 (2020)
Stevens	Bjorn	C. Acquistapace, A. Hansen, R. Heinze, C. Klinger, D. Klocke, W. Schubotz, J. Windmiller, P. Adamidis, I. Arka, V. Barlakas, J. Biercamp, M. Brueck, S. Brune, S. Buehler, U. Burkhardt, G. Cioni, M. Costa-Surós, S. Crewell, T. Crueger, H. Deneke, P. Friederichs, C. C. Henken, C. Hohenegger, M. Jacob, F. Jakub, N. Kalthoff, M. Köhler, T. W. Van Laar, P. Li, U. Löhnert, A. Macke, N. Madenach, B. Mayer, C. Nam, A. K. Naumann, K. Peters, S. Poll, **J. Quaas**, N. Röber, N. Rochetin, H. Rybka, L. Scheck, V. Schemann, S. Schnitt, A. Seifert, F. Senf, M. Shapkalijevski, C. Simmer, S. Singh, **O. Sourdeval**, D. Spickermann, J. Strandgren, O. Tessiot, N. Vercauteren, J. Vial, A. Voigt,	Large-eddy and storm resolving models for climate prediction - the added value for clouds and precipitation	doi:10.2151/jmsj.2020-021 J. Meteorol. Soc. Japan, 98 (2020)

		and G. Zängl		
Quaas	**Johannes**	A. Arola, B. Cairns, M. Christensen, H. Deneke, A. M. L. Ekman, G. Feingold, A. Fridlind, E. Gryspeerdt, O. Hasekamp, Zhanqing Li, A. Lipponen, P.-L. Ma, J. Mülmenstädt, Athanasios Nenes, J. Penner, D. Rosenfeld, R. Schrödner, K. Sinclair, Odran Sourdeval, P. Stier, **M. Tesche**, B. Van Diedenhoven, and **M. Wendisch**	Constraining the Twomey effect from satellite observations: Issues and perspectives	doi:10.5194/acp-20-15079-2020 Atmos. Chem. Phys., 20, 15079-15099 (2020)
Unglaub	**Claudia**	**K. Block, J. Mülmenstädt, O. Sourdeval,** and **J. Quaas**	A new classification of satellite-derived liquid water cloud regimes at cloud scale	doi:10.5194/acp-20-2407-2020 Atmos. Chem. Phys., 20, 2407-2418 (2020)
Von Savigny	Christian	C. Timmreck, S. A. Buehler, J. P. Burrows, M. Giorgetta, G. Hegerl, A. Horváth, G. A. Hoshyaripour, C. Hoose, **J. Quaas,** E. Malinina, A. Rozanov, H. Schmidt, L. Thomason, M. Toohey, and B. Vogel	The Research Unit VolImpact: Revisiting the volcanic impact on atmosphere and climate - preparations for the next big volcanic eruption	doi:10.1127/metz/2019/0999 Meteorol. Z., 29, 3-18 (2020)
Ohneiser	Kevin	Ansmann, A., Baars, H., Seifert, P., Barja, B., Jimenez, C., Radenz, M., Teisseire, A., Floutsi, A., Haarig, M., **Foth, A.**, Chudnovsky, A., Engelmann, R., Zamorano, F., Bühl, J., and Wandinger, U.	Smoke of extreme Australian bushfires observed in the stratosphere over Punta Arenas, Chile, in January 2020: optical thickness, lidar ratios, and depolarization ratios at 355 and 532 nm	doi:10.5194/acp-20-8003-2020 Atmos. Chem. Phys., 20, 8003–8015 (2020)
Bromwich	Dave	Bromwich, D., Werner, K., Casati, B., Powers, J., Gorodetskaya, I., Massonnet, F., Vitale, V., Heinrich,V., Liggett, D., Arndt, S., Barja, B., Bazile, E., Carpentier, S., Carrasco, J., Choi, T., Choi, Y., Colwell, S., Cordero, R., Gervasi, M., Haiden, T., Hirasawa, N., Inoue, J., Jung, T., **Kalesse, H.**, Kim, SJ., Lazzara, M., Manning, K., Norris, K., Park, S-J., Reid, P.,	The Year of Polar Prediction in the Southern Hemisphere (YOPP-SH)	https://doi.org/10.1175/BAMS-D-19-0255.1 Bull. Amer. Meteor. Soc. (2020)

		Rigor, I., Rowe, P., Schmithuesen, H., Seifert, P., Sun, Q., Uttal, T., Zannoni, M., and Zou, X.		
Stevens	Bjorn	**More than 200 authors...see website, a couple from LIM (HK, MW, AE, JR, MS, ...)**	EUREC4A	https://www.essoar.org/doi/10.1002/essoar.10504890.1 ESSOAr (2020)
Foth	**Andreas**	Zimmer, J., Lauermann, F., and, Kalesse, H.	Evaluation of micro rain radar-based precipitation classification algorithms to discriminate between stratiform and convective precipitation	https://doi.org/10.5194/amt-2020-290 Atmos. Chem. Phys. (2020)
Ansmann	Albert	Ohneiser, K., Mamouri, R.-E., Knopf, D. A., Veselovskii, I., Baars, H., Engelmann, R., **Foth, A.,** Jimenez, C., Seifert, P., and Barja, B.	Tropospheric and stratospheric wildfire smoke profiling with lidar: Mass, surface area, CCN and INP retrieval	https://doi.org/10.5194/acp-21-9779-2021 Atmos. Chem. Phys.

Choudhury	**Goutam**	Tyagi, B., Vissa, N. K., Singh, J., Sarangi, C., Tripathi, S. N., and **Tesche, M.**	Aerosol-enhanced high precipitation events near the Himalayan foothills	Atmos. Chem. Phys., 20, (2020) https://doi.org/10.5194/acp-20-15389-2020
Georgoulias	Aristeidis K.	Marinou, E., Tsekeri, A., Proestakis, E., Akritidis, D., Alexandri, G., Zanis, P., Balis, D., Marenco, F., **Tesche, M.**, and Amiridis, V.	A First Case Study of CCN Concentrations from Spaceborne Lidar Observations	Remote Sensing, 12, 1557 (2020) https://doi.org/10.3390/rs12101557
Kurgansky	Michael V.	**Seelig, T.**, Klein, M., Will, A., and Harlander, U.	Mean flow generation due to longitudinal librations of sidewalls of a rotating annulus	Geophysical & Astrophysical Fluid Dynamics, 114, 742-76 (2020) https://doi.org/10.1080/03091929.2019.1692829
Tesche	**Matthias**		Beyond optical profiling – Innovative use of the lidar technique in atmospheric research	Habilitation thesis, Leipzig University

Maahn	**Maximilian**	D. D. Turner, U. Löhnert, D. J. Posselt, K. Ebell, G. G. Mace, and J. M. Comstock	Optimal Estimation Retrievals and Their Uncertainties: What Every Atmospheric Scientist Should Know.	Bull. Amer. Meteor. Soc., https://doi.org/10.1175/BAMS-D-19-0027.1.
Maahn	**Maximilian**	Matrosov, S. Y., A. V. Ryzhkov, M. Maahn, and G. de Boer	Hydrometeor Shape Variability in Snowfall as Retrieved from Polarimetric Radar Measurements.	J. Appl. Meteor. Climatol. https://doi.org/10.1175/JAMC-D-20-0052.1.
Maahn	**Maximilian**	Mech, M., M. Maahn, S. Kneifel, D. Ori, E. Orlandi, P. Kollias, V. Schemann, and S. Crewell	PAMTRA 1.0: the Passive and Active Microwave radiative TRAnsfer tool for simulating radiometer and radar measurements of the cloudy atmosphere.	Geosci. Model Dev., https://doi.org/10.5194/gmd-13-4229-2020.

Name	E-Mail-Adresse
Alexandri, Fani	fani.alexandri@uni-leipzig.de
Becker, Sebastian	sebastian.becker@uni-leipzig.de
Block, Karoline	karoline.block@uni-leipzig.de
Bräuer, Peter	Peter.braeuer@uni-leipzig.de
Brückner, Marlen	m.brueckner@uni-leipzig.de
Cherian, Ribu	ribu.cherian@uni-leipzig.de
Choudhury, Goutam	goutam.choudhury@uni-leipzig.de
Ehrlich, André	a.ehrlich@uni-leipzig.de
Emmanouilidis, Alexandros	alexandros.emmanouilidis@uni-leipzig.de
Feck-Yao, Wolfgang	feckyao@uni-leipzig.de
Foth, Andreas	andreas.foth@uni-leipzig.de
Goren, Tom	tom.goren@uni-leipzig.de
Haghighatnasab, Mahnoosh	mahnoosh.haghighatnasab@uni-leipzig.de
Hörnig, Sabine	sabine.hoernig@uni-leipzig.de
Jacobi, Christoph	jacobi@rz.uni-leipzig.de
Jäkel, Evelyn	evi.jaekel@uni-leipzig.de
Kaiser, Falk	fkaiser@rz.uni-leipzig.de
Kalesse, Heike	heike.kalesse@uni-leipzig.de
Kirbus, Benjamin	benjamin.kirbus@uni-leipzig.de
Klingebiel, Marcus	marcus.klingebiel@uni-leipzig.de
Kretzschmar, Jan	jan.kretzschmar@uni-leipzig.de
Kuchar, Ales	ales.kuchar@uni-leipzig
Lindemann, Simone	simone.lindemann@uni-leipzig.de
Linke, Olivia	olivia.linke@uni-leipzig.de
Lochmann, Moritz	moritz.lochmann@uni-leipzig.de
Lonardi, Michael	michael.lonardi@uni-leipzig.de
Luebke, Anna	anna.luebke@uni-leipzig.de
Maahn, Maximilian	maximilian.maahn@uni-leipzig.de
Marjani, Sajadeh	sajedeh.Marjani@uni-leipzig.de
Mendes de Barros, Kátia	katia.mendes_de_barros@uni-leipzig.de
Metzner, Enrico	enrico.metzner@uni-leipzig.de
Papakonstantinou-Presvelo, Iris	i.presvelou@uni-leipzig.de
Quaas, Johannes	johannes.quaas@uni-leipzig.de
Rehnert, Jutta	rehnert@uni-leipzig.de
Ruiz Donoso, Elena	elena.ruiz_donoso@uni-leipzig.de
Saavedra Garfias, Pablo Andres	pablo.saavedra@uni-leipzig.de
Salzmann, Marc	marc.salzmann@uni-leipzig.de
Schäfer, Michael	michael.schaefer@uni-leipzig.de
Schandert, Katrin	schandrt@rz.uni-leipzig.de
Schimmel, Willi	willi.schimmel@uni-leipzig.de
Schmidt, Jörg	joerg.schmidt@uni-leipzig.de
Schwarz, Anja	anja.schwarz@uni-leipzig.de
Seelig, Torsten	torsten.seelig@uni-leipzig.de
Seydel, Birgit	birgit.seydel@uni-leipzig.de
Stapf, Johannes	johannes.stapf@uni-leipzig.de
Sudhakar, Dipu	dipu.sudhakar@uni-leipzig.de
Tesche, Matthias	matthias.tesche@uni-leipzig.de
Vaishnav, Rajesh Ishwardas	rajesh_ishwardas.vaishnav@uni-leipzig.de
Vogl, Teresa	teresa.vogl@uni-leipzig.de
Weiße, Frank	weisse@uni-leipzig.de
Wendisch, Manfred	m.wendisch@uni-leipzig.de

Anzahl der Studierenden am Institut für Meteorologie

BSC Meteorologie

Datum	Semester	1.FS	2. FS	3.FS	4.FS	5.FS	6. FS	7.FS	8.FS	9. FS	10.FS	>10.FS	Meteo_B
15.10.20	WS 20/21	34	1	32	7	21	0	9	2	2		1	109
15.10.19	WS 19/20	58		17		12		9					96
15.10.18	WS 18/19	48		14		9		5					76
15.10.17	WS 17/18	37		17		7		5					66
15.10.16	WS 16/17	48		7		5		3					63
15.10.15	WS 15/16	35		5		9		3					52
15.10.14	WS 14/15	35		14		15		3		3		1	71
15.10.13	WS 13/14	39		23		21		13		4			100
15.10.12	WS 12/13	60		29	1	22	2	16	1	2			133
15.10.11	WS 11/12	60		27		26	1	19		1			134
15.10.10	WS 10/11	64		34		20							118
15.10.09	WS 09/10	67	0	21	0	20	0						108
15.10.08	WS 08/09	71	0	28	0	12							111
15.10.07	WS 07/08	98	0	15									113
13.12.06	WS 06/07	31											31

MSC Meteorologie

Datum	Semester	1.FS	2. FS	3.FS	4.FS	5.FS	6. FS
15.10.20	WS20/21	14	4	6	1	3	1
15.10.19	WS 19/20	9		5		5	
15.10.18	WS18/19	5		5		9	
15.10.17	WS 17/18	5		9		10	
15.10.16	WS 16/17	9		13		17	
15.10.15	WS 15/16	13		19		18	
15.10.14	WS 14/15	19		18		16	
15.10.13	WS 13/14	18		16		20	
15.10.12	WS 12/13	18		20	1	15	
15.10.11	WS 11/12	21		17		10	
15.10.10	WS 10/11	20		9		5	
15.10.09	WS 09/10	11					

Ausbildung Diplom-Meteorologie beendet

Diplom Meteorologie													
Datum	Semester	1.FS	2. FS	3.FS	4.FS	5.FS	6. FS	7.FS	8.FS	9. FS	10.FS	>10.FS	Meteo_Diplom
15.10.2013	WS 13/14											2	2
17.10.2012	WS 12/13											3	3
16.10.2011	WS 11/12											3	3
15.10.2010	WS 10/11											14	14
15.10.2009	WS 09/10								0	14	0	7	21
15.10.2008	WS 08/09						0	14	0	23	1	25	63
15.10.2007	WS 07/08				0	22	0	26	1	18	2	19	88
13.12.2006	WS 06/07		0	40	0	36	0	24	2	14	1	17	175
15.10.2005	WS 05/06	109	0	49	0	30	2	16	1	17	1	13	237
08.12.2004	WS 04/05	97	0	35	1	20	0	19	0	12	1	15	200
03.12.2003	WS 03/04	68	1	25	0	20	1	13	1	12	1	13	155
14.10.2002	WS 02/03	45	0	19	0	16	0	15	1	12	1	9	118
06.12.2001	WS 01/02	43	0	21	0	16	0	13	0	7	0	5	105
07.12.2000	WS 00/01	41	1	27	0	22	0	8	0	6	1	6	112
01.12.1999	WS 99/00	40	0	24	0	9	0	9	0	6	1	6	95
16.12.1998	WS 98/99	36	0	11	0	17	1	9	1	5	0	8	88
10.11.1997	WS 97/98	29	0	17	0	10	1	8	0	7	0	4	76

Abschlüsse Meteorologie 2020

Bachelorarbeiten

Name	Thema
Thoböll, Jakob	Einfluss der Definition des bodengebunden und flugzeuggetragen ermittelten Bedeckungsgrades auf seinen Zusammenhang mit der solaren Strahlungsflussdichte
Hirche, Pascal	Erstellung von IWV und LWP für Barbados und den subtropischen Atlantik mit Hilfe eines Mikrowellenradiometers
Roschke, Johanna	Contrasting cloud properties in the trade wind region of Barbados in the dry and wet season
Engelhardt, Richard	Wolkenbestimmung am Amazon Tall Tower Observatory (ATTO)
Weikert, Hanna Luise	Untersuchung des Einflusses der Bildung von Kondensstreifen in bereits existierenden Zirruswolken mittels hochaufgelöster Satellitenbeobachtungen
Burzik, Annika	On the occurrence of multilayer clouds and ice-crystal seeding during the Arctic Ocean 2018 research cruise
Rosenburg, Sophie	Einfluss der Atmosphärenkorrektur bei flugzeuggetragenen Albedomessungen auf die Ableitung der Schneekorngröße
Hoffmann, Rasmus	Bestimmung der chemischen Zusammensetzung des Aerosols an der städtischen Messstation Eisenbahnstraße des TROPOS mit Hilfe eines Aerosol-Massenspektrometers (AMS)
Bayer, Nicolas	Observation and RT-Modelling of Spectrally Resolved UV-Radiation in Melpitz, Germany
Löbel, Sophie	Ableitung der Meeresoberflächentemperatur aus flugzeuggetragenen Messungen mit einem Infrarot Strahlungspyrometer
Kötsche, Anton	Niederschlagsmessungen eines vertikalen Mikro Regen Radars (MRR) im Vergleich zu In-Situ-Messungen am Leipziger Institut für Meteorologie (LIM)
Käpplinger, Hannah	Verbesserte Wettervorhersage dank räumlich aufgelöster Eingabedaten in einem künstlichen neuronalen Netz?

Masterarbeiten

Wollschläger, Niels	Evaluation of a new technique for determining the sensible heat flux of green roofs
Linke, Olivia	Variation of cloud horizontal sizes and cloud fraction over Europe 1985-2018 in high-resolution satellit data
Ort, Linda	The relative importance of turbulent fluctuations compared to the variability in aerosol particle properties on the formation and growth of cloud droplets

Dissertationen

Feuerstein, Stefanie Anna	Alluvial Dust Sources and their Implementation in a Dust-Emission Model
Gong, Xianda	Cloud Condensation Nuclei and Ice-Nucleating Particles Over Tropical and Subtropical Regions in the Northern Hemisphere
Hofer, Julian	Aerosol characterization over a Central Asian site: long-term lidar profiling at Dushanbe, Tajikistan
Wagner, Robert	Dust Emissions Driven by Pyro-Convection - A Model Perspective
Wolf, Kevin	Evaluation of the Radiation Scheme of a Numerical Weather Prediction Model by Airborne Measurements of Spectral Irradiance above Clouds
Hoffmann, Erik Hans	CAPRAM mechanism and model developments for investigating marine multiphase chemistry effects linked to air quality and climate: From process to regional scale modelling
Schmölter, Erik	The delayed ionospheric response to solar and geomagnetic activity

Wissenschaftliche Mitteilungen aus dem Institut für Meteorologie der Universität Leipzig

Band 1	*A. Raabe, G. Tetzlaff* und *W. Metz* (Edn.), 1995: Meteorologische Arbeiten aus Leipzig I
Band 2	*R. Devantier*, 1995: Wolkenbildungsprozesse über der südwestlichen Ostsee - Anwendungen eines neuen Wolkenschemas in einem mesoskaligen Modell
Band 3	*J. Laubach*, 1996: Charakterisierung des turbulenten Austausches von Wärme, Wasserdampf und Kohlendioxid über niedriger Vegetation anhand von Eddy-Korrelations-Messungen
Band 4	*A. Raabe* und *J. Heintzenberg* (Edn.), 1996: Meteorologische Arbeiten aus Leipzig II
Band 5	Wind- und Seegangsatlas für das Gebiet um Darß und Zingst *D. Hinneburg, A. Raabe* und *G. Tetzlaff*, 1997: Teil I: Windatlas
Band 6	*W. von Hoyningen-Huene* und *G. Tetzlaff* (Edn.), 1997: Sediment and Aerosol Teil I: Beiträge zur Alfred-Wegener-Konferenz, Leipzig 1997 Teil II: Aktuelle Beiträge aus dem Institut für Meteorologie
Band 7	*B.-R. Beckmann*, 1997: Veränderungen in der Windklimatologie und in der Häufigkeit von Sturmhochwassern an der Ostseeküste Mecklenburg-Vorpommerns
Band 8	*P. Posse*, 1997: Bestimmung klimarelevanter Parameter des maritimen Aerosols unter besonderer Berücksichtigung der Nichtkugelform realer Aerosolteilchen
Band 9	*A. Raabe, K. Arnold* und *J. Heintzenberg* (Edn.),1998: Meteorologische Arbeiten aus Leipzig III
Band 10	Wind- und Seegangsatlas für das Gebiet um Darß und Zingst, Teil II, 1998: *D. Hinneburg, A. Raabe* und *G. Tetzlaff*: Vergleich Windatlas –Beobachtungsdaten; *M. Börngen, H.-J. Schönfeldt, F. Riechmann, G. Panin* und *G. Tetzlaff:* Seegangsatlas; *M. Stephan* und *H.-J. Schönfeldt*: Sedimenttransportatlas
Band 11	*J. Rissmann, 1998*: Der Einfluss langwelliger Strahlungsprozesse auf das bodennahe Temperaturprofil
Band 12	*A. Raabe, K. Arnold* und *J. Heintzenberg* (Edn.), 1999*:*Meteorologische Arbeiten aus Leipzig IV
Band 13	*U. Müller, W. Kuttler und G. Tetzlaff (Edn.)*, 1999: Workshop Stadtklima 17. / 18. 02. 1999 in Leipzig
Band 14	*R. Surkow, 1999*: Optimierung der Leistungsverfügbarkeit von Windenergie durch ihre Integration in Wind-Biogas-Hybridanlagen
Band 15	*N. Mölders*, 1999: Einfache und akkumulierte Landnutzungsänderungen und ihre Auswirkungen auf Evapotranspiration, Wolken- und Niederschlagsbildung
Band 16	G. Tetzlaff und U. Grünewald (Edn.), 1999:2. Tagung des Fachausschusses Hydrometeorologie 15./16. 11. 1999 in Leipzig
Band 17	A. Raabe und K. Arnold (Edn.), 2000: Meteorologische Arbeiten aus Leipzig V
Band 18	K. Arnold, 2000: Ein experimentelles Verfahren zur Akustischen Tomographie im Bereich der atmosphärischen Grenzschicht
Band 19	*A. Ziemann*, 2000: Eine theoretische Studie zur akustischen Tomographie in der atmosphärischen Grenzschicht
Band 20	*Ch. Jacobi*, 2000: Midlatitude mesopause region dynamics and its coupling with lower and middle atmospheric processes
Band 21	*M. Klingspohn*, 2000: Interdekadische Klimavariabilität über dem Nordatlantik – Statistische Analysen und Modellstudien –
Band 22	*A. Raabe* und *K. Arnold* (Edn.), 2001: Meteorologische Arbeiten aus Leipzig VI
Band 23	*K. Arnold, A. Ziemann, G. Tetzlaff, V. Mellert* und *A. Raabe* (Edn.), 2001: International Workshop Tomography and Acoustics: Recent developments and methods 06. - 07.03.2001 in Leipzig
Band 24	*O. Fanenbruck*, 2001: Ein thermophysiologisches Bewertungsmodell mit Anwendung auf das Leipziger Stadtgebiet
Band 25	*M. Lange*, 2001: Modellstudien zum CO_2-Anstieg und O_3-Abbau in der mittleren Atmosphäre und Einfluss des Polarwirbels auf die zonale Symmetrie des Windfeldes in der Mesopausenregion
Band 26	*A. Raabe* und *K. Arnold* (Edn.), 2002: Meteorologische Arbeiten aus Leipzig VII
Band 27	*M. Simmel*, 2002: Ein Modul zur spektralen Beschreibung von Wolken und Niederschlag in einem Mesoskalenmodell zur Verwendung auf Parallelrechnern
Band 28	*H. Siebert*, 2002: Tethered-Balloon Borne Turbulence Measurements in the Cloudy Boundary Layer
Sonderband	*G. Tetzlaff* (Hrsg.), 2002:- Atmosphäre - Aktuelle Beiträge zu Luft, Ozon, Sturm, Starkregen und Klima
Band 29	*U. Harlander*, 2003: On Rossby wave propagation in atmosphere and ocean
Band 30	*A. Raabe* und *K. Arnold* (Edn.), 2003: Meteorologische Arbeiten aus Leipzig VIII
Band 31	*M. Wendisch*, 2003: Absorption of Solar Radiation in the Cloudless and Cloudy Atmosphere
Band 32	*U. Schlink*, 2003: Longitudinal Models in Biometeorology: Effect Assessment and Forecasting of Ground-level Ozone
Band 33	*H. Heinrich*, 2004: Finite barotrope Instabilität unter synoptischem Antrieb
Band 34	*A. Raabe* und *K. Arnold* (Edn.), 2004: Meteorologische Arbeiten aus Leipzig IX

Band 35 *C. Stolle*, 2004: Three-dimensional imaging of ionospheric electron density fields using GPS observations at the ground and on board the CHAMP satellite

Band 36 *A. Raabe* und *K. Arnold* (Edn.), 2005: Meteorologische Arbeiten (X) und Jahresbericht 2004 des Institutes für Meteorologie der Universität Leipzig

Band 37 *A. Raabe* und *K. Arnold* (Edn.), 2006: Meteorologische Arbeiten (XI) und Jahresbericht 2005 des Institutes für Meteorologie der Universität Leipzig

Band 38 *K. Fröhlich*, 2006: The Quasi Two-Day Wave – its impact on zonal mean circulation and wave-wave interactions in the middle atmosphere

Band 39 *K. Radtke, 2006: Zur Sensitivität von Starkwindfeldern gegenüber verschiedenen meteorologischen Parametern im Mesoskalenmodell LM*

Band 40 K. Hungershöfer, *2007: Optical Properties of Aerosol Particles and Radiative Transfer in Connection with Biomass Burning*

Band 41 *A. Raabe* (Hrsg.), 2007: Meteorologische Arbeiten (XII) und Jahresbericht 2006 des Institutes für Meteorologie der Universität Leipzig

Band 42 *A. Raabe* (Hrsg.), 2008: Meteorologische Arbeiten (XIII) und Jahresbericht 2007 des Institutes für Meteorologie der Universität Leipzig

Band 43 *A. Kniffka, 2008*: Einfluss der Inhomogenitäten von Aerosol, Bodenalbedo und Wolken auf das aktinische Strahlungsfeld der Atmosphäre

Band 44 *M. Barth, 2009*: Akustische Tomographie zur zeitgleichen Erfassung von Temperatur- und Strömungsfeldern

Band 45 *A. Raabe* (Hrsg.), 2009: Meteorologische Arbeiten (XIV) und Jahresbericht 2008 des Institutes für Meteorologie der Universität Leipzig

Band 46 *G. Stober, 2009:* Astrophysical Studies on Meteors using a SKiYMET All-Sky Meteor Radar

Band 47 *A. Raabe* (Hrsg.), 2010: Meteorologische Arbeiten (XV) und Jahresbericht 2009 des Institutes für Meteorologie der Universität Leipzig

Band 48 *A. Raabe* (Hrsg.), 2011: Meteorologische Arbeiten (XVI) und Jahresbericht 2010 des Institutes für Meteorologie der Universität Leipzig

Band 49 *A. Raabe* (Hrsg.), 2012: METTOOLS_VIII Tagungsband

Band 50 *A. Raabe* (Hrsg.), 2012: Meteorologische Arbeiten (XVII) und Jahresbericht 2011 des Institutes für Meteorologie der Universität Leipzig

Band 51 *A. Raabe* (Hrsg.), 2013: Meteorologische Arbeiten (XVIII) und Jahresbericht 2012 des Institutes für Meteorologie der Universität Leipzig

Band 52 A. Raabe (Hrsg.), 2014: Meteorologische Arbeiten (XIX) und Jahresbericht 2013 des Institutes für Meteorologie der Universität Leipzig

Band 53 *A. Raabe* (Hrsg.), 2015: Meteorologische Arbeiten (XX) und Jahresbericht 2014 des Institutes für Meteorologie der Universität Leipzig

Band 54 *A. Raabe* (Hrsg.), 2016: Meteorologische Arbeiten (XXI) und Jahresbericht 2015 des Institutes für Meteorologie der Universität Leipzig

Band 55 *A. Raabe, M.Wendisch* (Hrsg.), 2017: Meteorologische Arbeiten (XXII) und Jahresbericht 2016 des Institutes für Meteorologie der Universität Leipzig

Band 56 *A. Raabe, M.Wendisch* (Hrsg.), 2018: Meteorologische Arbeiten (XXIII) und Jahresbericht 2017 des Institutes für Meteorologie der Universität Leipzig

Band 57 *A. Raabe, M.Wendisch* (Hrsg.), 2019: Meteorologische Arbeiten (XXIV) und Jahresbericht 2018 des Institutes für Meteorologie der Universität Leipzig

Band 58 *M.Wendisch* (Hrsg.), 2020: Meteorologische Arbeiten (XXV) und Jahresbericht 2019 des Institutes für Meteorologie der Universität Leipzig

Band 59 *M.Wendisch* (Hrsg.), 2021: Meteorologische Arbeiten (XXVI) und Jahresbericht 2020 des Institutes für Meteorologie der Universität Leipzig

Wissenschaftliche Mitteilungen aus dem Institut für Meteorologie der Universität Leipzig

Band 59 (2021):

Meteorologische Arbeiten XXVI
Jahresbericht 2020

ISBN 978-3-9814401-9-5

Die einzelnen Beiträge dieses Heftes wurden in einem internen Verfahren begutachtet

Abbildung auf Umschlag

Institutsgebäude – Leipziger Institut f. Meteorologie (LIM)

Herausgegeben im Selbstverlag:
Institut für Meteorologie, Universität Leipzig

Herausgeber:
M. Wendisch

Bestellungen richten Sie bitte an:

Institut für Meteorologie, Universität Leipzig
Stephanstr. 3
D-04103 Leipzig

Tel: 0341 - 9732850
Fax: 0341 - 9732899
E-Mail: birgit.seydel@uni-leipzig.de
Preis pro Band: 20,-- €